3-4

Fizika

Cild

IX

2003

Bakı ✳ Elm

SPECTRUM OF SURFACE POLARITONS ON GaSe CRYSTALS

NADIR B. MUSTAFAEV

Institute of Physics, Azerbaijan National Academy of Sciences,
Baku Az-1143, H.Javid av., 33, Azerbaijan

The spectrum of surface vibrations on GaSe exited by the optical method of attenuated total reflection (ATR) has been studied theoretically. The ATR spectra have been calculated for the geometry when the normal to the crystal surface is perpendicular to the cleavage plane. The frequency-wavevector dispersion determined by positions of the ATR spectrum minima at various angles of incident light within frequency range $214 < \nu < 254$ cm^{-1} consists of two branches. The lower branch ($\nu < 245$ cm^{-1}) corresponds to the surface mode of type I (real mode) or type II (virtual mode) depending on the wavevector value. The upper branch ($\nu > 245$ cm^{-1}) corresponds to the type II surface mode. The results of the calculation have been compared with experimental data obtained by other methods. The calculated dispersion relation at small and large values of the wavevector agrees with experimental data of infrared and Raman spectroscopy.

1. Introduction

In papers [1,2], spectra of the Raman scattering (RS) in GaSe films were investigated. In high-frequency region ($240 < \nu < 320$ cm^{-1}), the RS peaks were observed at the frequencies of $\nu_1 = 245$ cm^{-1}, $\nu_2 = 254$ cm^{-1} and $\nu_3 = 309$ cm^{-1}. For the peaks at ν_2 and ν_3, the RS intensity decreases with the film thickness, whereas the intensity of the peak at ν_1 remains almost invariable. It was explained by a great contribution of surface vibrational states to the RS cross-section at the frequency of 245cm^{-1}. In papers [3,4], the peak near of 245cm^{-1} in the spectra of infrared absorption was observed owing to thin metal (Al) layer evaporated on GaSe films. Generally, the study of surface modes by Raman and infrared spectroscopy methods is difficult because of weak intensity of the scattering [5]. A sensitive and relatively easy technique to study the surface phonon-polaritons on crystals is the method of attenuated total reflection (ATR). By the ATR method a measurement is made of the reflection spectrum of electromagnetic wave incident on the boundary surface of two media (prism-spacing layer) which is a plane of total internal reflection. The presence of a crystal at a distance from this plane involves a violation of the total reflection condition. As a result, the reflection spectrum has sharply defined minima which correspond to the light absorption due to surface phonon-polaritons [5].

For the present, the ATR spectroscopy of surface modes in GaSe has not been done. Theoretical study made in the present paper shows that the ATR spectroscopy method can substantially supplement the results of papers [1-4]. In GaSe, the ATR method will also allow observations of the surface modes of type II (so-called 'virtual excitation' surface polaritons having no analogue in isotropic crystals).

2. Reflection Spectra

The reflection coefficient of light R has been calculated by the method used in paper [6] for uniaxial crystals in accordance with conventional experimental set-up. The prism region and the region of the crystal involved are assumed to be semi-infinite along the z-axis (this axis is perpendicular to the crystal surface and the prism base). The x-axis is brought into coincidence with the plane of light incidence. The case of p-polarized light (i.e. when light is polarized in the plane of incidence) has been considered because the interaction with surface phonons does not occur in s-polarization [5].

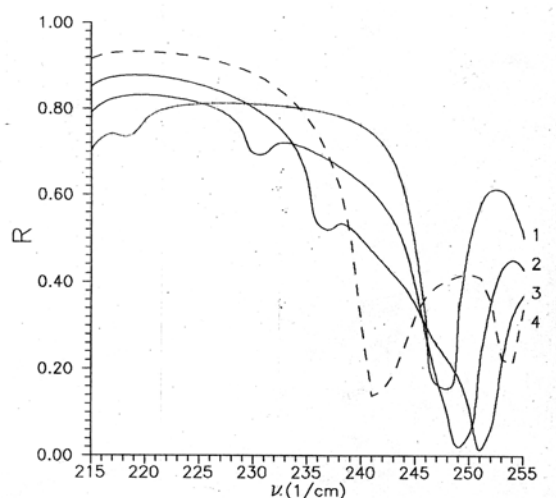The light absorption only by the crystal has been taken into account.

Fig.1. The frequency dependence of the light reflection coefficient R when the light incidence angle is equal to (1) 20^0, (2) 23^0, (3) 25^0 and (4) 28^0.
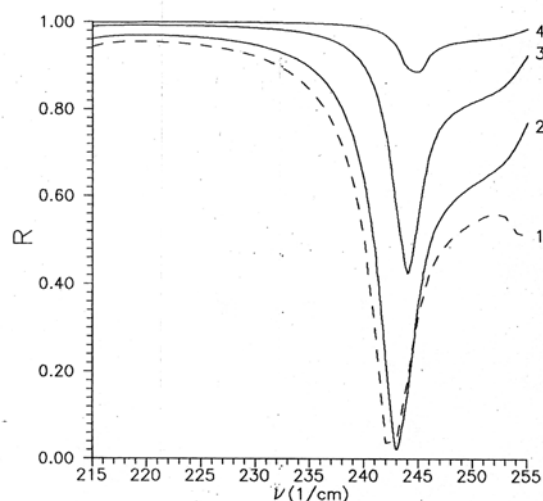

Fig.2. The frequency dependence of the light reflection coefficient R when the light incidence angle is equal to (1) 30^0, (2) 32^0, (3) 40^0 and (4) 60^0.

An expression for R has been found from the solution of a system of equations for the electric field vectors of incident and reflected waves on the prism-spacing and spacing-crystal boundaries. The expression for R has very comber some form (it is similar to that obtained in paper [6]). Numerical

calculations of the ATR spectra have been made for the most conventional geometry of experiments when the normal to the crystal surface is perpendicular to the cleavage plane. It is known that the GaSe crystals are easily cleaved parallel to the layers (the C axis of the highest symmetry is perpendicular to the cleavage plane). For calculations, the values of the transverse ν_{TO} and longitudinal ν_{LO} optical phonon frequencies, the damping constant γ and the high-frequency dielectric constant ε_∞ of GaSe given in Table 1 have been used.

Table 1.

Values of the transverse ν_{TO} and longitudinal ν_{LO} optical phonon frequencies, the damping constant γ and the high-frequency dielectric constant ε_∞ for the directions parallel and perpendicular to the optical axis C of the GaSe crystals [7].

	$\|C$	$\perp C$
ν_{TO} (cm^{-1})	237	213.5
ν_{LO} (cm^{-1})	245.5	254.7
γ (cm^{-1})	2.8	3
ε_∞	5.76	7.44

A thickness of air spacing between the prism and the crystal surface is taken to be 2.5 μm. The dependence $R(\nu)$ has been calculated for various angles of light incidence φ. In experiments, a set of silicon prisms ($\varepsilon_{Si} = 11.6$) with different base angles is often used to obtain the ATR spectra over a range from 18 to 60° [8]. The calculated reflection spectra are shown in figures 1 to 2.

3. Discussion

In figure 1, it is seen that the reflection spectrum has two minima if $\varphi < 30°$. When the angle of light incidence φ increases, then the depth of minima changes, and their position shifts towards the region of higher frequencies. At $\varphi = 28°$ these minima have comparable depth. If $\varphi > 30°$, the $R(\nu)$ dependence has one minimum (fig. 3).

Points on figure 3 corresponds to the position of the $R(\nu)$ minima depending upon the reduced wavevector of surface polariton $\kappa = q_x / 2\pi\nu$. The relation between κ and the angle of light incidence φ is expressed by the formula

$$\kappa = \sqrt{\varepsilon_{Si}} \, \sin \varphi$$

In figure 3, it is seen that there are two dispersion branches. If $\kappa < 1.5$, the lower branch corresponds to a surface mode of type II (virtual mode) because within the frequency range $214 < \nu < 237$ cm^{-1} the dielectric constant component ε_z is positive and greater that κ^2 (the z-axis is parallel to the C axis). If $\kappa > 1.5$, the lower branch corresponds to a surface mode of type I (it is a real mode because $\varepsilon_z < 0$): at $\kappa = 2$ its frequency reaches the value of 244cm^{-1} (the further change of the frequency is small). The upper branch corresponds to the type II surface mode ($\varepsilon_z < \kappa^2$ within the frequency range from 246 to 254cm^{-1}): if $\kappa > 1.6$, the vibrations corresponding to this branch vanish (according to [5], the point where $\varepsilon_z = \kappa^2$ and $\varepsilon_x = 0$ is a stop point for the vibrations). The region of small wavevectors ($\kappa < 1$) corresponds to the radiative surface modes studied in papers [3,4]. In figure 3, the frequency value of 245cm^{-1} is shown by dashed line. When $\kappa < 1$, the dashed line corresponds to the film mode observed in paper [3]. At $\kappa \gg 1$ (in papers [1,2] the measurements were made for this region), the dashed line corresponds to the peak ν_l observed in the RS spectra. From figure 3, it follows that the calculated dispersion curve agrees well with the experimental data available at small and great values of κ. The present paper to be a stimulus for setting up experiments on GaSe by the ATR metod. Results of such experiments will make the comparison in intermediate region of the wavevector values possible.
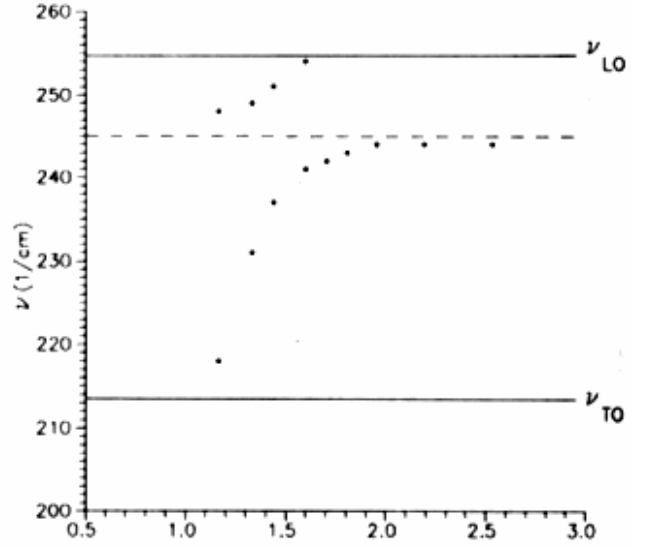

Fig. 3. The dispersion curve of surface polaritons. The points correspond to minima of the $R(\nu)$ dependence given in figures 1 and 2. Solid lines show the frequencies of transverse ν_{TO} and longitudinal ν_{LO} optical phonons in the directions parallel and perpendicular to the optical axis C of the GaSe crystals. The dashed line corresponds to the experimental data available at small ($\kappa < 1$) and great ($\kappa \gg 1$) values of the reduced wavevector κ.

4. Conclusion

The spectrum of surface vibrations on GaSe excited by the optical method of attenuated total reflection has been calculated. It is shown that the dispersion curve has two branches. One of the branches corresponds to the surface mode of type II (virtual mode). The other branch corresponds to the surface mode of type II or to the surface mode of type I (real mode): it depends on the wavevector value of surface polaritons. Results of the calculation agree well with experimental data obtained by other optical methods.

[1] *V.S.Gorelik, A.G.Abdullaev, T.D.Ibragimov.* Poverkhnost, 1988, №4, p.55.

[2] *T.D.Ibragimov, G.G.Kurbanova, V.S.Gorelik.* Phys. Status Solidi (b), 1989, v.155, p.113.

[3] *V.M.Burlakov, E.A.Vinogradov, G.N.Zhizhin, N.N.Melnik, D.A.Rzaev, V.A.Yakovlev.* Fiz. Tverd. Tela, 1979, v.21, p.2563.

[4] *V.M.Burlakov, E.A.Vinogradov, G.N.Zhizhin, D.A.Rzaev, V.A.Yakovlev.* Optika i Spektroskopiya, 1979, v.47, p.926.

[5] *V.M.Agranovich, D.L.Mills (Eds).* Surface Polaritons. North-Holland, Amsterdam, and Nauka Publishing, Moscow, 1985. *V.V.Bryksin, D.N.Mirlin, I.I.Reshina.* Fiz. Tverd. Tela, 1973, v.15, p.1118.

[6] *R. le Toullec, N.Piccioli, M.Mejatty, M.Balkanski.* Nuovo Cimento B, 1977, v.38, p.159.

[7] *V.V.Bryksin, Yu.M.Gerbshtein, D.N.Mirlin.* Fiz. Tverd. Tela, 1972, v.14, p.543.

Nadir B. Mustafaev

GaSe KRİSTALINDA SƏTHİ POLYARİTONLARIN SPEKTRİ

Laylı GaSe kristallarında işığın tam daxili qayıtmasını pozma metodu ilə həyəcanlandırılmış səth rəqslərinin spektri nəzəri cəhətdən tədqiq olunub. Spektrin hesablanması, kristal səthinin parçalanma müstəvisinə təsadüf etdiyi hal üçün aparılmışdır. İşığın düşmə bucağının müxtəlif qiymətlərində qayıtma spektrində müşahidə olunan minimumların vəziyyətinə görə müəyyən edilmiş dispersiya asılılığı 214<v254 sm-1 tezlik diapazonunda iki əyridən ibarətdir. Alt əyri (v<245 sm-1), dalğa vektorundan asılı olaraq ya I tip (real), ya da ki, II tip (virtual) səth modasına müvafiqdir. Üst əyri (v>245sm-1), II tip səth modasına aiddir. Alınan nəticələr başqa metodlarla aparılmış təcrübələrin nəticələri ilə müqayisə edilmişdir.

Надир Б. Мустафаев

СПЕКТР ПОВЕРХНОСТНЫХ ПОЛЯРИТОНОВ В КРИСТАЛЛАХ GaSe

Теоретически исследован спектр поверхностных колебаний в GaSe, возбуждаемых оптическим методом нарушенного полного внутреннего отражения (НПВО). Расчет спектров НПВО проведен для геометрии, когда нормаль к поверхности кристалла перпендикулярна плоскости скола. Дисперсионная зависимость, определенная по положению минимумов спектра НПВО при различных углах падения света, в диапазоне частот 214<v<254 см$^{-1}$ состоит из двух ветвей. Нижняя ветвь (v<245см$^{-1}$) соответствует, в зависимости от величины волнового вектора, поверхностной моде типа I (реальная мода), или же типа II (виртуальная мода). Верхняя ветвь (v>245 см$^{-1}$) относится к поверхностной моде типа II. Результаты расчета сопоставлены с экспериментальными данными, полученными другими методами.

THE SPECTRUMS OF INFRARED REFLECTION AND COMBINATIONAL DISPERSION OF LIGHT IN OXIDE-SULPHIDE OF LANTAN CRYSTALS

G.I. ABUTALYBOV, I.I. ABDULLAYEV, S.A. LOZITSKIY, A.A. MAMEDOV

Institute of Physics Azerbaijan National Academy of Sciences
H.Javid av.,33, Baku 1143

The frequencies of normal fluctuations of a crystal La_2O_2S, active in spectra of combinational dispersion of light are determined. The dispersion method of the analysis of spectra of reflection determines frequencies and constants of attenuation longitudinal (TO) and cross (LO) phonons, is calculated the imaginary part complex of dielectric permeability (ε'').

For realization of a number of physical researches and creation of devices on a basis oxide-sulphide rare-earth of elements is necessary the knowledge of such characteristics as width of lines of optical transitions, speed non-radiative relacsation, structure electron - oscillatory spectra. A basis for understanding of processes electron - oscillatory interaction and first investigation phase of dynamics of a crystal lattice is that information about single-phonon processes, which follows from optical oscillatory spectra of crystals.

The basic information on dynamics of a crystal lattice can be received at research single-phonon's of spectra of infra-red reflection and combinational dispersion of light. In single-phonon's processes of infra-red reflection participate phonons with a wave vector $\kappa < 10^3 sm^{-1}$, while at edge of a Brilljuen zone $\kappa \approx 10^8 sm^{-1}$. It gives the basis to carry out classification of fluctuations, active in the given processes, assuming $k=0$. Thus usually consider, that the equivalent atoms of a crystal distinguishing on a vector primitive compilations, change in phase in all primitive cells. Thus, the cell participates in fundamental fluctuations everyone primitive equally and at the analysis of types of fluctuations of a crystal it is possible to be limited only it to one consideration. The primitive cell lantan oxide-sulphide contains 5 atoms, that defines 15 fluctuations, from which three concern to acoustic (mixture of a cell as whole, the frequencies of these mixtures are close to zero), and stayed 12 fluctuations concern to optical.

The complete oscillatory representation of group D_{3d} will be, consist of the following not resulted representations:

$$\Gamma = 3A_{2u} + 2A_{1g} + 3E_u + 2E_g \qquad (1)$$

from which acoustic fluctuations: $\Gamma_{a\kappa} = A_{2u} + E_u$

The information on the stayed types of fluctuations can be received from spectra of combinational dispersion. (In these spectra the fluctuations A_{1g} and E_u) are active. Tensor of combinational dispersion for various types of fluctuations looks like:

$$A_{1g} = \begin{pmatrix} a & 0 & 0 \\ 0 & a & 0 \\ 0 & 0 & b \end{pmatrix} ; \quad E_{g1} = \begin{pmatrix} c & 0 & 0 \\ 0 & -c & d \\ 0 & d & 0 \end{pmatrix} ; \quad E_{g2} = \begin{pmatrix} 0 & -c & -d \\ -c & 0 & 0 \\ -d & 0 & 0 \end{pmatrix}, \qquad (2)$$

where: *a, b, c, d* - not zero tensor components of combinational dispersion. The spectra of combinational dispersion of light were raised by lines argon laser $\lambda_B = 476,3$ and 488,0 nm in $90°$ geometry and were registered at room temperature with the help double monochromator ДФС - 24, with the sanction it is not worse $1 sm^{-1}$. The radiation argon laser has sufficient intensity in a continuous mode for supervision active in spectra of combinational dispersion of light of fluctuations. In a fig. 1 the spectra of combinational dispersion of light for crystals $La_{1,95}Nd_{0,05}O_2S$ are given at various directions of polarization of falling and absent-minded light, and in tab.1 of frequency of normal fluctuations.

For crystals with spatial group D_{3d}^3 the circuit of dispersion XX and YY, agrees tensor of combinational dispersion, are identical, therefore was to lead researches in one of these geometry enough. In geometry YY by rules of selection all normal fluctuations of crystals Ln_2O_2S should be shown. For identification of normal fluctuations of a class E_g it is enough to investigate a spectrum of combinational dispersion in XZ of geometry, that unequivocally defines a low-frequency style of a class E_g (tab. 1). In geometry XY the high-frequency style of a class E_g is shown. The spectrum of combinational dispersion in ZZ of geometry unequivocally defines frequencies of normal fluctuations of a class A_{1g}.

Table 1

Frequencies of normal fluctuations in spectra of combinational dispersion of light.

Crystal	$\nu_1(A_{1g})$,sm^{-1}	$\nu_2(A_{1g})$,sm^{-1}	$\nu_3(E_g)$,sm^{-1}	$\nu_4(E_g)$,sm^{-1}
$La_{1,95}Nd_{0,05}O_2S$	193	402	110	352
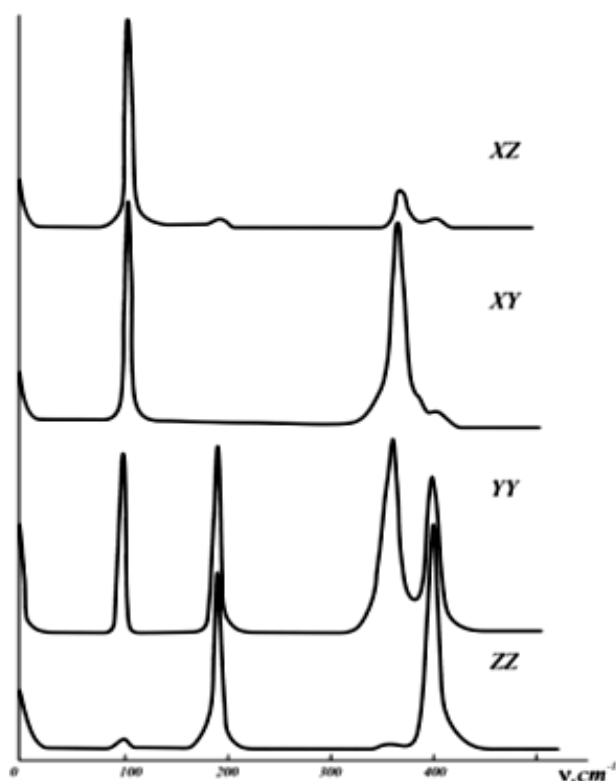
Fig. 1 Spectra of combinational dispersion of light of a crystal. La$_{1,95}$ Nd$_{0,05}$O$_2$S at T=293K λ_B = 488,0 nm.

The collateral maxima in spectra of combinational dispersion specify an error of orientation of crystals, and also discrepancy of exhibiting of samples during measurement. The polarized spectra of infra-red reflection were received by us with the help longwave infra-red spectrometer ИС АН USSR - ДВИКС. The experimental installation for research of optical properties of materials in longwave area of a spectrum represents one-beam spectrometer with difraction lattice assembled on the circuit Cherny-Terper. The optical circuit spectrometer is submitted in a fig. 2.
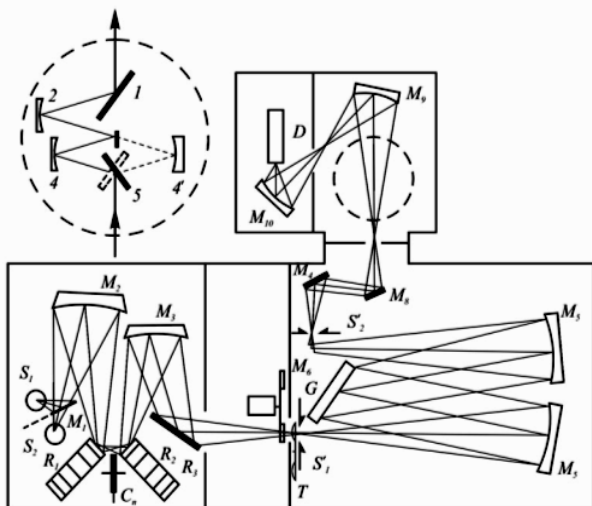

Fig. 2. Spectrometr's optical circuit. S$_1$, S$_2$– sources (globar and mercury lamp accordingly); M1,M6–flat mirrors; M2–M5, M7–M9–spherical mirrors; M10 – ellipsoid mirror; R1,R2 and R3–reflecting filters; T– passing filter; S1$^{'}$, S2$^{'}$- entrance and target crack; C$_n$ - modulator; G - diffraction lattice tice; Д – ; detector (Goley's cell) 1,5–flat mirrors of a prefix ИПО–22;2, 4, 4′-toroidal mirrors; 3 - location of a sample.

Essential difference spectrometer ДВИКС from industrial (HITACHI) ФИС- 21 is the presence in last of intermediate focus (prefix ИПО- 22 ЛОМО in tray branch spectrometer). The quantity of substance necessary for experiment, has decreased approximately in 40 times, thus became to possible research of reflection and missing of samples of the small sizes 4 x 5 mm^2 at an irradiation them monochromatic light. In quality of polarizator were used aluminium polyethylene lattices.

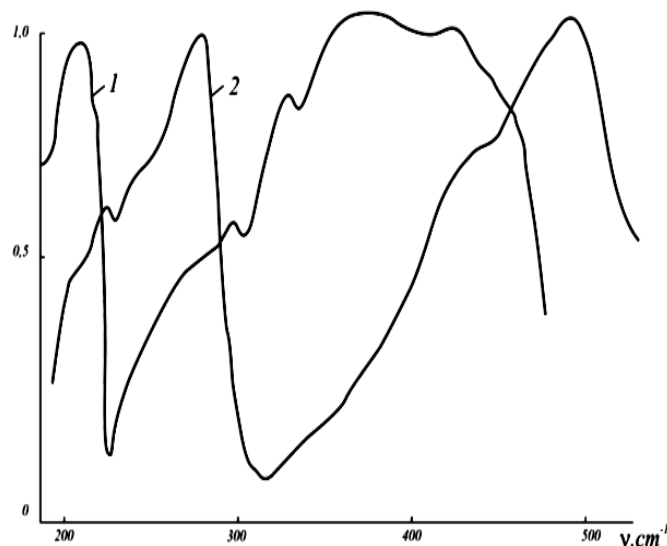*Fig. 3.* The polarized spectra of infra-red reflection of monocrystals La$_{1,95}$Nd$_{0,05}$O$_2$S at 293K for $E \perp C$ (1) and $E \parallel C$ (2) polarization.

We carried out measurements with the sanction not worse 1,5 sm^{-1}, with an error of definition of reflective ability it is not worse 3 %. In a fig. 3 the spectra of reflection of monocrystals La$_{1,95}$Nd$_{0,05}$O$_2$S in $E \perp C$ and $E \parallel C$ geometry . One of the basic tasks of mathematical processing of spectra of reflection is the reception from them of function complex dielectric of permeability:

$$\varepsilon(\omega) = \varepsilon'(\omega) + i\varepsilon''(\omega) \quad (3)$$

as it characterizes interaction of electromagnetic radiation with substance. The decision of the put task is searched or with the help dispersion of the attitudes Kramers-Kroning, or on the basis of model dispersion oscillator.

Elementary mathematical formula of a parity Kramers-Kroning allows to present factor of mirror reflection as:

$$\theta(\omega_i) = \frac{2\omega_i}{\pi} \int_0^\infty \frac{\ln R(\omega) - \ln R(\omega_i)}{\omega^2 - \omega_i^2} d\omega$$

$$(4)$$

Using the formulas

$$n^*(\omega) = n(\omega) + ik(\omega)$$

$$(5)$$

$$\varepsilon(\omega) = \varepsilon'(\omega) - i\varepsilon''(\omega)$$

$$n(\omega) = \left(1 - R^2(\omega)\right)\big/\left(1 - 2R(\omega)\cos\theta(\omega) + R^2(\omega)\right); \qquad (6)$$

$$k(\omega) = 2R(\omega)\sin\theta(\omega)\big/\left(1 - 2R(\omega)\cos\theta(\omega) + R^2(\omega)\right); \qquad (7)$$

$$\varepsilon'(\omega) = n^2(\omega) - k^2(\omega); \qquad (8)$$

$$\varepsilon'' = 2n(\omega)\cdot k(\omega), \qquad (9)$$

where $n^*(\omega)$ – complex parameter of refraction ; $R(\omega)$ – reflective ability of a crystal; $k(\omega)$ – the parameter of absorption, is possible to receive a spectrum $\varepsilon'(\omega)$, $\varepsilon''(\omega)$ – from a spectrum $R(\omega)$.

Knowing dependence dielectric permeability from frequency, we receive cross frequencies of phonons ω_{TO} as a maximum of function $\varepsilon''(\omega)$, and frequency ω_{LO} longitudinal phonons, as maxima of function - $I_m\left(1/\varepsilon(\omega)\right)$.

In a method Kramers-Kroning there is a mistake at calculation of integral (4), as the spectrum of reflection is measured only in the limited area, therefore integral is calculated not from 0 to ∞, and from $\omega_{нижн}$ to $\omega_{верх}$. The elementary approach for reception $\theta(\omega_i)$ is the acceptance $R=const$ outside area of integration [1].

The dispersion oscillator method allows to pick up parameters which are included in expression

$$\varepsilon(\omega) = \varepsilon_\infty + \sum_{n=1}^{N} \frac{S_{tn}}{\omega_{tn}^2 - \omega^2 - ig_{tn}\omega}; \qquad (10)$$

where S_{tn} –intensity; ω_{tn} and g_{tn} –frequency and constant of attenuation n's cross (TO) fluctuations; ε_∞ - the contribution of high-frequency electronic fluctuations, so that a deviation of a settlement spectrum of reflection from experimental was minimal [2].

For the analysis of complex spectra of the reflection consisting of close located strips of residual beams the expression for $\varepsilon(\omega)$, containing frequencies TO and LO phonons [3, 4] is used:

$$\varepsilon(\omega) = \varepsilon_\infty \prod_{n=1}^{N} \frac{\omega_{LOn}^2 - \omega^2 + i\omega\gamma_{LOn}}{\omega_{TOn}^2 - \omega^2 + i\omega\gamma_{TOn}}; \qquad (11)$$

Using expression for $R(\omega)$:

$$R(\omega) = \left| \frac{\sqrt{\varepsilon(\omega)} - 1}{\sqrt{\varepsilon(\omega)} + 1} \right|^2 , \qquad (12)$$

minimize criterion function $\delta\left(\omega_{TO_n}, \gamma_{TO_n}, \omega_{LO_n}, \gamma_{LO_n}, \varepsilon_\infty\right)$

$$\delta = \sum_{j=1}^{M} \left(R_{эксп}(\omega_j) - R_{расч}(\omega_j) \right)^2 \qquad (13)$$

where M –number of experimental points; $R_{эксп.}(\omega_j)$ – experimental factor of reflection on frequency ω_j ;

$R_{расч.}(\omega_j)$ –factor of reflections counted on the formulas (11) and (12).

The value ω_{TO}, ω_{LO}, at which the minimum of criterion function (13) is reached, corresponds to frequencies cross and longitudinal phonons.

The interaction phonons results to frequency dependences γ_{TO}, γ_{LO}, ω_{TO}, ω_{LO}. In a method dispersion oscillator these values are considered constant, that results in a mistake of account of frequencies of fluctuations and optical characteristics.

In our case (fig. 3) distance on a scale of frequencies between oscillators is more than attenuation of each of them, therefore application of a method dispersion oscillator does not result to essential errors in definition of parameters these oscillators [5].

The oscillators' parameters were defined with the help of the program ЕОДА [5]. The basis of the program ЕОДА is made by the subroutine FUMILI. Its algorithm represents a method of the short matrix second made $\dfrac{\partial^2\delta}{\partial x_m \partial x_k}$ [6]. The minimum is reached or on border of a range of definition, or in points of the decision of system of the equations

$$\frac{\partial\delta}{\partial x_i} = 0, X_{4n-3}=\omega_{TOn}, X_{4n-2}=\gamma_{TOn}, X_{4n-1}=\omega_{LOn},$$

$$X_{4n}=\gamma_{LOn}, X_{4N+1}=\varepsilon_\infty, n=1,2, \ldots\ldots, N, \qquad (14)$$

where N – number of oscillator.

By the form of spectrum of reflection it is possible to define parameters X_i with accuracy 10 % for and up to 50 % for γ and to take them as initial approach. The successful choice of initial approach excludes hit in a local minimum. At the large root-mean-square deviation it is necessary to use the designed oscillators' parameters and ε_∞ for the following approach. The process of calculation of oscillators' parameters ε_∞ also is considered completed, if values $к+1$ –s' approacsimates' coincides with settlement (k –s') to with some small positive size eps. The analysis of spectra of infra-red reflection by a method dispersion oscillator has allowed to define values of frequencies $\nu(\Gamma)$ for longitudinal TO and cross LO of fluctuations and parameters γ_{TO} and γ_{LO}, describing processes of attenuation oscillator (tab. 2), and also dispersion of dependence of an imaginary part complex dielectric permeability in various polarization of falling light (fig. 4).

Table 2

Frequencies of normal fluctuations and constants of attenuation oscillators in spectra of infra-red reflection of light in crystals $La_{1,95}Nd_{0,05}O_2S$

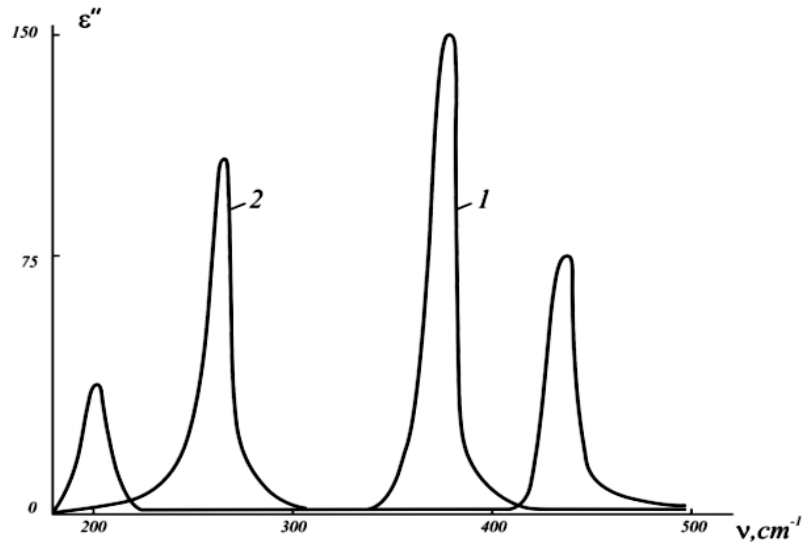| Crystal	Polarization	v (г)	v_{TO}, sm^{-1}	v_{LO}, sm^{-1}	γ_{TO}	γ_{LO}	ε_∞
$La_{1,95}Nd_{0,05}O_2S$	$E\,\|\,C$	$v_5(A_{2u})$	414	562	12	27	5,31
		$v_6(A_{2u})$	241	304	6,4	13	
	$E \perp C$	$v_4(E_u)$	325	488	11	15	7,17
		$v_8(E_u)$	198	221	3,1	3,6	

Fig. 4. Spectra of an imaginary part of complex permeability of a crystal $La_{1,95}Nd_{0,05}O_2S$ at 293K for $E \perp C$ (1) and $E\,\|\,C$ (2) polarization

We found vectors of mixtures of atoms at normal fluctuations.

In a fig. 5 they are given for active in spectra of infra-red absorption and combinational dispersion of optical styles. Really, the atoms *La* participate in all fluctuations. The reference of various fluctuations of the same symmetry on frequencies was carried out on the basis of the following reasons. In fluctuations v_6 and v_8 groups of atoms incorporated in parallelogram La_2O_2 go as whole (along an axis Z for v_6 and in a plane XOY for v_8), and thus connection S - La, weakest participates only in these fluctuations.

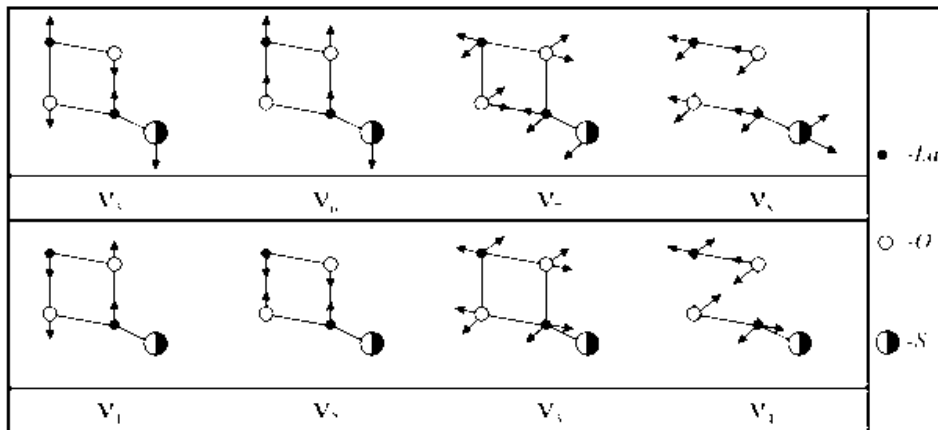*Fig. 5.* Vectors of displacement of atoms at normal fluctuations of a crystal La_2O_2S

Therefore it is natural to assume, what exactly these fluctuations will be low-frequency. From a fig. 5 follows, that the fluctuations v_7 result in prompting much greater dipolar moment, than v_8. It will be coordinated with much more LO - TO splitting for v_7 in comparison with v_8.

Let's note, that in all these fluctuations does not participate is sulphur. It explains affinity of frequencies of

fluctuations La_2O_2S and isostructure connection of La_2O_3.

[1] *M. Gottliev.* Optical properties of lithium floride in the infrared. – J. Opt. Soc. Am, 1960, V.50, №4 p. 343 – 349

[2] *W.G.Spitzer, R.C.Miller, D.A.Kleinman, L.E.Howarth.* Far infrared dielectric dispersion in Ba TiO_3, $ScTiO_3$ and TiO_3 – Phys. Rev, 1962, V 12^b, №5. P. 1710 – 1721

[3] *H.T. Bowlden, T.K. Wilmshesrst.* Evaluation of optical constants J. Opt. Soc. Amer. 1963. V.53. №9 p. 1073 – 1078.

[4] *M.V. Belousov.* Vosstanovlenie infrakrasnogo spektra dielektricheskoy pronitsaemosti iz spektrov kombinatsionnogo rasseyaniya. FEE, 1973, t. 15, № 10, s. 1206 – 1212.

[5] *V.M. Burlakov, D.A. Rzayev, V.M. Pirkov* Metodika raschota opticheskix xarakteristik iz spektrov IK otrajeniya monokristallov. Preprint № 6 Fronts, IS AN SSSR, 1985, s.28.

[6] *B.P. Demidovich, N.A. Maron.* Osnovi vichislitelnoy matematiki. M., Nauka,1980, s. 660.

H. İ. Abutalıbov, İ. İ. Abdullayev, S.A. Lozitskiy, A.A. Məmmədov

LANTAN OKSİSULFİDLİ KRİSTALLARINDA İNFRAQIRMIZI QAYITMA VƏ İŞIĞIN KOMBİNASİON SƏPİLMƏSİ

Kombinasion səpilmə spektrlərində La_2O_2S kristalının aktiv olan normal rəqslərin **t**ezliyi təyin edilmişdir. Qayıtma spektrlərindən dispersion analiz metodu ilə, uzununa (TO) və eninə (LO) fononların tezliyi və sönmə əmsalı təyin edilmiş, dielektrik nüfuzluğunun ($\varepsilon^{''}$) xəyali hissəsi hesablanmışdır.

Г.И. Абуталыбов, И.И. Абдуллаев, С.А. Лозицкий, А.А. Мамедов

СПЕКТРЫ ИНФРАКРАСНОГО ОТРАЖЕНИЯ И КОМБИНАЦИОННОГО РАССЕЯНИЯ СВЕТА В КРИСТАЛЛАХ ОКСИСУЛЬФИДОВ ЛАНТАНА

Определены частоты нормальных колебаний кристалла La_2O_2S, активные в спектрах комбинационного рассеяния света. Методом дисперсионного анализа спектров отражения определены частоты и константы затухания продольных (TO) и поперечных (LO) фононов, вычислена мнимая часть комплексной диэлектрической проницаемости ($\varepsilon^{''}$).

PHOTOOXIDATION OF DONOR MOLECULES ON THE SURFACE OF BN

N.H. HASANOV, M.A. MEHRABOVA

Radiation Problems Institute of Azerbaijan National Academy of Sciences,
370143, Baku,   H. Javid av. 31 a., Azerbaijan Republic

It has been provided photochemical reactions with participation of photoadsorbed O_2 on the surface of hexagonal BN. It has been found that the region of photoadsorption specter is the same with the photooxidation one. The photoadsorption and photooxidation processes take place on the same photoactive center of solid and both of these processes occurs owing to photoexcitation of this center. The NO forms during photooxidation processes, which do not takes place only in the absence of light. The life time of excited oxygen is lower than that of the oxygen photoadsorption centers by an order of magnitude. The initial velocity of photoadsorption of H_2 decreases with increase of concentration of one of the reagents.

Key words: Photoadsorption, boron nitride, hole centers, photooxidation, donor molecules.

The photochemical processes with participation of H_2, O_2, CH_4 and etc. for more of oxides and alkaline halloid compounds have been investigated [1-3]. But A_3B_5 type compounds haven't been examined as a photocatalytic active object earlier. The results of investigations of photochemical reactions with participation of photoadsorbed O_2 on the surface of disperse samples of hexagonal boron nitride are given in this work.

The object and method of investigations were described in [4]. The products of photooxidation were analysed by mass-spectroscopic, manometric and thermodesorption (TD) methods. The pressure of used donor gases H_2, C_2H_6, CH_4 was P~l Pa.

Two possible variants of photooxidation reactions were established. In first case BN was radiated by light with mixture of donor gases H_2, C_2H_6, CH_4, and O_2. In second case O_2 preliminarily photoadsorbed on the surface of BN and then this system was radiated in the presence of donor gases. In first case the reaction of oxidation takes place with a constant velocity up to a complete use of compounds. The second reaction takes place with decrease of donor gas pressure. In this case the more preliminarily photoadsorbed oxygen the more the absorbed gas quantity (fig. 1).

By the TD analyze method was determined that the quantity of O_2, remaining on the surface decreases with absorbed donor gas one (fig. 2).

Under the heating from the TD spectrum disappear zones, corresponding to molecules with a small binding energy. Then heating up to 7OOK temperatures show that absorbed donor molecules can't excreted to gas phase, but only the products of there photooxidation (H_2O, CO_2 and etc.) have been observed. This means that photooxidation of donor molecules takes place owing to repited photoexcitation preliminarily photoadsorbed O_2. The first stage of photooxidation is photoadsorption of O_2 (1) and the second one is repeated photoexcitation of unactive O_2. In dark (2):

$$K + O_2 + h\nu_1 \rightarrow O_2 + K \qquad (1)$$
$$K + O_2 + h\nu_2 \rightarrow O_2^* + M \rightarrow product + K \quad (2)$$
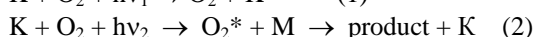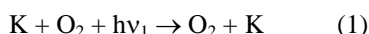
where K is photocatalysator, M is donor gas in gas phase, O_2 and O_2^* are unactive and active forms of photoadsorbed O_2, $h\nu 1$ and $h\nu_2$ are corresponding energies of light.

The region of photoadsorption spectrum is the same with the photooxidation one. To our mind this means the photoadsorption and photooxidation processes take place on

the same photoactive center of solid and both of these processes occurs owing to photoexcitation of this center.
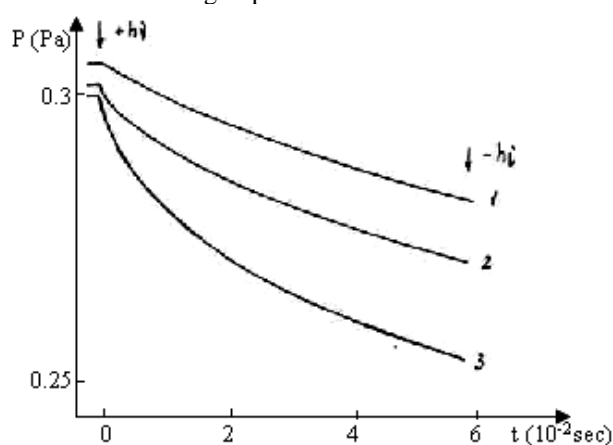
Fig. 1. The barogramms of photooxidation of H_2 (1), CH_4 (2) and C_2H_6 (3) at the same quantity of preliminarily photoadsorbed O_2 ($\Delta P_{O_2} = 5,7 \cdot 10^{-2}$ Pa)
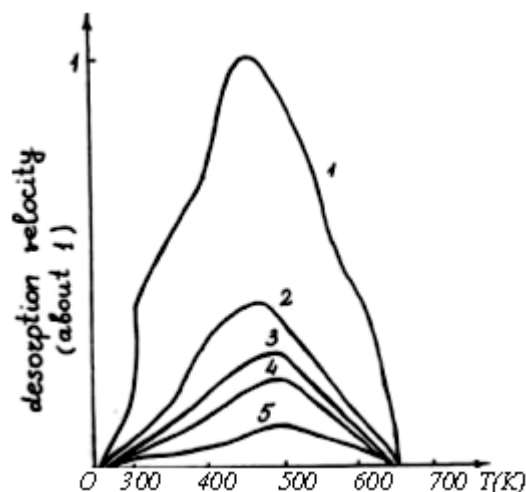
Fig. 2. TD-spectrums of photoadsorbed O_2 before (1) and after (2, 3, 4, 5) the photooxidation of C_2H_6.

TD spectrograms indicate forming also of NO during the photooxidation processes, which do not take place only on the absence of light. As a result of these processes take place partly oxidation on the surface of BN.

The life time of excited photoadsorbed oxygen has been

estimated from dependence of initial velocity of photoabsorption of H_2 on it pressure in value at the constant quantity of preliminarily photoadsorbed O_2, which is lower than that of the oxygen photoadsorption centers by an order of magnitude.

The dependence of initial velocity of photoabsorption of H2 on the quantity of preliminarily photoadsorbed O_2 has been investigated. The initial velocity decreases with increase of concentration of one of the reagents. The dependence is explained by a partial adsorption of photoadsorbed oxygen on the hole centers which are the photoadsorption centers for H_2 and blocks their for H_2 adsorption.

Thus observed effect is the result of addition of two processes: decreasing of photoadsorption velocity from blocking of some centers and increasing of photoabsorption velocity from increasing of concentration of photosorbed and photoexcited O_2.

[1] *L.L.Basov, Y.P.Solonitsin, A.N.Terenin*. Dokl. AN USSR, 164, 1965, 122.

[2] *V.K.Ryabchuk, L.L. Basov, Y.P. Solonitsin*. Kynetica and catalys, 19,3, 1978, 685-690.

[3] *Y.P. Solonitsin, L.L. Basov, V.K.Ryabchuk*. Journal of Phys. Chemistry, 54, 10, 1980, 2624-2628.

[4] *N.H.Hasanov, L.L. Basov*. Vestnik LGU, 4, 3, 18, 1991, 30-36.

[5] *L.L. Basov, N.H.Hasanov*. Vsesoyuznaya konferensiya po photoelectrochimii i photocatalizu, Minsk, 1992, 177-179.

N.H. Həsənov, M.A. Mehrabova

BN SƏTHİNDƏ DONOR MOLEKULLARININ FOTOOKSİDLƏŞMƏSI

Fotoadsorbsiya olunmuş O_2 molekulunun iştirakı ilə heksaqonal quruluşa malik nitrid borun səthində fotokimyəvi reaksiyalar aparılmışdır. Müəyyən edilmişdir ki, fotooksidləşmə effektinin spektral təsir oblastı fotoadsorbsiyanın spektral oblastı ilə üst-üstə düşür. Fotoadsorbsiya və fotooksidləşmə prosesləri bərk cismin səthində eyni mərkəzlərin fotohəyəcanlanması hesabına baş verir. O_2 molekulunun fotoadsorbsiyası və O_2 postsorbsiya olunmuş sistemin şüalanması zamanı TD–spektrdə NO-ya uyğun zolaq aşkar olunmuşdur. Fotoadsorbsiya olunmuş O_2-nin aktiv formasının yaşama müddəti fotoadsorbsiya mərkəzlərinin yaşama müddətindən bir tərtib kiçikdir.

Н.Г. Гасанов, М.А. Мехрабова

ФОТООКИСЛЕНИЕ ДОНОРНЫХ МОЛЕКУЛ НА ПОВЕРХНОСТИ НИТРИДА БОРА

Проведены фотохимические реакции с участием фотосорбированного O_2 на поверхности гексагонального BN. Определено, что спектр действия эффекта фотоокисления тот же, что и для фотоадсорбции. Процессы фотоадсорбции и фотоокисления происходят на одних и тех же фотоактивных центрах твердого тела за счет фотовозбуждения этих центров. При адсорбции O_2 непосредственно в момент облучения, а также при последующем облучении системы с постсорбированным кислородом в ТД спектре появляется NO. Время жизни возбужденной формы фотоадсорбированного на порядок меньше времени жизни центров фотоадсорбции для кислорода. Начальная скорость фотопоглощения H_2 уменьшается с увеличением концентрации одного из реагентов.

$(Ge_2S_3)_{1-x}$ $(GeS)_x$ BƏRK MƏHLULLARIN ELEKTRİK XASSƏLƏRİ

A.Ə. NƏBİYEV, H.R. QURBANOV
ADPU, Ü.Hacıbəyov, 34

Ge_2S_3-GeS sistemində Ge_2S_3 əsasında tərkibi 1, 2, 3, 4 mol% GeS olan bərk məhlul nümunələrin elektrikkeçirməsinin və termo-e.h.q.-nin temperaturdan asılılığı öyrənilmişdir. Məlum olmuşdur ki, bərk məhlul nümunəsində GeS-in miqdarı artdıqca onların elektrikkeçirməsi də artır və qadağan olunmuş zolağın eni isə azalır. Termo-e.h.q.-si isə temperatur artdıqca qanunauyğun olaraq azalır. Termo-e.h.q.-nin işarəsinin dəyişməsinə görə nümunələrdə keçiriciliyin tipi müəyyən edilmişdir. Bütün tərkib nümunələri "p"- tip keçiriciliyə malik olmuşdurlar.

Ge_2S_3-GeS sistemində Ge_2S_3 birləşməsi və onun əsasındakı bərk məhlul sahəsindəki ərintilərin elektrikkeçirmə və termo-e.h.q.-si öyrənilmişdir. Bu məqsədlə $(Ge_2S_3)_{1-x}$ $(GeS)_x$–də x=0,00; 0,01; 0,02; 0,03 və 0,04 tərkibli ərintilər ayrıca sintez edilmiş və 900K temperaturda 250 saat müddətində dəmləməyə qoyulmuşdur.

Elektrofiziki xassələri ölçmək üçün alınmış nümunələr xüsusi həndəsi formaya (uzunluğu l=8-10 mm, diametri d=4-6 mm) salınmışdır.

Ge_2S_3 birləşməsinin və onun əsasındakı 1, 2, 3, 4 mol% GeS tərkibli ərintilərin elektrikkeçirməsinin temperatur asılılığı qrafik olaraq şəkil 1(a)-da verilmişdir. Qadağan olunmuş zolağın eni və elektrikkeçirmənin tərkibdən asılı olaraq dəyişməsi isə şəkil 1(b)-də göstərilir.
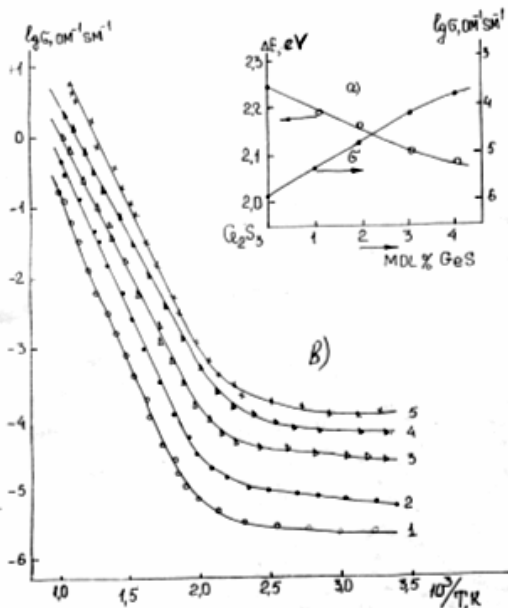
Şəkil 1(a). Ge_2S_3-GeS birləşməsinin və onun əsasındakı 1, 2, 3, 4 mol% GeS tərkibli ərintilərin elektrikkeçirməsinin temperaturdan asılılığı 1- Ge_2S_3; 2 -1 mol% GeS;3 -2 mol% GeS;4-3 mol% GeS;5-4 mol% GeS. *(b).* 1, 2, 3, 4 mol% GeS tərkibli ərintilərin qadağan olunmuş zolağın eni və elektrikkeçirmənin tərkibdən asılılığı.

GeS birləşməsinin bərk məhlul sahəsində 4 mol%-ə qədər artması ilə Ge_2S_3-ün elektrikkeçirməsinin 300K-də təxminən 100 dəfədən çox artmasına səbəb olur. Qadağan olunmuş zolağın eni isə Ge_2S_3 üçün ΔE_T=2,24eV olduğu halda, 4 mol% GeS tərkibli nümunə üçün azalaraq 2,08 eV olur.

Elektrikkeçirmənin qiyməti isə tədqiq olunan ərintilər üçün temperaturdan asılı olaraq (300-1000K intervalda) artır. $\sim T$=300÷480 K temperatur intervalında elektrikkeçirmə nisbətən az dəyişir və bu hal aşkar keçiricilik oblastına uyğun gəlir. T>500K qiymətlərində isə temperaturun artması ilə elektrikkeçirmə kəskin artır. Bu temperatur intervalı isə məxsusi keçiricilik oblastına uyğun gəlir. Hər iki temperatur oblastında $lg\sigma\sim(10^3/T)$ asılılıq qrafikindən istifadə edərək bərk məhlul ərintiləri üçün qadağan olunmuş zolağın eni hesablanmışdır. Aşağı temperatur oblastında (aşkar keçiricilik oblastı) qadağan olunmuş zolaq üçün alınmış qiymətlər ΔE_0=0,29÷0,36eV olub, aktivləşmə enerjisinin qiymətinə uyğun gəlir. Qadağan olunmuş zolaq üçün məxsusi keçiricilik oblastında hesablanmış qiymətlər kifayət qədər böyük olub, 2,02-2,24 eV intervalında dəyişir. Bu qiymətlər, Ge_2S_3 birləşməsi və onun əsasındakı bərk məhlul sahəsindəki ərintilər üçün qadağan olunmuş zolağın eni hesab edilə bilər. (ΔE_T=2,02÷2,24 eV)

$(Ge_2S_3)_{1-x}$ $(GeS)_x$ bərk məhlulunda x=0,01; 0,02; 0,03; 0,04 qiymətlərinə uyğun gələn ərintilərin termo-e.h.q.-nin temperatur asılılığı şəkil 2-də verilmişdir. $\alpha\sim f(T)$ asılılıq qrafikindən göründüyü kimi termo-e.h.q.-nin 300÷1000K temperatur intervalında dəyişməsini iki temperatur intervalına bölmək olar. Birinci temperatur intervalı ~300÷500K, ikinci temperatur intervalı isə ~530÷1000K-ə uyğun gəlir. Əsas komponentin (Ge_2S_3) və onun əsasındakı ərintilərin tədqiq olunan bütün temperatur intervalında termo-e.h.q.-si temperaturun yüksək qiymətlərində ($\sim T\geq 900K$) termo-e.h.q.-nin qiyməti temperaturunun artması ilə az da olsa artmağa doğru meyl edir.

$(Cl_2S_3)_{1-x}(GeS)_x$ bərk məhlul sahəsində 300K-də termo-e.h.q.-nin $x\geq 0,00$ qiymətlərində (x=0,00÷0,04) azalır. α-nın tərkibdən asılı olaraq belə azalması elektrikkeçirmənin göstərilən tərkibdə artması ilə əlaqələndirilə bilər. Bu yarımkeçiricilərdə termo-e.h.q.-nin elektrikkeçirmədən asılı olaraq dəyişməsi ilə izah oluna bilər. Göstərmək lazımdır ki, bu qanunauyğunluq bütün temperatur intervalında (300÷1000K) saxlanılır.

Ərintilərdə keçiriciliyin tipi (n və ya p- olması) termo-e.h.q.-nin işarəsinin dəyişməsinə görə təyin edilmişdir.

Müəyyən edilmişdir ki, həm Ge_2S_3 və həm də onun əsasındakı bərk məhlul sahəsindəki nümunələr "p"-tip keçiriciliyə malikdir və bu tədqiq olunan temperatur intervalında dəyişmir. Buna səbəb Ge_2S_3 birləşməsinin kristal qəfəsində Ge^{+3} ionun (Ge^{+3}=1,034 E) Ge^{+2} ionu ilə (Ge^{+2}=0,65 E) əvəz olunmasıdır. Başqa sözlə, əvəz olunan atoma nisbətən, əvəz edən atomun oksidləşmə

dərəcəsinin bir vahid az olması "p"-tip keçiriciliyin alınmasına səbəb olur.
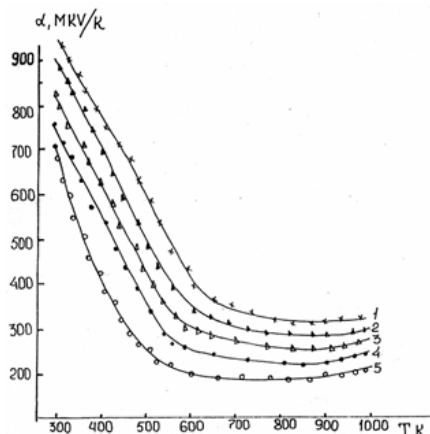
Şəkil 2. Ge$_2$S$_3$-GeS birləşməsinin və onun əsasındakı 1, 2, 3, 4 mol% GeS tərkibli ərintilərin termo e.h.q.-sinin temperaturdan asılılığı 1- Ge$_2$S$_3$; 2 - 1 mol%; 3 - 2 mol% Ges; 4 - 3 mol% GeS; 5 - 4 mol% GeS.

Termo-e.h.q.-nin GeS-in bərk məhlul sahəsində artması ilə azalması elektrikkeçirmənin tərkibdən asılı orlaraq dəyişməsi ilə və keçiricilik zonasındakı yükdaşıyıcıların artması ilə izah oluna bilər. Elektrikkeçirmənin və termo-e.h.q.-nin temperaturun artması ilə dəyişmə xarakteri qanunauyğun (yarımkeçiricilər üçün) olub, eyni zamanda yükdaşıyıcıların konsentrasiyasının temperaturdan asılı olaraq dəyişməsi ilə əlaqədardır.

ΔE-nin tərkibdən asılı olaraq dəyişməsi Ge^{+3} və Ge^{2+} atomlarının ion radiusların müxtəlif olması (r$_{Je}$$^{+3}$=1,034 E; r$_{Ge}$$^{+2}$=0,65 E) və eyni zamanda kristal qəfəs sabitlərinin tərkibdən asılı olaraq dəyişməsi ilə əlaqələndirilə bilər.

Beləliklə, GeS birləşməsinin Ge$_2$S$_3$-ün elektrikkeçirməsi və termo-e.h.q.-nə bərk məhlul sahəsində güclü təsir etdiyini demək olar.

[1] *K.A.Qşnaydner*. Splavı redkozemelnıx metallov. M., Mir, 1965.

[2] *N.X.Abrikosov,L.V.Şelimov*. Poluprovodnikovie materiali na osnove soedineniy A^{IV}B^{IV}. M., Nauka, 1975.

А.А. Набиев, Г.Р. Гурбанов

ЭЛЕКТРИЧЕСКИЕ СВОЙСТВА ТВЕРДЫХ РАСТВОРОВ (Ge$_2$S$_3$)$_{1-x}$(GeS)$_x$

Изучена температурная зависимость термо-эдс и электропроводности образцов твердых растворов системы Ge$_2$S$_3$-GeS на основе Ge$_2$S$_3$ с содержанием GeS 1, 2, 3, 4 mol %.

Обнаружено, что с увеличением содержания GeS в твердом растворе электропроводность растет, а ширина запрещенной зоны уменьшается. Термо-эдс с увеличением температуры уменьшается с определенной закономерностью. При изменении полярности термо-эдс был определен тип проводимости образцов. Во всех изученных образцах обнаруживается *p*-тип проводимости.

A.A. Nabiyev, G.R. Gurbanov

ELECTRICAL PROPERTIES OF SOLID SOLUTIONS (Ge$_2$S$_3$)$_{1-x}$(GeS)$_x$

Temperature dependence of thermal electromotive force and electric conduction of solid solution's samples of Ge$_2$S$_3$ – GeS systems on Ge$_2$S$_3$ - bases with 1, 2, 3, 4 mol % contain of GeS has been studied.

It has been revealed that with increase of GeS contain in solid solution's electric conduction increases, while forbidden area thickness decreases. Thermal electromotive force decreases with the increase of temperature due to the regularities. At the change of polarity of thermal electromotive force the conductivity type of samples were determined.

In all studied samples the *p* - type of conductivity has been revealed.

POSSIBLE MASSES OF PROGENITORS OF DIFFERENT TYPE NEUTRON STARS

A.O. ALLAKHVERDIEV, F.K. KASUMOV, S.O. TAGIEVA

National Academy of Sciences of Azerbaijan, Physics Institute,
Baku 370143, Azerbaijan Republic

An attempt to establish the mass of progenitors of different types of neutron stars having different degrees of activity by examining of the environments of supernova remnants connected to these neutron stars is done. It is found that there is no reliable relation between the mass of the progenitor star and the degree of activity (or passivity) of the neutron star. The S-type supernova remnants without point sources located in less dense media and their progenitors may be less massive stars compared to the progenitors of the neutron stars considered here.

1. Introduction

What does the type (or the activity) of a neutron star depend on? The activity depends on parameters of neutron stars. The most important ones among these parameters are magnetic field, spin period, and maybe mass of the neutron star. These parameters must depend on the mass of the progenitor star and it is important to know, whether the progenitor was single star or entered into binary system. If progenitor was in binary system, then the masses and the separation of the two components must be important [1]. Number of the neutron stars in binary systems is very small, and as the binary parameters change at SN explosion, so it is difficult to check if the pulsar phenomenon depends on the progenitor star being in a close binary system or not.

Today, various different types of single neutron stars having very different physical properties are known; these are classical PSR-s, dim radio quiet neutron stars (DRQNSs) which are the type of neutron stars having very low luminosity in the X-ray band and have no detected radio radiation, anomalous X-ray pulsars (AXPs) and soft gamma repeaters (SGR-s) (see [2] for review). Do the neutron stars with different physical properties have progenitors with different masses? This question was asked before in [3]. In this work, we examine the environments of the SNRs connected to different types of neutron stars and also of the S-type SNRs in which no sign of any kind of neutron star is seen. We discuss masses of the progenitors of these SNRs and neutron stars. We have approached the problem through 4 independent ways: we have examined surface brightness (Σ) - radius, Σ - age, and radius-age graphs as well as the observational data about density in the shock fronts and in the ambient media of the supernova remnants. We have also examined the environments of C- and S- type supernova remnants in which no point source has been observed.

2. Environments of SNRs and the types of the point sources connected to these SNRs

In Table 1, data of various types of neutron stars and SNRs are listed. The data of PSRs are taken from [4], and the data of AXPs and DRQNSs are taken from [5]. In this table, names of the point sources in the SNRs, ages, radio luminosities (at 1400 MHz) of these neutron stars and their distances are represented. In Table 2, data of the SNRs, which the neutron stars represented in Table 1 are connected to, as well as data of some nearby S- and C-type SNRs (without observed point sources and for which information

about the environments, ages, explosion energies are available) are listed.

The data of the SNRs are taken from [6] and [7]. In this table, Galactic coordinates, names, morphological types in radio and X-ray bands, radio surface brightness, diameter, and distance values of the SNRs as well as the OB-associations in which they are located and distances of these OB associations are given. In Table 2, explosion energies, ages, density in the shock waves of the SNRs, and data about the surrounding medium are also represented [7].

Various data about the density in the medium around SN explosion sites and in the shells of the SNR-s are given in Table 2. By examining these and some additional data we can get some information about the progenitor masses. Then we can check if there is a relation between progenitor masses and the types (different activity or total passivity) of neutron stars. For some of the SNRs average values of number density of particles in front of and just behind the shock front in the shell are given in Table 2 in the first part of the 12th column. In the same column, after the density of the shock wave, the existence of HI clouds around SNRs are represented (the densities of these clouds are also given, if available). If there is a bubble around the SNR it is also written (also its density if possible). In Table 2, we have listed only those SNRs which have reliable distance, age and density values and after carefully examining PSR-SNR connections we have selected reliable pairs (Table 1).

Three of the AXPs are connected to Galactic SNRs, whereas none of the SGRs were found to have reliable connections with Galactic SNRs. SGR 0526-66 may be connected to a SNR in LMC [7]. In [3] it is claimed that the SNRs connected to AXPs (and also SGRs) are located in a dense medium. They present a figure (SNR age versus SNR radius) to show that the media of the SNRs connected to AXPs and SGRs are denser than the media of all the other SNRs, on average. Theoretically found average constant density lines are also included in this figure to show the evolution of the SNRs (with the same explosion energy) evolving in different media which have different (constant) densities [3].

The SNRs which are at the same age have different radius values depending on the density of the medium [8]. In actuality, it is known that the explosion energy values vary in a wide range, about 3 orders of magnitude (e.g. kinetic energy of Crab SNR is $\sim 10^{49}$ erg, [9], whereas kinetic energy of Cas A SNR is $>10^{51}$ erg, [10]. In the Galaxy, the interstellar medium is inhomogeneous and has a cloudy structure. The observational parameters of SNRs strongly depend on the characteristics of the surrounding matter.

A.O. ALLAKHVERDIEV, F.K. KASUMOV, S.O. TAGIEVA

Table 1. Data of the Point Sources of the SNRs

Source Type	Point Source Name	l,b (SNR)	Characteristic Age (kyr)	Log $L_{1400\,MHz}$	d (kpc)	Progenitor Star
Radio Pulsars and Single Strong X-Ray Pulsars	J 1801-2451 R	5,27-0,9	15	1,05	4,5	
	J 1803-2137 R,X	8,7-0,1	16	2,25	3,5	O8-B1
	J 1811-1926 X	11,2-0,3	24		5	O
	J 1846-0258 X	29,7-0,3	0,72		5,7	O
	J 1856+0113 R	34,7-0,4	20	0,89	2,8	O
	J 1930+1852 R,X	54,1+0,3	2,9	0,17	5	
	J 1952+3252 R,X	69,0+2,7	107	0,6	2	
	J 2229+6114 R,X	106,3+2,7	10	0,97	5,5	
	J 2337+6151 R,X	114,3+0,3	41	1,04	2,8	O9-B3
	J 0205+6449 R,X	130.7+3,1 Nit.	5,38	-0,3	3,2	O8-B1
	J 0534+2200 R,O,X,G	184,6-5,8	1	1,75	2	
	J 0835-4510 R,O,X,G	263,9-3,3	20	2,31	0,45	
	J 1124-5916 R,X	292,0+1,8 Ox.	2,9	0,46	6	O8-B1
	J 1119-6127 R	292,2-0,5	1,6	1,65	7,5	B2-B3
	J 1341-6220 R	308,8-0,1	12	2,11	8	
	J 1513-5908 R,O,X,G	320,4-1,2	1,7	1,25	4,2	B0-B2
	J 1646-4346 R	341,2+0,9	40	1,67	6,8	
DRQNSs	RX J 2020.2+4026	78,2+2,1		<-0,1	1,5	O8-B1
	CXO J 2323+5848	111,7-2,1 Ox.		<1,18	3	massive O
	RX J 0007.0+7302	119.5+10 Ox.		<-0,2	1,4	B1-B3
	RX J 0832-4300	260,4-3,4 Ox.	7,9	<0,08	2	O
	1E 1207.4-5209	296,5+10	11, ~10	<-0,4 (4800MHz)	1,8	B1-B3
	1E 161348-5055	332,4-0,4	8,1, 8	<0,1 (1500 MHz)	3,7	O
	CXOU J 0617+2221	189,1+3,0		<2 (327 MHz)	1,5	
AXPs	AXP 1E 1841-045	27,4+0,0	4,7	<1,5	6,5	O
	AXP J 1845-0258	29,6+0,1	5--8		11	O
	AXP 1E 2259+586	109,1-1,0	200	<0,3	5	B0-B2

Notes:

R=Radio Pulsation, O=Optical Pulsation, X=X-Ray Pulsation

G=Gamma-ray Pulsation, T= Thermal X-Ray Radiation

CXOU J 0617+2221: DRQNS candidate

All of these should be taken into account while analyzing possible masses of progenitors of neutron stars and density of the matter in the environments of SNRs. Following [3], we have constructed similar SNR radius versus age diagrams including the average (constant) density lines as presented in [3]. Figure 1, SNR radius vs. age diagram for S- and C-type SNRs which are connected to PSRs and single strong X-ray pulsars is displayed using the ages of SNRs (see Table 2) and the characteristic ages of pulsars (see Table 1), separately. In Figure 2, SNR radius vs. age diagram for the SNRs which are connected to AXPs and DRQNSs is displayed, again using the ages of SNRs (see Table 2) and the characteristic ages of AXPs and DRQNSs (see Table 1), separately. In Figure 3, SNR radius vs. SNR age diagram for S- and C-type SNRs (for which no point source has been observed) is displayed.

3. Reliability of the positions of the SNRs in the Age-Radius diagram

Positions of the SNRs connected to PSRs and single strong X-ray pulsars are represented in figure 1. F-type SNRs are included in Table 1, but we did not show the positions of them in the figures; we want to examine the ambient medium of the SNRs through which the SNR's shell expands. The uncertainty in the age values of SNRs are represented with error bars in Figure 1. The real age of PSRs is given as

$$\tau = \frac{P}{(n-1)\dot{P}}\left(1 - \left(\frac{P}{\dot{P}}\right)^{n-1}\right)$$

where P and $\dot{P}$ are the spin period and time derivative of the spin period, and n is the braking index. For $n = 3$ and $P_0 \ll P$, τ is the characteristic age which is close to the real age of the PSR. For all of the SNRs in figure 1, characteristic ages of the pulsars connected to them are known and the positions of the SNRs using the τ values are shown in figure 1 by (+) sign.

POSSIBLE MASSES OF PROGENITORS OF DIFFERENT TYPE NEUTRON STARS

Table 2. Data of the SNRs

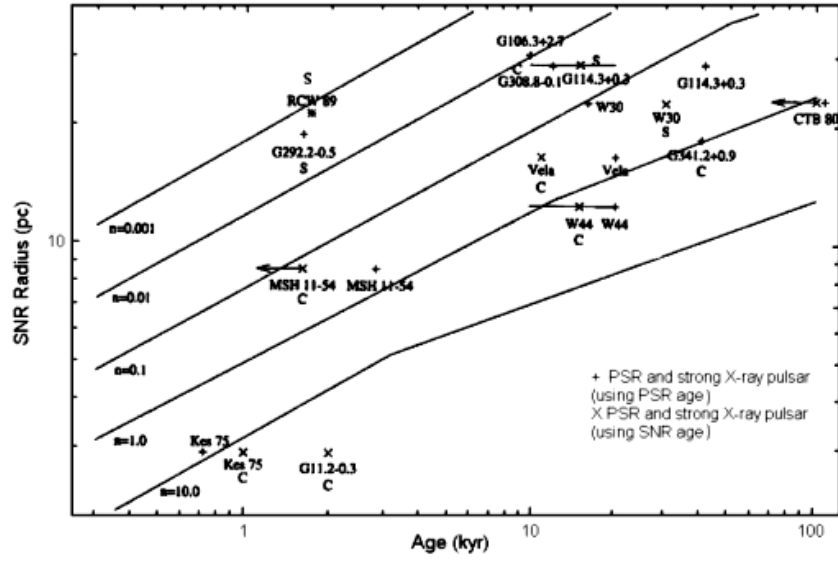| Type	l,b	Name	Type (Radio)	Type (X-Ray)	Σ (10^{-22})	d (kpc)	R (pc)	OB assoc.	d_{OB} (kpc)	E_0 (10^{51} erg)	Age (kyr)	Density (cm^{-3})
Radio Pulsars and Single Strong X-Ray Pulsars	5.27+0.9		F									
	8.7+0.1	W30	S		59	3,5	22,9			1--4	30	0,03
	11.2+0.3		C		2069	5	2,9			<0,24	2	MC,MS
	29.7-0.3	Kes75	C		1672	6,7	2,9				1	
	34.7-0.4	W44	C	C	366	2,8	12,5			~10	10--20	1-6, MC
	54.1+0.3		F	F	334	5	1,2					
	69.0+2.7	CTB80	?		28	2	23,3			10		
	106.3+2.7		?	C	6	5,5	30,4			0,7	<100	in HI bubble, MC
	114.3+0.3		S		2	2,8	28,7	CasOB5	2,3		10—20	0,1, low
	Nit.130.7+3.1	3C58	F		1104	3,2	2,9			0,2-0,4	0,8	
	184.6-5.8	Crab	F		44720	2	1,8			0,1-0,3	1	low
	263.9-3.3	Vela	C		40	0,45	16,7			10--20	11	high
	Ox.292.0+1.8	MSH 11-54	C	C?	235	6	7,2				<1,6	
	292.2-0.5		S		35	7,5	18,9			10		
	308.8-0.1		C?		38	8	28,5					
	320.4-1.2	RCW89	C		74	4,2	21,4			10--20	1,7	very high
	341.2+0.9		C		6	6,8	18,5					
DRQNSs	78.2+2.1	DR 4	S		142	1,5	13,1	CygOB1	1,3		5—10	in cavity, MC, >1
	Ox.111.7-2.1	Cas A	S		163744	3	2,2			30	0,32	high
	Ox.119.5+10	CTA1	S	C	7	1,4	18,4			0,3	15	0,01-0,02, H1 cl. 0,5-1,MC
	260.4-3.4	Puppis A	S		65	2	16				3,4	0,4-3, cl,100-180
	296.5+10	PKS 1209	S		12	1,8	20,1			>0,2-2	10	0,1-0,2, H1cl~10
	332.4-0.4	RCW 103	S		421	3,7	5,4				1—3	MS,MC>1000
	189.1+3.0	IC 443	C		119	1,5	9,8	Gem1	1,5		1—5	10-20, cl.100, MC 10000
AXPs	27.4+0.0	4C 0471	S		564	6,5	3,7				2	low
	29.6+0.1		S		90	11	8,1				<8	
	109.1-1.0	CTB 109	S		38	5	20,4			10-100	3~10	0,25, cl. 20
Without Point Sources	0.9+0.1		C		423	8	9,3				1--7	<0,001, MC
	6.4-0.1	W28	C	C	265	2,5	17,5			4~10	~50	0,1-0,23, MC~10000, MS
	42.8+0.6		S	C	8	6	21				10	low
	74.0-8.5	Gyg.Loop	S		9	0,8	22,3			0,17	5--10	H1 Cloud 4
	116.5+1.1		S		4	3,5	35,3				10--40	low
	132.7+1.3	HB 3	S	C	11	2,3	26,8			3,1	21	high
	315.4-2.3	RCW 86	S		42	2,7	16,5	CirOB1	2,5	6--7	9,5	0,2-0,3, in cloud
	326.3-1.8	MSH15-56	C		151	2	11			~10	10	0,1, medium
	327.1-1.1		C		33	6,5	17			~13	7	
	327.6+14	SN 1006	S		32	2	8,8			10	1	0,02, 0,1, 0,4

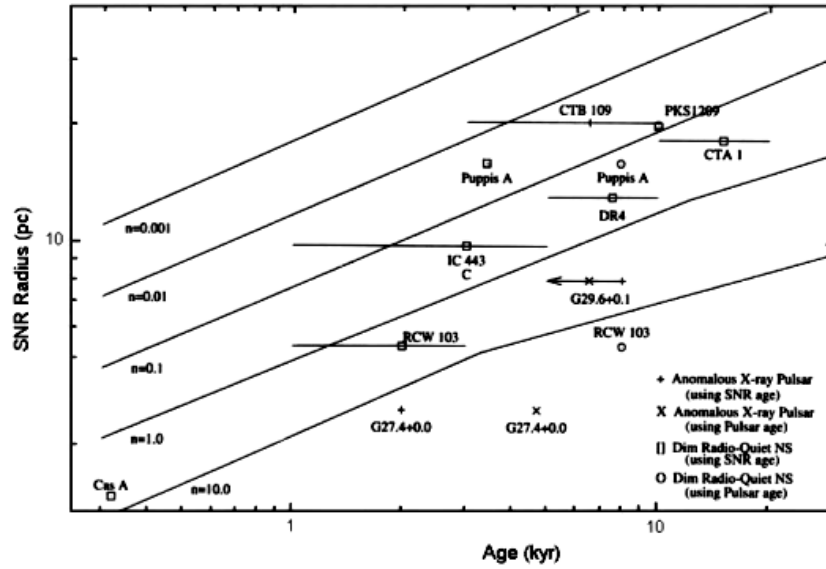*Fig.1.* SNR –s connected to PSRs and single strong X-ray pulsars

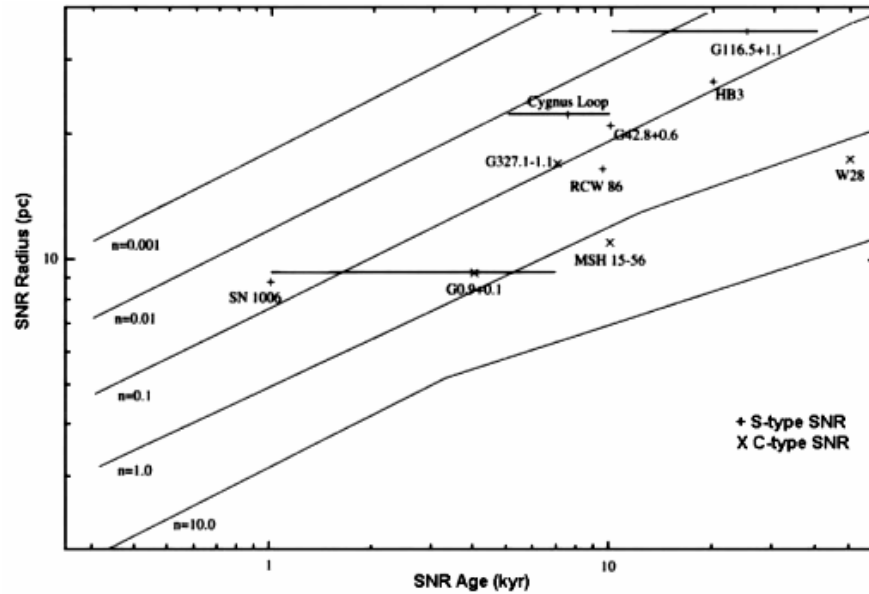*Fig.2.* SNR-s connected to AXP-s and DRONS-s.

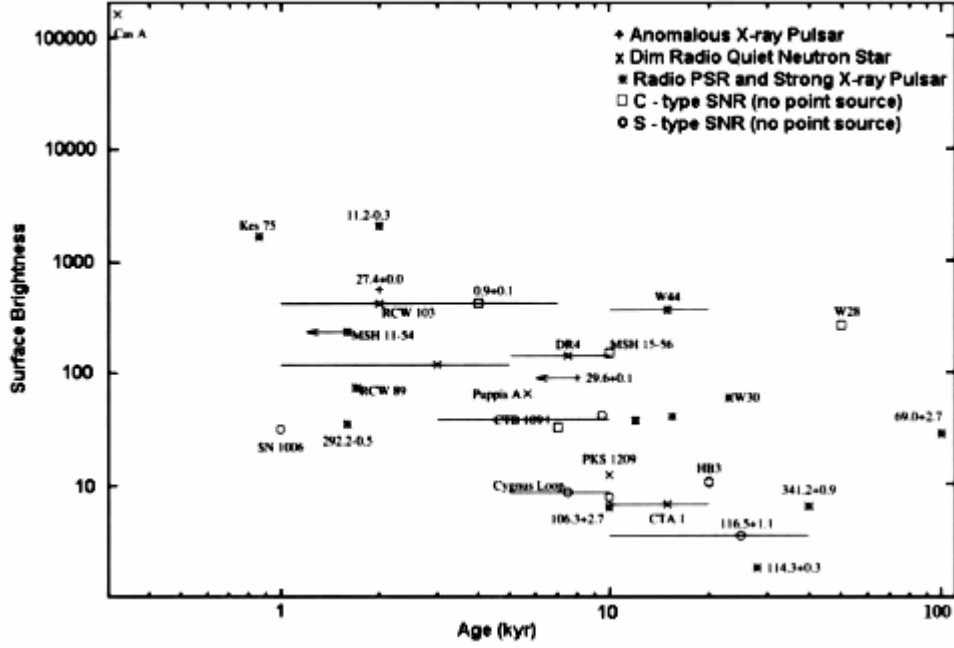*Fig.3.* The S- and C-type SNR-s without point sources.
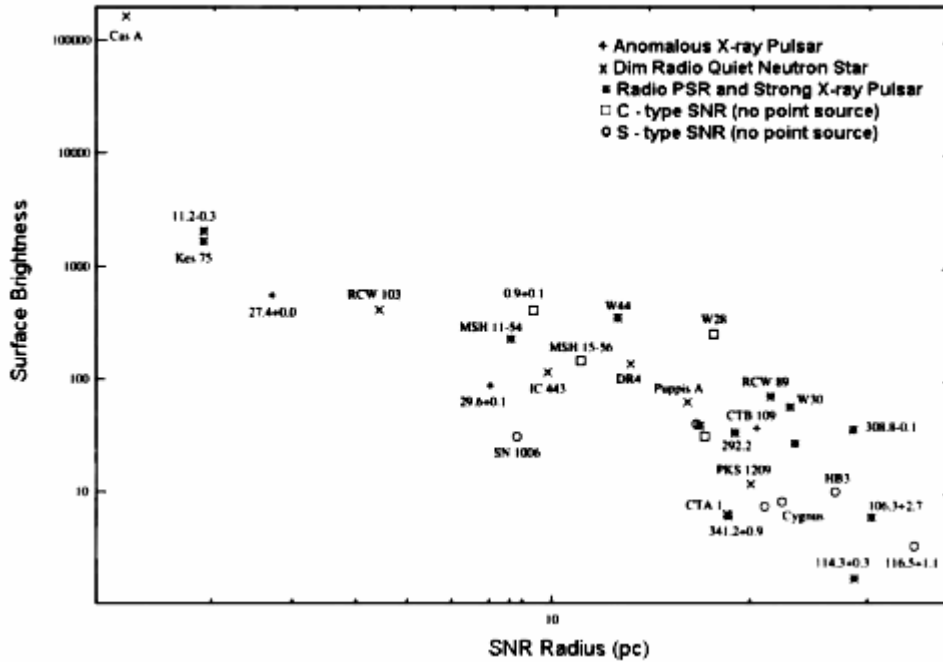
Fig.4. Surface Brigthness - Age

Fig.5. Surface Brigthness-Radius

Examining only the radius vs. age diagrams using an average value of explosion energy and constant density values for the ambient media does not give us enough information about densities of the ambient media. We have also constructed surface brightness (Σ) vs. age (Figure 4) and Σ vs. radius diagrams (Figure 5) of the SNRs in order to get more information about the densities. We have also collected observational density values of the ambient media of the SNRs (see Table 2) and we have compared these density values with the positions of the SNRs in Figures 1-5.

Although, independent age measurements are not available for all the SNRs, we have also shown the positions of the SNRs using the SNR's age (if it is known) by (X) sign in Figure 1.

When we take into account the morphological types in the radio band (see Table 2) of the SNRs given in Figure 1, we see that, in general, the C-type SNRs are evolving in a denser medium compared to the S-type SNRs. On the other hand, when we compare the density values corresponding to the positions of the SNRs in Figure 1 (i.e. the position of the SNR with respect to the constant density lines for expansion in a homogeneous medium) with the observationally found density values given in Table 2, we see that there are considerably large differences. It must be noted that, the observed density values correspond to the actual density values of the shell and the ambient medium depending on the diameter value of the SNR. The density values of the shell and the ambient medium change, because the medium is not homogeneous. The density values also change with respect to

the diameter if the progenitor is an O-type star; in such a case, the SNR (during its initial phase) expands inside an HII region formed by the O-type progenitor or inside a bubble, i.e. in a low-density medium. So, if the SNR is expanding inside a HII region, i.e. in a low density medium, it does not necessarily mean that the surrounding medium is not dense. If the SNR is in a star formation region where molecular clouds, OB associations are present, then the SNR will be in a dense medium and this may be an evidence for the progenitor being a massive star.

3.1 The SNRs connected to PSRs and single strong X-ray pulsars

As seen from Figure 1, SNRs Kes 75 and G11.2-0.3 are expanding through the densest media. There is no observational density data available for Kes 75 (Table 2). The SNR G11.2-0.3 is seen to be in a region in which there are molecular clouds and this SNR interacts with these clouds. In Figures 4 and 5, Σ-age and Σ-radius graphs for all the S- and C-type SNRs given in Table 2 are shown. As seen from these figures, SNRs Kes 75 and particularly G11.2-0.3 are expanding in dense media the progenitors of these SNRs may be O-type stars.

The positions of SNR W44 in Figures 1, 4 and 5, and the observational density of W44 given in Table 2 show that this SNR is expanding in a dense medium. So, the progenitor of SNR W44 and PSR J1856+0113 (which is connected to this SNR) may be an O-type star. As displayed in Figure 1, C-type SNR MSH 11-54 is expanding in a less dense medium compared to the media of the SNRs discussed above. The age of the PSR connected to this SNR is greater than the age of SNR MSH 11-54 (see Tables 1 and 2) and the uncertainty in the PSR's age is less than the uncertainty in the SNR's age. If the PSR and the SNR are connected genetically having an age of 2.9 kyr then, there is no contradiction between the positions of this remnant in Figure 2 and Figures 4, 5. There is no observational data directly available about the density of the ambient medium of MSH 11-54 (Table 2). SNR MSH 11-54 is an Oxygen-rich SNR; the progenitor of MSH 11-54 may be an O8-B1 type star.

As seen from Figure 1, the SNR RCW 89 is expanding in a very low density medium. On the other hand, observational data show that this SNR is in a very dense medium (Table 2). What is the reason for this contradiction? As seen in Table 2, the explosion energy of this SNR exceeds 10^{51} erg. So the progenitor may be B0-B2 type star. SNR G292.2-0.5 is situated in a very low density medium (Fig.1). There is no observational data about the density. PSR J1119-6127 is projected on the center of this SNR that the connection between the PSR and the SNR is most probably true [11]. Progenitor of this pair may be a B2-B3 type star in a low density environment. From Figure 1, we can conclude that SNR G114.3+0.3 is expanding in a low density medium and this is roughly in agreement with the observational density data given in Table 2. The positions of this remnant in Figures 4 and 5 also give evidence for this SNR to be expanding in a very low-density medium. The progenitor of this SNR may be an O9-B3 type star.

The position of SNR W30 in Figures 4 and 5 is in accordance with the position of this SNR in Figure 1, but contradicts with the observational low density value given in Table 2. It is not possible to get rid of the contradiction by changing the distance and age values of this remnant. We can suppose that either the actual density of the ambient medium of W30 is larger than the observed density value (Table 2) or the explosion energy of this SNR is higher than the value given in Table 2. Progenitor of the pair W30-J1803-2137 may be an O8-B1 type star.

3.2 The SNRs connected to AXPs and DRQNSs

In Figure 2, radius-age diagram of the SNRs connected to AXPs and DRQNSs is represented. Observed density data on SNR G27.4+0.0 and the positions of this SNR and SNR G29.6+0.1 in Figures 2, 4 and 5, show that the progenitors of these AXP-SNR pairs may be O-type stars. Among the AXP - SNR pairs, the most well examined one is 1E 2259+586 - SNR G109.1-1.0 (CTB 109) pair. As seen from Figure 2, this SNR (similar to Puppis A) is in a less dense medium compared to all the other SNRs which are connected to AXPs and DRQNSs. On the other hand, the ambient density of this SNR given in Table 2 and the positions of this remnant in Figures 4 and 5 do not confirm this result. If we take into account large energy of supernova explosion we can confidently say that the progenitor is a B0-B2 type star.

Next we will examine the SNRs connected to DRQNSs. Among the SNRs which are connected to DRQNSs, the densest ambient medium belongs to SNR RCW 103 as seen in Figure 2. The density in the ambient media of this SNR given in Table 2 and the data of this remnant shown in Figures 4 and confirm this result; SNR RCW 103 is expanding in a dense medium that its progenitor may be an O-type star. As seen in Figure 2, the next densest medium is the one in which SNR DR4 (which is connected to a DRQNS) is located. Again, the density data of this remnant given in Table 2 and the location of this remnant shown in Figures 4 and 5 do not contradict with this result. As seen in Table 1, this SNR is associated with Cyg OB1 that its progenitor may be an O8-B1 type star. Next we will examine the SNRs (connected to DRQNSs) which are in less dense ambient media. The age of SNR G260.4-3.4 (Puppis A) is 3.4 kyr, whereas, DRQNS RX J0822-4300, which is connected to Puppis A, has a characteristic age of 7.9 kyr. In Figures 4 and 5, we have adopted an average age value of 5.7 kyr for this remnant. There is a contradiction between the position of Puppis A in Figure 2 and value of the ambient medium density given in Table 2 (and also the positions of the remnant in Figures 4 and 5). It must be noted that Puppis A is an Oxygen-rich SNR like SNRs CasA and CTA 1. Cas A is in a dense medium and the thrown out mass was calculated to be ~4 solar mass [12]. As seen from the figures, the progenitor of SNR CTA 1 may be a massive B-type star. The density of the ambient medium of SNR Puppis A is in between the densities of the ambient media of SNRs Cas A and CTA 1, so the progenitor of Puppis A may be an O-type star. Since, the SNRs connected to AXPs are not in less dense media compared to Puppis A, in principle we can assume that the progenitors of AXPs and DRQNSs are often O-type stars.

3.3 The SNRs without observed point sources

Now let us examine the S- and C-type SNRs for which no point source has been observed (Table 2). As most of the PSRs are connected to C-type SNRs (in most of the cases PSRs create pulsar wind nebula), the C-type SNRs for which no point source has been observed most probably include

PSRs. As seen from Figure 3, C-type SNR W28 has the largest ambient density. The ambient density value of W28 in Table 2 and the positions of the SNR in Figures 4 and 5 confirm this result.

Similar to W28, the C-type SNR MSH 15-56 is in a dense ambient medium as seen from Figure 3. Its ambient density data (Table 2) and its positions in Figures 4 and 5 show that this SNR is in a medium which has a density value a bit less than the density in the ambient medium of W28. Progenitors of W28 and MSH 15-56 may be massive O-type stars. The third densest ambient medium may belong to SNR G0.9+0.1 (see Figure 3). So, we can confidently say that this SNR has large explosion energy and is expanding in a HII region which was created by its progenitor. This fact supports the idea that the progenitor of this SNR may be an O-type star.

As seen in Figure 3, the SNRs expanding in less dense media are SN1006, Cygnus Loop and G116.5+1.1 which are S-type SNRs. The positions of these 3 SNRs in Figures 4 and 5 also confirm this result. From Figures 3, 4 and 5, after examining the ambient media of S- and C-type SNRs (in which no point source has yet been found) we see that, on average, the C-type SNRs are expanding in denser media compared to the S-type SNRs.

4 Discussion and Conclusions

As is well known, average density values of the media, presence and sizes of HII regions, and the masses of OB stars are related with each other. Therefore, examining the average density of the media around the SNRs, the density in the shock wave, chemical abundances of the SNRs, and the existences of the OB associations in the regions of the SNRs we may roughly estimate the types of the progenitor stars. Possible types of the progenitor stars of the SNRs which contain neutron stars are given in the last column of Table 1.The progenitors of all the SNRs (except the S-type SNRs without point sources) discussed above are expected often to be O-type stars with different masses. At the end of their evolution massive B-type stars often must give birth to S-type SNRs in which it is difficult to detect point sources in radio and X-ray bands even if these SNRs are located at small distances. Since, the number of F-type SNRs is small and as F-type SNRs do not have shells (i.e. we can not put them in our figures for comparison), we can not discuss the density of their ambient media. But we know that the ambient medium of the Crab PSR has a low density and nearby the PSR there is no young open cluster. Therefore, the progenitor of Crab PSR may be a massive B-type star, rather than an O-type star.

Our investigations show that the type of activity (or passivity) of a neutron star practically does not or slightly depends on the mass of the progenitor star on the main sequence. So, it is necessary to examine the idea of connection of the type of activity to the parameters of binary systems (similar to the idea of the connection of the origin of PSRs to close binary systems as claimed in [1].

[1] *Iben, A.V. Tutukov*. 1996, ApJ, 456, 738.

[2] *S. Mereghetti, G.L. Israel, I. Stella.* 2002, ApJ, 569, 275.

[3] *D. Marsden, R.E. Lingenfelter, R.E. Rothschild, J.C. Higdon.* 2001, Ap. J, 550, 397..

[4] *O.H. Guseinov, S.K. Yerli, S. Ozkan, A. Sezer, S.O. Tagieva.* 2002, astro-ph/0206050.

[5] *B.M. Gaensler, P.D. Slane, E.V. Gotthelf, G. Vasisht.* 2001, ApJ, 559, 963.

[6] *D.A. Green.* 2001, 'A Catalogue of Galactic Supernova Remnants' (2001 December version), http://www.mras.cam.ac.uk/surveys/snrs/

[7] *O.H. Guseinov, A.Ankay, A. Sezer, S.O. Tagieva.* 2002, submitted to A&AT.

[8] *A.O. Allakhverdiev, O.H. Guseinov, F.K. Kasumov.* 1983, A&SS, 97, 287.

[9] *J. Sollerman, P. Lundqvist, D. Lindler,* 2000, ApJ, 537, 861.

[10] *M. Wright, J. Dickel, B. Koralesky, L. Rudnick.* 1999, AJ, 518, 284 21.

[11] *F.Crawford, B.M. Gaensler, V.M. Kaspi.* 2001, ApJ, 554, 152.

[12] *J. Vink J.S. Kaastra, J.A.M. Blecker.* 1996, A&A, 307, L4.

Ə.O. Allahverdiyev, F.Q. Qasımov, S.O. Tağıyeva

MÜXTƏLİF TİPLİ NEYTRON ULDUZLARIN ƏCDADLARININ MÜMKÜN KÜTLƏLƏRİ

Müxtəlif aktivliyə malik neytron ulduzları ilə genetik bağlı olan ifrat yeni ulduz qaliqlarini əhatə edən mühiti analiz edərək, neytron ulduzların əcdadları olan ulduzların kütlələrini təyin etməyə cəhd göstərilmişdir. Göstərilmisdir ki, əcdad kütlələri ilə neytron ulduzların aktivliyi arasında etibarlı bir asılılıq yoxdur. İçində nöqtəvi mənbə olmayan S- tipli ifrat yeni ulduz qalıqları daha seyrək mühitdə yerləşmişlər və onlarin əcdadlarının kütlələri baxılan neytron ulduzlarınsın əcdadlarının kütləsindən az ola bilər.

А.О. Аллахвердиев, Ф.К. Касумов, С.О. Тагиева

ВОЗМОЖНЫЕ МАССЫ ПРЕДШЕСТВЕННИКОВ НЕЙТРОНЫХ ЗВЕЗД РАЗНОГО ТИПА

Анализируя окружающую среду остатков сверхновых, связанных с нейтронными звездами, сделана попытка установить массу предшественников нейтронных звезд различных типов, имеющих разные степени активности. Установлено, что не существует надежной зависимости между массами предшественников и степенью активности (или пассивности) нейтронных звезд. Остатки сверхновых S-типа, не содержащие точечные источники, находятся в менее плотной среде, и их предшественники могут быть менее массивными, чем предшественники остальных типов нейтронных звезд.

MOLECULAR DYNAMICS OF NEUROMEDIN NmU-8 NEUROPEPTIDE

N.A. ISAKOVA, I.N. ALIEVA, N. M. GOJAYEV

Baku State University,
Z. Khalilov str.23, AZ 1073/1, Azerbaijan

Molecular dynamics simulations were performed for neuromedin NmU-8, the regulatory peptide isolated from porcine spinal cord. A single NmU-8 molecule was modeled in vacuum as well as in water. In the latter case it was surrounded by 264 SPC water molecules and a periodic boundary condition was applied. A large flexibility of the Tyr^1-Phe^4 amino acids sequence was observed in vacuum in contrast to water simulation. The Arg^5- Asn^8 backbone can adopt only a limited number of conformations, while the side chains may populate all three major rotamers.

Introduction

Neuromedin U-8 (NmU-8) is regulatory peptide initially isolated in 1985 from porcine spinal cord and then found in variety of mammals, birds, and reptile [1-5]. Besides its roles in smooth muscle contraction (human ileum, urinary bladder, rat stomach etc) NmU-8 has also been implicated in hypertension, blood flow in intestine, and neurotransmission. NmU-8 is present in nerves throughout the Gl-tracts, corticotrophs within the anterior and lobe of rat and human pituitary glands, parafollicular cells in rat thyroid gland, and in various regions of brain (spinal cord, hypothalamus, substantia nigra, hippocampus, amygdala). Low levels of NmU-8 are also found in human adipose tissue lymphocytes, and spleen. NmU-8 has a primary structure as follows: Tyr^1-Phe^2-Leu^3-Phe^4-Arg^5-Pro^6-Arg^7-Asn^8. In our previous paper, the theoretical conformational analysis method was employed to study the global conformational structure of the NmU-8 octapeptide [6]. Twelve types of stable conformations with significantly different values of dihedral angles are possible. The following study [7] was shown that substitution of the L-amino acid with corresponding D-amino acid at the various position leads to the formation of two possible binding sites to neuromedin NmU-8 receptors. One of them, the N-terminal fragment Tyr^1-Phe^4 has an extended backbone form, another C- terminus capable forms β-turn on the Arg^5-Asn^7 tetrapeptide fragment. A molecular conformation is largely determined by its environment, so the aim of this present work is the study the differences in the conformation of the NmU-8 neuropeptide in a vacuum and in aqueous environment using a molecular dynamics method.

Computational method

Molecular dynamics (MD) simulations were performed for NmU-8 neuropeptide in vacuum as well as in water solution using modeling package [8]. MD is widely applied to the study of biological systems, providing insight into the structure, function, and dynamics of biological molecules [9,10]. A wide range systems have been treated, from small molecules to proteins, in vacuum and in the presence of solvent [11, 12]. Molecular dynamics simulations generate trajectories of atomic positions and velocities and some general thermodynamic properties. MD involves the calculation of solutions to Newton's equations of motions. Often an MD trajectory will become trapped in a local minimum and will not be able to step over high energy conformational barriers. Thus, the quality of the results from a standard MD simulation is extremely dependent on the

starting conformation of the molecule. So, the twelve structures, including the best and the worst of the calculated structures from [6] were used as starting conformations for molecular dynamics simulations φ, ψ and χ_1 angles were analyzed for changes in conformation. Runs were performed for 300ps at 300K. The total length of the simulation depend on the system being studied and the type of information to be extracted. For example, in simulations of biological system a time step of 1 femtosecond is commonly used. To ensure that information about the highest frequency in the system is retained, generally the bond stretching frequency of water, the trajectory has to be recorded at an interval no larger than 4 femtoseconds. The length of the simulation (after equilibration) has to be long enough to enable the slowest modes of motion to occur. The force field parameters were those of the all atom version of AMBER by Cornell et al [13]. The total number of the water molecules was 264. A harmonic force towards the center of the sphere was added to atoms when they moved out of the sphere. The nonbonded cutoff distance was $12\mathring{A}$. The time step was 0,5fs. The program Hyper. Chem. 7.01 [14] was used for the MD simulations. All of the simulations were carried out for $2\cdot10^6$ to $1\cdot10^7$ steps.

Results and discussion

MD runs, using the 12 starting structures of NmU-8 from [6] were shown the significant differences in the conformations of the molecule in a vacuum and in an aqueous environment. Structures from the last 15ps of the run were energy-minimized and two of these are shown in Fig1. Corresponding changes of the potential energy and dihedral angle values are presented in Table 1. MD simulations show that the NmU-8 molecule backbone can adopt only a limited number conformations while the sidechains of the residues may populate all three major rotamers. A large flexibility of the Tyr^1-Phe^4 amino acids sequence was observed in vacuum in contrast to water simulation. The Arg^5-Asn^7 tetrapeptide fragment was found to be rigid in the conditions studies. Changes in intramolecular energy during simulations in water were negligible; they did not exceed 10-15 kJ/mol for NmU-8 molecule. At the same time, the molecule interaction energy was much higher due to the flexibility of the Tyr^1-Phe^4 part of the NmU-8. Interactions between aromatic side chains of the Tyr^1, Phe^2 and Phe^4 amino acids make the largest contributions to the global energy of the simulated molecule. Undoubtedly this contribution is overestimated in the vacuum approximation. The proline residue at position 6 makes an angle to the plane of the cycle and is seen to fluctuate by

$\pm 30°$ about a mean position during the molecular dynamics simulations. The backbone structure comprises a type II β-turn formed by residues Arg[5]- Pro[6]- Arg[7]- Asn[8] contains a hydrogen bond between Arg[5] CO and Asn[8] N[δ]H. Now consider the conformational properties of each amino acid residue in detail. The molecular dynamics simulations revealed the possible deviation by $\pm 120°$ from the optimal values of φ angle for Tyr[1] in vacuum as compared to $\pm 20°$ in water. The deviations of ψ for Tyr[1] by $\pm 80°$ from its optimal values are allowed in all calculated structures in vacuum and water environment. The low energy changes of χ_1 and χ_2 for Tyr[1] from 166 to 182° and from 70 to 89°, respectively, are possible. As can be seen from Table 1 of the Phe[2] and Phe[4] side chains are close to the minima of the torsional potential $\chi_1 = 60, 180°$ and $\chi_2 = 90°$. The deviations by $\pm 20°$ from minimal values are possible for χ_1 angle. The rotation of the χ_2 angle for Phe[2] and Phe[4] is considerably limited due to the effective interactions between the Phe[2] and Phe[4] amino acids.

The mobility of the backbone and side chain of the Leu[3] is more restricted as compared to preceding residues of NmU-8 in vacuum as well as in water. In contrast to water simulations, where the φ angle for Leu[3] may be changed by $\pm 20°$ from its optimal value, it is very mobile in vacuo. The possible deviations of ψ angle for Leu[3] in the later case are $\pm 40°$. Calculated results indicate that χ_1-χ_4 angles for Leu[3] have a noticeable conformational flexibility. All side chains angles (Leu[3]) were seen to be well-defined around 180° throughout the runs.

As can be seen from Table1. the mobility of the Arg[5]-Asn[8] amino acids stretch is considerably limited. So, the flexibility of φ and ψ angles of residues in the 5th and 7th positions is limited by 10° as compared to the preceding part of NmU-8. This fact can be explained due to the important role of these residues in the formation of β-turn.

Each φ angle varied about a single value, close to one of the set of possible angles calculated from molecular mechanics energy minimization [6]. The run with the high energy starting structure had an initial φ angle for Arg[5] around -60° which, during the run flipped to a value around -120°. The χ_1 angles of Arg[5] and Arg[7] were seen to vary between all 3 rotamers (-60, 60 and 180°) in the 5 runs while that for Asn[8] (χ_1) had only values around -60° and 60°.

NMU-8   a)
B$_3$B$_3$B$_2$R$_1$B$_2$RB$_3$R$_{32}$ (eeefefe)

NMU-8   b)
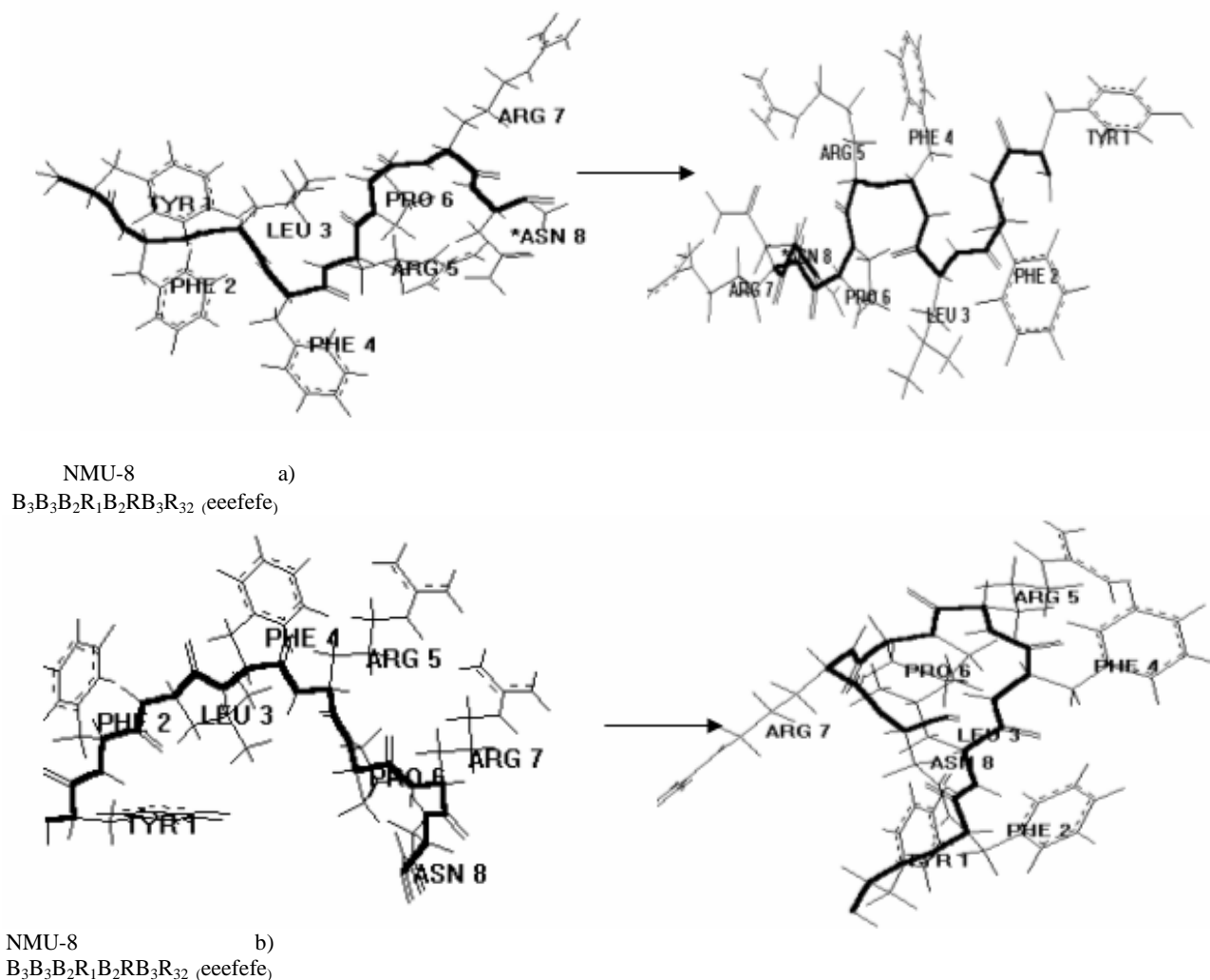B$_3$B$_3$B$_2$R$_1$B$_2$RB$_3$R$_{32}$ (eeefefe)

Fig.1 Computer-optimized structures of the NmU-8 neuropeptide in vacuum (a) and water (b). The initial conformation was an extended structure [6].

The potential energy changes during the MD simulations were examined (Fig 2). As can be seen, during the global sampling stage the potential energy rapidly decreased from 2000 to 337 kJ/mol. During the MD the energy changed

frequently and sometimes even experienced dramatic changes, suggesting the sampling of a fairly conformational space. The lowest energy obtained was –84 kJ/mol and corresponded to state of NmU-8 as shown in Fig.1 (b).
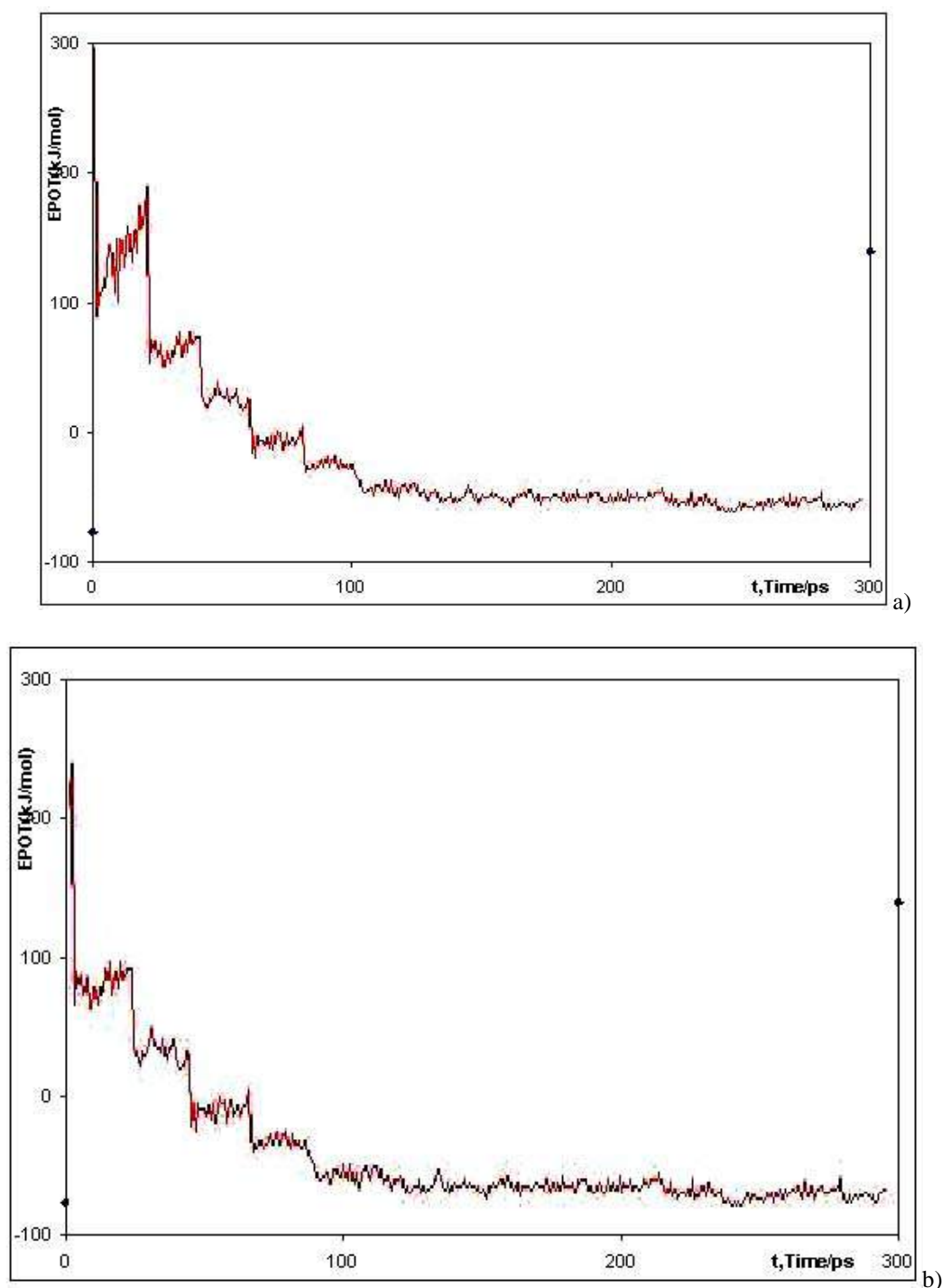

Fig.2. Energy of the NmU-8 neuropeptide during an MD simulation: a) in vacuum b) in water

Conclusion

We have carried out detailed analysis of the flexibility of the NmU-8 neuropeptide molecule by employing the molecular dynamics method. The foregoing results and discussion lead to the following conclusions:

(I). molecular dynamics simulations in vacuum as well as in aqueous solution confirm the considerable flexibility of the Tyr[1] -Phe[4]- sequence of NmU-8 neuropeptide;

(II). the turn conformations on Arg[5]- Asn[8] seqment of NmU-8 similar to the type II β-turn were more stabilized in water, with the predominant hydrogen bond between Arg[5] NH and Arg[7] C'O than the extended conformations.

The determined structure may be used as the basis for the design of further peptidic and/or non- peptidic selective antagonists.

Table 1.

The permissible ranges of values (in degrees) of φ, ψ, χ₁-χ₄ dihedral angles of NmU-8 neuropeptide under MD simulations in vacuum (upperline) and water (under line)

Amino acid residue	φ	ψ	χ₁	χ₂	χ₃	χ₄
Tyr[1]	-63 to 160 43 to 83	54 to 210 120 to 140	166 to182 	70to89 	181 	-
Phe[2]	-25 to -110 -90 to -105	120 to 140 140 to 160	150 to176 160 to182	90(±5) 	- 	-
Leu[3]	-60 to -117 -90 to -105	80 to 110 97 to 105	195 	171 	192 	180
Phe[4]	-83 to -105 -90 to -107	-23 to -60 -30 to -45	60(±5) 	89(±2) 	- 	-
Arg[5]	-110 to -129 -125 to -129	144 to 157 150 to 150	192 	180 	179 	180
Pro[6]	- 	-82 to -90 -87 to -92	- 	- 	- 	-
Arg[7]	-120 to -125 -122 to -125	101 to 110 101 to 110	-60 	180 	180 	180
Asn[8]	-90 to -92 -90 to -92	-60 to -66 -60 to -66	-52 	-80 	180 	-

[1] *N. Minamino, K. Kangawa, M. Matsuo* Biochem. Biophys. Res. Commun., 1985, 130, №3, 1078.

[2] *N. Minamino, T. Sudoh, K. Kangawa, M. Matsuo.* Peptides, 1985, 6, 245.

[3] *C. Austin et. al.* J.Mol.Endocrinol, 1995, 14, 157.

[4] *R. Murphy, C.A. Turner, J.B. Furness, L.Parker, A. Girand.* Peptides, 1990, 11, №3, 613.

[5] *F. O′ Harte, C.S. Bockman, P.W. Abel, J.M. Conlon.* Peptides, 1991, 12, №1, 11.

[6] *N.A. Isakova, I.N. Alieva, N.M. Godjaev.* Baku University News, 2002, №4, 66.

[7] *N.A. Isakova, I.N. Alieva, N.M. Godjaev.* J. "Knowledge", 2003, №3, 20.

[8] *W.F. Van Gunsteren, P.K. Weiner and A.K. Wilkinson* in Computer Simulation in Biological Systems (ESCOM Science), 1993.

[9] *J.A. Mc Cammon and S.C.Harvey* in: Dynamics of Proteins and Nucleic Acids (Cambridge Univ. Press, New York), 1987.

[10] *S.N. Rao and P.A. Kollman.* Prog. Natl. Acad. Sci. USA, 1987, 17, 6883.

[11] *M. Billeter, A.E. Howard, I.D. Kuntz and P.A. Kollman.* J. Am. Chem. Soc., 1998, 110 8385.

[12] *S.W. Chiu, J.A. Novontny and E. Jakobsson.* Biophysical J. 1989, 64, №1, 98.

[13] *W.D. Cornell, P.Cieplak, C.I. Bayly, I.R. Gould, K.M. Merz, et al.* J. Am. Chem. Soc., 1995, 117, 5179.

[14] *N.L. Allinger, V.Yuh.* QCPE-395, Indiana Univ., 2000.

N.Ə. İsakova, İ.N. Əliyeva, N.M. Qojayev

NEYROMEDİN NmU-8-İN MOLEKULYAR DİNAMİKASI

Donuzun onurğa sümüyündən alınmış tənzimləyici peptid neyromedin NmU-8-in molekulyar dinamika üsulu ilə konformasiya mütəhərrəkliyi öyrənilmişdir. NmU-8 üçün hesablamalar molekulun ölçüləri verilməklə vakuumda və su mühitində aparılmışdır. II-ji halda peptid 264 SPC-su molekulundan ibarət düzbucaqlı qutuya salırlar. Müəyyən edilmişdir, ki N-uclu Tyr[1]- Phe[4] fraqmentinin mütəhərrəkliyi vakuumda və su mühitində qeyri-müəyyən quruluşa malikdir. Əsas zəncirin Arg[5]- Asn[8] fraqmenti məhdud sayda konformasiya halında olmasına baxmayaraq, yan zəncirlər bütün mümkün hallarda ola bilirlər.

Н.А. Исакова, И.Н. Алиева, Н.М. Годжаев

МОЛЕКУЛЯРНАЯ ДИНАМИКА НЕЙРОМЕДИНА NmU-8

Методом молекулярной динамики изучена конформационная подвижность нейромедина NmU-8, регуляторного пептида, выделенного из спинного мозга свиньи. Расчет молекулярной динамики NmU-8 проводился в вакууме и в условиях явно заданных молекул воды. В последнем случае пептид помещали в прямоугольный ящик с 264 молекулами SPC- воды с наложенными периодическими граничными условиями. Установлено, что благодаря подвижности N- концевого фрагмента Tyr[1]- Phe[4] пептид имеет неупорядоченную структуру в вакууме и в водном растворе, а фрагмент Arg[5]- Asn[8] основной цепи принимает ограниченное число конформационных состояний.

GREEN FUNCTION METHOD IN A FERROMAGNETIC SUPERLATTICE

V.A.TANRIVERDIYEV

Institute of Physics of the National Academy of Sciences of Azerbaijan
Baku Az -1143, H. Javid ave.33.

The expression of Green function for different layers in a ferromagnetic superlattice is derived by the recurrence relations technique. The elementary unit cell of the superlattice under consideration consists of alternating layers of two simple-cubic Heisenberg ferromagnets. The results are illustrated numerically for a particular choice of parameters

In the past few years, there has been growing interest in the magnetic properties of artificially layered structures. With the advance of modern vacuum science, in particular the epitaxial growth technique, it is possible to grow very thin films of predetermined thickness, even of a few monolayers [1-3]. Superlattice structures composed of two different ferromagnetic layers (Fe/Co, Fe/Cr, Fe/Ni, Co/Cr, Dy/Gd etc.) have already been artificially fabricated. They have potential applications in magnetic information technology. Green's function method interface rescaling technique transfer matrix formalism as well as recurrence relations technique is used for their studies [4-6]. Green function method is the most useful among these methods. The physical characteristics, such as spectrum of magnons, the temperature dependence of magnetization, magnetic susceptibility and others of magnetic layered structures are

obtained using Green function method [7,8]. The investigation of Green function in SLs is not new, but many earlier papers considered only the case the SLs composed of two different ferromagnetic or antiferromagnetic atomic layers [9,10]. J. Mathon derived the exact local spin-wave Green function in an arbitrary ferromagnetic interface, superlattice and disordered layer structure in ref. [11].

As indicated in fig1. we consider in this article a superlattice in which the elementary unit cell n_1 layers of material 1 alternate with n_2 layers of material 2. Both material are taken to be simple-cubic Heisenberg ferromagnets, having exchange constant J_1 and J_2 and lattice constant a. The exchange constant between constituents is J. The expression of Green function for different layers in the superlattice under consideration is derived by the recurrence relations technique.
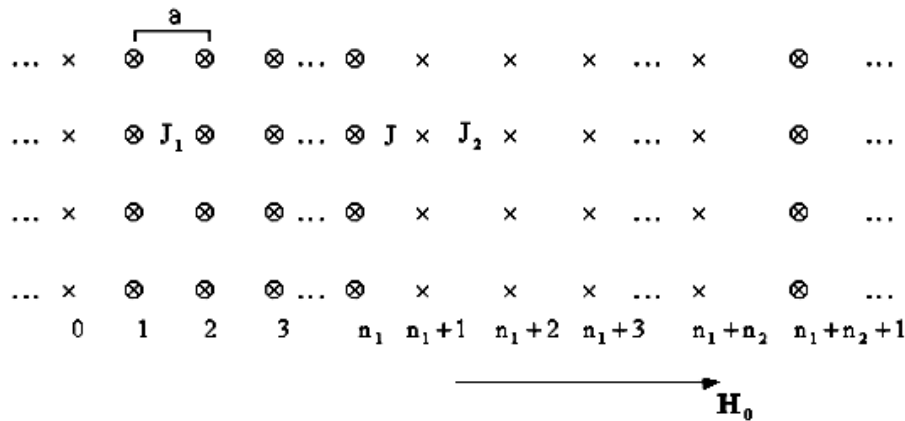

Fig.1. The elementary unit cell of *SL* consisting *N* different simple-cubic Heizenberg antiferromagnetic materials. The same lattice parameter *a* is assumed for all the materials. Antiferromagnetic layers consist of n_j $(j=1,2,…,N)$ atomic layers. The layers are infinite in the direction perpendicular to the axes *z*.

The Hamiltonian of the system can be written in the form

$$\mathrm{H} = -\frac{1}{2}\sum_{i,j} J_{i,j}\left(\vec{S}_i\vec{S}_j\right) - \sum_i g_i\mu_B\left(\mathrm{H}_i^{(A)} + \mathrm{H}_0\right), \qquad (1)$$

where the first term describes exchange interactions between the neighbouring spins and the last terms include the Zeeman's energy and magnetic anisotropy energy. The axis *z*

of the coordinate system is normal to the film interfaces [001] and external field H_0 is assumed to be parallel to the axis z. $H_i^{(A)}$ $(i=1, 2)$ anisotropy field for *a* ferromagnetic with simple uniaxial anisotropy along the *z* axis.

Employing the equation of motion for the Green function $G_{i,j}(t, t') = \langle\langle S_i^+(t); S_j^-(t')\rangle\rangle$ one obtains the following equation after two dimensional Fourier transform [9]

$$\left\{\omega - g_i\mu_B\left(H_0 + H_i^{(A)}\right) - 4J_{n,n}\gamma(k_{||})\langle S_n^z\rangle - J_{n,n+1}\langle S_{n+1}^z\rangle - J_{n,n-1}\langle S_{n-1}^z\rangle\right\}G_{n,n'}(\omega, k_{||}) +$$
$$+ J_{n,n+1}G_{n+1,n'}(\omega, k_{||}) + J_{n,n-1}G_{n-1,n'}(\omega, k_{||}) = 2\langle S_n^z\rangle\delta_{n,n'} \qquad , \qquad (2)$$

here, *n* is the index of an atomic layer and $\gamma(k_{||})$ is defined as follows $\gamma(k_{||})=1-0.5(\cos k_x a+\cos k_y a)$. Equation (2)

are valid in the low-temperature limit and random-phase-approximation (RPA) has already been done.

The equation (2) can be solved by recurrence relations technique [12] to relate the Green functions for interface layers of the elementary unit cell

$$\begin{pmatrix} G_{n_1+n_2+1,n'} \\ G_{n_1+n_2,n'} \end{pmatrix} = T \begin{pmatrix} G_{1,n'} \\ G_{0,n'} \end{pmatrix} - \begin{pmatrix} \delta_1 \\ \delta_2 \end{pmatrix} \qquad (3)$$

where $T = T_{2R}T_2^{n_2-2}T_{2L}T_{1R}T_1^{n_1-2}T_{1L}$ and the matrix T_{2R}, T_2, T_{2l}, T_{lR}, T_l and T_{ll} have the form:

$$T_{1(2)} = \begin{pmatrix} 2\cos(\theta_{1(2)}) & -1 \\ 1 & 0 \end{pmatrix}$$

$$T_{1(2)R} = \frac{-1}{J\langle S_{2(1)}\rangle}\begin{pmatrix} \omega - \lambda_{12(21)} & J_{1(2)}\langle S_{1(2)}\rangle \\ -J\langle S_{2(1)}\rangle & 0 \end{pmatrix},$$

$$T_{1(2)L} = \frac{-1}{J_{1(2)}\langle S_{1(2)}\rangle}\begin{pmatrix} \omega - \lambda_{12(21)} & J\langle S_{2(1)}\rangle \\ -J_{1(2)}\langle S_{1(2)}\rangle & 0 \end{pmatrix} \qquad (4)$$

$$\begin{pmatrix} \delta_1 \\ \delta_2 \end{pmatrix} = \begin{cases} T_{2R}T_2^{n_2-2}T_{2L}T_{1R}T_1^{n_1-2}\begin{pmatrix} -2/J_1 \\ 0 \end{pmatrix} & n'=1 \\[2ex] T_{2R}T_2^{n_2-2}T_{2L}T_{1R}T_1^{n_1-n'-1}\begin{pmatrix} 0 \\ -2/J_1 \end{pmatrix} & 2\leq n'\leq n_1-1 \\[2ex] T_{2R}T_2^{n_2-2}\begin{pmatrix} 2\langle S_1\rangle(\omega - \lambda_{21})/JJ_2\langle S_2\rangle^2 \\ -2\langle S_1\rangle/J\langle S_2\rangle \end{pmatrix} & n'=n_1 \\[2ex] T_{2R}T_2^{n_2-2}\begin{pmatrix} -2/J_2 \\ 0 \end{pmatrix} & n'=n_1+1 \\[2ex] T_{2R}T_2^{n_2-n'-1}\begin{pmatrix} -2/J_2 \\ 0 \end{pmatrix} & n_1+2\leq n'\leq n_1+n_2-1 \\[2ex] \begin{pmatrix} -2\langle S_2\rangle/J\langle S_1\rangle \\ 0 \end{pmatrix} & n'=n_1+n_2 \end{cases} \qquad (5)$$

$$\lambda_{12(21)} = g_{1(2)}\mu_B(H_0 + H_{1(2)}^{(A)}) + J_{1(2)}\langle S_{1(2)}^z\rangle + J\langle S_{2(1)}^z\rangle + 4J_{1(2)}\langle S_{1(2)}^z\rangle\gamma(k_{//}),$$

θ_1 and θ_2 are defined by the expression

$$\cos(\theta_{1(2)}) \equiv b_{1(2)} = \left(g_{1(2)}\mu_B(H_0 + H_{1(2)}^{(A)}) + 2J_{1(2)}\langle S_{1(2)}^z\rangle + 4J_{1(2)}\langle S_{1(2)}^z\rangle\gamma(k_{//}) - \omega\right)/2J_{1(2)}\langle S_{1(2)}\rangle \qquad (6)$$

For $|b_{1(2)}| > 1$, $b_{1(2)} = \cosh(\theta_{1(2)})$, and one replaces $\sin(n\theta_{1(2)})$ by $\sinh(n\theta_{1(2)})$ for $b_{1(2)} > 1$ and $(-1)^n \sinh(n\theta_{1(2)})$ for $b_{1(2)} < -1$. The matrix elements of T is given by the following expression

$$T_{11} = (x_{11}Y_{11} - x_{12}Y_{12})/(J^2 J_1 J_2\langle S_1\rangle^2\langle S_2\rangle^2 \sin(\theta_1)\sin(\theta_2))$$

$$T_{12} = (x_{12}Y_{11} + x_{22}Y_{12})/(J^2 J_1 J_2\langle S_1\rangle^2\langle S_2\rangle^2 \sin(\theta_1)\sin(\theta_2))$$

$$x_{11} = (\omega - \lambda_{12})^2 \sin((n_1-1)\theta_1) + 2J_1\langle S_1\rangle(\omega - \lambda_{12})\sin((n_1-2)\theta_1) + J_1^2\langle S_1\rangle^2\sin((n_1\ 3)\theta_1) \qquad (7)$$

$$x_{12} = J\langle S_2\rangle[(\omega - \lambda_{12})\sin((n_1-1)\theta_1) + J_1\langle S_1\rangle\sin((n_1-2)\theta_1)]$$

$$x_{22} = -J^2\langle S_2\rangle^2 \sin((n_1-1)\theta_1)$$

the matrix elements T_{21}, T_{22} and Y_{11}, Y_{12}, Y_{22} by replacing all subscript 1 by 2, 2 by 1 in - T_{21}, T_{22} and Y_{11}, Y_{12}, Y_{22}, respectively.

The system is also periodic in the z direction, which lattice constant is $L = (n_1 + n_2)a$. According to Bloch's theorem we can write [13,14]

$$\begin{pmatrix} G_{n_1+n_2+1,n'} \\ G_{n_1+n_2,n'} \end{pmatrix} = exp[iK_zL] \begin{pmatrix} G_{1,n'} \\ G_{0,n'} \end{pmatrix} \quad (8)$$

The expression of Green function $G_{1,n'}(\omega, k_{//})$ and $G_{0,n'}(\omega, k_{//})$ are obtained by using equation (3) and (8).

$$G_{1,n'}(\omega,k_{//}) = \frac{(\delta_1 T_{22} - \delta_2 T_{12})exp[-iK_zL] - \delta_1}{2cos(K_zL) - T_{11} - T_{22}}, \quad G_{0,n'}(\omega,k_{//}) = \frac{(\delta_2 T_{11} - \delta_1 T_{21})exp[-iK_zL] - \delta_2}{2cos(K_zL) - T_{11} - T_{22}} \quad (9)$$

The Green's function for all layers of elementary unit of superlattice are related with $G_{1,n'}(\omega, k_{//})$ and $G_{0,n'}(\omega, k_{//})$ by reccurence relation technique. Using (4), (5) and (8) one can calculate the Green's function for different layers in elementary unit cell of the superlattice under the consideration.

Green function for the left-hand $(n' = 1)$ and right-hand $(n' = n_1)$ layers of components 1 in elementary unit cell of the superlattice have the form

$$G_{1,1}(\omega, k_{//}) = G_{n_1,n_1}(\omega, k_{//}) = (2S_1 T_{12}/(JS_2))/(2cos(K_zL) - T_{11} - T_{22}) \quad (10)$$

Green function for the bulk layers $(2 \le n' \le n_1 - 1)$ of components 1 in elementary unit cell of the superlattice has the form

$$G_{n',n'}(\omega, k_{//}) = [x'_{22}x'_{12}(T_{22} - T_{11}) + (x'_{22})^2 T_{21} - (x'_{12})^2 T_{12}]/[0.5J_1^2 J^3 \langle S_1 \rangle sin^2(\theta_1)(2cos(K_zL) - T_{11} - T_{22})] \quad (11)$$

$$x'_{11} = (\omega - \lambda_{12})^2 sin((n' - 1)\theta_1) + 2J_1\langle S_1 \rangle(\omega - \lambda_{12})sin((n' - 2)\theta_1) + J_1^2\langle S_1 \rangle^2 sin((n' - 3)\theta_1)$$

$$x'_{12} = J\langle S_2 \rangle[(\omega - \lambda_{12})sin((n'-1)\theta_1) + J_1\langle S_1 \rangle sin((n'-2)\theta_1)], \quad x'_{22} = -J^2\langle S_2 \rangle^2 sin((n' - 1)\theta_1)$$

Green function for the left-hand layer $(n' = n_1 + 1)$, the bulk layers $(n_1 + 2 \le n' \le n_1 + n_2 - 1)$ and right-hand layer $(n' = n_1 + n_2)$ of components 2 in elementary unit cell of the superlattice are obtained by replacing all subscript 1 by 2, 2 by 1 and $(n' \to n' + n_1)$ in the Green's function for the same layers of components 1 in elementary unit cell of the superlattice, respectively.

For numerical illustration of our result we consider the spin wave dispersion-curve of the superlattice under consideration. As known the spin-wave spectrum is obtained from the poles of Green function. fig 2(a) shows the bulk spin-wave dispersion curves of the component 1 and 2 for a particular choice of parameters, while fig.2(b) shows the spin-wave dispersion curves of the superlattice. In the frequence range, where k_{1z} and k_{2z} are real, the superlattice dispersion curve exhibits broad pass bands and narrow stop bands. The pass bands are narrow and the stop bands are broud where at least one of the wave vectors is complex.
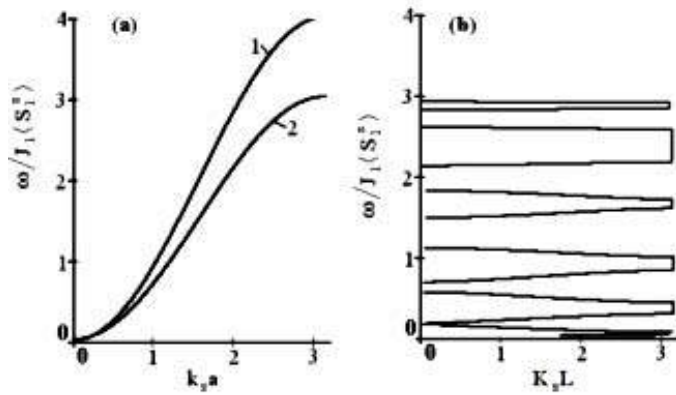

Fig.2. Bulk spin – wave dispersion graphs for [001] propagation with parameters $J_2/J_1 = 2$; $g_1 = g_2$;

$$g_1\mu_B H_1^{(A)}/J_1\langle S_1^z \rangle = 0.01;$$

$$g_2\mu_B H_2^{(A)}/J_1\langle S_1^z \rangle = 0.03.$$

[1] J. J. Chen, G. Dresselhaus, M.S. Dresselhaus, G. Sprinhoulz, C. Picher, G. Bauer. Phys. Rev. B54,1996, 4020.
[2] C. A. Ramos, D. Lederman, A.R. King, V. Jaccarino Phys. Rev. Lett. 1990, 65, 2913.
[3] T. M. Giebultowicz, P. Klosovski, N. Samarth, H. Lou, J. K. Furdyna, J. J. Rhyne, Phys. Rev. B48, 1993, 12817.
[4] R..L.Stamps and R.E.Camley. Phys. Rev. B54, 15200, 1996.
[5] V.A.Tanriverdiyev, V.S.Tagiyev, M.B.Guseynov, Phys. Stat. Sol. (b). 2003, 240, 183.
[6] E.L. Albuquerque, R.N. Costa Filho, M.G. Cottam, J. Appl. Phys. 2000, 87, 5938.

[7] H. T. Diep, Physics Lett. A 138, 1989, 69.
[8] V.A.Tanriverdiyev, V.S.Tagiyev, M.B.Guseynov, FNT, №12, 2003.
[9] Yi-fang Zhou, Phys Lett. A, 1989, 134, 257.
[10] J. Mathon, J. Phys. Condens. Matter. 1,1989, 2505.
[11] Feng Chen and H.K.Sy, J. Phys. Condens. Matter. 1995, 7, 6591.
[12] E.L.Albuquerque, P.Fulko, E.F.Sarmento, D.R.Tilley. Solid State Commun. 58, 41 (1986).
[13] J. Barnas, J. Phys.C: Sol.St.Phys. 21, 1021 (1988).

V.Ə. Tanrıverdiyev

FERROMAGNİT İFRAT QƏFƏSDƏ QRİN FUNKSİYASI METODU

Rekurens əlaqələr metodu ilə ferromagnit ifrat qəfəsin müxtəlif layları üçün Qrin funksiyasının ifadəsi tapılıb. Baxılan ifrat qəfəsin elementar özəyi   iki müxtlif sadə kubik Heyzenberq tip ferromaqnit layların növbələşməsindən   təşkil olunub. Alınan nəticələr parametrlərin seçilmiş qiymətləri üçün kəmiyyətcə təsvir olunub.

В. А. Танрывердиев

МЕТОД ФУНКЦИЙ ГРИНА В ФЕРРОМАГНИТНОЙ СВЕРХРЕШЕТКЕ

С помощью техники рекуррентных соогношений найдены выражения функции Грина для различных слоев ферромагнитной сверхрешетки. Элементарная ячейка расматриваемой сверхрешетки состоит из чередующихся слоёв двух различных простых Гейзенберговских ферромагнетиков. Результаты проиллюстрированы количественно для выбранных значений параметров.

THE DIFFUSE PHASE TRANSITION IN HTSC AND THE MAGNETIC FIELD INFLUENCE ON IT

S.A. ALIEV, S.S. RAGIMOV, V.M. ALIEV

Institute of Physics National Academy of Sciences
H.Javid ave.33, Baku-1143, Azerbaijan

The results of electrical properties of bismuth (2212, 2223), yttrium (123), $YBa_2Cu_{2.87}Fe_{0.13}O_{7-y}$, and $La_{2-x}Sr_xCuO_4$ crystals in the superconducting phase transition (SCPT) region are interpreted within the framework of the theory of diffuse phase transition (SPT). The parameters of PT, characterizing the region and the degree of diffuse of SC transition are determined: T_0, a_B, $L(T)$, dL/dT, $2\Delta T^*$ and $2\Delta T^*/T_0$ at different values of a magnetic fields (B).

It was shown that in HTSC the supercoducting PT, without "premature" decreasing region of $\rho(T)$ and $\alpha(T)$ has the diffuse character. The SC transitions take placed under the $m_{SCP}/m_{NP}=exp[a_B(T-T_0)]$ law, and under magnetic field (B) strongly increased the diffuse degree. It was founded the most probably defects, which stipulate the diffuse of PT in HTSC and the reason leading to rise of degree of diffuse in magnetic field.

The study of processes take placed near by and in range of phase transformations (FT) is one of developing directions of solid-state physics. The interest to this, widely investigated, direction has increased after discovering high temperature superconductors (HTSC). One of actual questions of the given direction is the study of regularity of transition of one of coexisting phases in other, detection of classification FT, namely in what extent the transition is pointy or blurred. For this purpose the calculations of arguments FT is necessary, by which one are possible are to reveal the range and extent of diffusion FT. Such problems are reviewed in [1-4] for crystals Ag_2Te, Ag_2Se and $AgFeTe_2$, having structural FT. In particular, in [2,3] at study of electrical and thermal properties Ag_2Te and Ag_2Se near by and in range FT were observed a number of a feature. For interpretation of the obtained data the theory blurred FT was involved [5-7]. Proceeding from the theoretical reasons, the procedure of determination of masses coexisting in range FT of phases (m_α, m_β), by data, which were, calculated the parameters of FT, defining range and extent of diffusion FT. It was shown, that the electronic processes, which are flowing at FT, by virtue of them on many smaller inertness effect, than thermal processes, are most responsive to a subtle structure FT and can be applied for determination of parameters FT, irrespective of their origin. The given procedure was used for study FT in bismuth HTSC [8-9], where is shown, that SC FT in them have blurred nature. Under of an external magnetic field the diffusion hardly increases, the asymmetry FT and etc. feature occurs.

With the purpose of generalization and developments obtained in works [8-9] of result in whole for HTSC it is necessary to increase number considered HTSC, to expand a range of magnetic and electrical fields, to involve the data of crystalline samples etc. It to allow to reveal regularity of transitions SFT - NF, influencing on these transitions of external factors, to study variations take placed in range of "premature" decreasing of specific receptivity (ρ) in HTSC, to determine range and extent of diffusion FT in wide-spread HTSC, and also influencing on them of an anisotropy, related by layered crystalline structure of HTSC. Therefore in the given work is analyzed the electrical properties of specific receptivity $\rho(B,T)$ and thermal power $\alpha(B,T)$ in range FT most widely investigated HTSC: $YBa_2Cu_3O_{7-\delta}$ [10], $YBa_2Cu_{2.87}Fe_{0.13}O_{7-\delta}$ [11], in directions $B//$ to a plain (ab) and $B\perp(ab)$; $Bi_{1.72}Pb_{0.34}Sr_{1.83}Ca_{1.97}Cu_{3.13}O_{10+\delta}$ (2223) and $Bi_2Sr_2CaCu_2O_{10+\delta}$ (2212) and $La_{2-x}Sr_xCuO_4$ (214). The experimental data are interpreted within the framework of the theory DFT [5-7] on procedure offered in [2, 3].

Theory and procedure of determination of parameters FT

The theory DFT in solids is reviewed in [5-7]. With this purpose was used the theory DFT in condensate systems, founded on the introducing of a function of inclusion $L(T)$, describing a relative part of phases in range of their coexistence. It is supposed that, if thermodynamic potentials of α and β- phases to designate through Φ_α and $\Phi_\beta\Phi$, the thermodynamic potential $\Phi(T)$ in range FT can be introduced by

$$\Phi(T) = \Phi_\alpha(T) + \Delta\Phi \cdot L(T) \qquad (1)$$

Where $\Delta\Phi(T)=\Phi_\beta(T)-\Phi_\alpha(T)$. In a case, when FT take placed in $\Delta T=T_2-T_1(T_2>T_1)$ interval, the function $L(T)$ should fit asymptotic conditions

$$L(T)=\begin{cases} 0 & T < T_1 \\ 0 < L < 1 & T_1 < T < T_2 \\ 1 & T > T_2 \end{cases} \qquad (2)$$

According to the theory DFT, for a function $L(T)$ is obtained

$$L(T) = \frac{1}{1 + exp[-a(T - T_0)]} \qquad (3)$$

Where T_0- temperature, at which mass of both phases are quantitatively equal, a – temperature dependent constant describing extent of diffusion FT, depending from a volume of possible fluctuations, and also energy and temperature FT. Informative the derivative $L(T)$ on temperature is also

$$\frac{\partial L}{\partial T} = \frac{a}{2} \frac{1}{1 + ch[-a(T - T_0)]} \qquad (4)$$

defining temperature speed of phase transformations in each transition point. Allowing, that $L(T)$ characterizes a relative part of phases in range FT, it can be determined and under the data of masses of each phase (m_α, m_β) by

$$L(T) = \left[1 + \frac{m_\alpha(T)}{m_\beta(T)} \right]^{-1} \qquad (5)$$

From the joint solution (3) and (5) follows

$$a = \frac{1}{T_0 - T} \ln \frac{m_\alpha}{m_\beta} \qquad (6)$$

According to (6) the dependence $ln\left(\dfrac{m_\alpha}{m_\beta} = y \right)$ from T gives straight, the interception which with a temperature axis corresponds to T_0, and slope $ln\ y / \Delta T$ - to a temperature constant - a.

In works [2-4] enabling, that in region of FT a temperature change of a differential - thermal analysis DTA and electrical properties of Ag_2Te and Ag_2Se in region of FT are related by, basically, quantitative change of α and β phases, the parameters of FT were determined: a, T_0, $L(T)$, dL/dT and change of some thermodynamic parameters in FT region. For this purpose it was necessary to achieve a linear temperature variation nearly and in FT region. Then from a beginning up to the end of transition the interval of ΔT may be to divide into equal intervals and corresponding values of investigated effects to refer to suspected phases, for example

$$\Delta T_y = T_{y,\alpha}(1 - m_\beta/m_\alpha) + \Delta T_{y,\beta}(m_\beta/m_\alpha) \qquad (7)$$

If by analogy Ag_2Te and Ag_2Se to accept for one phase normal (NF), and for other superconducting (SCF), the offered procedure can be applied and for HTSC. Then the conforming masses will accept values m_{nf} and m_{scf}.

Discussion of obtained results

In a fig.1 are submitted the $\rho(T,B)$ and $\alpha(T,B)$ dependencies for a crystalline sample $Bi_2Sr_2CaCu_2O_{7+\delta}$ (2212) and $\rho(T,B)$ for a crystalline sample $Ag(Bi_{1.72}Pb_{0.34}Sr_{1.83}Ca_{1.97}Cu_{3.13}O_{10+\delta}$ (2223), investigated in [12] up to magnetic fields 12 T. For analysis are involved the data of [10], in which $\rho(T,B)$ of crystalline $YBa_2Cu_3O_{7-\delta}$ are investigated up to 5 T (fig. 2a), the data [11] in which $\rho(T,B)$ of $YBa_2Cu_{2.87}Fe_{0.13}O_{7-\delta}$ is investigated in a direction $B||(ab)$ of plain and $B\perp(ab)$, accordingly up to 5 T and 4 T, and also $La_{2-x}Sr_xCuO_4$ (214) [13]. For each of introduced curves $\rho(T,B)$ and $\alpha(T,B)$ in FT region the masses m_{sf} and m_{nf} are found, the relations $ln(m_{nf}/m_{sf})$ from T are constructed and are determined T_0 and a_B at different values of a magnetic field. In a fig. 3(a) are presented the characteristic dependencies of $ln(y,T)$ only for $YBa_2Cu_{2.87}Fe_{0.13}O_{7-\delta}$ in a case $B//(ab)$ plain. It is shown, that in all reviewed HTSC crystals with increasing of B the value T_0 and a_B hardly decreases. From the data of a fig. 3a

are seen, that the temperature dependencies of distribution of coexisting phases (in FT region), by excepting of high temperature part of transition corresponding to "premature" region of $\rho(T)$, are well layed on straight $\ln (m_{scf}/m_{nf} = y$, T). But the dependencies of $ln(y,T)$ and in high temperature region also is linear, but with other slope independent of value B. The values of a on this segment (a_{sf}) on the order are less, than in a main segment SCFT (a_0) at B=0. In a fig. 3b are shown the a_B/a_0 dependencies from a magnetic field. As is seen the strong decreasing of a is occurred at weak fields. The data analysis are shown, that this segment of B corresponds to ranges of the lower critical field B_{c1}, at which one is always watched a fracture of communal dependencies of a critical field $B_c(T)$ from T. From the obtained here results it may be to conclude, that for reviewed HTSC the superconducting phase transformation, irrespective of value of a magnetic field, is realized under the law $m_{scf}/m_{nf} = \exp[a_B(T-T_0)]$, where a a_B - temperature-dependent constant for each crystals depending only on value B. It means, that the process of despairing of SC electronic pairs (or process of formation of vortex currents) in a magnetic field is realized by the indicated exponential law.
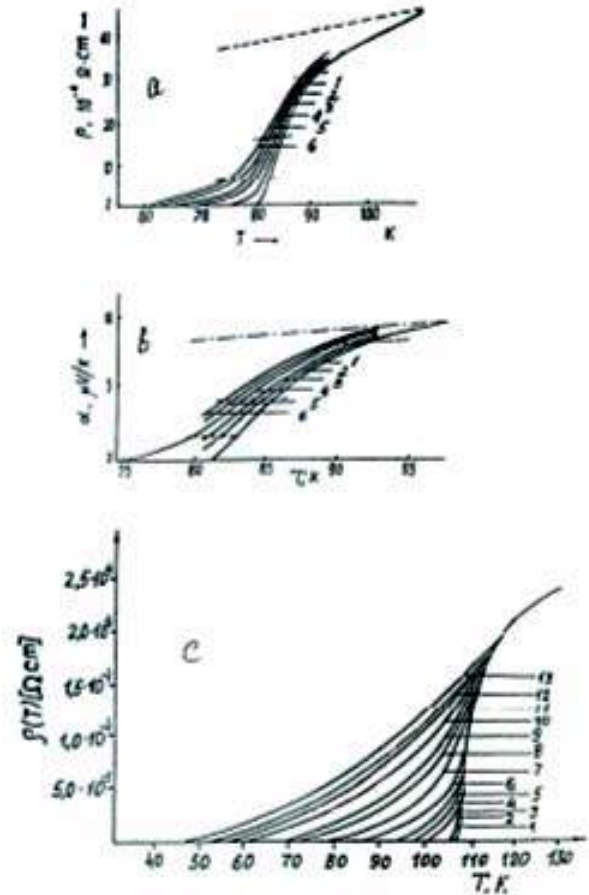

Fig. 1. Temperature dependencies of specific resistance (a), thermal power (в) of Bi-SC (2212) at B: 1 - 0; 2 - 0.1; 3 – 0.2; 4 - 0.5; 5 - 0.9; 6 - 2.2 T and Bi (2223) (c) at B: 1- 0; 2 - 0.01; 3 - 0.05; 4 - 0.1; 5 - 0.2; 6 - 0.5; 7 - 1; 8 – 2; 9 - 3; 10 - 5; 11 - 7; 12 - 9; 13 - 12T.

It should be noted, that on a segment of "premature" decreasing of $\rho(T)$ of FT also is realized by the exponential law $m_{scf}/m_{nf} = \exp [a_{sf}(T-T_{0s})]$, but with the data a_{sf} and T_{0sf}, intrinsic to this region. It confirms opinion that the mechanism of pairing on a segment of "premature"

decreasing of resistance differs from the mechanism of a main segment of SC transition.
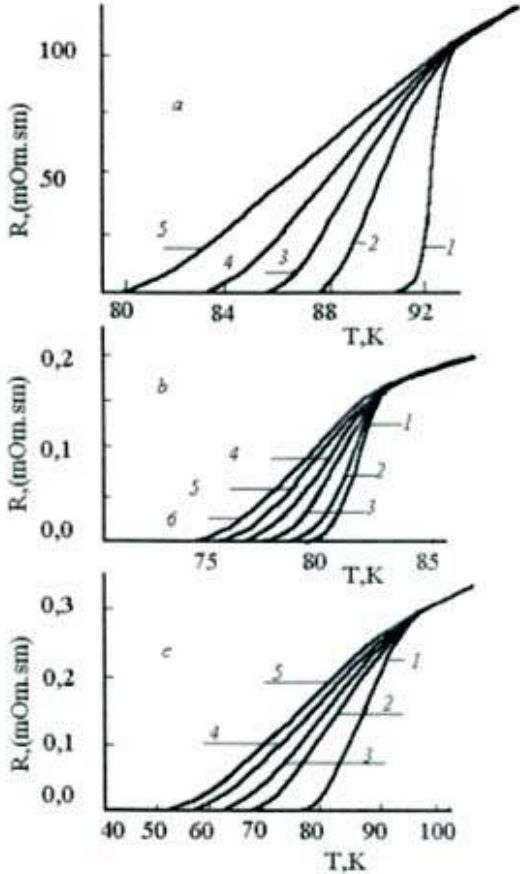

Fig. 2. Temperature dependencies of specific resistance of YBa$_2$Cu$_3$O$_{7-\delta}$ (a) at B: 1 - 0; 2 - 1; 3 - 2; 4 - 4; 5 - 5T [10], YBa$_2$Cu$_{2.87}$Fe$_{0.13}$O$_{7-\delta}$ at B||(ab) B: 1 - 0; 2 - 1; 3 – 2; 4 - 3; 5 - 4; 6 - 5T and B $\perp$ (ab) B: 1 - 0; 2 - 1; 3 - 2; 4 - 3; 5 - 4T [11].
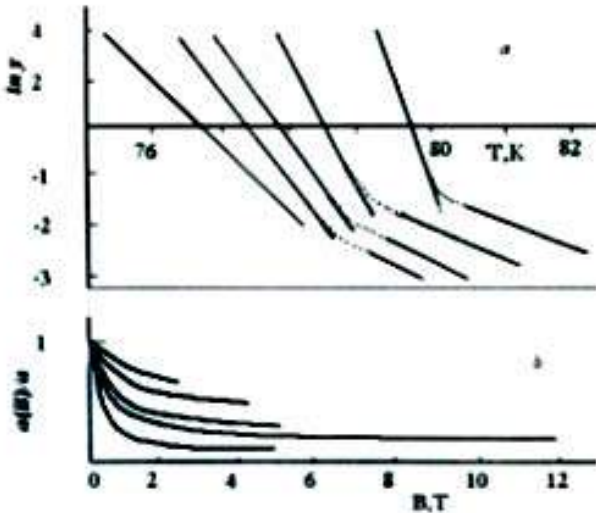

Fig. 3. Temperature dependence of mass distribution lny (a) in YBa$_2$Cu$_{2.87}$Fe$_{0.13}$O$_{7-\delta}$ In a case B || (ab) at B: 1 - 0; 2 –1; 3 - 2; 4 - 3; 5 - 4T and dependence of a tempera-ture constant a_B (b) from a magnetic field: 1-Bi (2212); 2 - Bi (2223); 3 - Y (123); 4 - YBa$_2$Cu$_{2.87}$Fe$_{0.13}$O$_{7-\delta}$ B|| (ab) and 5 - YBa$_2$Cu$_{2.87}$Fe$_{0.13}$O$_{7-\delta}$ B$\perp$ (ab).

According the data of a_B and T$_0$ for each dependencies ρ(B,T) and α(B,T) were calculated a inclusion function L (T) and temperature speed FT dL/dT. In fig. 4 are shown the

dependencies *L (T)* and *dL/dT* only for bismuthic (2223) HTSC at different values B. These characteristic and for remaining HTSC crystals data visually demonstrate a diffusing of SC phase transition in HTSC and influencing on them magnetic fields. It follows that according to the theory [5-7] at point FT tangent to inflection point L (T) there should be a vertical axis, and in a case DFT tangent will derivate a definite angle with a vertical axis, depending on value a. The calculations shows, that for the reviewed crystals the value of this angle reaches up to 45º. The rate of change of a function dL (T) /dT according to the theory DFT is figured by a curve with a final maximum at T$_0$ (as in a fig. 4), where as for point FT she can aspire in this point to infinity. For the quantitative characterize of diffusion FT it may be to use a half-width of a curve dL/dT i.e. interval ΔT^*, counted from T$_0$, in which dL/dT decreases twice as contrasted to with maximum rating dL/dT (ΔT^*) = 1/2, from which one,

with allowance for (4) follows: $\Delta T^* = \dfrac{arcch3}{a_B} = \dfrac{1.76}{a_B}$

or, allowing the left and right party from T$_0$ we shall receive $2\Delta T^* = T_1 - T_2 = 3.52/a_B$. Then in the formulas (3) and (4) in a place *a* using 3.52 / (T$_1$-T$_2$) it is possible to calculate L (T) and *dL/dT* for region of diffusion IF. The calculations shows, that to an interval $2\Delta T^*$ there corresponds variation of a function L (T) from value 0.15 (at T$_1$) up to value 0.85 (at T$_2$). In a fig. 4 these regions are indicated with broken lines, the values which one coincides with counted on the data an a_B. It is expedient to enter into the table the value of the most relevant parameters for all reviewed HTSC at different values of a magnetic field. In particular: ΔT_{ST} - interval of temperature of SC phase transition (without region of "premature" decreasing ρ); T$_K$ (B) - critical temperature; T$_0$ (B) temperature at which one m$_{SF}$=m$_{NF}$; a_B- temperature constant; *dL/dT* at T$_0$; $2\Delta T^*$ - interval of diffusion of SCFT and $2\Delta T^*$/T$_0$ - relative value of region of diffusion FT. Let's remark, what there is a tendency - than above temperature SCFT, the more FT interval ΔT_{ST}, therefore and region of diffusion FT, but ratio $2\Delta T^*$/T$_0$ excludes such relation and demonstrates an extent of diffusion FT temperature-independent of transition.
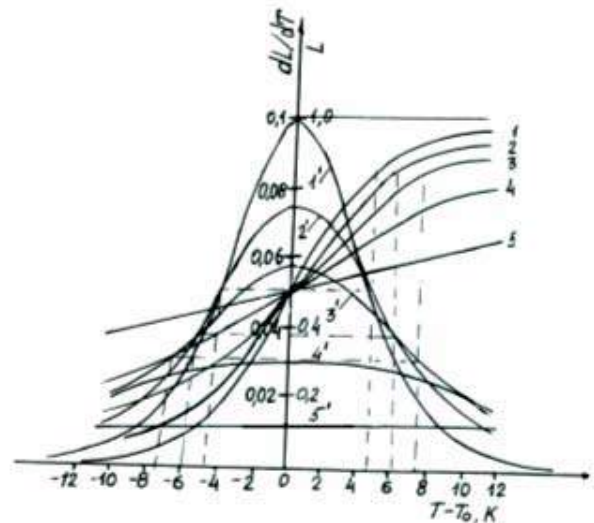

Fig. 4. Temperature dependencies of include function L (T) and its derivative dL/dT for Bi (2223) at B: 1 and 1 ' - 0; 2 and 2 ' - 0.1; 3 and 3 ' - 0.2; 4 and 4 ' - 2; 5 and 5 '- 12T.

From the reduced data follows, that among reviewed HTSC yttrium have the least diffusion SCFT, the replacement of $Cu_{0.13}$ atoms by $Fe_{0.13}$ atoms does not result in noticeable variation of diffusion FT. In a direction B⊥ (ab), J|| (ab) region of diffusion hardly extends, as enhances influence a magnetic field on an extent of diffusion in it. The data on $La_{2-X}Sr_XCuO_4$ (X=0,15; 0,16; 0,18) demonstrate, that, despite of rather low extreme temperature, in them the diffusions SCFT are higher, than in yttrium HTSC. For comparison in the table are brought the data for classic SC 1 kind of stannum (Sn) at different values of a current density (j), flowing through it [14]. As is seen, in Sn the value of a_i, though and on three orders it is more than in HTSC, but SC transition is not pointy, and the diffusion increases with increase of a current density, which one acts to an identically external magnetic field. From these data also follows, that the degree of diffusion of FT in SC- I of a kind, approximately one order is less, than in HTSC (in relative units $2\Delta T^*/T_0$).

Concerning the nature of defects resulting in to diffusion in SCFT in HTSC in absence of a magnetic field is possible to indicate on a non-uniformity, related by deviation from a stoichiometry of multicomponent structures, defect or excess of oxygen etc. imperfection. In case of bismuthic HTSC the presence of other phases (2201, 2212, 2223) is possible. Probably in bismuthic HTSC these factors cause a high scale of diffusion of FT. The defects resulting in to strong diffusion SCFT in a magnetic field, undoubtedly, are conditioned by a vortex state of SC- II kind, in which one, since very weak fields, are spontaneously arisen vortex currents. At further increasing of B the dimensions of vortexes and value of a flow of a magnetic field, which one they carry out, remains invariable, but quantity of vortexes is increased, forming similarly to atoms of a crystal an exact lattice, which leads to increase of diffusion degree of SCFT.

The table

The title of HTSC	B,T	$\Delta T_{СП}$ К	$T_K(B)$, К	$T_0(B)$, К	a_B, К[1]	dL/dT At $\Delta T=0$	$2\Delta T^*(B)$ К	$\dfrac{2\Delta T^*}{T_0}$
$YBa_2Cu_3O_{7-\delta}$ (123) [10]	0	1.1	91.4	91.8	6	1.5	0.6	0.0065
	1	3.5	88	89.3	1.25	0.31	2.8	0.03
	2	6	85.8	87.75	1.1	0.28	3.2	0.036
	5	11	80	83.75	0.75	0.19	4.7	0.05
$YBa_2Cu_{2.87}Fe_{0.13}O_{7-\delta}$ B|| (ab),B⊥J J⊥ (ab) [11]	0	1.5	79	79.85	5	1.25	0.7	0.0088
	1	2.7	77.3	78.6	2.9	0.72	1.2	0.0153
	3	4	75.5	77.5	1.94	0.49	1.8	0.023
	5	4.5	74.5	76.75	1.36	0.34	2.6	0.034
$YBa_2Cu_{2.87}Fe_{0.13}O_{7-\delta}$ B⊥ (ab), B⊥J , J ||(ab) [11]	0	7	78	79.5	1.2	0.30	2.9	0.0365
	1	17	68	73.4	0.64	0.16	5.5	0.075
	2	20	62	69.6	0.43	0.11	8.2	0.118
	4	27.3	52.7	63.9	0.25	0.08	14	0.22
$Ag(Bi_{1.72}Pb_{0.34}Sr_{1.83}$ $Ca_{1.97}Cu_{3.13}O_{10+\delta})$ (2223) [12]	0	10	107	109.5	0.4	0.1	8.8	0.08
	0.5	28	85	107	0.18	0.045	19.6	0.23
	2	38	72	106	0.12	0.03	29	0.27
	12	62	45	90	0.05	0.012	70	0.78
$Bi_2Sr_2CaCu_2O_{10+\delta}$ (2212)	0	12.5	80	86.5	0.3	0.075	11.7	0.13
	0.5	27	65	83.5	0.24	0.06	14.7	0.18
	2	32	60	82.5	0.2	0.05	16	0.19
$La_{1.85}Sr_{0.15}CuO_4$	-	10	40	41.75	0.65	0.16	5.6	0.13
$La_{1.84}Sr_{0.16}CuO_4$	-	5.4	40	41.25	0.8	0.2	4.8	0.12
$La_{1.82}Sr_{0.18}CuO_4$	-	4.6	36.75	37.30	0.43	0.11	7.6	0.2
Sn [14]	10µA	0.0038	3.721	3.722	2.088	522	0.00266	0.0007
	20µA	0.0045	2 3.721	3.721	1.75	436	0.00315	0.00085
	40µA	0.006	3.72 3.718	3.719	1.382	345	0.0042	0.001

[1] .S.A.Aliev, F.F.Aliev, G.P.Pashaev, Neorganicheskie Materiali, 1993, 29, 1073.

[2] S.A.Aliev, F.F.Aliev, Z.S.Gasanov. FTT, 1998, 40, 1693.

[3] S.A.Aliev, Z.S.Gasanov, Z.F.Agaev, R. Guseynov. Izv. NAN of Azerbaijan, ser. Phys, mat.and tech. nauk 5, 2002, 76.

[4] S.A.Aliev, Z.S.Gasanov, S.M.Abdullaev. J. Physica (Azerbaijan), 2002, 3, 24.

[5] B.N. Rolov. Diffusion of phase transformations, Riga 1972, 311p.

[6] B.N.Rolov, V.E.Yurkevich. Physics of diffusion phase transformations, Print. the Rostov University, 1983, 319 p.

[7] B.N.Rolov. Izv. AN.Lat.SSR, ser. Phys. and tech. nauk, 1983, 4, 33.

[8] S.A.Aliev, S.S.Ragimov, V.M.Aliev. Izv.NAN of Azerbaijan, ser. Phys, mat.and tech. nauk, 2002, 2, 67.

[9] S.A.Aliev. J. Physica (Azerbaijan), 2002, 4,32.

[10] U.Welp, W.K.Kwok, G.W.Grabtlee. Phys. Rev. Lett., 1989, 62,1908.

[11] M.D. Lan, I.Z. Lin and al. Phys. Rev. B, 1993, 47, 454.

[12] G. Crasso, F. Marti and al. Physica C, 1997, 281, 271.

[13] Migaki Oda, Naoki Momono and Masayuki Ido. Supercond. Sci. Technol., 2000, 3,57.

[14] Low temperature physics, under edit. A.I.SHalnikov, Moscow, 1959, 612p.

S.A. Əliyev, S.S. Rəhimov, V.M. Əliyev

YTİK-DƏ FAZA KEÇİDLƏRİNİN YAYILMASI VƏ ONLARA MAQNİT SAHƏSİNİN TƏSİRİ

Bismut (2212, 2223), ittrium (123), $YBa_2Cu_{2.87}Fe_{0.13}O_{7-\delta}$, və $La_{2-x}Sr_xCuO_4$ kristallarının ifratkeçirici faza keçidi oblastında (İKFK) elektrik xassələrinin nəticələri yayılmış faza keçidi (YFK) nəzəriyyəsi əsasında izah edilmişdir. Maqnit sahəsinin (B) müxtəlif qiymətlərində İK keçidlərin yayılma dərəcələri və oblastlarını xarakterizə edən T_0, a_B, L(T), *dL/dT*, $2\Delta T^*$ и $2\Delta T^*/T_0$ kimi FK parametrləri təyin edilmişdir. Göstərilmişdir ki, YTİK-də ifratkeçirici FK vaxtından əvvəl azalma oblastını nəzərə almadıqda yayınıq xarakterli olur, sahənin (B) təsiri altında yayınıqlıq dərəcəsi artır və $m_{СПФ}/m_{НФ} = \exp[a_B(T-T_0)]$ qanunu ilə baş verir. YTİK-də FK-nin yayınıqlığını təmin edən defektlər və maqnit sahəsində yayınıqlıq dərəcəsini artıran səbəblər göstərilmişdir.

С.А. Алиев, С.С. Рагимов, В.М. Алиев

РАЗМЫТИЕ ФАЗОВЫХ ПЕРЕХОДОВ В ВТСП И ВЛИЯНИЕ НА НИХ МАГНИТНОГО ПОЛЯ

Результаты электрических свойств висмутовых (2212, 2223), иттриевых (123), $YBa_2Cu_{2.87}Fe_{0.13}O_{7-\delta}$, и $La_{2-x}Sr_xCuO_4$ кристаллов в области сверхпроводящего фазового перехода (СПФП) интерпретированы в рамках теории размытых фазовых переходов (РФП). Определены параметры ФП, характеризующие область и степень размытия СП переходов: T_0, a_B, L(T), *dL/dT*, $2\Delta T^*$ и $2\Delta T^*/T_0$ при различных значениях магнитного поля (B). Показано, что в ВТСП сверхпроводящие ФП, без учета области "преждевременного" уменьшения ρ(T) и α(T), носят размытый характер, СП переходы, происходят по закону $m_{СПФ}/m_{НФ} = \exp[a_B(T-T_0)]$ и под действием B сильно возрастает степень размытия. Обоснованы наиболее вероятные дефекты, обуславливающие размытие ФП в ВТСП и причина, приводящая к возрастанию степени размытия в магнитном поле.

Received: 26.12.03

THERMODYNAMICS OF QUANTUM WIRES WITH A PARABOLIC POTENTIAL IN TILTED MAGNETIC FIELDS

G.B. IBRAGIMOV

Institute of Physics Azerbaijan National Academy of Sciences
H. Javid av.,33, Baku 1143

The magnetic susceptibility, specific heat and entropy of parabolic quantum wires in tilted magnetic fields is studied. The dependence of the magnetic susceptibility, specific heat and entropy on the magnitude of the magnetic field and the direction of the magnetic field, and parameters of a parabolic wells is shown explicitly.

During the past three decades, the physics of low-dimensional semiconductors has become a vital part of present –day research. Low - dimensional structures allow the study of a variety of new mechanical, optical,, and transport phenomena. In this context, one dimensional systems have been of particular interest for past decade [1-8].

The improvements of the semiconductor growth techniques have offered the possibility to obtain low-dimensional semiconductor structures with any desired well shapes. One of those structures is the so-called parabolic quantum well. Theoretically, parabolic confining potentials are very attractive, since the spectrum and wave functions of one-electron states have a simple analytical form, it is possible to derive explicit analytical expressions for the different physical parameters.

The magnetic field is an interesting additional parameter, since it can be applied experimentally in a well-controlled way and modifies fundamentally the electronic structure. The application of a magnetic field to a crystal changes the dimensionality of electronic levels and leads to a redistribution of a density of states. The magnetic field is assumed to be tilted with respect to the normal, it serves to add an extra confining potential to the initial confinement, gives rise to two different kinds of Landau level indices, and causes a dramatic change in the energy spectrum, leading to so-called hybrid magnetoelectric quantization.

As is known, thermodynamic properties is very important aspect for a low – dimensional electron gas [9-12]. This paper reports the thermodynamic properties of electrons in parabolic quantum wires in tilted magnetic fields. We consider the transport of an electron gas in a Q1D electron quantum wire structure as treated in [5, 6], in which a Q1D electron gas is confined by two confinement frequencies ω_l and ω_2 in the x and z directions, respectively, and the conduction electrons are free along only one direction (y direction) of the wire. Considering the magnetic field transverse tilt direction, $H=(H_x, 0, H_z)$ with the Landau gauge $A=(0, xH_z-zH_x,0)$, the eigenvalues $E_{nl}(ky)$ are written as [5,6]

$$E_{nl}\left(k_y\right)=\left(n+1/2\right)\hbar\Omega_1+\left(1+1/2\right)\hbar\Omega_2+\frac{\hbar^2k_y^2}{2\widetilde{m}} \qquad (1)$$

where $\Omega_1^2=\omega_1^2+\omega_z^2$, $\Omega_2^2=\omega_2^2+\omega_x^2$, $\omega_x=eH_x/m^*c=\omega_c\ cos\ \vartheta$, $\omega_z=eH_z/m^*c=\omega_c\ sin\ \vartheta$, $x_0=-b_1l_{B1}^2k_y$, $z_0=b_2l_{B2}^2k_y$, $\widetilde{m}=m^*\left(\Omega_1^2\Omega_2^2\right)\left(\omega_1^2\omega_2^2-\omega_x^2\omega_z^2\right)^{-1}$. Here $l_{B1}=\left(\hbar/m^*\Omega_1\right)^{1/2}$, $l_{B2}=\left(\hbar/m^*\Omega_2\right)^{1/2}$, $b_1=\omega_z/\Omega_1$ and $b_2=\omega_x/\Omega_2$.

It is known that all of the thermodynamic properties of a system can be obtained as derivatives of the free energy of system. The free energy of the nondegenerate electron gas is [13]

$$F=K_BTN\ ln\ \frac{e}{N}\sum_{n,l,k_y}exp\left[-E_{nl}\left(k_y\right)/K_BT\right] \qquad (2)$$

Summing geometric series in (2) we have

$$F = K_BTN\ln\left[\frac{eL_y\sqrt{m^*K_BT}}{4\sqrt{2\pi}N\hbar sh\left(\hbar\Omega_1/2K_BT\right)sh\left(\hbar\Omega_2/2K_BT\right)}\right] \qquad (3)$$

Magnetic susceptibility is determined by the formula [9]

$$\chi_{ij} = -\frac{1}{V}\left(\frac{\partial^2 F}{\partial H_i\partial H_j}\right) \qquad (4)$$

where $i,j=1,2$; $H_l=H_x$; $H_2=H_y$; V is the volume of the crystal.

The components of the magnetic susceptibility are

$$\frac{\chi_{11}}{\chi_0} = sh^{-1}\left(\frac{\hbar\Omega_1}{2K_BT}\right)\left\{\frac{K_BT}{\hbar\Omega_1}\left(1-\frac{\omega_c^2}{\Omega_1^2}\right)-cth\left(\frac{\hbar\Omega_1}{2K_BT}\right)\frac{\omega_c^2}{2\Omega_1^2}\right\}$$

$$\frac{\chi_{22}}{\chi_0} = sh^{-1}\left(\frac{\hbar\Omega_2}{2K_BT}\right)\left\{\frac{K_BT}{\hbar\Omega_2}\left(1-\frac{\omega_c^2}{\Omega_2^2}\right) - cth\left(\frac{\hbar\Omega_1}{2K_BT}\right)\frac{\omega_c^2}{2\Omega_1^2}\right\} \tag{5}$$

where

$$\chi_0 = \frac{N}{2K_BT}\left(\frac{e\hbar}{m^*}\right)$$

$$C = -T\frac{\partial^2 F}{\partial^2 T} \tag{6}$$

After some manipulation one obtains

The specific heat is given as [10]

$$C = K_BN\left(sh^{-2}\left(\frac{\hbar\Omega_1}{2K_BT}\right)\left(\frac{\hbar\Omega_1}{2K_BT}\right)^2 + sh^{-2}\left(\frac{\hbar\Omega_2}{2K_BT}\right)\left(\frac{\hbar\Omega_2}{2K_BT}\right)\right) \tag{7}$$

The entropy $S = -\left(\partial F/\partial T\right)_V$ [13], can be calculated from (3) to give

$$S = K_BN\left\{\ln\left[\frac{L_ye\sqrt{m^*K_BT}}{4\sqrt{2\pi}\hbar N}sh^{-1}\left(\frac{\hbar\Omega_1}{2K_BT}\right)sh^{-1}\left(\frac{\hbar\Omega_2}{2K_BT}\right)\right] - cth\left(\frac{\hbar\Omega_1}{2K_BT}\right)\left(\frac{\hbar\Omega_1}{2K_BT}\right) - \frac{1}{2}\right\} -$$
$$- K_BNcth\left(\frac{\hbar\Omega_2}{2K_BT}\right)\left(\frac{\hbar\Omega_2}{2K_BT}\right) \tag{9}$$

Thus, expressions for the magnetic susceptibility, specific heat and entropy of parabolic quantum wires in tilted magnetic fields have been obtained. As seen from expressions (5), (7) and (9), the components magnetic susceptibility, specific heat and entropy depend on the magnitude of the magnetic field and the direction of the magnetic field, and parameters of a parabolic wells $\omega_{1,2}$. The typical diagrams of this dependence are given in a fig. 1-2.

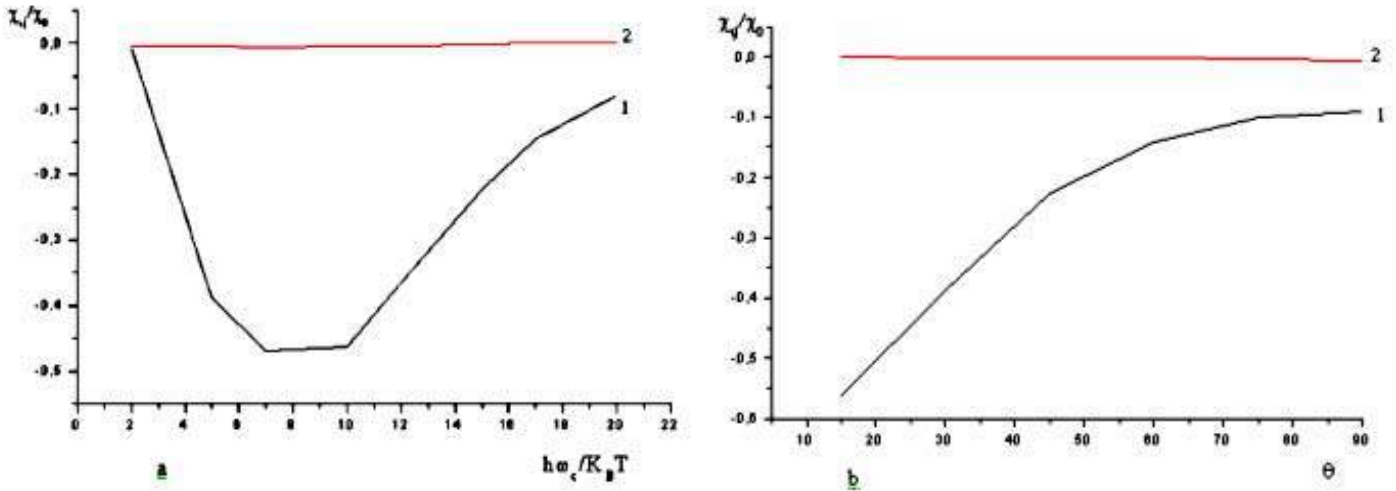*Fig. 1*. a. Magnetic-field dependence of the components of the magnetic susceptibility ($\vartheta=30^\circ$, $\frac{\hbar\omega_1}{K_BT}=5$, $\frac{\hbar\omega_2}{K_BT}$). 1-χ_{11}, 2-χ_{22};

b. Dependence of the components of the magnetic susceptibility on the angle ϑ, $\left(\frac{\hbar\omega_c}{K_BT}=\frac{\hbar\omega_1}{K_BT}=5, \frac{\hbar\omega_2}{K_BT}=10\right)$. 1-$\chi_{11}$, 2-$\chi_{22}$.
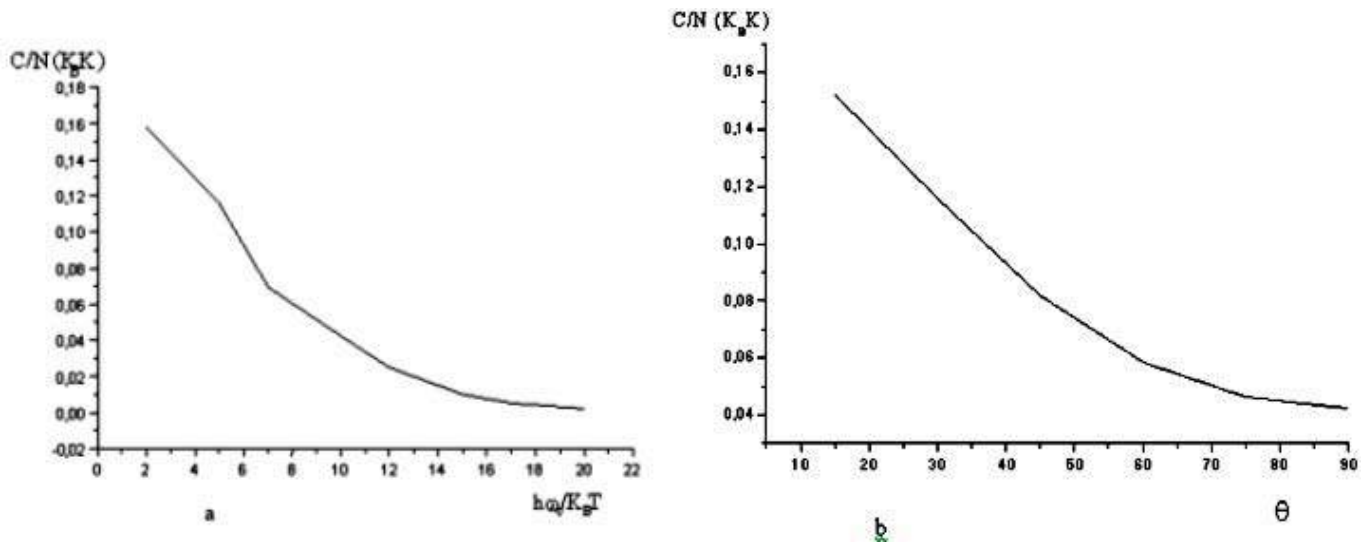
*Fig.2.*a. Magnetic-field dependence of the specific heat ($\vartheta=30^\circ$, $\dfrac{\hbar\omega_1}{K_B T}=5$, $\dfrac{\hbar\omega_2}{K_B T}$).

b. Dependence of the specific heat on the angle $\vartheta\left(\dfrac{\hbar\omega_C}{K_B T}=\dfrac{\hbar\omega_1}{K_B T}=5,\ \dfrac{\hbar\omega_2}{K_B T}=10\right)$.

The magnetic-field and angle (ϑ) dependence of the components on the magnetic susceptibility are shown in Fig.1a and Fig.1b, respectively. Figures 2a and 2b show the specific heat per electron in units of K_B.

[1] *L. Brey, N.E. Johnson and. B. J. Halperin.* Phys. Rev. B, 1989, 40, 10647.

[2] *P. Vasilopoulos, F.M. Peeters.* Phys.Rev.B, 1989, 40, p. 10079.

[3] *D. Jovanovic, S. Briggs and J.P. Leburton.* Phys. Rev. B, 1990, 42, p. 11108.

[4] *V.D. Shadrin and F.E. Kistenev.* J. Appl. Phys., 1994, 75, p. 985.

[5] *G. Ihm, M.L Falk, S.K. Noh and J.I. Lee.* Phys.Rev.B, 1992, 46, p. 15530.

[6] *Jai Yon Ryu, G.Y. Hu and R.F. O'Connell.* Phys.Rev. B, 49, p. 10437(1994).

[7] *C.C. Wu and C.J. Lin.* J. Appl. Phys., 1998, 83, p. 1390.

[8] *G.B. Ibragimov.* J.Phys:Condens.Matter., 2002, 14, p. 8145; 2003, 15, p.1427; 2003, 15, p. 8949.

[9] *V.A. Geyler, V.A. Margulis, A.G. Nesmelov, I.I.Chuchaev.* FTT, 1994, 36, c. 1994.

[10] *Tong-zong Li, Ke-lin Wang and Jin-long Yang.* J.Phys.: Condens. Matter., 1997, 9, p.9299.

[11] *W. Zawadzki.* In Two-Dimensional Systems, Heterostructures, and Superlattices. Editors: *G.Bauer, F.Kuchar, and H. Heinrich.* p.79. Springer – Verlag Berlin, 1984.

[12] *F.M. Gashimzade, A.M. Babaev, KH.A. Gasanov.* Fizika, 2002, 8, p.28.

[13] *L.D. Landau and E.M. Lifshich.* Statistical Fizika (in Russian) M.Nauka 1964.p.567.

H.B. İbrahimov

MEYLLİ MAQNİT SAHƏSİNDƏ PARABOLİK POTENSİALLI KVANT NAQİLLƏRİN TERMODİNAMİKASI

Meylli maqnit sahəsində yerləşmiş parabolik potensial çuxurlu kvant naqillərdə maqnit qavrayıcılığı, entropiya və xüsusi istilik tutumu öyrənilmişdir. Maqnit qavrayıcılığının, entropiyanın və xüsusi istilik tutumunun maqnit sahəsindən, onun meyl bucağından və kvant çuxurun parametrindən asılı analitik ifadə alınmışdır.

Г.Б.Ибрагимов

ТЕРМОДИНАМИКА КВАНТОВОЙ ПРОВОЛОКИ С ПАРАБОЛИЧЕСКИМ ПОТЕНЦИАЛОМ В НАКЛОННОМ МАГНИТНОМ ПОЛЕ

Изучена магнитная восприимчивость, энтропия и теплоемкость электронного газа в квантовой проволоке, образованной потенциалом параболической ямы, помещенной в наклонное магнитное поле. Найдены аналитические зависимости теплоемкости, энтропии и компонент тензора магнитной восприимчивости от величины и направления магнитного поля и параметров ям.

THE STUDING OF THE INFLUENCE OF THE ULTRA HIGH FREQUENCY (UHF) FIELD ON THE PROCESSES OF THE DRYING AND FERMENTATION OF THE TOBACCO LEAVES

N.N. GADJIEVA, M.Z. VELIDJANOVA, E.S. DZHAFAROV

Institute of Radiation Problems of Azerbaijan National Academy of Sciences
Baku-1143, H. Javid av., 31a.

The influence of the UHF field on the processes of the drying and fermentation of the tobacco leaves has been studied. The changes, accompanying these processes were controlled by the spectrophotometric and derivatographic methods. It is shown, that the qualitatively ecological pure product with the given color and afterhumidity can be obtained by the changing of the UHF field, powers of UHF generator and prolonged treatment.

Introduction

The photo- and thermochemical reactions play very important role in the processes of the drying and fermentation of the tobacco leaves [1]. The progression of these processes under the standard conditions, which are characterized for the usual fermentation factories, connects with the some difficulties, that negatively influence on the product quality.

That's why we begin the search of the new methods of the drying and fermentation, deprived of these disadvantages. One of these methods is the dielectric heating of the tobacco, because the advantage of the dielectric heating reveals strongly on the materials with the low heat conduction and heat-resistant properties, as the tobacco is [2].

The influence on the tobacco leaves as the dielectric of the electromagnetic (HF and UHF) fields would allowed the progression of the photo- and thermochemical reactions not only on surface, but in the full volume. However, the method of the dielectric heating of the kiptongo in the aim of the intensification fermentation process doesn't give the welcome effect, as the fermentation progresses only in the think subsurface levels [3].

The welcome high effectiveness and accelerations of the fermentation process were achieved by the UHF field treatment of the tobacco leaves. One of the advantages of the UHF method is that UHF field besides local thermal influence initiates also the probability of the uniform progression of the photochemical reactions of the separate ferments, which gives the opportunity to obtain the qualitative products with the minimal ecological pollutions. [4,5].

As well known, the chemical composition of the tobacco leaves, changes the color and becomes uniform and approaches to the one-color, the green disappears at the fermentation. The one of the main reasons of the most counts of green in the tobacco leaves is the residual chlorophyll. The high residual content of the chlorophyll leads to the significant storage of the substances, with the negative properties, which limit the action of the 'positive' components in the tobacco [2]. That's why it is possible to follow the process of the fermentation and tobacco quality on the changing of the dark-green color in the tobacco leaves and on the chlorophyll decomposition correspondingly.

In the given paper the influence of the high-frequency electric field on the processes of the drying and fermentation of the tobacco leaves has been studied. The changes, accompanying these processes were controlled by the spectrophotometric and derivatographic methods.

The experiment part

The UHF drying and fermentation of the tobacco green leaves were carried out on the laboratory installation "UHF tobacco" on the method, written in [5] in details. The parameters of the treatment (the frequency of the UHF field, the power of UHF generator, the length of the light of the ultraviolet (UV) rays, treatment time) change in the such manner that it is possible to obtained the dry tobacco leaves with the yellow shadows. The choosing of the spectral range 400-700nm is caused that the absorption band of the residual chlorophyll states at $\lambda=665$nm. As the control experiments show, the photoradiation of the tobacco leaves in this spectral region doesn't worse the quality of the ready product and the quantity of the resin doesn't increase.

By the way of the investigation object were choosen about 100 samples of the tobacco green leaves of the different types (Samsun, Trapezond, Ostralis and Imun), grown in Azerbaijan.

The UV absorption spectrums of the alcoholic drawing of the tobacco have been obtained by the method [5] in the spectrophotometre Specord UV VIS. The derivatographic analysis was carried out on the devatograph MOM-4 (the heating velocity 5K min^{-1}.

The results and their discussion

The alcohol extract of the tobacco leaves gives the absorption in the visual spectral region at the wave length $\lambda=665$nm this band is connected with the residual chlorophyll [6]. The intensity of this band characterises the quantity of the residual chlorophyll in the dark-green tobacco leaves and its change can be used as the coefficient of the acceleration of the chlorophyll's decomposition at the high-frequency electric field action.

The absorption spectrums of the alcohol extract unfermented (green) and the tobacco leaves of Trapezond type, tormented by the UHF field are given on the fig. 1. It is clear, that if the tobacco quality is worse (the big content of chlorophyll, the fermentation of the low level), so it absorbs more at $\lambda=665$nm.

The observable dependence between spectral characteristics (intensity, optical density) and the residual chlorophyll of the dark-green color, and the taste parameters (taste-B and aroma-A) also has the line character and allows

to define and control the change of the qualities of the tobacco leaves, tormented by the UHF field with the help of the express-method [6].
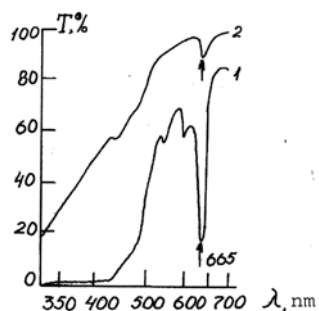

Fig.1. The absorption spectrums of alcohol extracts from tobacco by Trapezond type in the visual region:
   1. initial (green, unfermented)
   2. UHF tormented (fermented)

The objective criterion for the fact establishment and fermentation level of tobacco can serve exothermic effect, characterising the intensity of the heat transfer at the different processes, and the burning process also [7]. As the DT investigations showed the exoeffect is observed at the temperature $T\sim340K$ (fig.2). As it is shown from the fig 2 (curve 1) the given exoeffect is observed weakly in the green, unfermented tobacco samples. The deep of the exopeak increases (curves 2, 3) with the increase of the fermentation degree, that connects with the tobacco heat transfer. The comparison of the dates on the tobacco heat transfer, fermented under the isothermic conditions and the constant humidity of the material shows that the deep of this exoeffect gives the possibility to establish the tobacco fermentation degree.
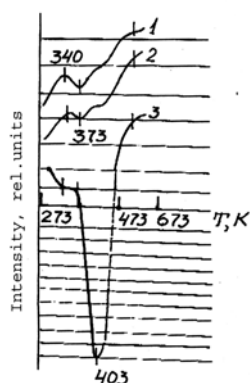

Fig.2. Thermogramms of tobacco leaves, UHF tormented, dried (1), unfermented, dried (2), green (3)

The humidity of the tobacco leaves is the one of the main parameters, which strongly influences on the fermentation process and the quality of the ready product accordingly [2]. The tobacco fermentation is usually carried out at the optimal humidity and temperature. The humidity deflection from the optimal value (~14%) leads to the undesirable circumstances. The dry tobacco loses elasticity, becomes brittle, and the excess by moist raw material goes mouldy easily.

Among wide spread methods of the regulation of the tobacco humidity is the method of the standartization of the humidity by the way of the standartization in the drying board [1].

The UHF drying allows to obtain the dry tobacco leaves with the given humidity, moreover the needed time for this process decreases till the minimum.

As the DT- investigations show the green untormented tobacco leaves at $T\sim403K$ are characterised by the strong exoeffect, which is caused by the presence of the big amoubt of humidity. As a result of the UHF drying the endopeak intensity decreases and its maximum shifts to the low temperatures (on $\Delta T\sim30K$) till $T\sim373K$. The humidity of the tobacco leaves after UHF drying can be controlled by the endopeak intensity (fig2).

The taste qualities of the tobacco leaves, tormented by the UHF field become better, and it is shown by the spectrophotometric and taste of the aroma (A) and taste (B). The values of these estimates and the values of the residual humidity after the UHF drying are given in the table.

№	Sample	Rating in points to 20 ball system				Afterhumidity %
		$A_{deg.}$	A_{spectr}	$B_{deg.}$	B_{spectr}	
1	Initial unfermented tobacco of Samsun type	13.2	13.0	13.4	13.2	18.2
2	UHF tormented tobacco of Samsun type					
	a) third kind	17.0	17.2	16.9	17.0	16.4
	b) second kind	19.0	18.9	19.1	19.0	15.2
	c) first kind	19.2	19.1	18.8	18.7	14.5

So, changing the frequency of the UHF field, power of the UHF generator and the duration we can obtain the dry tobacco leaves with the given color and the afterhumidity and later choose the optimal mode of the UHF drying and fermentatio

[1] Y.S. Arkhangelskiy, I.I. Devyatkin. Sverhvisokochastotniye nagrevatelniye ustanovki dlya intensifikacii tekhnologicheskikh processov. Izd-vo Saratovskogo universiteta, 1983, 254s. (in Russian).

[2] A.A. Shmuk. Khimiya ii tekhnologiya tabaka, M.: Pishshepromizdat, 1953. (in Russian).

[3] Pat. 57-2192, Japan, 1981.

[4] A.s. 969239, SSSR, 1980. (in Russian).

[5] N.N. Gadzieva, Kh.B. Gezalov. Otchet sektora RI AN Azerb. Na temu "Razrabotat tekhnologicheskiy process sushki I fermentacii listyev svervisokochastotnim (CVCh)-izlucheniya" Baku, 1985, s.50. (in Russian).

[6] S.V. Kamenshshikova, A.M. Smirnov, I.G. Mokhnachev. Tabak, 1975, №3, s.36. (in Russian).

[7] N.N. Gadziyeva, Kh.B. Gezalov, M.A. Eyubova I dr. Izv. AN Azerb. SSR, ser. biologicheskaya, 1990, №4-6, s.86. (in Russian)

N.N. Hacıyeva, M.Z. Vəlicanova, E.S. Cəfərov

N.N. GADJIEVA, M.Z. VELIDJANOVA, E.S. DZHAFAROV

İFRATYÜKSƏKTEZLİKLİ (İYT) SAHƏNİN TÜTÜN YARPAQLARININ QURUDULMASI VƏ FERMENTLƏŞDİRİLMƏSİ PROSESLƏRİNƏ TƏSİRİRİ TƏDQİQİ

İYT sahənin tütün yarpaqlarının qurudulması və fermentləşdirilməsi proseslərinə təsiri öyrənilmişdir. Bu proseslər zamanı yaranan dəyişikliklərə spektrometrik və derivatoqrafik metodlarla nəzarət edilmişdir. İYT sahənin tezliüini, İYT – generatorunun gücünü və emal müddətini dəyişməklə verilmiş çalarlı və qalıq rütubətə malik ekoloji cəhətdən təmiz və keyfiyyətli məhsul olmağın mümkünlüyü göstərilmişdir.

Н.Н. Гаджиева, М.З. Велиджанова, Э.С. Джафаров

ИЗУЧЕНИЕ ВЛИЯНИЯ СВЕРХВЫСОКОЧАСТОТНОГО (СВЧ) ПОЛЯ НА ПРОЦЕССЫ СУШКИ И ФЕРМЕНТАЦИИ ЛИСТЬЕВ ТАБАКА

Изучено влияние СВЧ – поля на процессы сушки и ферментации листьев табака. Изменения, сопровождающие эти процессы контролировались спектрографическим и деривафотрографическим методами. Показано, что варьируя частоты СВЧ – поля, мощности СВЧ – генератора и продолжительности обработки можно получить качественный экологически чистый продукт с заданной окраской и остаточной влажностью.

THE SPECTRAL DISTRIBUTION OF THE PHOTOSENSITIVITY OF THE TWO-COMPONENT ELECTROPHOTOGRAPHICAL LAYERS OF TRIGONAL Se/CdInGaS₄

N.I. IBRAGIMOV, V.G. AGAYEV, N.B. SOLTANOVA

Institute of Physics, Azerbaijan National Academy of Sciences,
Baku Az-1143, H.Javid av., 33, Azerbaijan

The two-component electrophotographical (EP) layers of the trigonal Se/CdInGaS₄ in connecting with optimal EP parameters (U_H=300V, $\tau_{1/2}$=40s, $S_{int.}$=0,13Lk^{-1}·s^{-1}) at the relation 1:1 of components and with spectral region of photosensitivity till $\lambda \geq$800nm are obtained.

Earlier the electrophotographical (EP) layers on the base of the trigonal Se and the compound CdInGaS₄ in the connecting [1-3] were investigated by us. The measures of the main electrophotographical parameters show that layers from the trigonal Se have high light sensitivity (0.6Lk^{-1}·s^{-1} in the visible region of the spectrum), but they have the low initial potential the layers from the trigonal Se in the connecting charge positively till the surface potential $\leq$250V, have the high velocity of dark slump, the half-slump time ~35s.The small value of the initial potential of the layers from the trigonal Se is caused by the respectly low specific resistance of the photosemiconductor (10^{7}Ohm·cm). The EP layers on the base Cd InGaS₄ in the connecting have the low light sensitivity (0.003Lk^{-1}·s^{-1}), but they charge till the initial potential U_h=1000V.

Taking into consideration above mentioned, the obtaining of the two-component EP layers, which will be combine the high light sensitivity of layers on the Se base and the big initial potential of the layers from CdInGaS₄ is very interesting.

The used by us the compound CdInGaS₄ had the specific resistance $\rho \approx 10^{10}$Ohm·cm in the darkness, the ρ decrease on 3 points was observed at the lightening by the white light (200 Lk).

The trigonal Se was obtained from the initial material by the mark Osch 17-4 by the preliminary thermotreatment in the quartz ampoules (p<10^{-4}mmHg) at 700°C during 3 hours, the quick cooling of the melt firstly till 250°C, later in the running water and crystallization at 210°C during 40 hours. The specific resistance of the trigonal Se, obtained by the such manner in the darkness was $\approx$10^{7}Ohm·cm and it decreased on the 3 points at the lightening by the white light (200 Lk).

The layers of the 3 types were obtained by the method of the dispergation in the connecting: substrate –CdInGaS₄ - trigonal Se(I); substrate - trigonal Se - CdInGaS₄ (II); substrate - the mixture of trigonal Se and CdInGaS₄ at the different rates of the components (III).

The layers of I type were obtained by the following manner. The substrate from the aluminum foil by the thickness 150mkm was skimmed, poisoned and conserved. The layer of emitted in the spherical mill CdInGaS₄ in the connecting from the polyvinylbutyral, dissolved in the ethyl alcohol, by the thickness 15-20mkm, was carried on the substrate by the method of swimming roller. The middle size of the semiconductor particles was 15mkm. The trigonal Se in the connecting by the thickness 5-10mkm after drying on in the usual conditions during one hour crushed by the such manner was carried on the first layer.

The layers of II type were obtained by this method, but in the beginning the substrate was covered by the layer from the tetragonal Se in the connecting (20-30mkm), later the CdInGaS₄ on the first layer was carried on the first layer in the connecting by the thickness 5-10mkm.

The layers of III type were obtained by the carrying on the ready substrate of the mixture of two semiconductors in the connecting by the thickness 25-30mkm. Moreover CdInGaS₄ and the trigonal Se firstly were crushed till the middle size of particles 15mkm differently, later the joint crushing of the components in the different weight rate was carried out in the spherical mill with the addition of the connecting and the obtained dispergant was carried on the substrate. All layers were drying on the usual conditions at the room temperature.

The charging of the layers was carried out in the corona discharge (+7kV). The measurement of the main EP parameters was carried out on the electrometric installation with the oscillating electrode on the surface layer [4]. The light characteristics of the EP layers were measured by the exposuring through photoshutter with the use of the incandescent lamp and neutral photofilters. The illumination intensity was 125Lk, the exposuring time was variated by the photoshutter. .

The spectral distributing of the photosensitivity (S_λ) of the EP layers was defined in the interval λ=400÷900 nm with the use of the monochrometer of the spectrophotometer VSU2-P. The source of the lightening was graduated by the radiated compensated thermoelement PTH - 30.

The integral light sensitivity of the EP layers is defined by the velocity of slump of the potential at the lightening. The integral light sensitivity is characterized by the exposuring time t (in s) in the case of the constant illumination intensity L (in Lk), during of which the surface potential decreases in two times:

$$S = \left(\frac{1}{L \cdot t} \right)_{\frac{\Delta U}{U}} = \frac{1}{2} \qquad , \qquad \text{Lk}^{-1}\cdot\text{c}^{-1}$$

(1)

The defined photosensitivity is called integral one.

The illumination intensity at the defining of the spectral photosensity of the EP layers is measured in the energetic unit (Vt/m^2) or number of the incident quantum on the unit area of the surface layer in the time unit:

$$S_\lambda = \left(\frac{1}{L_\lambda \cdot t}\right)_{\frac{\Delta U}{U}} = \frac{1}{2} \text{ , cm}^2 \cdot \text{Joule}^{-1} \quad (2)$$

The parameters of the EP layers of I type seemed in the following manner: the initial potential U_H was 180 and 870 V of the makeup and subjected to the annealing at 160°C during 1 hour, accordingly; dark half-slump time $\tau_{1/2}$ was 4 and 15s, the integral sensitivity S_{int}, calculated by (1), till the annealing was 0.04, after 0.08 $Lk^{-1} \cdot s^{-1}$, the residual potential 20 and 60V, correspondingly.

The high velocity of the dark relaxation of the surface potential is observed on the initial area of the slump curve, as much as measured just after charging U_H=870V, later 5s U_H=600V. This reflects on the dark half-slump time correspondingly. Thus, measured just after charging $\tau_{1/2}$=15s, later 5s is equal 25s.

The measurements show that layers of II type have U_H, which is equal to 225 and 700V, but $\tau_{1/2}$ =5 and 20s till and after annealing at 160°C (1 hour). The light sensitivity of these layers is smaller, than the layers of I type have and it is equal 0,032 and 0,027 $Lk^{-1} \cdot s^{-1}$ till and after annealing. Thus the some slump of the integral light sensitivity is observed with the annealing, and the increase is observed in the photoreceptors with the surface layer of their trigonal Se in the connecting (I type).

The light sensitivity of the one-layer photoreceptors from $CdInGaS_4$ in the connecting with the annealing decreases, but the light sensitivity of the trigonal Se layers in the connecting increases. This explains the resolving of the defects in the particles of the trigonal Se during annealing, as Se has the low fusing point, and the annealing at 160°C can provide the given process. In the case of $CdInGaS_4$, having the high fusing point (950°C), the annealing at 160°C can't change the structure of the particles mainly.

The investigations of the photoreceptors of I and II types show that the dominating role in the forming of the EP parameters play the outside sublayer, accessible to the light.

The parameters of the layers of III type depend on the rate of the components and temperature of the following annealing significantly. Thus, the initial potential and the time of its dark half-slump of the layers with the different rate $CdInGaS_4$/Se increase with the annealing, achieving maximal value at $T_{an}\approx$160-170°C. U_H and $\tau_{1/2}$ decrease with the following growth T_{anl}. The integral light intensity S_{int} of these layers increases strongly with the growth T_{anl} (fig.1), saturating at $T_{an}\geq$180°C.
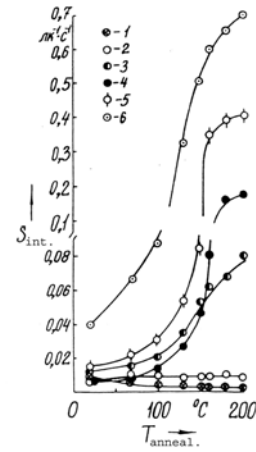

Fig.1. The dependence S_{int} of the layers of III type on T_{an} at the different content of the trigonal Se (1- 0; 2- 10; 3- 30; 4- 50; 5- 75; 6- 100% Se).

The dependences of the initial potential (U_H), half-slump time ($\tau_{1/2}$), integral light sensitivity (S_{int}) and the residual potential (U_{res}) from the content of trigonal Se in the layers of III type after annealing at 170°C(1 h) are presented on the fig 2, 3. It is seen, that the monotone change of all EP parameters is observed. The initial potential and the half slump time decrease with the growth of content of the trigonal Se in the layer (fig.2). Moreover the essential increase of the integral light sensitivity is observed with the growth of Se content (from 0.003 $Lk^{-1} \cdot c^{-1}$ for the layers from $CdInGaS_4$ till 0.6 $Lk^{-1} \cdot c^{-1}$ for the layers from the trigonal Se). At the same time the residual potential decreases from 300 till 10V. The analysis of the dependence of the parameters of the EP layers from the trigonal Se content allows to establish that the most optimal EP parameters have the layers with the rate 1:1.
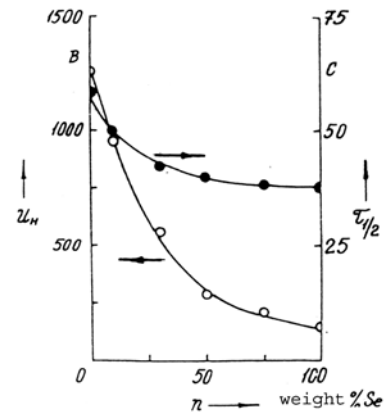

Fig.2. The dependence U_H and $\tau_{1/2}$ of the layers of III type from the content of the trigonal Se(T_{anl}=170°C, 1h).
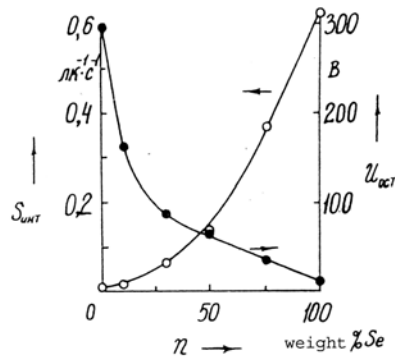
Fig.3. The dependence S_{int} and U_{res} of the layers of III type on the content of the trigonal Se (T_{an}=170°C, 1h)

The results of the measurements S_λ, calculated by the formula (2) are given on the fig.4. It is seen, that S_λ of the layers from the trigonal Se is more big than S_λ layers from CdInGaS$_4$ in the region λ=400÷900 nm (in 4÷2 times in dependence on λ). The photosensitivity of the two component layers of the trigonal Se/CdInGaS$_4$ (at the rate 1:1) in the given interval λ is smaller, than for the layers from the trigonal Se have, but the significantly bigger, than for layers from CdInGaS$_4$ have. However, the interesting peculiarity is observed: the photosensitivity of two-component layers is higher in region λ>650 nm, i.e. S_λ goes in the long-wave region of the spectrum.

In the process of the unit dispergation CdInGaS$_4$ and the trigonal Se the crushing of the both components was carried out and it is possible the enrichment of the surface of the separate scorns of the more solid CdInGaS$_4$ by Se. The last one leads to the sensibilization of the CdInGaS$_4$ photosensitivity during the annealing and to the increase of the light sensitivity of the EP layers. Moreover the crystals of the both semiconductors, rounded by the connecting

substance lay on the substrate statistically uniformly with the alternation of the particles of that or another semiconductors at the carrying of the layer. The two electrographical layers form, the one in the matrix of the another, i.e. the two-layer photoreceptor is formed as a fact. Each of the separate layers carriers in the deposit in the parameters of such system.
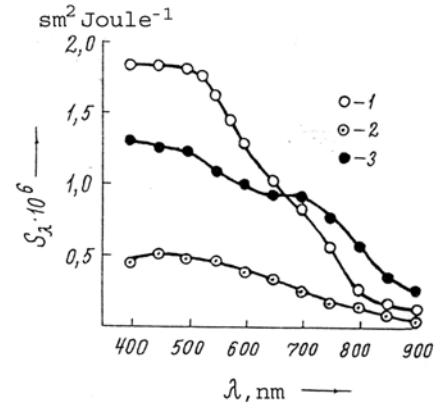

Fig.4. The spectral dependence S_λ of the layers on the base: the pure trigonal Se(1), pure CdInGaS$_4$ (2) and mixture of the trigonal Se/ CdInGaS$_4$ at the components' rate 1:1 ($T_{an.}$=170°C, 1h).

The above mentioned, we notice, that the two-component photoreceptors of the trigonal Se/ CdInGaS$_4$ in the connecting with the optimal EP parameters (U_H=300V, $\tau_{1/2}$=40s, $S_{int.}$=0.13 Lk^{-1}·c^{-1}) at the rate of the components 1:1, the photosensitivity of which is till ≥800 nm are obtained.

[1] *N.I. Ibragimov, Z.M. Abutalibova, V.G. Agaev*. Thin Solid Films, 2000, 359, p.125.

[2] *N.I. Ibragimov, Z.M. Abutalibova, N.A. Muzaffarov, V.G. Agaev*. Avt. Sv. SSSR, № 1675837. Bull. №33, 1991. (in Russian)

[3] *N.I. Ibragimov, V.G. Agaev, Z.M. Abutalibova, N.B. Soltanova*. Fizika, 2001, c.VII, №2, 32.

[4] *V.I. Gaydyalis, N.N. Markevich, E.A. Montrimas*. Fizicheskiye processi velektrofotograficheskikh sloyakh ZnO. 1968, Izd. "Mintis", Vilnus, s.85. (In Russian).

N.İ. İbrahimov, V.N. Ağayev, N.B. Soltanova

TRİQONAL Se/CdInGaS$_4$ İKİKOMPONENTLİ ELEKTROFOTOQRAFİK LAYLARIN FOTOHƏSSASLIĞININ SPEKTRAL PAYLANMASI

Optimal elektrofotoqrafik (EF) parametrlərə (U_i= 300 B, $\tau_{1/2}$=40 s, S_{int}=0,13 Lk-1(s-1) və λ≥800 nm-ə qədər spektral fotohəssaslığa malik olan, əlaqələndiricidə komponentlərin 1:1 nisbətində triqonal Se/CdInGaS$_4$ ikikomponetli EF laylar alınmışdır.

Н.И. Ибрагимов, В.Г. Агаев, Н.Б. Солтанова

СПЕКТРАЛЬНОЕ РАСПРЕДЕЛЕНИЕ ФОТОЧУВСТВИТЕЛЬНОСТИ ДВУХКОМПОНЕНТНЫХ ЭЛЕКТРОФОТОГРАФИЧЕСКИХ СЛОЕВ ТРИГОНАЛЬНОГО Se/CdInGaS$_4$

Получены двухкомпонентные электрофотографические слои тригонального Se/CdInGaS$_4$ в связующем с оптимальными ЭФ параметрами (U_H=300 В, $\tau_{1/2}$=40c, $S_{инт.}$=0,13Лк$^{-1}$(c^{-1}) при соотношении компонент 1:1 и со спектральной областью фоточувствительности до λ≥800 нм.

THERMOELECTROMOTIVE FORCE AND THERMAL CONDUCTIVITY IN Ag_2Te

F.F. ALIYEV

Institute of Physics NAS of Azerbaycan, Baku 370143, pr. H. Javid 33,

M.A. KERIMOV, F.M. GASHIMZADE

Azerbaycan Technical University, Baku 370143, pr. H. Javid 25

In this work the temperature dependences of the thermoelectromotive force and the thermal conductivity in Ag_2Te have been analyzed at next approaches the elektron spectrum dispersion law, the charge carries scattering mechanizm, Debay model of fonon spectrum and Kallarvay thery of the relaxation time.

The telluride of argentum (Ag_2Te) is respected to compounds by the type $Ag_2^IX^{VI}$ (X-Te, Se, S), having the polimorphysm property [1], caused by the content of the big amount of intrinsic defects [2] - metal atoms in the interstices and vacancies in the lattice points of crystals. The number of these defects increases with the temperature increase and at the given temperature T the disorder of the cation sublattice appears with the simultaneous reconstruction of the close lattice of chalcogen, that leads to the phase transformation (PT). The excess or lack of each of the components leads to the according change of defects concentration [3]. The investigation of the temperature dependence of the thermoelectromotive force (α_0) and thermal conductivity (χ), is the one of the methods of the revealing and studying of the defects nature and interphonone processes, especially at the low temperatures. That's why their combined investigation represents the special interest.

The given paper is devoted to the investigation α_0 and χ Ag_2Te of the stoichiometric composition and compositions with the excess Te and Ag in the temperature interval $3 \div 300K$.
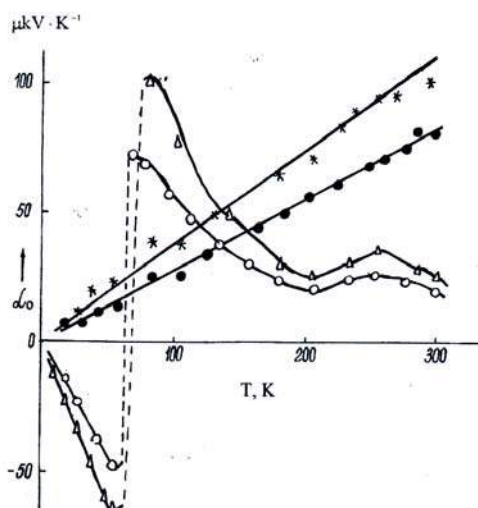

Fig.1. The temperature dependences of thermoelectromotive force $\alpha_0(1)$ Δ-0.25; 0-0.75 at % Te; $\bullet$-0.25 at Ag. The solid lines are calculated.

The samples had been obtained by the unit technology [4, 5]. The experimental and calculated data are given on the figures 1-2. From the fig. 1 it is seen, that $\alpha_0(T)$ for p-Ag_2Te

increases linearly up to $T \leq 45K$, later the sign p changes on n. At $T \approx 80$ and $270K$ the maximums of the dependence $\alpha_0(T)$ appear. The analysis has been carried out for the revealing of the dependence $\alpha_0(T)$ taking into consideration the dispersion law of the electronic spectrum and mechanism of scattering on the ion impurities and acoustic phonons [4].

From the fig. 1 it is seen, that $\alpha_0(T)$ for n-Ag_2Te is characteristics for the semiconductors with the one kind of the carriers of current in the degenerate state and Kein's dispersion law [5]. From the analysis $\alpha_0(T)$ in the p- and n-Ag_2Te it is established, that Ag atoms in the Ag_2Te create the small donor levels [5], and Te atoms create the acceptor levels [6], situating from the bottom of the conduction band on the distances $(7 \cdot 10^{-5}T \cdot K^{-1}\text{-}0.002)$ and $(7 \cdot 10^{-5}T \cdot K^{-1}\text{-}0.030)$ eV, accordingly.
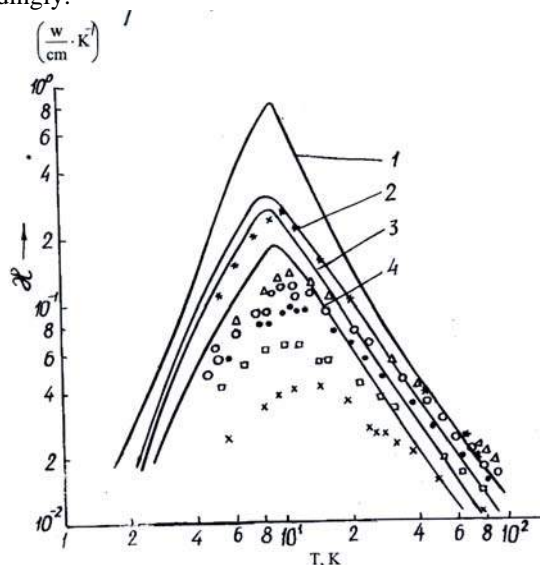
Fig.2. The temperature dependences of the thermoconductivity $\chi(T)$: $\bullet$-0.25 at % Ag. The solid lines are calculated by the formulae (1), where 1 - stoichiometric composition, which $A=6.64 \cdot 10^2 c^{-1}K^{-4}$
2 - with the excess Te 0.1 at % $A=6.64 \cdot 10^2 c^{-1}K^{-4}$
3 - with the excess Te 0.1 at % $A=9.96 \cdot 10^2 c^{-1}K^{-4}$
4 - with the excess Te 0.15 at % $A=6.64 \cdot 10^2 c^{-1}K^{-4}$

The experimental results $\chi(T)$ for the five samples Ag_2Te are given in the fig. 2. As it is shown for all samples χ_{ph} has maximum at $\sim 10K$; in the interval 20-80K the dependence $\chi_{ph}(T)$ for the stoichiometric composition has the form $\chi \sim T^{1,2}$; the excess of Te and Ag decreases the value of χ_{ph} on the

law $\chi_{ph} \sim T^\alpha$. The going throw the maximum of $\chi_{ph}(T)$ is caused by the phonons scattering on the crystal boundary and defects, and relatively weak temperature dependence in the interval 20-80K and decrease of the exponent α in the dependence on the deflection of Ag$_2$Te from the stoichiometric is connected with the presence in Ag$_2$Te of the intrinsic defects and increase of their concentrations at the presence of excess of Ag and Te atoms.

For the approving of the such quality conclusion and quantity estimation of defects concentrations, it is need the

obtained results combine with the existing theoretic models of thermal conductivity in the solid bodies. In the given case the excess atoms of Te and Ag can be considered as point defects of Raileigh type. According to the Kallarvay theory [7], takes into consideration the phonon scattering on the boundaries, point defects and phonons (processes of transfer and normal processes), the temperature dependence of thermal conductivity is calculated by the Debay model of phonon spectrum in the approximate relaxation time by the following formulae:

$$\chi_{ph} = GT^3 \left\{ \int_0^{\theta/T} \frac{\tau_c x^4 dx}{Sh^2\left(\frac{x}{2}\right)} + \frac{\left[\int_0^{\theta/T} \frac{\tau_c}{\tau_N} \frac{x^4 dx}{Sh^2\left(\frac{x}{2}\right)} \right]^2}{\int_0^{\theta/T} \frac{\tau_c}{\tau_N \tau_R} \frac{x^4 dx}{Sh^2\left(\frac{x}{2}\right)}} \right\} = GT^3 \left(I + \frac{I_2^2}{I_3} \right) \quad (1)$$

where $G = \hbar/2(2\pi)^2 \upsilon(k/\hbar)^{-4}$, υ - mean velocity, $X = \hbar\omega/KT$, ω - phonon frequency, $\tau^{-1} = \tau^{-1}_R + \tau^{-1}_N$, τ_R τ_N - relaxation times of the resistive and normal processes. $\tau_R^{-1} = \tau^{-1}_{pp} + \tau^{-1}_b + \tau^{-1}_{pd}$ where τ^{-1}_{pp}, τ^{-1}_b, τ^{-1}_{pd} - relaxation times of phonon processes of the transfer, boundary and phonon-defect scattering accordingly. The following dependences of the outside relaxation times from X and T are as follows [8],

$$\tau^{-1}_{pp} = AX^2 T^4 e^{-\theta/aT}; \ \tau^{-1}_B = \upsilon/L.$$

$$\tau^{-1}_{pp} = BX^4 T^4; \ \tau^{-1}_N = cx^n T^4.$$

Here $L = 0,2$ cm, the effective size of the crystal. The parameters A, c, a, n and θ had been defined by the method of the shortest squares numerically by the way of the comparison of the expression (1) with the experimental curves $\chi(T)$. As at the breath of the stoichiometric in Ag$_2$Te the changes of the fluctuating density $\Delta\delta/\delta$ aren't mentionable, so the scattering on the point defects appears only at the mass change $\dfrac{\Delta M}{M}$. At this approximation we write according with [8].

$$\tau_{pd}^{-1} = \frac{V_0}{n} N\left(\frac{\Delta M}{\overline{M}}\right)^2 \frac{\omega^4}{2\pi\upsilon^3} = \frac{V_0}{n} N\left(\frac{\Delta M}{\overline{M}}\right)^2 \left(\frac{K}{\hbar}\right)^4 \frac{1}{4\pi\upsilon^3} X^4 T^4$$

where V_0 - volume of the elementary cell, n - number of atoms in the elementary cell, $\overline{M}$ - middle mass of crystal atoms, ΔM - mass variation at the exchange of the main atom on the impurity atom, N - atom concentration of impurities (in the respect of the volume of atoms number of crystal). We obtain parameter B from the following expression.

$$B = \frac{V_0}{n} \left(\frac{K}{\hbar}\right)^4 \frac{N}{4\pi\upsilon^3} \left(\frac{\Delta M}{M}\right)^2$$

Trimming parameters (A, C) were taken from the work [8], calculated for $L_i \cdot F$ and $a = 11.53$, $N = 1.23$ from the work [9], calculated by the methods of the shortest squares.

The results of the calculation $\chi(T)$ are given in the fig.2 in the form of the solid lines, in comparison with the experimental data. As it is seen, the curve $\chi(T)$, which has more stoichiometric composition Ag$_2$Te goes lower than calculated curve. This shows that the argentum telluride has the big amount of the intrinsic defects. From the fig.2 it is seen, that these data are suitable for the curve, calculated for Ag$_2$Te with the impurities concentration $7 \cdot 10^{19}$cm^{-3}. Later it is seen, that calculated curves $\chi(T)$ always go throw higher than experimental ones with the increase of Ag and Te content, as the divergence increases with the Te and Ag excess.

The experimental curves aren't parallel to the calculated ones, i.e. with the temperature increase the scattering probability increases, as such deflection in the samples with Te excess, is more big than with the Ag excess.

This is connected with the phonons' scattering on the carriers of the current. That's why this type of the scattering is more effective on the p-type samples.

Thus, the analysis of the experimental and calculated data on $\alpha_0(T)$ and $\chi_{ph}(T)$ approves that argentum telluride is the defect material, and Te and Ag excesses play roles of acceptor and donor centers.

The authors are thankful to the academic M.I.Aliyev for the usifull discussions and notes.

[1] *S.A. Aliyev, F.F. Aliyev, Z.S. Gasanov.* FTT, 1998, 40, 9, 1693 (in Russian).

[2] *F.F. Aliyev.* Dokl. Azerbaijana TLVI, 2000, № 1-3, 85 (in Russian)..

[3] *F.F. Aliyev, V. Atashirov, T.F. Yusifova, M.A. Kerimova, F.M. Gashimzade.* Fizika VII, №3.2001, 22.

[4] *F.F. Aliyev, E.M. Kerimova, S.A. Aliyev.* FTP, 2002, 36, 8, 932 (in Russian).

[5] *F.F. Aliyev.* Izv. RAN, Neorg. Mater., 2002, 38, 10, 1184 (in Russian).

[6] *F.F.Aliyev/* Sekond International Simpozium on Matical and computational Applications. Baku, Azerbaycan, September 1-3/80 ,1999.

[7] *J. Callarvay.* Phys.Rev., 1959, 113.4.1046.

[8] *L.N. Vasilyev, I. Dzhabbarov, V.S. Oskotskiy, L.S. Parfenyeva, V.V. Popov, I.A. Smirnov.* FTT, 1984, 26, 9, 2710.

[9] *R. Berman, I.C.Brock.* F.Proc.Roy.oc. 1965, 289, 1416, 46.

F.F. Əliyev, M.A. Kərimov, F.M. Haşımzadə

Ag$_2$Te KRİSTALINDA TERMOELEKTRİK VƏ İSTİLİK XASSƏLƏRİ

Məqalədə Ag$_2$Te kristalında termoelektrik və istilikkeçirmə əmsallarının temperatur asılılıqları uyğun olaraq: elektron spektri üçün dispersiya qanunu və yükdaşıyıcılar səpilmə mexanizmləri, ələcədə Katavey nəzəriyyəsi əsasında fonon spektrinin debay modelində relaksasiya müddəti nəzərə alınmaqla izah olunmuşdur.

Ф.Ф. Алиев, М.А. Керимов, Ф.М. Гашимзаде

ТЕРМОЭДС И ТЕПЛОПРОВОДНОСТЬ В Ag$_2$Te

В работе анализированы температурные зависимости термоэдс $\alpha_0(T)$ и теплопроводности $\chi(T)$ Ag$_2$Te в рамках теории: с учетом закона дисперсии электронного спектра и механизмов рассеяния носителей тока, также дебаевской модели фононного спектра в приближенном времени релаксации согласно моделью Каллавея.

THE THERMOMAGNETICAL EFFECTS IN n-Pb$_{0.8}$Sn$_{0.2}$Te

E.I. ZULFUGAROV

Institute of Radiation Problems of Azerbaijan National Academy of Sciences
31a, H.Javid av., Baku - 1143

In this paper on the data of thermomagnetic coefficients and electron component of thermoconductivity the temperature dependence of Lorentz number L is defined in n-Pb$_{0.8}$Sn$_{0.2}$Te. It is shown, that experimental value $L(T)$ in the interval 40-250K is less than its standard Zommerfield's value. It is established that lowered value L is caused by the inelastic electron-electron collisions.

During investigation of the thermomagnetic effects in HgSe, PbTe and HgTe, with the degenerative electron gas [1,2,5,6] the set of the pecularities which wasn't accepted in the framework of the existing theories was observed. Particularly, it was observed, that maximums of the dimensionless field of the transversal Nernst-Ettingsgausen effect (N-E) E_y and Rigi-Leduc (R-L) (-SH) shift to the big values ($uH/c>1$) but at the elastic character of scattering they should go through the maximum at $uH/c=1$. These experiments were explained after theoretical discussion of the question about inelasticity [3-5]. It was shown, that in the case of inelastic interaction of carriers of charge it wasn't allowed to carry out the unit relaxation time for all processes. But with it all the unequilibrium part of distribution function can formally express through functions, playing the role of relaxation time. Such two functions should be carried out: the one for the isothermic effects, the second for the addition for the distribution functions, connected with the gradient temperature. In the case of the interelectron interaction at the absent of the magnetic field the unequilibrium part of distribution function can be introduce in the following form:

$$\Delta f = \tau_1 \frac{\partial f_0}{\partial E} \overline{V} \Delta(\mu - e\varphi) + \tau_2 \frac{\partial f_c}{\partial E} \cdot \frac{E-\mu}{T} \overline{V}\Delta T \quad , \tag{1}$$

where $\overline{V}$ and E are velocity and energy of the electron, f_0 is Fermi's function, φ is electrostatic potential, μ is Fermi's energy. The values of relaxation times τ_1 and τ_2 are energy functions (the concentrations of the ionized impurities are equal to electron concentrations). Here τ_1 is connected with the momentum relaxation and scattering on the small angles don't influence on the τ_1. The function τ_2 is caused by relaxation of energy beam near Fermi's surface if the energy changes on the value of kT order at the collision.

The interelectron collisions don't change spontaneously the electric current, their role is the redistribution of the energy between collising carriers. At the calculation of the mobility it can be limited by the first summand in the expression (1) and in the case of the high degeneration consider $E=\mu$. The energy redistribution is insignificantly at this, the interelectron collisions don't influence on the value $\tau_1(E-\mu)$, and on the mobility, accordingly.

At the calculation of the thermoelectromotive force, thermoconductivity and thermomagnetic effects, when the second member of the expression (1) is significant, it isn't allowed to consider $E=\mu$, but it is need to consider the blured distributions of the step function. The flux of the hot and cool electrons moves to meet someone and the energy redistribution, between fluxes influences strongly on the heat effects [7] in the conditions of the observing of these facts. From this it is followed, that interelectron collisions can influence on the thermoelectric and thermomagnetic effects, the analytic expressions for which include the values τ_2 and $\partial \tau / \partial E$. That's why the complex investigation of the field, temperature and concentration dependences of the thermoelectromotive force and thermomagnetic effects can give the additional information about inelasticity of scattering.

The measurement of the coefficients was carried out: 1) the thermoelectromotive force α; 2) transversal effect N-E;
3) the magnithermoelectromotive force $\Delta\alpha$; 4) effect of M-R-L; 5) effect R-L; SH; 6) electroconductivity σ; 7)Hall R coefficient.

The results of the experiment are analised on the base of the above mentioned theory, considering the inelastic character of the scattering, in compliance which thermomagnetic coefficient have the following expression at the strong degeneration of the current carriers:

$$\Delta\chi(H) = \Delta\chi_\infty \frac{\left(\dfrac{UH}{c}\right)^2 \left(\dfrac{L}{L_0}\right)^2}{1 + \left(\dfrac{uH}{c}\right)^2 \left(\dfrac{L}{L_0}\right)^2} \tag{2}$$

$$- SH = \frac{\dfrac{uH}{c} \dfrac{L}{L_0}}{1 + \dfrac{\chi_p}{L_0 \sigma T}\left[1 + \left(\dfrac{uH}{c} \dfrac{L}{L_0}\right)^2\right]\dfrac{L_0}{L}} \tag{3}$$

$$\Delta\alpha(H) = \Delta\alpha_\infty \frac{\left(\dfrac{uH}{c}\right)^2 \left(\dfrac{L}{L_0}\right)^2}{1 + \left(\dfrac{uH}{c}\right)^2 \left(\dfrac{L}{L_0}\right)^2} \tag{4}$$

$$E_y^{iz} = \frac{\Delta\alpha_\infty}{\frac{k_0}{e}} \frac{\frac{uH}{c}\frac{L}{L_0}}{1+\left(\frac{uH}{c}\right)^2\left(\frac{L}{L_0}\right)^2} + \frac{\frac{L}{k_0}}{e} \frac{\frac{uH}{c}\frac{L}{L_0}}{1+\frac{\chi_p}{L_0\sigma T}\left[1+\left(\frac{uH}{c}\frac{L}{L_0}\right)^2\right]\frac{L_0}{L}} \quad (5)$$

$$E_y^{iz} = \frac{\Delta\alpha_\infty}{\frac{k_0}{e}} \frac{\frac{uH}{c}\frac{L}{L_0}}{1+\left(\frac{uH}{c}\right)^2\left(\frac{L}{L_0}\right)^2}, \quad (6)$$

where $E_y = k_0 H Q_\perp / e$.

From (1-5) it is followed, that ratio L/L_0, noticing the inelasticity degree, can be defined on the dependences $\Delta\alpha$, $\Delta\alpha$, E_y and SH from the intensity of the magnetic field, by the формула value, according maximum is dependences $E_y(uH/c)$ and $SH(uH/c)$ (as it was mentioned in the case of elastic scattering the maximums are equal to $(uH/c)=1$, but in the case of the inelastic scattering the maximums are equal to $uH/c>1$, moreover L/L_0 is defined as $(uH/c)=L/L_0$ and with the help of the defined ratios between different thermomagnetic effects, as for example:

$$\frac{L}{L_0} = \frac{\Delta\alpha}{HQ_\perp^{iz}\frac{uH}{c}} \text{ and } \frac{L}{L_0} = \frac{Q_\perp^{iz}}{R\sigma\Delta\alpha_\infty} \quad (7).$$

The character data about dependence $\Delta\alpha(H)$ and two theoretical curves, calculated on the expression (1) at $L/L_0=1$ and $L/L_0=0,69$, obtained from the limit value $\Delta\alpha_{H\to\infty}$ at 100K are given on the fig.1.

Vt/cm*K
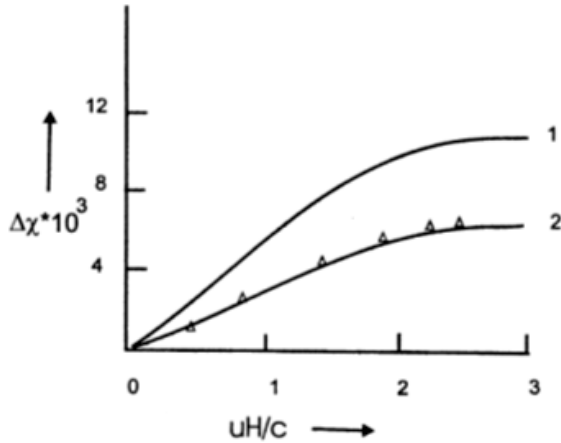
Fig.1. The dependence $\Delta\alpha$ on uH/c for the sample with $u=9.6\cdot10^{18}$cm^{-3} at 100K curve 1 - $L/L_0=1$; 2 - $L/L_0=0.69$.

The dependences $E_y(uH/c)$ and $-SH(uH/c)$ at 300K in the comparison with the theoretical curves are given on the fig.2. It is seen, that the 300K the experimental data are good agree for curve, calculated at $L/L_0=1$, and maximums E_y and SH are equal to uH/c.
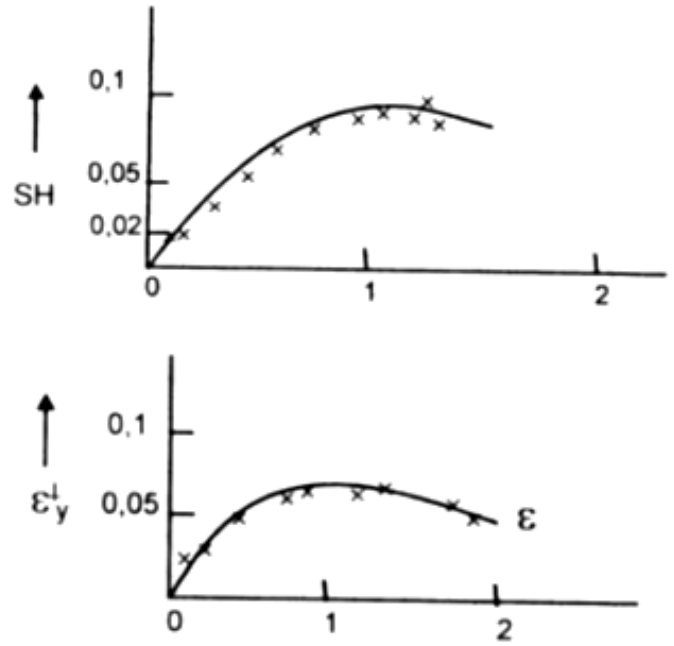
Fig.2. The dependence E_y and –SH on uH/c with $n=1.16\cdot10^{18}$cm^{-3} at 300K.

The values L/L_0, obtained by the different methods for формула n-Pb$_{0.8}$Sn$_{0.2}$Te are given in the table 1. Thus, on the data $\Delta\alpha_{el.}$ and thermomagnetic coefficients the temperature dependence of Lorentz number L is defined in n-Pb$_{0.8}$Sn$_{0.2}$Te. It is shown, that experimental value $L(T)$ in the interval 40-250K is less than its standard Zommerfield value. It is established that lowered value L is caused by the inelastic electron-electron collisions.

Author thanks to professor S.A. Aliyev for useful discussion and notes.

Table 1.

The value of share of inelasticity of electron scattering (*L/L$_0$*) in *n*-Pb$_{0.8}$Sn$_{0.2}$obtained by different calculated methods.

№ samp	T, K	n·10^{-18}, cm^{-3}	U, cm$^{2.}$·V^{-1}s^{-1}	L/L$_o$				
				Δæ$_\infty$	Δæ (*uH/c*)	Δα (*uH/c*)	SH (*uH/c*)	
1	15	2,5	3.000	1,01	1	1	1	1
	21			0,81	0,8	0,79	-	-
	30,4			0,61	0,55	0,6	-	-
	104			0,59	0,6	0,52	0,60	0,60
	118			0,57	-	-	-	-
	205			0,55	0,6	0,62	0,6	-
	16			0,99	1	1	1	-
	23,6			0,72	0,8	0,76	-	-
2	90	1,16	4.000	0,58	0,5	0,53	0,54	-
	102			0,58	0,5	0,52	0,55	-
	122			0,55	-	-	-	-
	204			0,53	0,5	0,52	0,55	-
	16			0,96	1	1	1	1
	27,6			0,79	0,8	0,85	-	-
3	41,3	9,6	3.200	0,74	0,75	0,74	-	-
	84			0,68	0,69	0,65	0,67	0,65
	205			0,67	0,66	0,65	0,66	-
	300						1	1

[1] *S.A. Aliyev, L.L. Korenblit, S.S., Shalit*. FTP, 1966, 8, 3, p.705. (in Russian).

[2] *V.M. Mudzhdaba, V.K. Ogorodnikov, S.A. Aliyev, S.S. Shalit*. FTP, 1969, II, №2, p.545. (in Russian).

[3] *L.L. Korenblit, B.E. Sherstobitov*. FTP, 1968, t.2, v.5, 688. (in Russian).

[4] *V.I. Tamarchenko, Yu.I. Ravich, L.Yu. Morgovskiy, L.H. Dubovskaya*. FTP, 1969, II, v.12,3206. (in Russian).

[5] *Y.I. Ravich, V.A. Ephimova, V.J. Tomarchenko*. Phys.State Solid, 1971, 43, №11, p.453.

[6] *T. Knitel and H.J. Goldsmit*. Phys. C. Solid. State Phys, 1979, v. 12.

[7] *Yu.I. Ravich, B.A. Yephimova, I.A. Smirnov*. Metodi issledovaniya poluprovodnikov v primenenii k khalkogenodam svinca PbTe, PbSe, PbS. Nauka, 1968. (in Russian).

E.İ. Zülfüqarov

n-Pb$_{0.8}$Sn$_{0.2}$Te TERMOMAQNİT HADİSƏLƏRİ

İşdə *n*-Pb$_{0.8}$Sn$_{0.2}$Te kristalının termomaqnit əmsallarının və istilikkeçirmə əmsalının elektron komponentinin qiymətinə görə *L* Lorens ədədinin temperaturdan asılılığı müəyyən edilmişdir. Göstərilmişdir ki, temperatur 40÷250 K intervalında *L(T)*–nin təcrübi qiymətləri onun standart zommerfeld qiymətindən kiçikdir. Müəyyən edilmişdir ki, *L*-in belə kiçik qiymətlər alması qeyri-elastiki elektron-elektron toqquşmaları ilə bağlıdır.

Э.И. Зульфугаров

ТЕРМОМАГНИТНЫЕ ЯВЛЕНИЯ В *n*-Pb$_{0.8}$Sn$_{0.2}$Te

В работе по данным термомагнит коэффициентов и электронной составляющей теплопроводности определена температурная зависимость числа Лоренса *L* в кристалле *n*-Pb$_{0.8}$Sn$_{0.2}$Te. Показано, что экспериментальное значение *L(T)* в интервале 40÷250К меньше его стандартного зоммерфельдского значения. Установлено, что заниженное значение *L* обусловлено неупругими электрон-электронными столкновениями.

ON THERMOMAGNETIC TRANSDUCERS OF IR RAYS
ON THE BASE OF $Cd_xHg_{1-x}Te$

E.I. ZULFUGAROV

Institute of radiation Problems of Azerbaijan National Academy of Sciences
31a, H.Javid av., Baku - 1143

Thermomagnetic properties of the solid solution of $Cd_xHg_{1-x}Te$ ($0 \leq x \leq 0.3$) and possibilities of creation of non cooled trancducer on the basis of them using traverse effect of Nernst-Ettingsgausen are studied. The analysis of the influence of the main physical parameters of the sensitive element on the main characteristics of the thermomagnetic transolucers is carried out. It is established, that as the sensitive element of infrared receiver from the investigated solid solutions the more suitable is the composition $Cd_{0.2}Hg_{0.8}Te$. Moreover, it is observed that electronic irradiation (with the integral doze $\sim 5.6 \cdot 10^{17}$ El/cm^2) at 300K leads to the increase of the specific sensitivity in two times.

The solid solutions $Cd_xHg_{1-x}Te$ are widely used as the sensitive element of cooled phototransducers in infrared-range [1]. In this direction the big successes have been achieved, the kinds of the receivers of the infrared rays have been created and are used. Moreover, the perspective of he uncooled warm transducers and receivers of the infrared rays on the base narrow-band semiconductors and on the base of Cd mercury, telluride system (CMT) [1-2] takes place. The thermomagnetic receivers of the infrared rays are one of the differences of the warm receivers of the infrared rays, having the defined advantages in respect of others. The set of the unique properties of the CMT system promote to the creation the same transducers on their base. Particularly, he minor effective mass of the electron, and their high mobility, low lattice thermoconductivity as conscience are caused by this. Therefore, the necessity of the study of the thermomagnetic properties of CMT and observing the probability of the use them as the sensitive elements in the uncooled thermomagnetic transducers of the infrared rays, based on he transversal effect Nernst-Ettingsgausen (N-E) effect, appear.

The given paper is devoted to the technical development of the thermomagnetic infrared transducers and the methods of the improving their technical characteristics. Unlikethe photoelectric gauges the thermomagnetic transducers don't ask for the additional power sources, and the cooling and thermostable systems also.

The action principle of thermomagnetic transducers is caused by the appearing of the temperature drop in the semiconductor in the direction of thermal radiation at the thermal absorption. At the action of the transversal magnetic field on the faces of the samples the N-E field appears, the value of which is caused by the thermal flux.
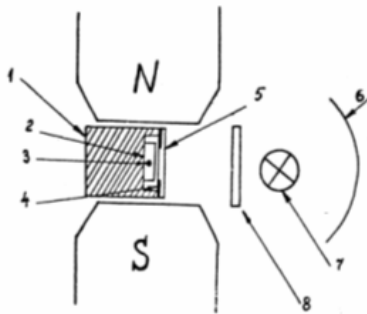

Fig.1. Construction of receiver of the infrared rays on N-E effect.

The most simple table of such transducers is given on the fig.1. This transducer includes the heat-eliminating core1, the sensitive element 2, the metallic contacts 3, screen 4, and the glass window 5. The sensitive element is situated between magnet fields before the radiation source. The filter 8, is situated between element situating in the focus of the mirror 6 and the calibration lamp 7.

The main characteristics of the thermomagnetic transducers on the base of N-E effect are:

specific sensitivity δ:
$$\delta = \frac{\varepsilon_y}{\frac{W}{S}} = \frac{Q_\perp B}{\text{ж}} \qquad (1)$$

thermomagnetic quality $Z_{T\mu}$:
$$Z = \frac{(Q_\perp B)^2}{\text{ж} S} \qquad (2)$$

factor of Quality F:
$$F = \frac{Q_\perp B}{\text{ж}^{3/4} c^{1/4} \rho^{1/2}} \qquad (3)$$

detective property D:
$$D = \frac{\delta \left(\dfrac{d}{4kT\rho}\right)^{1/2}}{\left(1 + \sqrt{ZT}\right)^{-1}} \qquad (4)$$

inertialness τ:
$$\tau = \frac{0,4 \ cd^2}{\text{ж}} \qquad (5)$$

where ε_y – N-E field; W/S is radiation power, adsorbed by the unit surface of the gauge; d is the thickness of the sensitive element; æ, ρ, c are coefficients of heat conduction, specific resistance and specific heat capacity accordingly. As it is seen, the main physic parameters of the semiconductor, defining the suitableness of the material for this purpose, are N-E coefficients, heat conduction and resistances. From the expression (1) it is followed, hat for the creation thermomagnetic transducer of the infrared rays with the high sensitivity it is necessary to choose the material with the low формула, with the big value of N-E coefficient. In [2] it is shown, that thermomagnetic force $Q_\perp B$ goes through minimum, the N-E coefficient achieves the big values in the materials with he high value of mobility ratio $U_n/U_p \gg 1$ outside the area of the intrinsic conductivity. From the expression (2) it is followed that for the creation of the transducer with he high quality there are need the materials with the low thermoconductivity with he high value $Q_\perp$, and with the low resistance also. Thus, if $Q_\perp$ increases because of the participation of the carriers of II type in the conductivity,

but ρ increases and Z falls. Sluggishness of the receivers is defined by the thermoconductivity and the thickness of the sensitive element (5). For the creation of the low inertial receivers it is need the sensitive element with the minimum thickness with the high æ. From the expression (4) it is followed, that detective property can be grown because of the high specific sensitivity δ and electroconductivity. Thus, the carried out analysis show, that demands to the materials for the thermomagnetic infrared transducers are different. The materials with the high δ, but a little bit worse exponents F, D, τ are used for the creation of the measurements of the thermal flux, with the high F are used for the creation of detectors of infrared rays, and with the high $Z_{T\mu}$ – for the energy transducers.

The solid solutions of CMT have the low lattice thermoconductivity, small effective mass and high mobility of the electrons. The crystals of CMT can be obtained as by n-, so by p-type of conductivity and changed its parameters at external action (temperature, pressure, radiation, magnetic and electric field, e.t.c.). The unique properties of the CMT crystals are in the base of the using in the quality as the gauge of the thermomagnetic transducers of the infrared rays.

The investigation of the transversal N-E effect was carried out on the swarm of the samples with $x=0\div0.3$ at 300K with the purpose of the definition of the ways of the practical use of the solid solutions of CMT. Because of the mixed conductivity the temperature and magnetic-field dependences of the value $Q_\perp B$ have the maximums. The problem is the observing the conditions, when these maximums are equal to T room and not high B. The maximum $Q_\perp B$ can be shifted, changing the ratio of concentrations of the electrons and holes in the initial material. The dependence curve of the specific sensitivity δ of CMT samples from the composition (fig.2; $B=1$Tl) was obtained. As it is seen, the dependence achieves the maximum value at $x=0,2$. The obtained results show the probability of the use of CMT solid solutions $(0.15 \leq x \leq 0.25)$ as the sensitive element in the devices on the detection of the radiation object, based on the N-E effect.

The comparison of the value of specific sensitivity of gauge on the base CMT with $x=0,2$

$$\left(\delta = 9 \cdot 10^{-5} B \frac{M}{B_T} \right)$$ with data on Cd$_3$As$_2$-NiA

$$\left(\delta = 1 \cdot 10^{-5} B \frac{M}{B_T} \right) : \text{JnSb-NiSb}$$

$$\left(\delta = 2.7 \cdot 10^{-5} B \frac{M}{B_T} \right) [2, 3] \text{ shows the perspective}$$

of CMT $(0.15 \leq x \leq 0.25)$ in the quality as the sensitive element in the installation on the detection of the radiation object.

According to the theory the value of thermomagnetic force $Q_\perp B$ can increases, increasing the ratio between concentrations n/p [2]. There are several methods of the influence on the ratio n/p (thermal treatment, doping, inclination from the stoichiometric). In the case JnSb-NiSb and Cd$_3$As$_2$-NiAs the above mentioned methods of the treatment lead to the to a change for the worse of δ [4], that is connected with the high initial electron concentrations in them $(\sim 2 \cdot 10^{17}$ and $6 \cdot 10^{18}$cm^{-3}). The longed temperature annealing of CMT crystals $(0 \leq x \leq 0.25)$ at 180-200°C in the

pores of mercury leads to the insignificant increase of δ [5, 6]. The later relieving, lightening, doping don't leads to the significant increase of δ. This is caused by the difficulty of the influence on the ratio of electrons and holes in it.

As it was mentioned in the work [7], the irradiation by the electrons at 10K and 20K don't influence of the significant influence on the parameters of the receivers of the infrared rays on the base Cd$_{0.2}$Hg$_{0.8}$Te. Such conclusion is the consequence of the influence of the small doze and low radiation temperature. It is no need to create the enough quantity of the radiation defects (RD), which are stable higher than radiation temperature that can lead to δ increase at such conditions. As it was shown in work [8] the electron irradiation leads of the increase of the electron concentration in the CMT crystals.

The results of the detailed investigation of the influence of the electron irradiation on the specific sensitivity δ are given on the fig.2, from this it is followed, that $(\Phi=5.6 \cdot 10^{17}$cm$^{-2})$ goes through maximum at $0.15 \leq x \leq 0.25$ at the electron radiation. These results show that the irradiation by electrons at 300K by the energy 4MeV in the doze interval $(4\div7) \cdot 10^{17}$cm^{-2} of CMT crystals with $p \gg n$ and $pU_p \geq nU_n$, used earlier in the photo- and thermomagnetic receivers, as the sensitive element in the installations on the detection of radiation object, based on the N-E effect, leads to the increase of δ in 2 times.
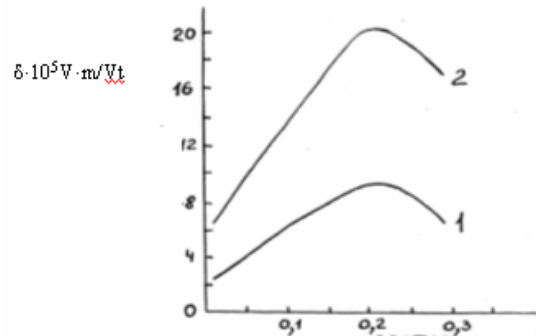
Fig.2. The dependence of specific sensitivity on composition of thermomagnetic transducer on the base CMT. The doze of irradiation 1 – 0; 2 - $5,6 \cdot 10^{17}$ el/cm^2.

The obtained results are explained that CMT in the conductivity always participate holes and electrons with the different concentrations and mobility at the same time.

The electron irradiation leads to the increase of n, which is followed by the according increase of N-E coefficient. Indeed, the last leads to the increase, as the phonon spectrum isn't sensitive to the electron irradiation.

It is known the several types of the thermomagnetic transducers on the base of N-E effect. The most simple from them it was described in the work [4]. This receiver includes the heat-conducting core, sensitive element, metallic contacts, screen and glass window.

The sensitive element is situated between magnet poles before radiation source. The filter is situated between calibration lamp and element, situating in the focus of the mirror. The most original construction of N-E receiver is used for the detection of the location of the radiation source. The construction of this receiver is ipresented on the figure 3. The front surface of the element turns back and closes by the thin glass (or quartz) window 8. The sensitive element 1 is situated between 4 and 5 magnet poles. The electromotive force of N-E appearing on the side faces of the sensitive

element, is taken by the contacts 6 and given on the focusing installation. The action principle of this receiver of heat radiation is based on the temperature drop, appearing in the sensitive element at the decrease of the infrared rays. The N-E electric field appears at the action of magnetic field B. The fall point of the infrared beam on the working solid moves from the area of the one magnet to the area of another at the moving of the radiation source. Moreover, the output signal changes the polarity going through «dead point– O » (where $B=0$), but the signal value increases with the increase of the inclination of the fall point of the radiation in respect of «dead point» of the sensitive element. The output signal changes and thus the transmission of the radiation source is fixed with the inclination of source beam in respect of «O» point. Such devices can be used in the industry, for example, in the control systems with the help of the infrared beams, especially on the heat tube mill.
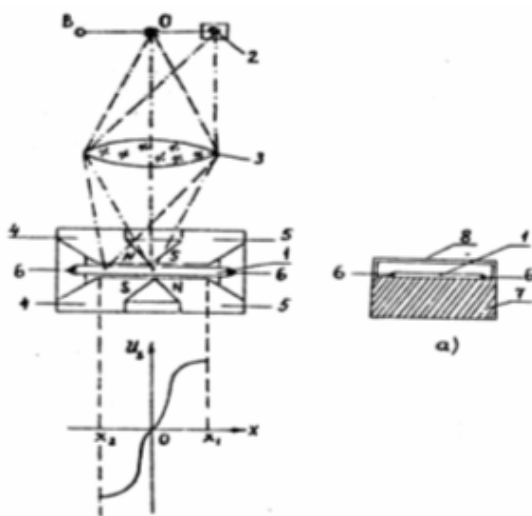

Fig.3. Construction of receiver IR radiation on the N-E effect for detection of the location of source radiation. 1-sensitive element (working body); 2 – source of IR radiation; 3 – lens; 4,5 – magnet; 6 – contacts; 7 – heat conducting core; 8 – glass window.

The thermomagnetic N-E effect is used for the creation of the amplifier of the direct current also. For this it is used the hybrid thermoelectric-thermomagnetic transducer of the intensity on the Peltie and N-E effects, including Peltie thermoelements of n and p branches Bi_2Te_3 and the sensitive thermomagnetic element from JnSb-NiSb. The action principle of the transducer is: the constant voltage of such polarity, that the heat will generate on the contact, is given on the thermoelement. The generating heat creates the temperature gradient on the sensitive element in the direction of y axe. The field N-E appears at the appearing of the magnetic field on the sensitive element in the direction, transversal to dT/dy. Moreover, the ratio of the output signal to the input signal can be estimate by the ratio:

$$\frac{V_2}{V_1} = \frac{\left(\dfrac{QB}{\alpha_1}\right)\left(\dfrac{\ell}{d}\right)}{1 + Z \cdot T\left(1 + \dfrac{\text{ж}_2}{\text{ж}_1}\right)}$$

where α_1 is the electromotive force of the thermoelement, æ_1 is its thermal conduction, Z is thermoelectric quality, l is common length of the sensitive element in the direction of the output signal, d is thickness in the direction of heat flux.

Because of α, æ and Z aren't almost depend on B at the room temperature till $B=1Tl$, so output intensity becomes proportional to QB. That's why the one more important demand to the such devices is the linear change of thermomagnetic force (QB) of the sensitive element from the B induction, which leads to the line changing V_2 from B.

As it was above mentioned, the specific sensitivity δ for CMT crystals have linear character. The creation of the sensitive element from the semiconductor solid solution $Cd_xHg_{1-x}Te$ ($0.15 \leq x \leq 0.25$) allows to increase significantly of the amplification factor in the hybrid transducers on Peltie's and N-E effects (fig. 3), consideringly. Such transducers can be used in the measuring technics for the amplify of the weak electric signals.

Thus, it is established, that $Cd_xHg_{1-x}Te$ (with $x=0.15 \div 0.25$) can be used as in the sensitive element in the thermomagnetic receivers of the infrared rays. The electronic irradiation (with the integral doze $\sim 5.6 \cdot 10^{17}$el/cm^2) of CMT crystals (with $x=0.15 \div 0.25$) at 300K leads to the increase of the specific sensitivity of the receivers of the infrared rays in two times.

[1] Infrared Detectors. (Ed. By *R.D.Hadson*- New-York). A Division of J.Wiley and Sons Inc. 1975, 392 p.

[2] *S.A. Aliyev, D.G. Arasli*. Fizicheskiye ocnovi termomagnitnikh preobrazovateley IK izlucheniya. Baku, 1981-27 s. (Preprint № 42 Instituta fiziki AN Azerb. SSR) (in Russian).

[3] *H.J. Goldsmid, K.R. Sydney*. A thermal radiation detectors employing the Nernst effect in Cd_3As_2-NiAs.- J.Phys. Appl. Phys., 1971, v.4, №6, p.869-875.

[4] *E.I. Zulfugarov*. Vliyaniye elektronnogo oblucheniya na elektrofizicheskiye svoyctva tverdikh rastvorov $Cd_xHg_{1-x}Te$ (0 x 0,25). Diss. kand. fiz.- mat.nauk. Baku, 1985- 132 p. (in Russian).

[5] *G. Dittmaz, B. Forbrig, F. Schubert*. Tempern von $Cd_{0.2}Hg_{0.8}Te$ im Quecksilberdampf., Krist. Und Techn/ 1978, v.13,N 7,p.817-821

[6] *B.M. Askerov*. Kineticheskiye effekti v poluprovodnikakh. Nauka, L., 1970, 303 p. (in Russian).

[7] *C.E. Mallon, B.A. Green, R.E. Leadon, J.A. Nabar*. Radiation effects in $Hg_{1-x}Cd_xTe$. e EEE, Trans. Nucl. Sci., 1975, v.22, №6, p.2283- 2288.

[8] *S.A. Aliyev, T.G. Gadzhiyev, E.I. Zulfugarov, R.I. Selimzade*. Vliyaniye elektronnogo oblucheniya na parametri nositeley zaryada v tvyordikh rastvorakh $Cd_xHg_{1-x}Te$ tezisi dokl. Vsecoyuz. konf. «Radiacionnaya fizika poluprovodnikov I rodstvennikh materialov». Tashkent, 1984, s.66. (in Russian).

E.İ. Zülfüqarov

$Cd_xHg_{1-x}Te$ KRİSTALLARI ƏSASINDA İQ ŞÜALARIN TERMOMAQNİT ÇEVİRİCİLƏRİ

Məqalədə $Cd_xHg_{1-x}Te$ kristalları əsasında düzəldilmiş İQ (infraqırmızı) şüaların termomaqnit qəbulediçilərinin düzəldilməsi və onların iş prinsipindən danışılır.

$Cd_xHg_{1-x}Te$ kristallarının 300K temperaturda eninə *N-E* (Nernst-Ettinqsqauzen) effekti ölçülmüşdür. Müəyyən olunmuşdur ki, $Cd_{0.2}Hg_{0.8}Te$ kristalları İQ qəbulediciləri üçün daha yararlıdır. Belə ki, $Q_\perp B$ maksimumu məhz *x*=0,2 kristallarında ən çox olur.

Məqalədə hərəkətdə olan obyektləri aşkar edən İQ qəbuledicinin quruluşu və iş prinsipi haqqında da məlumat verilir.

Э.И. Зульфугаров

О ТЕРМОМАГНИТНЫХ ПРЕОБРОЗОВАТЕЛЯХ ИК ИЗЛУЧЕНИЯ НА ОСНОВЕ $Cd_xHg_{1-x}Te$

Исследованы термомагнитные свойства твердых растворов и возможности создания на их основе неохлаждаемых преобразователей ИК излучения, основанных на поперечном эффекте Нернста-Эттингсгаузена. Проведен анализ влияния основных физических параметров чувствительного элемента на основные характеристики термомагнитных преобразователей. Установлено, что в качестве чувствительного элемента ИК приемника из исследованных твердых растворов наиболее подходит состав . Наряду с этим выявлено, что электронное облучение (с интегральной дозой) при 300К приводит к возрастанию удельной чувствительности ИК приемника в два раза.

MATHEMATICA SOFTWARE IN INTEGRATION OF CHIRAL FIELD MODEL

M.A. MUKHTAROV

Institute of Mathematics and Mechanics
370602 Baku, F.Agaev str.9, Azerbaijan

The *Mathematica* algorithm for recurrent procedure of integration of the principal chiral field problem is presented.

1.   *Mathematica* is the world's only fully integrated environment for technical computing. First released in 1988, it has had a profound effect on the way computers are used in many technical and other fields. In this article we show the application of this powerful tool to solution of the principal chiral field problem.

The principal chiral field problem may be written in the form:

$$g_\xi g^{-1} = f_\xi \ , \ g_\eta g^{-1} = -f_\eta \qquad (1),$$

where g and f are respectively, group and algebra-valued functions,
which are solutions of the principal chiral field problem

$$\left(g_\xi g^{-1}\right)_\eta + \left(g_\eta g^{-1}\right)_\xi = 0 \ , \ 2f_{\xi\eta} = \left[f_\xi, f_\eta\right] \qquad (2)$$

In the case of $SL(2,C)$ algebra these equations can be solved completely for the following initial condition [1]:

$$f = \begin{pmatrix} \tau & \alpha \\ 0 & -\tau \end{pmatrix} , \ \tau_{\xi\eta} = 0 , \ \alpha_{\xi\eta} = \alpha_\eta - \alpha_\xi \qquad (3)$$

The result of integration of the system (3) can be expressed in terms of chains of solutions of the following system of linear equations

$$\alpha[n+1]_\xi = \alpha[n]_\xi - 2\alpha[n]$$
$$-\alpha[n+1]_\eta = \alpha[n]_\eta + 2\alpha[n] \qquad (4)$$

which are nothing more than Backlund transformations.
The solutions of (4) in the explicit form are presented in [2].
The discrete symmetry transformation allows carrying out the recurrent procedure of finding the solution of (2)

$$g_{n+1} = S_n w g_n$$

The solutions are expressed in terms of chains (4) starting from the 0-step (3).
We are using the following parameterization of the group element:

$$g_{n+1} = Exp(\alpha[n]X^+)Exp(t[n]h)Exp(\beta[n]X^-)$$

2. Below one can find the *Mathematica* program of the first two steps of recurrent procedure.
The *input* is written in Bold style, the results – in Normal.

```
In[1]:= X⁺ = ( 0  1 );   X⁻ = ( 0  1 );   h = ( 1   0 );   w = ( 0   1 );
        ( 0  0 )         ( 0  0 )         ( 0  -1 )        ( -1  0 )
```

```
G₀ = MatrixExp[n X⁺].MatrixExp[r h];
S₁ = MatrixExp[s[1] X⁺].MatrixExp[s₀[1] h]; G₁ = S₁.w.G₀;
G₁
```

Out[4]= {{-e^(r-s₀[1]) s[1], e^(-r+s₀[1]) - e^(-r-s₀[1]) n s[1]}, {-e^(r-s₀[1]), -e^(-r-s₀[1]) n}}

```
In[5]:= G₁ = FullSimplify[G₁ /. s[1] → a[1] /. n → a[-1] /. s₀[1] → Log[a[0]]]
```

Out[5]= {{- (e^r a[1])/a[0] , (e^(-r) (a[0]² - a[-1] a[1]))/a[0] }, {- e^r/a[0] , - (e^(-r) a[-1])/a[0] }}

```
In[6]:= β[1] = G₁[[2, 1]] / G₁[[2, 2]]; α[1] = G₁[[1, 2]] / G₁[[2, 2]];
        t[1] = -Log[G₁[[2, 2]]];
        FullSimplify[α[1]]
```

Out[8]= - a[0]²/a[-1] + a[1]

```
In[9]:= FullSimplify[t[1]]
```

$$Out[9]= -Log\left[-\frac{e^{-r}\,a[-1]}{a[0]}\right]$$

```
In[10]:= β[1] = G₁[[2, 1]] / G₁[[2, 2]]
```

$$Out[10]= \frac{e^{2r}}{a[-1]}$$

```
In[11]:= s₀[2] = Log[ (Det[ a[0]  a[1] ; a[1]  a[2] ]) / a[0] ];
```

$$s[2] = \frac{a[0]\,Det\begin{bmatrix} a[0] & a[2] \\ a[1] & a[3] \end{bmatrix} - a[1]\,Det\begin{bmatrix} a[0] & a[1] \\ a[1] & a[2] \end{bmatrix}}{a[0]^2};$$

```
S₂ = MatrixExp[s[2] X⁺].MatrixExp[s₀[2] h];
G₂ = S₂.w.G₁;
β[2] = G₂[[2, 1]] / G₂[[2, 2]];
α[2] = G₂[[1, 2]] / G₂[[2, 2]];
t[2] = -Log[G₂[[2, 2]]];
FullSimplify[β[2]]
Null
```

$$Out[18]= \frac{e^{2r}\,a[1]}{-a[0]^2 + a[-1]\,a[1]}$$

```
In[20]:= FullSimplify[t[2]]
```

$$Out[20]= -Log\left[\frac{e^{-r}\,(a[0]^2 - a[-1]\,a[1])}{a[1]^2 - a[0]\,a[2]}\right]$$

```
In[21]:= FullSimplify[α[2]]
```

$$Out[21]= \frac{a[1]^3 - 2\,a[0]\,a[1]\,a[2] + a[-1]\,a[2]^2}{a[0]^2 - a[-1]\,a[1]} + a[3]$$

3. The last expression is nothing more than

$$\alpha[2] = \frac{Det\begin{pmatrix} a[-1] & a[0] & a[1] \\ a[0] & a[1] & a[2] \\ a[1] & a[2] & a[3] \end{pmatrix}}{Det\begin{pmatrix} a[-1] & a[0] \\ a[0] & a[1] \end{pmatrix}}$$

Using the expressions for the group-value elements and the relations (1), one can easily come to final expressions for the algebraic solutions, presented in [1]:

$$f_n^- = \frac{Det_{n-1}(a)}{Det_n(a)}\,,\, f_n^0 = \tau + \frac{\tilde{D}_n(a)}{Det_n(a)}\,,\, f_n^+ = \frac{Det_{n+1}(a)}{Det_n(a)}\,,$$

where $Det_n(a)$ are the minors of order n of the following matrix:

$$\alpha = \begin{pmatrix} a[0] & a[1] & a[2] & ... \\ a[1] & a[2] & a[3] & ... \\ a[2] & a[3] & a[4] & ... \\ ...... & ...... & ...... & ... \\ ...... & ...... & ...... & ... \end{pmatrix}$$

Here $\tilde{D}_n(a)$ denotes that in the last row of the corresponding matrix the indices of $a[i]$ have been increased by one.

[1] *A.N.Leznov,M.A.Mukhtarov and W.J.Zakrzewski.* Tr.J.of Physics 19, 1995, 416

[2] *M.A. Mukhtarov.* Fizika 5, 2002, 38

[3] *M.A. Mukhtarov.* Proc.Ins.Math.Mech., 10(18), 2000, 123

M.A. Muxtarov

KİRAL SAHƏNİN MODELİNİN İNTEQRALLANMASINDA *MATHEMATICA* PROQRAMI

Əsas kiral sahəsinin məsələsinin inteqrallama prosedurun *Mathematica* alqoritmi təqdim olunub.

М.А. Мухтаров

ПРОГРАММА *MATHEMATICA* В ИНТЕГРИРОВАНИИ МОДЕЛИ КИРАЛЬНОГО ПОЛЯ

Представлен *Mathematica* алгоритм рекуррентной процедуры интегрирования задачи главного кирального поля.

Klein Paradox in Modified Dirac and Salpeter Equations

Nina Kevlishvili, Giorgi Piranishvili
Tbilisi State University

1. Introduction

It is well known, that Dirac equation in central symmetry field has unusual properties, like the leak of particle through the infinite wall, that means oscillation of solution in asymptote, for infinitly increasing potential, when the interaction is the zero component of Lorenz-vector. This unusual property is known as Klein Paradox [1]. The same lack has two particle Dirac equation [2,3].

By considering quarks and antiquarks the problem is being tried to solve by introducing additional scalar interaction [4,5]. So let us consider Dirac equation

$$(\vec{\alpha}\,\vec{p} + \beta m)\Psi(x) = (E - V)\Psi(x) \tag{I}$$

with infinitly increasing potential

$$\lim_{r \to \infty} V(r) = \infty$$

there wave function is represented as spinor

$$\Psi = \begin{pmatrix} a(r)\Omega_{jlm} \\ b(r)\Omega_{jl'm} \end{pmatrix}$$

we get radial equations

$$\frac{dA}{dr} + \frac{\chi}{r}A - (E - V + m)B = 0$$
$$\frac{dB}{dr} - \frac{\chi}{r}B + (E - V - m)A = 0 \tag{II}$$

there

$$A(r) = ra(r) \qquad B(r) = rb(r) \qquad \chi = l(l+1) - j(j+1) - \frac{1}{4}$$

After obvious transformations the equations (2) will look like

$$\frac{d^2A}{dr^2} - \frac{2\chi}{r^2}A + \left((E - V)^2 - m^2\right)A = 0$$

When $r \to \infty$, the second term can be neglected

$$\frac{d^2A(r)}{dr^2} + V^2A(r) = 0 \tag{III}$$

The sign "+" shows, that there are no bound states. That means, the Klein Paradox takes place.

On the other hand, if we consider scalar potential in 4-space the Dirac Equation will look like

$$(\vec{\alpha}\,\vec{p} + \beta(m + S(r)))\Psi(\vec{r}) = E\Psi(\vec{r}) \tag{IV}$$

After the transformation of corresponding radial equations we will get equation

$$\frac{d^2A(r)}{dr^2} - S^2(r)A(r) = 0 \tag{V}$$

which has bound states and is free of Klein Paradox.

As a rule there are considered potentials containing both fields

$$U = aS(r) + bV(r) \qquad a, b = const \tag{VI}$$

In this case the existing of Klein Paradox depends on the correlation between two constants.

Besides that particular importance has equal mixture of scalar and vector potentials, which excludes spin-orbital interaction in Dirac equation [3,5] and Klein Paradox in two particle Dirac equation [2,3,6].

It would be natural to check the existing of this problem in field's quantum theory equations. I mean Bethe-Salpeter (BS) equation. There is an opinion that only vector interaction is not recommended here either because of Klein Paradox. But this fact is not proved yet. For example, in case of quark's confinement in hadrons the situation is not clear. There is not necessary to introduce an additional scalar field, it actually exists as potential's fourth component.

In last years a lot of works discused 3-dimensional relativistic equations which are results of BS equation's different reductions. 3-dimensional equations are interesting because they give us possibility to study quarkonium spectrum for different potentials. The great attention is paid to the formulation where by means of one particle mass rushing to infinity the problem reduces to Dirac equation of one particle in external field [7]. But in our opinion, not eveything is clear there. The information about second quantization could not be lost when we make one particle heavier. For instance, if we use 3-dimensional Kernel in BS equations the problem reduces to Salpeter equation which differs from two-particle Dirac equation in interaction term which contains projecting operator only on positive and only on negative frequencies. In this case this projecting operator is the only relict of second quantization.

In the 80-s was supposed, that equations of field's quantum theory must be free of Klein Paradox [3,6]. So Salpeter equation was studied from this point of view [8,9] by Krolikowski and Turski. But final conclusions were made based on Dirac modified equation, which is the result of making one particle infinitly heavy.

For example, the author of work [8] was studing the following Salpeter equation:

$$\left[E - \left(\vec{\alpha}^{(1)}\vec{p} + \beta^{(1)}m_1\right) - \left(-\vec{\alpha}^{(2)}\vec{p} + \beta^{(2)}m_2\right) - \Pi(\vec{p})V(r)\right]\Psi(\vec{r}) = 0 \qquad (1)$$

where $\Pi(\vec{p})$ is above mentioned projectiong operator:

$$\Pi(\vec{p}) = \Lambda_+^{(1)}(\vec{p})\Lambda_+^{(2)}(-\vec{p}) - \Lambda_-^{(1)}(\vec{p})\Lambda_-^{(2)}(-\vec{p}) \qquad (2)$$

and

$$\Lambda_\pm^{(i)}(\vec{p}) = \frac{\omega_p \pm (\vec{\alpha}^{(i)}\vec{p} + \beta^{(i)}m_i)}{2\omega_p} \quad , \qquad \omega_p = \sqrt{\vec{p}^2 + m^2}$$

are projecting operators on poitive and negative frequences for free spinors. They are nonlocal integral operators in coordinate space.

In the limit when $m_1 = m_2 = m \to \infty$ the kernel of this integral representation (Bessel function) becomes local $\delta(\vec{r} - \vec{r}')$ function and the equation (1) becomes local either. After this it is not difficult to determine asymptotic behaviour of wave function when $r \to \infty$. It will exponentialy fall for increasing potential V(r).

Turski considered the case of tending one particle's mass to infinity. Then equation (1) reduces to modified Dirac equation for light particle motion in "projected' field:

$$\left[\vec{\alpha}\vec{p} + \beta m + \Lambda_+(\vec{p})V(r)\right]\Psi(\vec{r}) = E\Psi(\vec{r}) \qquad (3)$$

The author showed, by means of above mentioned integral representation and asymptotic restrictions on wave function and potential, that modified Dirac equation is free of Klein Paradox.

We consider, that all such statements are scanty because they are based on approximations and simplified assumptions about potential's behaviour. One is clear from these works, if modified Dirac equation is free of Klein Paradox the same is true for Salpeter equation.

In the following we consider our problem in momentum space and show that modified Dirac equation (3) has discrete spectrum if such spectrum has Schrödinger equation for the same potential V(r). This statement is equivalent to absence of Klein Paradox, by our opinion.

2. Dirac Modified Equation in Foldy-Wouthausen Representation

Consequently, we learn Dirac modified equation (3). If we act on this equation with projecting operator $\Lambda_{\pm}(\vec{p})$ in succession we get the following equations:

$$[E - (\vec{\alpha}\,\vec{p} + \beta m)]\Lambda_+(\vec{p})\Psi = \Lambda_+ V\Psi \tag{4}$$

and

$$\Psi_- = \Lambda_-\Psi = 0 \tag{5}$$

By using these equations (4) will look like:

$$[E - (\vec{\alpha}\,\vec{p} + \beta m)]\Lambda_+\Psi = \Lambda_+ V\Lambda_+\Psi \tag{6}$$

Consequently, we have a problem of proper value with following hermitian Hamiltonian

$$H = \vec{\alpha}\,\vec{p} + \beta m + \Lambda_+ V\Lambda_+ \tag{7}$$

It is convenient to use Foldy-Wouthausen's transformation[11]:

$$e^{iS}(\vec{\alpha}\,\vec{p} + \beta m)e^{-iS} = \beta\omega_p \qquad \omega_p = \sqrt{\vec{p}^2 + m^2} \tag{8}$$

It is clear, that

$$e^{iS}\Lambda_+(\vec{p}) = \sqrt{\frac{2\omega_p}{\omega_p + m}}\frac{1}{2}(1 + \beta)\Lambda_+(\vec{p})$$

$$\Lambda_+(\vec{p})e^{-iS} = \sqrt{\frac{2\omega_p}{\omega_p + m}}\Lambda_+(\vec{p})\frac{1}{2}(1 + \beta) \tag{9}$$

For the transformed $\Psi_{FW} = e^{iS}\Psi$ function we get the following equation

$$(E - \beta\omega_p)\Psi_{FW} = \sqrt{\frac{2\omega_p}{\omega_p + m}}\frac{1 + \beta}{2}\Lambda_+(\vec{p})\int d^3k V(\vec{p} - \vec{k})\Lambda_+(\vec{k})\frac{1 + \beta}{2}\sqrt{\frac{2\omega_k}{\omega_k + m}}\Psi_{FW}(\vec{k}) \tag{10}$$

It is natural to represent Ψ_{FW} as a two component spinor

$$\Psi_{FW} = \begin{pmatrix} \varphi \\ \chi \end{pmatrix} \tag{11}$$

Then equation (10) will give us the following system:

$$(E - \beta\omega_p)\varphi(\vec{p}) = \sqrt{\frac{2\omega_p}{\omega_p + m}}\frac{1 + \beta}{2}\Lambda_+(\vec{p})\int d^3k V(\vec{p} - \vec{k})\Lambda_+(\vec{k})\sqrt{\frac{2\omega_k}{\omega_k + m}}\varphi(\vec{k})$$

$$(E + \omega_p)\chi(\vec{p}) = 0 \tag{12}$$

The second equation does not have untrivial solutions, so far as $E \neq -\omega_p$, $\chi = 0$

Now we can calculate the matrix structure of the right side of the equation (12) in evident form. After simple transformations we get

$$(E - \omega_p)\varphi(\vec{p}) = \sqrt{\frac{2\omega_p}{\omega_p + m}}\int d^3k\left[\frac{\omega_p + m}{2\omega_p}V(\vec{p} - \vec{k})\frac{\omega_k + m}{2\omega_k} + \frac{\vec{\sigma}\,\vec{p}}{2\omega_p}V(\vec{p} - \vec{k})\frac{\vec{\sigma}\,\vec{k}}{2\omega_k}\right]\sqrt{\frac{2\omega_k}{\omega_k + m}}\varphi(\vec{k}) \tag{13}$$

3. The Radial Form of Modified Dirac Equation

Let us analyse the equation (13) by angles. For this purpose we can use basis of spherical spinors [12]:

$$\varphi(\vec{p}) = f(p)\Omega_{jlm}(\vec{n}_p) \qquad \vec{n}_p = \frac{\vec{p}}{|\vec{p}|} \tag{14}$$

where Ω_{jlm} functions satisfy following equation

$$(\vec{\sigma}\,\vec{n}_p)\Omega_{jlm}(\vec{n}_p) = -\Omega_{jl'm}(\vec{n}_p) \qquad (l + l' = 2j) \tag{15}$$

59

In explicit form this functions are expressed by spherical harmonics and corresponding Klebsh-Gordon coefficients:

$$\Omega_{jlM}(\vec{n}_p) = \begin{pmatrix} C^{jM}_{l,M-1/2,1/2,1/2} \, Y_{l,M-1/2}(\vec{n}) \\ C^{jM}_{l,M+1/2,1/2,-1/2} \, Y_{l,M+1/2}(\vec{n}) \end{pmatrix} \tag{16}$$

Therefore, if we express $V(\vec{p}-\vec{k})$ potential as series of spherical harmonics

$$V(\vec{p}-\vec{k}) = \sum_{l=0}^{\infty} \sum_{m'=-l}^{l} v_l(p,k) Y_{lm'}(\vec{n}_p) Y^*_{lm'}(\vec{n}_k) \tag{17}$$

and insert everything mentioned above in the equation (13) and use properties of orthogonality the equation will not depend on angles. So we get the following radial equation

$$(E-\omega_p) f(p) = \int_0^{\infty} k^2 dk V_l(p,k) \chi(p,k) f(k) \tag{18}$$

where $\chi(p,k)$ is an additional factor, which is the result of projecting operator's existing:

$$\chi(p,k) = \sqrt{\frac{\omega_p+m}{2\omega_p}} \left[1 + \frac{pk}{(\omega_p+m)(\omega_k+m)} \right] \sqrt{\frac{\omega_k+m}{2\omega_k}} \tag{19}$$

Equation (18) is our main result.

4. **Properties of Radial Equation Spectrum**

The kind of spectrum of radial (integral) equation (18) depends on the properties of it's kernel, which now contains FW-factor $\chi(p,k)$ together with radial component of potential. Just this factor expresses nonlocality of effective potential.

First of all let us discuss some properties of $\chi(p,k)$ factor:

1) It loks like the sum of two members factorized by p and k variables. This can be important by studying various factorized potentials.

2) When k=p (on the energetical surface in scattering problem) $\chi=1$.

3) It is positive-definite and bounded when $p,k \to \infty$.

4) It has not any singularity for physical values of variables.

5) To reach the nonrelativistic limit in equation (18) it is enough to expand it into a series of p^2 and k^2. This operation does not affect the smallness of $v_l(p,k)$ potential.

Based on the properties mentioned above we can answer our main question – does Klein Paradox take place or not?

It is clear, that integral equation (18) without $\chi(p,k)$ is Salpeter spinless equation's radial form in momentum space. As it is known [10,13] Salpeter spinless equation for unlimited, increased potential has confinement type solutions – only discrete spectrum. Because of above mentioned properties of $\chi(p,k)$ the kernel of equation (18) is Fredholm-Smith type. It is multiplied on limited nonsingular function, according to well known theorem [14,15] the kernel remains Fredholm-Smith type and therefore the spectrum of equation(18) will be only discrete if Schrödinger (or spinless Salpeter) equation has discrete spectrum for the same potential.

In our opinion, this conclusion is equivalent to absence of Klein Paradox in modified Dirac (and Salpeter) equation.

It is strange that in our equation (13) remains dependent on orbital momentum only. That means, projecting operator Λ_+ separates spin-orbit coupling.

By introducing additional scalar interaction the same result is obtained for equal mixture of scalar an vector potentials.

Consequently, all above mentioned results can be naturally obtained be considering vector potential only. That is why it is not necessary to introduce the scalar potential artificially.

5. <u>References</u>

[1]. J.D. Bjorken, S.D. Drell. Relativistic Quantum Mechanics. Mc.Graw-Hill, New York (1964).

[2]. W. Krolikowski, A. Turski, J. Rzewuski. Z. Phys. C1, 369 (1979).

[3]. A.A. Khelashvili. Bull. of Georgian Acad. Sci. 104, 569 (1981)

[4]. D.W. Rein. Nuovo Cim., A38, 19 (1977)

[5]. E. Magyary. Phys. Letters, B95, 295 (1980)

[6]. A.A. Khelashvili. Theor. Math. Phys. 51, 447 (1982)

[7]. T.I. Kopaleishvili, Particle and Nuclei.,32, 1061, Dubna (2001)

[8].W. Krolikowski. Acta Phys. Austriaca, 51, 243 (1979)

[9]. A. Turski. Bull de l'acad. Polon. des Sciences, 27, 195 (1979)

[10]. G. Hardekopf, J. Sucher. Phys. Rev. A30, 703 (1984)

[11]. L.L.Foldy, S.A. Wouthuysen. Phys.Rev , 78, 29 (1950)

[12]. A.Akhiezer, V. Berestetski, Quantum Electrodynamics, Interscience, New York (1965)

[13]. L.J. Nickish, L. Durand, B. Durand. Phys. Rev. D30, 660 (1984)

[14]. C. Lovelace. Three-Particle System and Unstable Particles. Scottish Univ. Summer School, Edinburgh (1963) p. 437

[15]. N. Dunford, J. Schwartz. Linear Operators, I. Interscience, (1958)

ROENTGENDETECTORS ON THE BASE OF TlInSe$_2$<LI$^+$>

S.N. MUSTAFAEVA, E.M. KERIMOVA, M.M. ASADOV, R.N. KERIMOV

Institute of Physics, Azerbaijan National Academy of Sciences,
Baku. Az-1143, H.Javid av.33

High sensitive and durable roentgen-detectors were created on the basic of semiconductor crystals TlInSe$_2$. The dose sensitivity of created roentgen-detectors was $1.1\cdot10^{-10}\div5.9\cdot10^{-9}$ A/R·min·V in the range of the measured power $E=0.75\div78.0$R/min. The registered range of the X-rays energy was $10\div50$keV. The detectors delay time was $3\div5$s and the working voltage is $10\div20$V. The ratio of coefficients of roentgenosensitivity after and prior to lithium intercalation amounts to $2\div4$. It was shown that dependence of roentgenocurrent ΔI_r on radiation dose E is described as: $\Delta I_r \sim E^{\alpha}$, where $\alpha = 0.5\div1.1$ at $25\div50$ keV for pure TlInSe$_2$ and $\alpha = 0.65\div1.5$ for TlInSe$_2$<Li$^+$>.

The research of electric; photoelectric and roentgen-dozimetric characteristics of semiconductive single crystals TlInSe$_2$, belonging to material class of TlMeX$^6_2$ (Me-In, Ga; X-S, Se, Te) [1-9], showed; that they have a high sensitivity to the X-ray irradiation.

Single crystals TlInSe$_2$ were obtained by the following way [10]. Thallium; indium and selenium; taken in the stechiometric ratio 1:1:2 were charged in the quartz ampoule by the diameter 16 mm and the length 100mm (the selenium excess from stechiometric made 0,4 mass %). The ampoule is pumped out up to the pressure $1.3\cdot10^{-3}$Pa and is soldered.

The compound TlInSe$_2$ was synthesized by the direct melting of initial components by the method of the double-temperature synthesis with the use of the vibrating mixing at the temperature on 50-70° higher than the fusing temperature (T_{fus}=1040K) during 3-4 hours. For the homogenizing obtained alloys were annealed at the temperature, equal to 2/3 of the fusing temperature T_{an}=693K during 200 hours. The single-phasing of obtained alloys was controlled by the method of diffirentional-thermal (DTA) and roentgenophase analysises (RPA).

DTA was carried out on the device NTR-92, allowing to fix the temperature of phase transformations with accuracy $\pm3\div5$K. The heating rate made 2-4K/min. The temperature was controlled by the thermocouple *Pt-Pt/Rh*; graduated by the reference substance in the range 472-1560K DTA results showed; that the compound TlInSe$_2$ melts congruently at 1040K. Thermodynamic parameters of the compound TlInSe$_2$ were determined by the measurements data of EMF concentration chains, composed of alloys of Tl-In-Se system: Gibs standard free energy of the formation ΔG^o_{298}=-180 kJoule/mole; standard enthalpy of the compound formation: ΔH^o_{298} =-190 kJoule/mole; the enthalpy of the compound melting: ΔH_m =40 kJoule/mole. The RPA was realized on the device DRON-3 at the radiation CuK$_\alpha$. RPA results shows, that TlInSe$_2$ crystallizes in the tetragonal lattice of TlSe (space group 14/mcm) with parameters: a=8.002Å; b=7.015Å; z=4.

For the growth of large single crystals obtained polycrystals TlInSe$_2$ were plunged into the special ampoule, pumped out up to 10^{-3}Pa and placed in the double-chamber furnace. Single crystals were grown by Bridgemen method from the melt at the rate of the crystallization front transformation 0.6 mm/hour with the following cooling of obtained crystals with the rate 5K/min.

Samples of sizes (2.0x0.8x0.2)mm^3 were prepared on the base of obtained chained single crystals TlInSe$_2$, which were split off along the direction [001].

Contacts to them were applied by indium melting on the crystal surface and provided by the ohmity of voltampere characteristics (VAC) up to the electric intensity $\leq$200V/cm. The electric field was applied along the direction [001], and the X-ray radiation was directed perpendicularly to the crystal surface. Measurements were carried out at 300K; and the voltage was taken in limits of the linear part of VAC. The device URS-55A with the tube BSV-2 served the X-rays source.

X-rays intensity was registered at the measurement by means of the current variation on the tube at each given value of the accelerating potential on it. Absolute values of X-rays doses were measured by the crystal dosimeter of DRGZ-02 type.

The detector roentgenosensitivity was determined by the formula:

$$k = \frac{\Delta J_r}{V_s \cdot E} \quad ,$$

where $\Delta J_r = J_r - J_d$;

J_d is the dark current; J_r is the current in the sample at the X-ray irradiation; E is the X-ray power; V_s is the supply voltage (the working voltage).

The dose sensitivity of studied detectors on the base of crystals TlInSe$_2$ made $1.1\cdot10^{-10}\div5.9\cdot10^{-9}$Amin/R·V in the range of the measured power $E=0.75\div78.0$R/min. The registered range of the X-rays energy made $10\div50$keV. The detectors delay time made $3\div5$s; and the working voltage V_s=$10\div20$Volt.

Suggested by us X-rays detectors on the base of crystals TlInSe$_2$ yield in the sensitivy to the detectors on the base of single crystals CdS (approximately on one order); but they have a number of advantages. Firstly; at low dose rate studied detectors had much lesser time of response, than CdS. Secondly; saturation sings up to dose rates in 100R/min and the fatigue effect are absent in our detectors.

So, X-rays detectors on the base of TlInSe$_2$ is quick-response, miniature; uncooled (works at the room temperature) crystal detector with the stable and reproducing dosimetric characteristics.

Preliminary researches showed, that doping of TlInSe$_2$ crystals in some cases leads to the considerable improvement of operating characteristics of roentgen-detectors. Thus the task of the gain in the roentgen-detectors sensitivity by means of intercalation of single crystals TlInSe$_2$ is put in the present work.

The sampler TlInSe$_2$ were intercalated with lithium ions by the method of pulling electric field. The intercalation degree j.t. (j is the current density, t is the intercalated time) amounted to 15-20 Coulomb·cm^{-2}.

Roentgendosimetric characteristics of the pure and lithium-intercalated TlInSe$_2$ single crystals were investigated. Electric field was applied along [110] -direction and amounted to 10 Volts. Compared to pure single crystal, this intercalated single crystal is more sensitive to roentgen radiation. The ratio of coefficients of roentgenocurrent (K) after and prior to intercalation to 2÷4.

Dependence of roentgen current on dose rate at various X-radiation hardnesses (from 25 to 50 keV) was interesting in TlInSe$_2$ and TlInSe$_2$ <Li$^+$> single crystals. It was shown that dependence of roentgenocurrent ΔJ_r on radiation dose E is described as:

$$\Delta J_r \sim E^\alpha$$

where α=0.5÷1.1 at 25÷50keV for pure TlInSe$_2$ and α=0.65÷1.5 for lithium-intercalated single crystal.

The operation by the roentgendosimetric parameters of the studied ternary single crystals due to intercalation gives perspective for the use of these objects as sensitive roentgendetectors.

[1] *K. Okazaki, K. Tanaka, J. Matsuno, A. Fujimori, L.F.Matthesis, E.M. Kerimova, N. Mamedov.* Angle-resolved photoemission and band -structure results for linear chain TlGaTe$_2$. Physical Review B, 2001, vol.64. p.045210-1045210-5.

[2] *Z. Seidov, H.A. Krug von Nidda, J. Hemberger, A. Loidl, G. Sultanov, E. Kerimova, A. Panfilov.* Magnetic susceptibility and ESR study of the covalent-chain antiferromagnets TlFeS$_2$ and TlFeSe$_2$. Physical Review B, 2001, v.65, p.014433-1-7.

[3] *G.D. Guseinov, S.N. Mustafaeva, E.F. Bagirzade, E.G.Abdullaev, S.G. Guseinov.* Photoelectrical properties of lithium-intercalated TlInSe$_2$ chain crystals. Solid State Communications. 1985. v.55. №11. p.991-992.

[4] *G.D. Guseinov, S.N. Mustafaeva, E.G. Abdullaev, et. al.* Photosensitive material. Patent of USSR №1289331. 1986.

[5] *G.D. Guseinov, S.N. Mustafaeva, R.G. Guseinova, E.G.Abdullaev.* The nature of electric memory in lithium-intercalated chain-structure TlInSe$_2$ single crystals. Phys. Status Solidi (a) 1986. v.95. p. k159-k164.

[6] *G.D. Guseinov, R.G. Guseinova, S.N. Mustafaeva, N.Z.Gasanov, S.G. Guseinov, E.G. Abdullaev.* Relaxation of electron-ionic processes in intercalated layer and chain crystals of A^{III}B^{III}C$_2^{VI}$ -type semiconductors./ Physics Letter A, 1986, v.116, №6, p.281-283.

[7] S.N. Mustafaeva, V.A. Ramazanzade, M.M. Asadov Influence of intercalation on electrical and photoelectrical properties of ternary chain and layer semiconductors, Materials Chemistry and Physics, 1995, v.40, №2, p. 142-145.

[8] *E.M. Kerimova, S.N. Mustafaeva, D.A. Guseinova et.al.* The influence of hydrostatic pressure on the electrical conductivity and optical properties of chain-layered TlInSe$_2$ TlInSe$_2$-TlInS$_2$ solid solutions. Phys. Stat. Sol. (a). 2000. v. 179. p.199-203.

[9] *A.Z. Abasova, E.M. Kerimova, G.A. Muradova*, Pashaev A.M. Ionizing irradiation of photoresistors and diode structure on the base of TlGaSe$_2$ and TlInSe$_2$ single crystals. Inst. Phys. Conf. Ser. №152: Section H: single crystal and thin film devices. 1998. 1OP, published LTD. P. 983-988.

[10] *M.M. Asadov, S.N. Mustafaeva*. The method of production of tallium chalcogenides. Patent of USSR №1464518. 1988.

С.Н. Мустафаева, Э.М. Керимова, М.М. Асадов, Р.Н. Керимов

РЕНГЕНОДЕТЕКТОРЫ НА ОСНОВЕ TlInSe$_2$ <Li$^+$>

На основе полупроводниковых кристаллов TlInSe$_2$ sozdanı высокочувствительные рентгенодетекторы. Дозовая чувствительность созданных рентгенодетекторов составляла

$1.1 \cdot 10^{-10} \div 5.9 \cdot 10^{-9}$ А/Р·мин·В при дозах облучения Е = 0.75÷78.0 Р/мин. Энергия рентгеновского излучения составляла 10÷50 кэВ. Инерционность детекторов составляла 3÷5 с, а рабочее напряжение 10÷20 В. Отношение коэффициентов рентгеночувствительности после и до интеркалирования литием составляло 2÷4. Показано, что зависимость рентгенотока ΔI_r от дозы облучения Е носила степенной характер: $\Delta I_r \sim E^{\alpha}$, где α=0.5÷1.1 при 25÷50 кэВ для TlInSe$_2$ и α= 0.65÷1.5 для TlInSe$_2$<Li$^+$>.

S.N. Mustafaeva, E.M. Kərimova, M.M. Asadov, R.N. Kərimov

TlInSe$_2$ <Li$^+$> ƏSASINDA RENTQENDETEKTORLAR

Yarımkeçiriji TlInSe$_2$ kristalları əsasında yüksək həsaslığa malik olan rentgen detektorları hazırlanmışdır. Şüalanma dozası E=0.75÷78.0 R/dəq olduqda rentgendetektorların doza həsaslığı $1.1 \cdot 10^{-10} \div 5.9 \cdot 10^{-9}$ A/R·dəq·V olmuşdur. Rentgen şüalanmasının enercisi 10÷50 keV-dir. Bu detektorların ətalətliliyi 3÷5 s, işçi gərginliyi isə 10÷20 V – dir. TlInSe$_2$ kristallarının litium ionları ilə interkalyasiyasından sonra və əvvəl rentgen həssaslığının əmsallarının nisbəti 2÷4 olmuşdur. Təyin edilmişdir ki, rentgen jərəyanının ΔI_r şüalanma dozasından E asıllığı üstlü funksiya ilə xarakterizə olunur :

$\Delta I_r \sim E^{\alpha}$, burada TlInSe$_2$ üçün 25÷50 kgV- də α =0.5÷1.1 və TlInSe$_2$ <Li$^+$> üçün isə α =0.65÷1.5 olmuşdur.

Porous Silicon-Based Hydrogen Detectors

T.D. Dzhafarov[1,2], C. Oruc[1], S. Aydin[1], E.Cingi[1], D.Oren[1]

[1]Department of Physics, Yildiz Technical University, Davutpasa, 34210 Istanbul, Turkey
[2]Institute of Physics, Azerbaijan National Academy of Sciences, 370143 Baku, Azerbaijan

Abstract In this work the humidity-voltaic effect, i.e. generation of open-circuit voltage (V_{oc}) in metal (Cu, Ag, Au)-Porous silicon structures under humid exposition is discovered. Besides, influence of porosity of free-standing PS and humidity on optical and electrical properties of films were investigated.

Relatively to the optical and electrical properties of free-standing PS films the next main results were received. (a) The rising of film porosity (from 30% to 90%) results in both the increase of band gap of PS films (from 1.4 to 1.9 eV) and resistivity (from 2×10^4 to 4×10^4 Ω cm), (b) The resistivity of films along pores approximately two tenth as large as than that in across direction, (c) The band gap of films in humid ambient in the range of 55-95 %RH increases from 1.6 to 1.8 eV. The observed porosity-stimulated and humidity-stimulated changes optical and electrical characteristics were interpreted on the base model including the quantum confinement of charge carries in the PS microcrystallites and chemical activity of PS surfaces.

Formation of open-circuit voltage up to 450mV, 280mV and 200mV for Au-PS, Cu-PS and Ag-PS structures under humidity or hydrogen exposition is observed. It is suggested that the humidity-voltaic effect, i.e. generation of V_{oc} in humid atmosphere is mainly caused by splitting of water and hydrogen molecules on surfaces of Ag, Cu or Au catalyst and hydrogen diffusion from humid ambient to metal-PS interface. Approximately the linear increase of V_{oc} depending on the average porosity of PS films is established. Generation of V_{oc} (up to 550 mV) have been also observed on dipping of Au-PS structures in different hydrogen-containing solutions (ethanol, benzine, sodium tetraborate pentahydrate etc.). These results open the perspective for using of metal-PS structures as both gas (hydrogen) detectors and mini hydrogen cells.

1. Introduction

The discovery of visible photoluminescence from porous silicon (PS) has attracted considerable interest due to its potential application in the development of silicon-based optoelectronic devices. However, the origin of photoluminescence in PS is still controversial. A few models are suggested for explanation mechanism of photoluminescence. According model proposed by Canham [1] radiative recombination of electron-hole pairs occurs within nanometer silicon wires and their energy gaps become larger than that of bulk Si (quantum confinement effect). This model modified by Koch et al. [2] suggests that electron-hole pairs are photo-excided in nanometer silicon particles and radiatively recombined via Si intrinsic surface states. Another model [3] suggests that luminescence from PS was caused by some special luminescence materials, such as SiH_x complexes, polisilanes, or SiO_2 rather than an intrinsic property of nanometer Si. A third model believes that excitation of charge carriers occurs in nanometer silicon particles and the photoexcitated carriers transfer into the luminescence centers (defects and impurities) in the surrounding SiO_x layers [4].

In general, main models proposed for explaining the origin and mechanism of visible photoluminescence in PS can be divided on three groups. The first group comprises an intrinsic effects in nanometer Si, whereas the second group of model is related with processes proceeding an external surfaces of nanocrystals, i.e. on surfaces of PS. These processes are determined with composition and structure of materials on PS surfaces. The third group combines models of the first and second group. The structure of PS is characterised by an extremely large surface aria to volume ratio (up to $10^3 m^2 cm^{-3}$). It is known that surface bonds, in particular Si-H and Si-O bonds play an important role in regulating of

electrical, optical, luminescence and gas sensing propertiesof PS. These properties of PS are very sensitive to humidity of ambient. Investigations of optical properties of the free-standing PS films can promote understanding mechanism of photoluminescence. The optical and electrical characteristics of free-standing films depending on porosity are rarely considered [5]. Xu et al. [6] have measured evolution of the optical absorption of free-standing PS films during thermal oxidation in air and decreasing of the gap have explained due to the Si-O bond formation. Sagnes et al. [7] have measured the absorption spectra of the free-standing PS films with porosities in a range of 45-79 % and observed a blue-shift of curves with an increase of the porosity. As far as our knowledge goes, data on effect of humidity on optical absorption spectra of free-standing PS films are absent in literature.

It is noting that the gaseous environment exerts influence on electrical and photoluminescence characteristics of PS and metal-PS structures. The composition and optical property changes of PS caused by hydrogen and oxygen diffusion are considered [8,11]. Numerous gas and humidity sensors based on PS have been presented [12,13]. Humidity-stimulated changes of I-V characteristics and generation of open-circuit voltage in Ag-PS and Cu-PS Schottky-type structures have been observed [14,15]. These changes are attributed to penetration of hydrogen from humid ambient and diffusion via porous silicon surfaces to metal-PS interfaces. It will be noted that the response and recovery time of PS based gas sensors is limited by diffusion coefficient of gas atoms and molecules along inner PS surfaces. Therefore knowledge of diffusion parameters of atoms influencing on gas-sensing characteristics of PS is very important for fabrication of gas sensors with the low response and recovery times.

In this work the optical and electrical properties of free-standing PS films in dependency on porosity and humid exposition were investigated. Humidity (hydrogen)-stimulated open-circuit voltage generation in metal (Au, Ag, Cu)-PS structures is discovered and mechanism of this phenomenon was discussed. Besides data on diffusion coefficient of hydrogen on PS surfaces, determining the response characteristics of gas sensors were determined.

2. Experimental Procedure

PS films were formed by anodization of (111)-oriented n-type silicon wafers (0.01 Ω.cm) in HF-ethanol solution at constant current density under the white light illumination. The PS films were then detached from the Si substrates by electropolishing [8]. The free-standing PS films were characterized by porosity, thickness, resistivity and optical measurements. Free-standing PS films of thickness 5-20 μm and porosities of P= 30-90 % were analysed in this work.

The transmission spectra of free-standing PS films were measured from 300 to 1000 nm at room temperature by using 'UV/VIS Lambda 2S' (Perkin Elmer) spectrometer. Resistivity measurements were performed along and across of pores. Optical and electrical measurements of PS films were examined on the normal room conditions (T=300 K, 40 %RH) and in the measuring cell at different ambient humiditiy (water vapour) in the range of 40-95 %RH. The relative humidity (RH) in cell was measured by using 'Extech-444701' Hygro-Thermometer.

This investigation focuses on the analysis the transmission spectra and resistivity in dependency on both porosity of PS films (for normal room conditions) and relative humidity of ambient (for PS films with given porosity). Time-dependence transmission spectra and resistivity under humidity exposition in cell were measured after succsessive 5- or 10-min cycles of humid exposition.

The absorption coefficient (α) is deduced from transmission spectra by solving α in the equation [8]

$$T = \frac{(1-R)^2 \exp(-\alpha d)}{1 - R^2 \exp(-2\alpha d)}$$

(1)

Here R is reflectivity and d is the effective sample thickness.

The next values $n=1.42$ and $R=0.03$ were recieved for the refractive index and the reflectivity from experimentally measured the interference spectrum of free-standing PS film. This value of the refractive index is close to $n=1.33$ measured in [7].

Metal-PS structures and Au-PS-Si structures have been fabricated by evaporation of Au, Ag or Cu film onto the PS surface at room temperature using electron-beam evaporation technique. The thickness of metal film (80-160 nm) was measured during evaporation by using 'Deposition Controller' (Inficon, Leybold). In or In/Ga alloy was used as ohmic contact to PS layers . The current-voltage characteristics, humid-stimulated voltage generation in metal-PS structures were examined in the measuring cell at different ambient humidity (water vapour, hydrogen or oxygen). Humidity-stimulated voltage (V_{oc}) between the open contacts to metal film and PS under gas exposition (moisture, hydrogen or oxygen) or on dipping of metal-PS structure in hydrogen-containing solution (ethanol, benzine, sodium tetraborate pentahydrate etc) is directly measured using 'Thurlby' 1503 Digital Multimeter.

The photosensitive properties of metal-PS structures were analysed by measurements of current-voltage characteristics in dark, day-light and under illumination by a tungsten-halogen lamp (150 mW/cm^2). All investigated structures showed very slight photosensitiveness. Value of the open-circuit photovoltage in day-light and under tungsten-halogen lamp illumination was about of 1-3 mV. Therefore most of humidity-sensitive measurements have been performed at day-light illumination.

3. Results and Discussion

Measuring of transmission spectra at room conditions (T=300 K, 40 %RH) was carried out for free-standing PS films with porosity of 46%. Fig. 1 shows the absorption coefficient spectrum for PS film with thickness of 8 μm and porosity of 46%. Analysis of measured curves of absorption coefficient (α) versus photon energy (hν) for PS films with porosity in range of 30-90 % showed that spectra displayed behavior expected for the direct semiconductors

$$\alpha^2(h\nu)^2 = A(h\nu - E_g) \qquad (2)$$

Here E_g is energy gap and A is constant. Absorption coefficient curves for PS films discovered a continuous blue-shift with increase of porosity in range of 30-90 %.
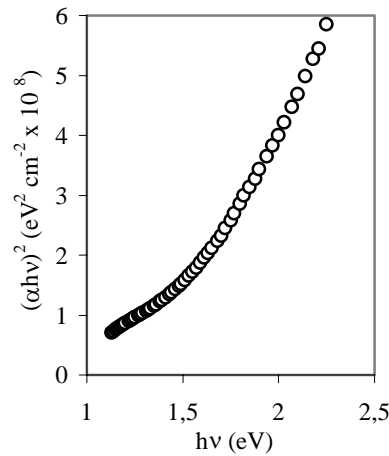
Figure 1. Optical absorption spectrum of PS film of P= 46 % porosity (40 %RH).
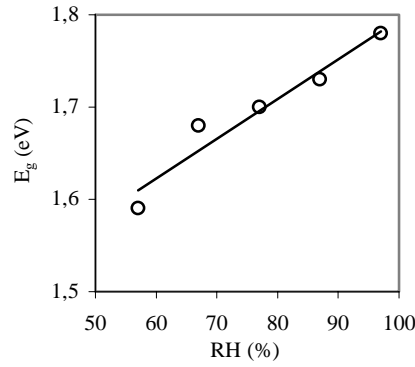
Figure 2. Energy gap of PS films in dependency on porosity (40 %RH).

Fig. 2 shows the energy gap in dependency on porosity of the free-standing PS films, determined from extrapolution of high energy part of (α - hν) spectra. Near linear increase of band gap from 1.4 to 1.9 eV with rising of porosity of PS films in the range of 30-90 % is observed.
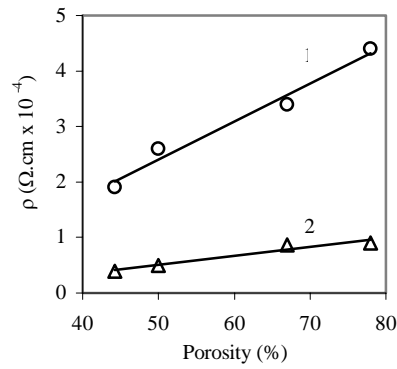
Figure 3. Resistivity of PS films (1) along and (2) across of pores (40 %RH).

Fig. 3 presents resistivity along and across of pores for free-standing PS films with porosity in a range of 45-78 %. Increase of resistivity with increase of porosity is observed for both directions. The data on resistivity - porosity dependence (Fig. 3) correlate with increase of energy band gap of PS films with rising in porosity (Fig. 2). Lower low values of resistivity across of pores can be related with presence of low-porosity layer along PS film - Si substrate interface.
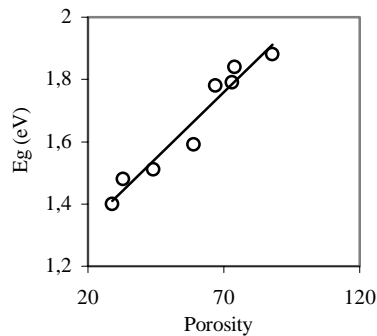
Figure 4. Energy gap of PS film in dependency on relative humidity (P=68 %).

Fig. 4 presents the energy band gap of PS films (with porosity of 68%) in dependency on relative humidity. These data were received from optical transmission measurings carried out after exposition of PS film in humid ambient for 30 min. As it is seen from Fig. 6, E_g – RH dependence, similarly energy gap versus relative humidity curve (Fig. 2), shows nearly linear increasing of energy gap.
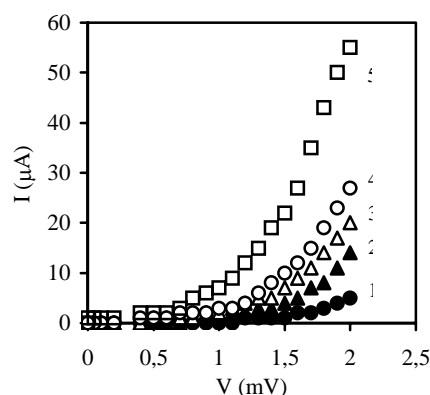
Figure 5. Reverse I-V characteristics of Au-PS structure in humid ambient (1) 45 %RH,
(2) 70 % RH, (3) 83 % RH, (4) 90 %RH and (5) 99 % R H (T=300K).

Data on Fig. 2 and Fig. 4 concerning increase of the energy gap in dependency on porosity of PS films and humidity respectively, can be explained by a model including the quantum confinement of carriers in the PS microcrystallites and the formation of the Si-H bonds on pore surfaces in humid atmosphere.
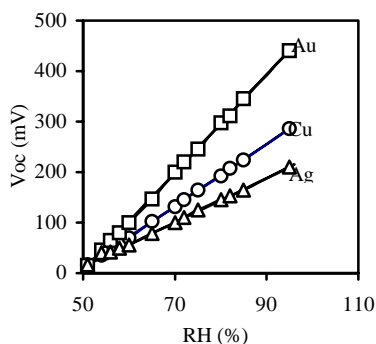
Figure 6. The open-circuit voltage - relative humidity dependence for Au-PS, Cu-PS and
Ag-PS structures (T=300K).

Below it is presented data on humidity-sensitive properties of metal-PS structures.
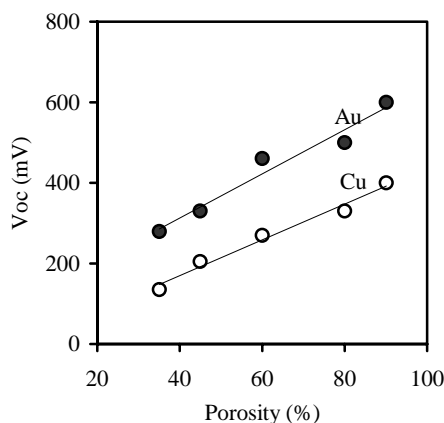
Figure 7. The open-circuit voltage versus the porosity of porous silicon (90%RH).

The typical reverse I-V characteristics of Au-PS structure in air ambient at 45 %RH, 70 %RH, 83 %RH, 90 %RH and 99 %RH at room temperature are presented in Fig. 5. Increase of reverse currents with rising of the relative humidity have been observed. The value of the current at 90 %RH (for 2V) increases in comparison with that at 45 %RH (for 2V) by factor 12.
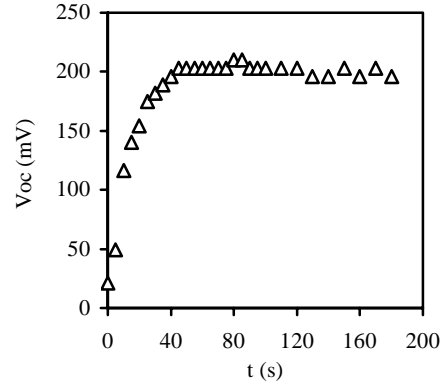
Figure 8. The open-circuit voltage in dependency on duration of exposition in humid ambient (70 % RH) for Au-PS structure (323 K).

The humidity-voltaic effect i.e. generation of a voltage between contacts to metal film and PS layer under humidity exposition is discovered for metal-PS structures. Fig. 6 illustrates the open-circuit voltage in dependency on the relative humidity for one of such Au-PS structures. It is seen that the V_{oc} approximately linearly increases from 15 mV to 450 mV with rise of the relative humidity from 51 %RH to 95 %RH. The humidity-sensitivity of Au-PS structure estimated from curve of Fig. 6 is about 10 mV/(%RH). Data on formation of V_{oc} in humid for Cu-PS and Ag-PS structures have been also presented in Fig. 6 [14,15]. Increasing of V_{oc} for Ag-PS, Cu-PS and Au-PS Schottky-type junctions (200, 280 and 450 mV respectively) correlates with values of work function of Ag, Cu and Au (4.4, 4.6 and 4.8 eV respectively).

Figure 9. The temperature dependence of the effective diffusion coefficient of hydrogen in PS (for 70 %RH).

Formation of the open-circuit voltage in Au-PS structures is not observed under pure oxygen gas exposition. Contrary to oxygen, exposition under pure hydrogen gas (about of 0.5 atm) results in generation of open-circuit voltage (up to 490 mV). These results suggest that the humidity-stimulated

formation of the open-circuit voltage is mainly caused by hydrogen component of water molecules. It will be noted that generation of the open-circuit voltage have been also observed on dipping of Au-PS junctions in different hydrogen-containing solutions (440 mV for ethanol (C_2H_5OH), 500 mV for benzine ($C_5H_{12} – C_{16}H_{34}$), 550mV for sodium tetraborate pentahydrate ($Na_2B_4O_7\ 5H_2O$) etc).

Data on generation of open-circuit voltage in Au-PS and Cu-PS structures with different porosity in humid ambient (90%RH) were presented in Fig. 7. For both structures nearly linear rising of V_{oc} (up to 600 mV for Au-PS structure) with increase of porosity was observed. Herewith values of V_{oc} for Au-PS structure are more than those for Cu-PS structures.

It will be noted that the response time i.e. duration of reaching of the most value of V_{oc} after placing of Au-PS structure in humid atmosphere depends on temperature. For example, data on influence of exposition duration in humid air atmosphere (70 %RH, T=323 K) on the open-circuit voltage of Au-PS structure are presented in Fig. 8. An increase of temperature from 323K to 353K is accompanied by decrease of response time of Au-PS structure from about 2 min to 40 s.

For Au-PS structures just as Ag-PS and Cu-PS structures [14,15] we suppose the next model of humidity-stimulated diffusion of hydrogen and generation of the open-circuit voltage. Before discussion of V_{oc} generation mechanism we consider briefly the peculiarities of Au-PS structure forming by electron-beam evaporation of Au on PS layer. Gold atoms deposit primarily on external surface of PS layer at the initial stage of evaporation. Herewith the high-speed gold atoms penetrate also in pores with deposition predominantly onto bottom of pores and formation the numerous inner Au-PS junctions [16]. Then, as Au film thickness on external surface of PS layer increases, pores are fully closed by Au film. For this two-step model of formation of Au-PS structure, Au film on the external surface of PS layer plays role of catalytic membrane layer which splits water and hydrogen molecules and transmits small hydrogen atoms or ions (protons). If hydrogen is accepted as a donor impurity in PS [17], then adsorption and dissolution of the water molecules on surface of Au film due to interaction with the Au surface, subsequent penetration of hydrogen ions (protons) through Au film, diffusion via inner pore surfaces and reaching the Au-PS interfaces is accompanied by separation of charges and origin of the open-circuit voltage across Au-PS interfaces.

Data on V_{oc} - RH dependence (Fig. 6) shows that value of the open-circuit voltage is determined by quantity of water molecules in air ambient i.e. by quantity of hydrogen. Other than for given RH the velocity of V_{oc} rising on Au-PS Schottky-type barriers (Fig. 9) is determined by diffusion coefficient of hydrogen via inner porous silicon surfaces. On fulfilling these conditions the effective diffusion coefficient of hydrogen on PS surfaces may be estimated from V_{oc} - t curve [9,15]. Dat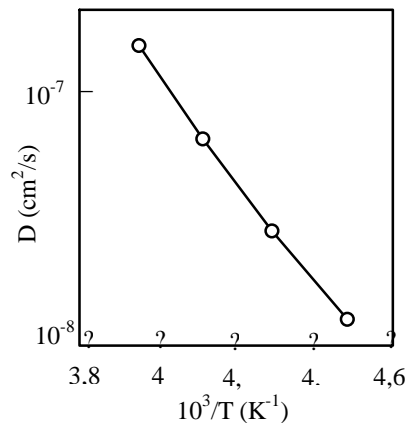a on the effective diffusion coefficient of hydrogen along PS surfaces for temperature range of 323-353 K for 70 %RH were presented in Fig.9. The temperature dependence of the effective diffusion coefficient of hydrogen on the PS surfaces is described as

$$D = 1.3 x 10^{-2} \exp\left(-\frac{0.25}{kT} \right) \qquad (3)$$

One can conclude that the activation energy (0.25 eV) finding in this work is rather related with the energy necessary for diffusion of hydrogen via a net of Si-H bonds on PS surfaces. There is reason to beleive that hydrogen in Si-H bonds is not electrically active state. On splitting of Si-H bonds, hydrogen migrates across PS surfaces as H^+ ions (protons) with further trapping in Si-H bonds. Herewith the diffusion process of hydrogen across PS surfaces consists of series of successive three-step acts (splitting of Si-H bonds, migration of hydrogen ions on PS surfaces and trapping of hydrogen by Si-H bonds). To put the other way round, activation energy determined in this work is rather related with the energy necessary for splitting of Si-H bonds and migration of hydrogen across PS surfaces.

4. Conclusion

It is shown that the band gap of free-standing PS films increases from 1.2 to 1.9 eV with rising porosity (from 30 to 90%), that is attiributed to quantum effect arisen at special confinement of charge carries in nanometers-size crystallites and chemical activity of PS surfaces.

The generation of the open-circuit voltage in metal-PS interfaces in humid atmosphere is discovered. Comparative data on values of open-circuit voltages forming in Au-PS (450mV), Cu-PS (280mV) and Ag-PS (200mV) Schottky-type junctions correlate with work functions of Au, Cu and Ag metals. The humidity sensivity of Au-PS structures is about 10mV/(%RH). It is supposed that humidity-stimulated generation of V_{oc} is mainly caused by hydrogen diffusion from metal surface to metal-PS interface.

The effective diffusion coefficient of hydrogen via pore surfaces of PS (for 70%RH) in the range of 323-353 K increases from 2.9×10^{-8} to 1.3×10^{-7} cm^2/s. Generation of V_{oc} (up to 550 mV) have been also observed on dipping of Au-PS structures in different hydrogen-containing solutions (ethanol, benzine, sodium tetraborate pentahydrate etc). Data of this work indicate on possibility for using metal-PS structures as both gas (hydrogen) sensors and mini hydrogen cells.

Acnowledgement

References
[1] L. T. Canham, Appl. Phys. Lett., 57 (1990) 1046.
[2] F. Koch, V. Petrova, T. Muschik, A. Nikolov, V. Gavrilenko, *Mater. Res. Soc. Symp.Proc.*, 283 (1993) 197.
[3] M. S. Brandt, H. D. Fuchs, M. Stutzman, J. Weber, M. Cardona, *Solid State Commun.*, 81 (1992) 307.
[4] G. G. Qin and Y. Q. Jie, *Solid State Commun.*, 86 (1993) 559.
[5] O. Bisi, S. Ossicini, L. Pavesi, *Surface Science Reports*, 38 (2000) 1-126.
[6] D. Xu, G. Guo, L. Gui, Y. Tang, G. Qin, *Pure Appl. Chem.*, 72 (2000) 237.
[7] I. Sagnes, A. Halimaoui, G. Vincent, P. A. Badoz, *Appl. Phys. Lett.*, 62 (1993) 1155.
[8] T. D. Dzhafarov, B. Can, *J. Mater. Sci. Lett.*, 19 (2000) 287.
[9] G. B. Abdullaev, T. D. Dzhafarov, *Atomic Diffusion in Semiconductor Structures*, (New York: Harwood Academic Publishers) 1987.
[10] R. Rerino in: L. Canham (Ed.), *Properties of Porous Silicon* (London: INSPEC) 1998.
[11] G.Gracium, S. Bercus, M. Flueraru, L. Matica , C. Dafinci, V. Grecu , *J. Molecular Structure* 410/4111 (1997) 129.
[12] Z.C. Feng, R. Tsu (Eds), *Porous Silicon* (Singapore: World Scientific)1994.
[13] A. Foucaran, F. Pascal-Delannay, A. Grani, A. Sackda, P. Combette, A. Boyer, *Thin Sol. Films,* 297 (1997) 317.
[14] T.D. Dzhafarov, B. Can Omur, Z.A. Allahverdiev, *Surf. Sci.* 482-485 (2001) 1141.
[15] T.D. Dzhafarov, C. Oruc, B. Can Omur, Z.A.Allahverdiev, *J. Phys. D: Appl. Phys.* 35 (2002) 3122.
[16] C. Baratto, G. Sberveglieri, E. Comini, G. Faglia, *Sensors and Actuators,* B68 (2000) 74.
[17] D.N. Goryachv, L.V. Belyakov, O.M. Sreseli, G. Polisskii, *Semicond.* 32 (1998) 529.

Модель виртуального кристалла в применении к слоистым полупроводникам типа TlGaSe$_2$.

С.Г.Абдуллаева[*] *, Т.Г. Мамедов*[*] *, Р.А. Сулейманов*[**]

[*] *Институт Физики НАН Азербайджана AZ-1143, Баку, пр. Г.Джавида, 33*

[**]*Бакинский Государственный Университет*

1. Введение

Известно что, в ряде случаев образование твердых растворов двух изоструктурных и изоэлектронных соединений приводит к таким же изменением в зонной структуре каждой из компонент, что и соответствующее давление. Под «соответствующим» подразумевается такое давление, которое приводит к таким же изменением параметров элементарной ячейки, что и изменение состава. Поскольку твердый раствор, строго говоря, не является просто «деформированным» идеальным кристаллом, описанный выше подход в литературе носит название модели виртуального кристалла [1].

Если применимость такой модели к кристаллам кубической структуры кажется вполне оправданной, то в случае кристаллов слоистой структуры справедливость модели виртуального кристалла требует специальных доказательств. В то же время, результаты влияния двух типов внешнего воздействия-давления и изменения состава могут существенно дополнить друг друга и дать новую информацию об особенностях зонной структуры.

Слоистые полупроводники TlGaSe$_2$, TlGaS$_2$ и TlInS$_2$, являющиеся объектами исследований настоящей работы, кроме сложной кристаллической структуры обладают еще одной важной особенностью: согласно имеющимся данным [2-10], по крайней мере, в двух из них, TlGaSe$_2$ и TlInS$_2$ надежно идентифицированы структурные фазовые переходы (ФП), происходящие как с температурой, так и с давлением. Последнее затрудняет интерпретацию экспериментальных данных в рамках проверки справедливости модели виртуального кристалла в случае полупроводников типа TlGaSe$_2$. Ниже будет показано, что анализ всей совокупности имеющих данных о влиянии давления, температуры и изменения состава в твердых растворах TlGaS$_{2x}$Se$_{2(1-x)}$ позволяет утверждать, что и в случае кристаллов изучаемого типа, несмотря на сложность строения элементарной ячейки и происходящие под давлением и с температурой ФП модель виртуального кристалла остается справедливой.

2. Поведение ширины запрещенной зоны в твердых растворах TlGaS$_{2x}$Se$_{2(1-x)}$

Полупроводники TlGaSe$_2$, TlGaS$_2$ и TlInS$_2$ кристаллизуются в слоистой структуре и, согласно имеющимся данным имеют моноклинную решетку при комнатной температуре и атмосферном давлении [4,11-13]. Параметры элементарной ячейки указанных кристаллов таковы (см. напр. обзор 4), что их можно рассматривать как кристаллы квазитетрогональной сингонии. Более того, из-за отсутствия анизотропии ряда физических свойств в плоскости слоев эти кристаллы можно рассматривать и как кристаллы гексагональной сингонии [14,15]. Наибольшее количество работ было посвящено изучению ФП в кристаллах указанного семейства. По крайней мере, в случае кристаллов TlGaSe$_2$ и TlInS$_2$ ФП с температурой надежно идентифицированы [2,3]: при T_i=216K в TlInS$_2$ и T_i=120K в TlGaSe$_2$ происходит ФП в несоизмеримую фазу, а затем при дальнейшем понижении температуры в соразмерную сегнетоэлектрическую фазу (T_c=202K в TlInS$_2$ и T_i=107K в TlGaSe$_2$). Имеющиеся исследования [4-10] свидетельствуют, что и с ростом гидростатического давления в кристаллах типа TlGaSe$_2$ возможны ФП.
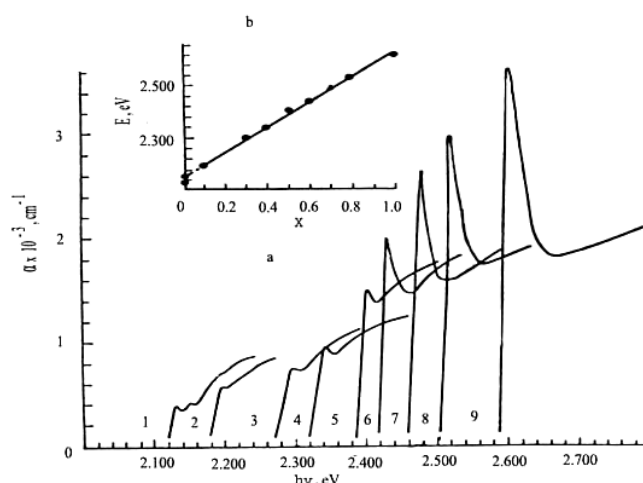
Рис.1. a-спектры поглощения TlGaS$_{2x}$Se$_{2(1-x)}$, зарегистрированные при падении неполяризованного света перпендикулярно плоскости слоя при T=6K. x: 1-0; 2-0,1; 3-0,3; 4-0,4;5-0,5; 6-0,6; 7-0,7; 8-0,8; 9-1; б-зависимость энергетического положения прямой экситонной зоны кристаллов TlGaS$_{2x}$Se$_{2(1-x)}$ от состава x при T=6K [16].
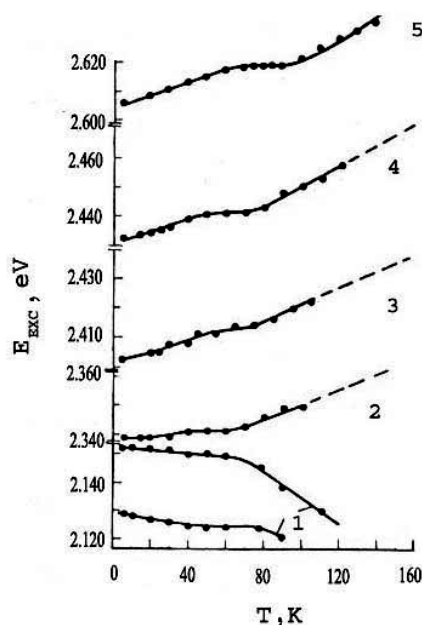
Рис.2. Температурная зависимость энергетического положения линий поглощения прямых экситонов в кристаллах TlGaS$_{2x}$Se$_{2(1-x)}$. x: 1-0; 2-0,4; 3-0,5; 4-0,6; 5-1.[16]

TlGaSe$_2$ и TlGaS$_2$ образуют непрерывный ряд твердых растворов и на рис.1a показаны спектры экситонного поглощения, зарегистрированные при 6K в кристаллах   TlGaS$_{2x}$Se$_{2(1-x)}$ с 0≤x≤1. В TlGaSe$_2$ пики поглощения соответствуют экситонным состояниям, связанным с двумя зонами. В TlGaS$_{2x}$Se$_{2(1-x)}$ с x≥0,1 наблюдается лишь один ярко выраженный пик поглощения, соответствующий образованию прямых экситонов [16]. Из рис.1б видно, что зависимость от состава энергетических положений экситонных состояний, E$_{эхс}$(x), является с большой точностью линейной. Подчеркнем, что описанные выше пики поглощения соответствуют прямым экситонным переходам. В [16] предполагается, что природа переходов в TlGaS$_{2x}$Se$_{2(1-x)}$ с x<0,1 и 0,1≤x≤1 можеть быт различной. Этот вывод основывается на различном поведении с температурой энергетических положений экситонных состояний в кристаллах TlGaS$_{2x}$Se$_{2(1-x)}$ с x<0,1 с одной стороны и с x≥0,1 с другой (рис.2). Мы покажем в разделе 4, что различное поведение E$_{эхс}$(T) в кристаллах TlGaS$_{2x}$Se$_{2(1-x)}$ с x<0,1 не связана с различной природой экситонных состояний, и будем

полагать, что зависимости $E_{эхс}(T)$, показанные на рис.2, соответствуют экситонным состояниям единой природы.

3. Влияние давления на зонную структуру кристаллов TlGaSe₂.
Модель виртуального кристалла

Результаты влияния гидростатического давления на край оптического поглощения кристаллов TlGaSe₂, TlGaS₂ и TlInS₂ при комнатной температуре приведены на рис.3. Как видно из рис.3 поведение барического коэффициента dE_g/dP при давлениях P<0,5 ГПА практически одинаково для всех трех кристаллов. С повышением давления поведение dEg/dP меняется и становится существенно различным в разных кристаллах. Мы не будем рассматривать поведение dE_g/dP при больших давлениях (этот вопрос подробно рассмотрен в [17,18]) и обсудим природу изменений ширин запрещенных зон кристаллов типе TlGaSe₂ при малых (P<0,5 ГПА) давлениях. Отрицательность барического коэффициента, описывающего поведение ширины запрещенной зоны, свойственно для всех кристаллов со слоистой структурой. Это связано, по-видимому, с тем, что наиболее важные особенности формирования зонной структуры являются общими для всех слоистых кристаллов.
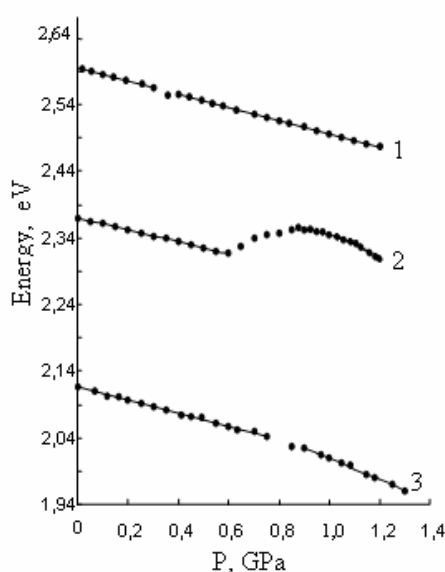
Рис.3. Зависимости энергетических зон от давления, определенные из поведения спектров поглощения кристаллов TlGaS₂ (1), TlInS₂ (2) и TlGaSe₂ (3) с давлением при T=300К [6].

Эти особенности заключаются в том, что потолок валентной зоны и дно зоны проводимости слоистого полупроводника расщепляются при учете взаимодействия между слоями [19], и приложение гидростатического давления ведет к росту такого расщепления и к итоговому уменьшению E_g. В то же время, сжатие отдельных слоев, ведет к росту E_g. По указанной причине слоистые кристаллы описываются деформационными потенциалами $D_\parallel$ и $D_\perp$ имеющими разные знаки. В [19] обобщены результаты влияния давления на зонную структуру многих слоистых кристаллов и показано, что деформационные эффекты в них можно описать на основе простой модели, согласно которой изменение ширины запрещенной зоны можно описать с помощью простого выражение: $\Delta E_g = U_\perp D_\perp + 2U_\parallel D_\parallel$.

В [17,18,20] определены величины $D_\parallel$ и $D_\perp$ для кристаллов типа TlGaSe₂: $D_\perp$ =11.9 эВ, $D_\parallel$ =-7.3 эВ Воспользовавшись значениями деформационных потенциалов и рассматривая изменение параметров элементарной ячейки при переходе от TlGaSe₂ к TlGaSn₂ (см.табл.) как эффективное сжатие TlGaSe₂ , можно сделать вывод, что такое "сжатие" TlGaSe₂ должно вести к росту E_g на величину ~0,4эВ, что приводит к величине очень близкой к экспериментально определенной. Таким образом, модель виртуального кристалла оказывается справедливой для системы твердых растворов TlGaS₂ₓSe₂₍₁₋ₓ₎. Связано это, по-видимому, с тем, что, как и в кристаллах типа A_3B_6 , замена анионной подсистемы (GaSₓSe₁₋ₓ) приводить к таким изменениям параметров элементарной ячейки, которые можно рассматривать как макроскопическую деформацию

кристаллов как целого. Подчеркнем, что такой подход оказывается неоправданным в случае замены катионной подсистемы в слоистых кристаллах группы A_3B_6 [21].
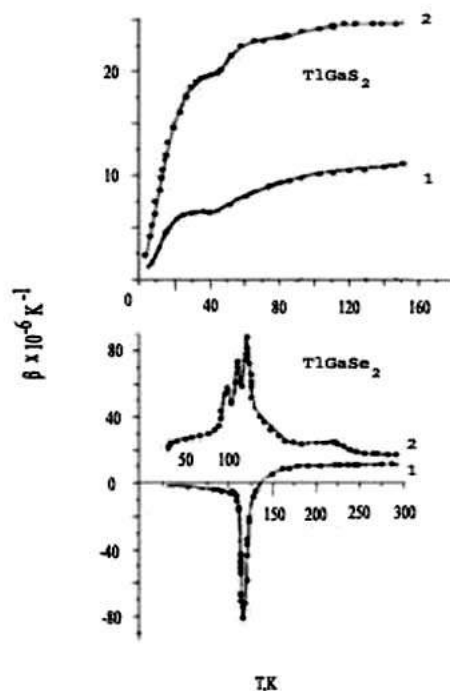
Рис.4. Температурные зависимости коэффициентов теплового расширения для кристаллов $TlGaS_2$ и $TlGaSe_2$ в направлениях: параллельном (1) и перпендикулярном (2) плоскости слоев [22,23]
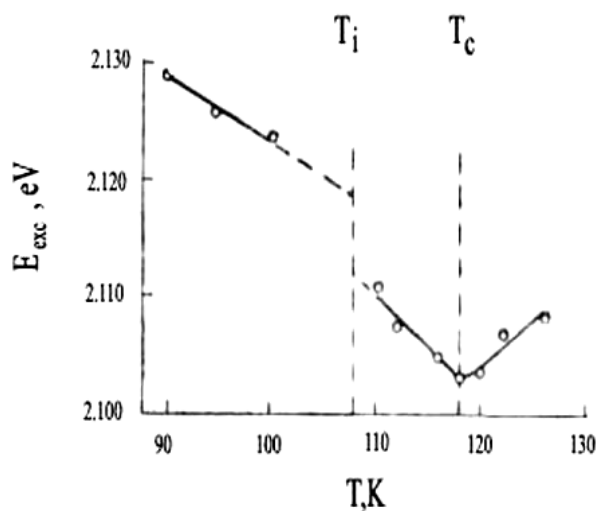
Рис.5. Температурная зависимость энергетического положения экситонной линии в спектрах поглощения кристаллов $TlGaSe_2$ [25]

4. Температурное поведение ширин запрещенных зон в $TlGaS_{2x}Se_{2(1-x)}$

Хотя, как было показано выше в разделе 2,3 аналогия «давление-изменение состава» оказывается справедливой и для кристаллов $TlGaSe_2$ -$TlGaS_2$, существуют экспериментальные факты, которые, на первый взгляд, противоречат такой аналогии. Действительно, на рис.2 приведены зависимости от температуры положений экситонных пиков поглощения в ряду

TlGaS$_{2x}$Se$_{2(1-x)}$. Бросается в глаза резкое отличие в поведении E$_{эxc}$(T) в TlGaSe$_2$ с одной стороны и в твердых растворах TlGaS$_{2x}$Se$_{2(1-x)}$ с x≥0,1 с другой. В TlGaSe$_2$ зависимость E$_{exc}$(T) обычная - она объясняется обычным уменьшением с ростом температуры ширины запрещенной зоны проводника. В TlGaS$_{2x}$Se$_{2(1-x)}$ с x≥0,1 и в самом TlGaS$_2$ наблюдается необычный для полупроводников рост E$_g$ с повышением температуры. Известно, что рост E$_g$ с температурой при низких температурах в полупроводниках бывает обусловлен вкладом теплового расширении в изменение E$_g$. Можно было бы предположить, что разное поведение E$_g$ с температурой в TlGaSe$_2$ и TlGaS$_2$ обусловлено различием в тепловом расширения этих кристаллов. Такое различие действительно наблюдается (рис.3), однако простая оценка вклада теплового расширения в изменение E$_g$ с температурой в TlGaSe$_2$ и TlGaS$_2$, основанная на кривых теплового расширения должен был бы приводит к росту E$_g$ с температурой. При этом в TlGaSe$_2$ этот рост должен быть даже большим, чем в TlGaS$_2$. Этот вывод заставляет на первый взгляд, усомнится в одинаковой природе экситонных состояний в TlGaSe$_2$ с одной стороны и в TlGaS$_{2x}$Se$_{2(1-x)}$ X≥0.1 с другой, а, следовательно, и в правомочности сделанных выше выводов о справедливости модели виртуального кристалла. Для разрешения этого противоречия необходимо учесть, что с понижением температуры в TlGaSe$_2$ происходит структурный ФП и при T<120K кристалл переходит из парафазы в несоразмерную фазу, а затем при T<100K в соразмерную сегнетофазу. Известно, что согласно имеющимся данным с ростом содержания серы в кристаллах TlGaSe$_x$Se$_{2(1-x)}$ температура ФП смещается в сторону более низких температур, а при x~0,2 признаки ФП в TlGaSe$_x$Se$_{2(1-x)}$ вообще не наблюдаются[24].Таким образом, существенное различие в поведении E$_{exc}$(T) в TlGaSe$_2$ с одной стороны и в TlGaS$_{2x}$Se$_{2(1-x)}$ (x≥0.1) другой связано с тем, что в исследуемой области температур TlGaSe$_2$ находится в другой фазе, в которой роль электрон-фононного взаимодействия существенно выше. Дополнительным доказательством в пользу сказанного являются эксперименты, в которых удалось проследить за поведением экситонного поглощения в TlGaSe$_2$ в широкой области температур [25] (рис.5). Видно, что при низких температурах вплоть до T~120K E$_{exc}$ смещается в сторону более низких энергий, затем при T>120K начинает смешаться в сторону больших энергий, как и в случае кристаллов TlGaSe$_x$Se$_{2(1-x)}$.

В заключении можно указать, что и в кристаллах TlInS$_2$, в которых надежно идентифицированы ФП, аналогичные происходящим в TlGaSe$_2$, поведение E$_{exc}$(T) в области существования низкотемпературной сегнетофазы, аналогично поведению E$_{exc}$(T) в TlGaSe$_2$.

5.Заключение

Сравнение результатов влияния гидростатического давления на край поглощения слоистых полупроводников TlGaSe$_2$, TlGaS$_2$ и TlInS$_2$ с результатами изменений, происходящих в экситонных спектрах при образовании твердых растворов TlGaSe$_x$Se$_{2(1-x)}$, показывает, что изменения энергетической зонной структуры при образовании твердого раствора можно с большой точностью уподобить эффективной деформации кристаллов типа TlGaSe$_2$. Таким образом, несмотря на сложную кристаллическую структуру, модель виртуального кристалла в случае замены Se $\leftrightarrow$ S остается справедливой и для кристаллов типа TlGaSe$_2$. Этот вывод остается верным даже с учетом происходящих в кристаллах семейства TlGaSe$_2$ фазовых переходов. Причиной справедливости модели виртуального кристалла в случае кристаллов типа TlGaSe$_2$ служит на наш взгляд тот факт, что принципы формирования электронной зонной структуры и её изменения с изменением давления остаются общими для широкого класса полупроводников, имеющих слоистую структуру.

Литература

1. R.H.Parmenter.Phys.Rev. **97**,p.587-598 (1955)
2. С.Б. Вахрушев, В.В.Жданова, Г.Е. Квятковский, Н.М. Окунева Письма в ЖЭТФ **39**, 6, 291 (1984)
3. D.F. Mc.Morrow, R.A. Cowley, P.O. Hatton, J. Banys. J.Phys.: Condens. Matter. **2**, 16 3699 (1990). K.R.Allakhverdiev, T.G. Mamedov, B.G. Akinoglu and Sh.S. Ellialtioglu. Turkish J. of Phys. **18**, 1, 1 (1994).

5. E.A. Vinogradov, G.N. Zhizhin, N.N. Melnik, S.I. Subbotin, V.V. Panfilov, K.R. Allakhverdiyev, E.Yu. Salaev, R.Kh. Nani. Phys. Stat. Sol. (b), **95**, 1, 383 (1979).

6. K.R.Allakhverdiev, T.G. Mamedov, V.V. Panfilov, M.M. Shukurov, S.I. Subbotin. Phys. Stat. Sol. (b), **131**, 1, k 23 (1985).

7. К.Р. Аллахвердиев, А.И. Баранов, Т.Г. Мамедов, В.А. Сандлер, Я.Н. Шарифов. ФТТ, **30**, 6, 1751 (1988).

8. E. Bairamova, K.R. Allakhverdiyev, B.G. Akinoglu, T. Arai, T.G. Mamedov. Turkish J. of Phys. **18**, 4, 497 (1994).

9. К.Р. Аллахвердиев, Т.Г. Мамедов, М.М. Тагиев. Физика и техника высоких давлений Сб. науч. Тр.-Киев: Наукова Думка, вып. 28, 1 (1988).

10. К.Р. Аллахвердиев, Т.Г. Мамедов, Г.И. Пересада, Е.Г. Понятовский, Я.Н. Шарифов. ФТТ **27**, 3, 927 (1985).

11. D. Muller, F.E. Poltman, H.Z. Hahn. Naturforsch. 29b, 1,117 (1974).

12. D. Muller and H.Z. Hahn. Anorg. Allg. Chem. 438, 1, 258 (1978).

13. W. Henkel, H.D. Hochheimer, C.l Carlone, A. Werner, S. Ves and H.G. von Schnering. Phys.Rev.B **26**,6, 3211 (1982).

14. Р.А. Сулейманов, М.Ю. Сеидов, Ф.М. Салаев. ФТТ **33**,6, 1797 (1991).

15. Н.А. Абдуллаев, Т.Г. Мамедов, Р.А. Сулейманов. ФНТ **27**,8, 915 (2001).

16. С.Г. Абдуллаева, Г.Л. Беленький, Н.Т. Мамедов. ФТП.**15**,5,943 (1981)

17. Т.Г. Мамедов, Р.А. Сулейманов. Известия НАН Азербайджана , сер.физ.-мат.и техн.наук XIII,2, 19 (2003).

18. Т.Г. Мамедов, Р.А. Сулейманов. ФТТ, **45**,12,2141 (2003).

19. Г.А. Беленький, Э.Ю. Салаев, Р.А.Сулейманов. УФН,155, 1, 89 (1988).

20. K.R.Allakhverdiev,T.G.Mammadov,R.A.Suleymanov and N.Z.Gasanov.J. Phys.:Condens.Matter., **15**,1291 (2003).

21. Г.Л.Беленький, Л.Н.Алиева, М.А.Гезалов, Р.Х.Нани , Э.Ю.Салаев, Р.А.Сулейманов. ФТТ,**12**,1,106-108 (1978)

22. G.L. Belenkii, S.G. Abdullaeva, A.B. Solodukhin and R.A. Suleymanov. Solid State Commun. **44**, 12, 1613 (1982).

23. Н.А. Абдуллаев, К.Р. Аллахвердиев, Г.Л. Беленкий, Т.Г. Мамедов, Р.А. Сулейманов, Я.Н. Шарифов. Доклады АН Азерб. ССР, XLI, 12, 21 (1985).

24. А.А. Волков, Ю.В. Гончаров, Г.В. Козлов, К.Р. Аллахвердиев, Р.М. Сардарлы. ФТТ, **26**, 9, 2754 (1984).

25. С.Г.Абдуллаева, Н.Т.Мамедов. ФТТ,**28**,3,894 (1986).

Модель виртуального кристалла в применении к слоистым полупроводникам типа TlGaSe$_2$.

С.Г.Абдуллаева[*] , Т.Г. Мамедов[*] , Р.А. Сулейманов[**]

[*] Институт Физики НАН Азербайджана AZ-1143, Баку, пр. Г.Джавида, 33

[**] Бакинский Государственный Университет

Проведено сравнение результатов изменений, происходящих в экситонных спектрах при образовании твердых растворов $TlGaS_{2x}Se_{2(1-x)}$ с данными влияния гидростатического давления на край поглощения слоистых полупроводников $TlGaSe_2$ и $TlInS_2$. Показано, что модель виртуального кристалла в случае замены Se-S справедлива и для сложных кристаллов типа $TlGaSe_2$.

Application of virtual crystal model to layer semiconductor TlGaSe₂

S.G.Abdullayeva[*], T.G.Mamedov[*], R.A.Suleymanov[**]

[*]Institute of Physics National Academy of Sciences, Azerbaijan, AZ_1143,H.Javid ave,33,Baku

[**]Baku State University

HAMILTONIAN-TYPE OPERATORS AND q-ORTHOGONAL POLYNOMIALS

N. M. Atakishiyev[1] and A. U. Klimyk[1,2]

[1]Instituto de Matemáticas, UNAM, CP 62210 Cuernavaca, Morelos, México
[2]Bogolyubov Institute for Theoretical Physics, 03143 Kiev, Ukraine

E-mail: natig@matcuer.unam.mx and anatoliy@matcuer.unam.mx

Abstract

It is known that self-adjoint operators, which belong to a certain class of operators for the discrete series representations of the quantum algebra $\mathrm{su}_q(1,1)$, may serve as Hamiltonians of some physical systems. These operators are expressed in the canonical basis by Jacobi matrices. The problem of diagonalization of these operators (eigenfunctions, spectra, overlap coefficients, etc.) is solved for a wide class of such operators by using their connection with the theory of q-orthogonal polynomials.

1. Introduction

It is well known that all eigenvalues of self-adjoint operators are real. This mathematical fact has been vital for formulating one of the fundamental constructive postulates of quantum mechanics: the variables used for describing a dynamical system in quantum mechanics are represented by self-adjoint operators; the values, which a given variable can take, correspond to observable physical quantities and they are found as eigenvalues of the associated self-adjoint operators (see, for example, [1]). So, the study of explicit instances of relevant self-adjoint operators, related to particular physical systems, is of clear interest. To be more specific, we refer to recent studies in quantum optics (see [2] and references therein), where it was shown that many models, such as Raman and Brillouin scattering, parametric conversion and the interaction of two-level atoms with a single mode radiation field (Dicke model), can be described by interaction Hamiltonians, which are certain self-adjoint difference operators from representations of the quantum algebra $\mathrm{su}_q(2)$.

In this paper we wish to discuss yet another self-adjoint difference operators, which may serve as Hamiltonians of some physical systems. They belong to a certain class of operators for the discrete series representations of the quantum algebra $\mathrm{su}_q(1,1)$ and can be expressed in the canonical basis by a Jacobi matrix. We show that the problem of diagonalization of such operators (eigenfunctions, spectra, overlap coefficients, etc.) is solved by using the connection of these operators with the theory of q-orthogonal polynomials. The point is that an orthogonality measure for a family of q-orthogonal polynomials, associated with a certain Hamiltonian operator, determines a spectrum of this operator and its spectral decomposition.

It is essential to note that our study of Hamiltonian-type operators was first started in [3] and [4], and then has been developed in [5–7]. In particular, in [7] we considered examples of Hamiltonians for physical systems in non-commutative world (see in this connection [8]).

A summary of what the remaining sections contains is as follows. Section 2 gives some useful results on the quantum algebra $\mathrm{su}_q(1,1)$ and its discrete series representations. In section 3 we detail general properties of those Hamiltonian-type operators, which are operators of the discrete series of the algebra $\mathrm{su}_q(1,1)$. In sections 4 and 5, some examples of Hamiltonians with bounded continuous spectra are studied. Section 6 is devoted to Hamiltonians with bounded discrete spectra.

Throughout the sequel we always assume that q is a fixed positive number such that $q < 1$. We extensively use the theory of q-special functions and notations of the standard q-analysis (see, for example, [9]). In particular, we assume that

$$[a]_q := \frac{q^{a/2} - q^{-a/2}}{q^{1/2} - q^{-1/2}}, \tag{1.1}$$

where a can be a number or an operator.

2. The algebra $\mathrm{su}_q(1,1)$ and its discrete series representations

The classical Lie algebra $\mathrm{su}(1,1)$ is generated by the elements $J_0^{\mathrm{cl}}, J_1^{\mathrm{cl}}, J_2^{\mathrm{cl}}$, satisfying the relations

$$[J_0^{\mathrm{cl}}, J_1^{\mathrm{cl}}] = \mathrm{i}J_2^{\mathrm{cl}}, \qquad [J_1^{\mathrm{cl}}, J_2^{\mathrm{cl}}] = -\mathrm{i}J_0^{\mathrm{cl}}, \qquad [J_2^{\mathrm{cl}}, J_0^{\mathrm{cl}}] = \mathrm{i}J_1^{\mathrm{cl}}.$$

In terms of the raising and lowering operators $J_\pm^{\mathrm{cl}} = J_1^{\mathrm{cl}} \pm \mathrm{i}J_2^{\mathrm{cl}}$ these commutation relations can be written as

$$[J_0^{\mathrm{cl}}, J_\pm^{\mathrm{cl}}] = \pm J_\pm^{\mathrm{cl}}, \qquad [J_-^{\mathrm{cl}}, J_+^{\mathrm{cl}}] = 2J_0^{\mathrm{cl}}.$$

The discrete series representations T_l^+ of $\mathrm{su}(1,1)$ with lowest weights are given by a positive number l and they are realized on the spaces $\mathcal{L}_l$ of polynomials in x. The basis in $\mathcal{L}_l$ consists of the monomials

$$g_n^l(x) = \{(2l)_n/n!\}^{1/2} x^n, \qquad n = 0, 1, 2, 3, \cdots.$$

Assuming that this basis consists of orthonormal elements, one defines a scalar product in $\mathcal{L}_l$. The closure of $\mathcal{L}_l$ leads to a Hilbert space, on which the representation T_l^+ acts.

We consider an explicit realization of the representation operators J_i^{cl}, $i = 0, 1, 2$, in terms of the first-order differential operators:

$$J_0^{\mathrm{cl}} = x\frac{d}{dx} + l, \qquad J_1^{\mathrm{cl}} = \frac{1}{2}(1 + x^2)\frac{d}{dx} + lx, \qquad J_2^{\mathrm{cl}} = \frac{i}{2}(1 - x^2)\frac{d}{dx} - ilx. \tag{2.1}$$

Then

$$J_0^{\mathrm{cl}} g_n^l = (l + n)g_n^l, \quad J_+^{\mathrm{cl}} g_n^l = \sqrt{(2l + n)(n + 1)}g_{n+1}^l, \quad J_-^{\mathrm{cl}} g_n^l = \sqrt{(2l + n - 1)n}g_{n-1}^l.$$

In some physical models a Hamiltonian is represented by the self-adjoint operator $J_0^{\mathrm{cl}} - J_1^{\mathrm{cl}}$. For instance, the n-dimensional harmonic oscillator in nonrelativistic quantum mechanics is governed by the Hamiltonian

$$H(x) = \frac{\hbar\omega}{2}\sum_{k=1}^n \left(\xi_k^2 - \frac{d^2}{d\xi_k^2}\right) = \hbar\omega\left[\sum_{k=1}^n a^+(x_k)\,a(x_k) + \frac{n}{2}\right],$$

where $x = \{x_1, x_2, \cdots, x_n\}$, the dimensionless variables $\xi_k = \sqrt{m\omega/\hbar}\,x_k$, $k = 1, 2, \cdots, n$, and the annihilation and creation boson operators $a(x_k) = \frac{1}{\sqrt{2}}(\xi_k + d/d\xi_k)$ and $a^+(x_k) = \frac{1}{\sqrt{2}}(\xi_k - d/d\xi_k)$, respectively, satisfy the Heisenberg commutation relations

$$[a(x_k), a^+(x_j)] = \delta_{kj}, \quad k, j = 1, 2, \cdots, n.$$

The dynamical symmetry algebra for this model is known to be the Lie algebra $\mathrm{su}(1,1)$ with the generators

$$J_0(x) = \frac{1}{2}\sum_{k=1}^n a^+(x_k)\,a(x_k), \quad J_1(x) = \frac{1}{2}\sum_{k=1}^n a^2(x_k), \quad J_2(x) = \frac{1}{2}\sum_{k=1}^n [a^+(x_k)]^2. \tag{2.2}$$

One readily verifies that, for example, the n-dimensional Laplace operator $\Delta = \sum_{k=1}^{n} d^2/d\xi_k^2$ in terms of the su$(1,1)$-generators (2.2) is just $2[J_1(x) - J_0(x)] - n/2$. Hence, the problem of funding spectrum and eigenfunctions of the Laplace operator Δ in this n-dimensional Euclidean space is equivalent to that of the operator $J_1(x) - J_0(x)$.

Now we return to the realization (2.1). It is not hard to show that the eigenfunctions of the operator $J_0^{\text{cl}} - J_1^{\text{cl}}$ are of the form

$$[J_0^{\text{cl}} - J_1^{\text{cl}}]\, \eta_\lambda^l(x) = \lambda\, \eta_\lambda^l(x), \tag{2.3}$$

$$\eta_\lambda^l(x) = (1-x)^{-2l} \exp\left(\frac{2\lambda x}{x-1}\right). \tag{2.4}$$

The quantum algebra su$_q(1,1)$ and its irreducible representations are obtained by deformation of the corresponding relations for the Lie algebra su$(1,1)$ and its irreducible representations. The algebra su$_q(1,1)$ is defined as the associative algebra, generated by the elements J_+, J_-, and J_0, which satisfy the commutation relations

$$[J_0, J_\pm] = \pm J_\pm, \quad [J_-, J_+] = \frac{q^{J_0} - q^{-J_0}}{q^{1/2} - q^{-1/2}} \equiv [2J_0]_q, \tag{2.5}$$

and the conjugation relations $J_0^* = J_0$, $J_+^* = J_-$.

We are interested in the discrete series representations of su$_q(1,1)$ with lowest weights. These irreducible representations will be denoted by T_l^+, where l is a lowest weight, which can be any positive number (see, for example, [10]). These representations are obtained by deforming the corresponding representations of the Lie algebra su$(1,1)$.

As in the classical case, the representation T_l^+ can be realized on the space $\mathcal{L}_l$ of all polynomials in x. We choose a basis for this space, consisting of the monomials

$$f_n^l \equiv f_n^l(x) := c_n^l\, x^n, \quad n = 0, 1, 2, \cdots, \tag{2.6}$$

where

$$c_0^l = 1, \quad c_n^l = \prod_{k=1}^{n} \frac{[2l + k - 1]_q^{1/2}}{[k]_q^{1/2}} = q^{(1-2l)n/4} \frac{(q^{2l}; q)_n^{1/2}}{(q; q)_n^{1/2}}, \quad n = 1, 2, 3, \cdots, \tag{2.7}$$

and $(a; q)_n = (1-a)(1-aq)\ldots(1-aq^{n-1})$. The representation T_l^+ is then realized by the operators

$$J_0 = x\frac{d}{dx} + l, \quad J_\pm = x^{\pm 1}[J_0 \pm l]_q. \tag{2.8}$$

As a result of this realization, we have

$$J_0\, f_n^l = (l + n)\, f_n^l, \quad J_+\, f_n^l = \sqrt{[2l + n]_q\, [n+1]_q}\, f_{n+1}^l, \tag{2.9}$$

$$J_-\, f_n^l = \sqrt{[2l + n - 1]_q\, [n]_q}\, f_{n-1}^l. \tag{2.10}$$

We know that the discrete series representations T_l^+ can be realized in a Hilbert space, on which the conjugation relations $J_0^* = J_0$ and $J_+^* = J_-$ are satisfied. In order to obtain such a Hilbert space, we assume that the monomials $f_n^l(x)$, $n = 0, 1, 2, \cdots$, constitute an orthonormal basis for this Hilbert space. This introduces a scalar product $\langle \cdot, \cdot \rangle$ into the space $\mathcal{L}_l$. Then we

3

close this space with respect to this scalar product and obtain a Hilbert space, which will be denoted by $\mathcal{H}_l$. The Hilbert space $\mathcal{H}_l$ consists of functions (series)

$$f(x) = \sum_{n=0}^{\infty} b_n f_n^l(x) = \sum_{n=0}^{\infty} b_n c_n^l x^n = \sum_{n=0}^{\infty} a_n x^n,$$

where $a_n = b_n c_n^l$. Since $\langle f_m^l, f_n^l \rangle = \delta_{mn}$ by definition, for $f(x) = \sum_{n=0}^{\infty} a_n x^n$ and $\tilde{f}(x) = \sum_{n=0}^{\infty} \tilde{a}_n x^n$ we have $\langle f, \tilde{f} \rangle = \sum_{n=0}^{\infty} a_n \tilde{a}_n / |c_n^l|^2$, that is, the Hilbert space $\mathcal{H}_l$ consists of analytical functions $f(x) = \sum_{n=0}^{\infty} a_n x^n$, such that

$$\|f\|^2 \equiv \sum_{n=0}^{\infty} |a_n / c_n^l|^2 < \infty.$$

It is directly checked that for a function $f(x) \in \mathcal{H}_l$ we have $q^{cx \frac{d}{dx}} f(x) = f(q^c x)$. Therefore, taking into account formulas (2.8), we conclude that

$$q^{J_0/2} f(x) = q^{\frac{1}{2}(x \frac{d}{dx} + l)} f(x) = q^{l/2} f(q^{1/2} x), \tag{2.11}$$

$$J_+ f(x) = \frac{x}{q^{1/2} - q^{-1/2}} \left[q^l f(q^{1/2} x) - q^{-l} f(q^{-1/2} x) \right], \tag{2.12}$$

$$J_- f(x) = \frac{1}{(q^{1/2} - q^{-1/2})x} \left[f(q^{1/2} x) - f(q^{-1/2} x) \right]. \tag{2.13}$$

3. Hamiltonian operators and q-orthogonal polynomials

We are interested in spectra, eigenfunctions and overlap functions for operators in the representations T_l^+, which correspond to elements of the quantum algebra $su_q(1,1)$ of the form

$$H := q^{p\,J_0}(J_+ + J_-)\,q^{p\,J_0} + f(q^{J_0}), \quad p \in \mathbb{R}, \tag{3.1}$$

where f is some polynomial (or function). These operators have the following properties:

(i) They are representable in the basis (2.6) by a Jacobi matrix.
(ii) They are symmetric operators.
(iii) They are not necessarily self-adjoint operators.

Recall that a Jacobi matrix is a matrix, with all entries vanishing except for those which occur on the main diagonal and on two neighboring (upper and lower) diagonals.

Note that in the case (iii) a symmetric operator has self-adjoint extensions. These extensions can serve as Hamiltonian operators. However, finding of self-adjoint extensions is a complicated problem in the each particular case.

The most important example of the operators of the form (3.1) is

$$H^{(p)} := q^{pJ_0/4}(J_+ + J_-)q^{pJ_0/4}, \quad p \in \mathbb{R}.$$

For these operators the following theorem is true [11].

Theorem 1. *If $p > 1$, then the operator $H^{(p)}$ is bounded and has a discrete simple spectrum. Zero is a unique point of accumulation of the spectrum. If $p < 1$, then the closure $\overline{H^{(p)}}$ of the symmetric operator $H^{(p)}$ is not a self-adjoint operator and it has deficiency indices (1,1), that is, $\overline{H^{(p)}}$ has a one-parameter family of self-adjoint extensions. These extensions*

4

have discrete simple spectra. If $p = 1$, then $H^{(p)}$ has a continuous simple spectrum, which covers the interval $(-b, b)$, $b = 2/(q^{-1/2} - q^{1/2})$.

This theorem describes spectra of the operators $\overline{H^{(p)}}$ and does not explain how to find eigenfunctions. To find them, one can employ the theory of q-orthogonal polynomials.

There exist close relationship between the following directions, which we exploit to study Hamiltonian-type operators:

(i) the theory of symmetric operators L, representable by a Jacobi matrix;
(ii) the theory of orthogonal polynomials;
(iii) the theory of classical moment problem

(see [12] and [13]). Let us describe briefly this relationship. Let L be a closed symmetric operator on a Hilbert space $\mathcal{H}$. Let $e_1, e_2, \cdots$ be a basis in $\mathcal{H}$ such that

$$L\, e_n = a_n\, e_{n+1} + b_n\, e_n + a_{n-1}\, e_{n-1}.$$

Let $|x\rangle = \sum_{n=0}^{\infty} p_n(x) e_n$ be an eigenvector of L with the eigenvalue x, that is, $L|x\rangle = x|x\rangle$. Then

$$L\,|x\rangle = \sum_{n=0}^{\infty} \left[p_n(x)a_n e_{n+1} + p_n(x)b_n e_n + p_n(x)a_{n-1}e_{n-1} \right] = x \sum_{n=0}^{\infty} p_n(x)e_n.$$

Equating coefficients of the vector e_n, one comes to a recurrence relation for the coefficients $p_n(x)$:

$$a_n\, p_{n+1}(x) + b_n\, p_n(x) + a_{n-1}\, p_{n-1}(x) = x\, p_n(x).$$

Since $p_{-1}(x) = 0$, then setting $p_0(x) \equiv 1$, we see that this relation completely determines the coefficients $p_n(x)$. Moreover, $p_n(x)$ are polynomials in x of degree n. If coefficients a_n and b_n are real, then all coefficients of the polynomials $p_n(x)$ are real and they are orthogonal with respect to some positive measure $\mu(x)$. If the operator L is self-adjoint, then this measure is uniquely determined and

$$\int p_m(x)p_n(x)d\mu(x) = \delta_{mn},$$

where the integration is taken over some subset (possibly discrete) of $\mathbb{R}$. Moreover, the spectrum of the operator L is simple and coincide with the set, on which the polynomials are orthogonal. The measure $\mu(x)$ determines the spectral decomposition of the operator L (for details see [13], Chapter VII).

If a closed symmetric operator L is not self-adjoint, then the measure $\mu(x)$ is not determined uniquely. Moreover, in this case there exist infinitely many measures, with respect to which the polynomials are orthogonal. Among these measures there are so-called extremal measures (that is, such that a set of polynomials $\{p_n(x)\}$ is complete in the Hilbert space L^2 with respect to the corresponding measure). These measures determine self-adjoint extensions of the symmetric operator L.

On the other hand, with the polynomials $p_n(x)$, $n = 0, 1, 2, \cdots$, the classical moment problem is associated [12]. Namely, with these polynomials (that is, with the coefficients a_n and b_n in the corresponding recurrence relation) positive numbers c_n, $n = 0, 1, 2, \cdots$, are related, which enter into the classical moment problem. The definition of classical moment problem consists in the following. One looks for a measure $\mu(x)$, such that

$$\int x^n d\mu(x) = c_n, \qquad n = 0, 1, 2, \cdots, \tag{4.1}$$

5

where the c_n, $n = 0, 1, 2, \cdots$ are some positive numbers and integration is taken over some fixed subset of $\mathbb{R}$. There are then two main questions:

(i) Does exist a measure $\mu(x)$, such that relations (4.1) are satisfied?
(ii) If such a measure exists, is it determined uniquely?

If the answer to the first question is positive, then the numbers c_n, $n = 0, 1, 2, \cdots$, are those, which correspond to a particular family of orthogonal polynomials. Moreover, a measure $\mu(x)$ then coincides with the measure, with respect to which these polynomials are orthogonal.

If a measure in (4.1) is determined uniquely, then we say that we deal with determinate moment problem. It is the case when the region of integration is bounded. If there are many measures, with respect to which relations (4.1) hold, then we say that we deal with indeterminate moment problem. In this case there exist infinitely many measures $\mu(x)$, for which (4.1) takes place. In the second case the corresponding polynomials are orthogonal with respect to all these measures and the corresponding symmetric operator L is not self-adjoint.

Thus, we see that one can study the operator L by investigating the corresponding sets of orthogonal polynomials and their moment problems. To illustrate that, we confine our attention below to certain examples of Hamiltonian-type operators.

4. Hamiltonians with bounded continuous spectra

In this section we are interested in the operator

$$H_1 := \frac{a}{2}\, q^{J_0} - b - \frac{1}{2}\, (q^{1/4} J_+ + q^{-1/4} J_-)\, q^{J_0/2} \tag{5.1}$$

of the discrete series representation T_l^+, where

$$a = (q^{1/4} + q^{-1/4})\, b, \quad b = (q^{1/2} - q^{-1/2})^{-1}\,.$$

The representation operator $(q^{1/4} J_+ + q^{-1/4} J_-) q^{J_0/2}$ is bounded. Since J_0 has the eigenvalues $m = l, l+1, l+2, \cdots$, the operator q^{J_0} is also bounded (recall that $0 < q < 1$). Thus, the operator H_1 is bounded. It is easy to check that H_1 is a self-adjoint operator since

$$H_1\, f_k^l = \beta_k\, f_k^l - \alpha_k\, f_{k+1}^l - \alpha_{k-1}\, f_{k-1}^l\,,$$

where

$$\alpha_k := \frac{1}{2} \left\{ q^{l+k+1/2}\, [2l+k]_q\, [k+1]_q \right\}^{1/2}, \quad \beta_k = \frac{(q^{1/4} + q^{-1/4}) q^{l+k} - 2}{2(q^{1/2} - q^{-1/2})}.$$

The constants a and b in (5.1) are chosen in such a way that in the limit as $q \to 1$ the operator H_1 reduces to the $\mathrm{su}_{1,1}$-operator $J_0^{\mathrm{cl}} - J_1^{\mathrm{cl}}$ (see formula (2.3)).

Eigenfunctions of the operator H_1,

$$H_1\, \xi_\lambda^l(x) = \lambda(q)\, \xi_\lambda^l(x)\,, \tag{5.2}$$

and its spectrum can be found by using the explicit realization (2.8) for the generators J_0 and $J_\pm$. Indeed, from formulas (2.11)–(2.13) it follows that

$$H_1\, f(x) = \frac{b}{2x}\, q^{(2l-1)/4} \left[(1 - q^{(1-2l)/4}\, x)^2\, f(x) - (1 - q^{l/2}\, x)(1 - q^{(l+1)/2}\, x)\, f(qx) \right] \tag{5.3}$$

for an arbitrary function $f(x)$. It is thus natural to look for the eigenfunctions $\xi_\lambda^l(x)$ of the operator H_1 in the form

$$\xi_\lambda^l(x) = \frac{(\alpha x; q)_\infty\, (\beta x; q)_\infty}{(\gamma x; q)_\infty (\delta x; q)_\infty}\,, \tag{5.4}$$

6

where $(a;q)_\infty = \prod_{r=0}^\infty (1 - aq^r)$. Since $(a;q)_\infty = (1-a)(aq;q)_\infty$ by definition, we have

$$\xi_\lambda^l(qx) = \frac{(1-\gamma x)(1-\delta x)}{(1-\alpha x)(1-\beta x)}\,\xi_\lambda^l(x;q)\,. \tag{5.5}$$

Substituting (5.4) and (5.5) into (5.3), one gets

$$H_1\xi_\lambda^l(x) = \frac{b}{2x}q^{(2l-1)/4}\left\{(1-q^{(1-2l)/4}x)^2 - (1-q^{l/2}x)(1-q^{(l+1)/2}x)\frac{(1-\gamma x)(1-\delta x)}{(1-\alpha x)(1-\beta x)}\right\}\xi_\lambda^l(x).$$

This equation can be written as

$$H_1\,\xi_\lambda^l(x) = \frac{b}{2}\,q^{(2l-1)/4}\frac{Ax^3 + Bx^2 + Cx + D}{(1-\alpha x)(1-\beta x)}\,\xi_\lambda^l(x), \tag{5.6}$$

where the constant coefficients A, B, C, and D are equal to

$$A = q^{1/2}(q^{-l}\alpha\beta - q^l\gamma\delta),$$

$$B = q^{1/2}[q^l(\gamma+\delta) - q^{-l}(\alpha+\beta)] + (1+q^{1/2})q^{l/2}\gamma\delta - 2q^{(1-2l)/4}\alpha\beta,$$

$$C = \alpha\beta - \gamma\delta + 2q^{(1-2l)/4}(\alpha+\beta) - (1+q^{1/2})q^{l/2}(\gamma+\delta) - q^{1/2}\,(q^l - q^{-l}),$$

$$D = \gamma + \delta - \alpha - \beta + (1+q^{1/2})q^{l/2} - 2q^{(1-2l)/4}.$$

It is clear from (5.6) that the $\xi_\lambda^l(x)$ is an eigenfunction of the operator H_1 if the factor in front of $\xi_\lambda^l(x)$ on the right-hand side of (5.6) does not depend on x. It is the case if

$$A = 0, \qquad B = \alpha\beta D, \qquad C = -(\alpha+\beta)D\,. \tag{5.7}$$

Then eigenvalues of the operator H_1 on the right-hand side of (5.6) will be equal to $\lambda = q^{(2l-1)/4}D/2(q^{1/2} - q^{-1/2})$. Requirements (5.7) are equivalent to the following three relations between the parameters $\alpha, \beta, \gamma, \delta$:

$$\alpha\beta = q^{2l}\gamma\delta, \quad (q^{1/2-l} - \alpha\beta)(\alpha+\beta) = (q^{l+1/2} - \alpha\beta)(\gamma+\delta) - (1+q^{1/2})q^{-l/2}(q^l - q^{-l})\alpha\beta,$$

$$(q^l - q^{-l})(q^{1/2} - q^{-l}\alpha\beta) = [\alpha + \beta - (1+q^{1/2})q^{l/2}](\gamma + \delta - \alpha - \beta).$$

From these relations it follows that

$$\alpha = q^{l/2}, \quad \beta = q^{(l+1)/2}, \quad \gamma = q^{(1-2l)/4}\,e^{i\theta}, \quad \delta = q^{(1-2l)/4}\,e^{-i\theta},$$

where θ is an arbitrary angle. Consequently, the eigenfunctions of the operator H_1 are equal to

$$\xi_\lambda^l(x) = \frac{(q^{l/2}x;q)_\infty\,(q^{(l+1)/2}x;q)_\infty}{(q^{(1-2l)/4}e^{i\theta}x;q)_\infty\,(q^{(1-2l)/4}e^{-i\theta}x;q)_\infty}, \tag{5.8}$$

and the corresponding eigenvalues are

$$\lambda \equiv \lambda(q) = (1 - \cos\theta)/(q^{-1/2} - q^{1/2})\,.$$

The eigenfunctions (5.8) are in fact the generating functions for the continuous q-Laguerre polynomials

$$P_n^{(\alpha)}(y|q) = (q^{(2\alpha+3)/4}e^{-i\theta};q)_n(q;q)_n^{-1}\,q^{(2\alpha+1)n/4}e^{in\theta}$$

$$\times\,{}_2\phi_1(q^{-n},\ q^{(2\alpha+1)/4}e^{i\theta};\ q^{-n-(2\alpha-1)/4}e^{i\theta}\,;\ q;q^{-(2\alpha-1)n/4}e^{-i\theta}),$$

where $y = \cos\theta$ and $_2\phi_1$ is the basic hypergeometric function, defined by formula (1.2.14) in [9]. In order to make this evident, one needs to represent (5.8) in the form

$$\xi^l_\lambda(x;q) = \frac{(q^{2l-1/2}ax;q)_\infty (q^{2l}ax;q)_\infty}{(q^{l-1/4}e^{i\theta}ax;q)_\infty (q^{l-1/4}e^{-i\theta}ax;q)_\infty}, \tag{5.9}$$

where $a = q^{(1-3l)/2}$. Consequently, due to formula (3.19.11) in [14], the desired connection is

$$\xi^l_\lambda(x) = \sum_{n=0}^{\infty} q^{n(1-3l)/2} P_n^{(2l-1)}(\cos\theta|q)\, x^n = \sum_{n=0}^{\infty} \frac{q^{n(1-3l)/2}}{c_n^l} P_n^{(2l-1)}(\cos\theta|q)\, f_n^l(x),$$

where $\cos\theta = 1 - (q^{-1/2} - q^{1/2})\lambda$.

Thus, we have proved that the eigenfunctions $\xi^l_\lambda(x)$ are connected with the basis elements $f_n^l(x)$ by the formula

$$\xi^l_\lambda(x) = \sum_{n=0}^{\infty} p_n(\lambda) f_n^l(x), \tag{5.10}$$

where the overlap coefficients $p_n(\lambda)$ are explicitly given by

$$p_n(\lambda) = q^{(1/4-l)n}(q;q)_n^{1/2}(q^{2l};q)_n^{-1/2} P_n^{(2l-1)}(1 - (q^{-1/2} - q^{1/2})\lambda|q). \tag{5.11}$$

To find a spectrum of H_1, we take into account the following. The self-adjoint operator H_1 is represented by a Jacobi matrix in the basis $f_n^l(x)$, $n = 0, 1, 2, \cdots$, with nonvanishing entries α_k and β_k. As is evident from (5.10), the eigenfunctions $\xi^l_\lambda(x)$ are expanded in the basis elements $f_n^l(x)$ with the coefficients (5.11). According to the results of Chapter VII in [13], these polynomials $p_n(\lambda)$ are orthogonal with respect to some measure $d\mu(\lambda)$ (this measure is unique, up to a multiplicative constant, since the operator H_1 is bounded). The set (a subset of $\mathbb{R}$), on which the polynomials are orthogonal, coincides with the spectrum of the operator H_1 and $d\mu(\lambda)$ determines the spectral measure of this operator; the spectrum of H_1 is simple (see Chapter VII in [13]).

We remind the reader that the orthogonality relation for the continuous q-Laguerre polynomials $P_n^{(2l-1)}(y|q)$ has the form

$$\frac{1}{2\pi} \int_{-1}^{1} P_m^{(2l-1)}(y|q) P_n^{(2l-1)}(y|q) \frac{w(y)dy}{\sqrt{1-y^2}} = \frac{(q^{2l};q)_n\, q^{(2l-1/2)n}}{(q;q)_\infty (q^{2l};q)_\infty (q;q)_n} \delta_{mn},$$

where

$$w(y) = \left| \frac{(e^{i\theta};q^{1/2})_\infty (-e^{i\theta};q^{1/2})_\infty}{(q^{l-1/4}e^{i\theta};q^{1/2})_\infty} \right|^2, \quad y = \cos\theta$$

(see formula (3.19.2) in [14]). Therefore, the orthogonality relation for the overlap coefficients (5.11) is

$$\int_0^{2q^{1/2}/(1-q)} p_m(\lambda) p_n(\lambda) \hat{w}(\lambda) d\lambda = \delta_{mn}, \tag{5.12}$$

where

$$\hat{w}(\lambda) = \frac{1}{2\pi}(q;q)_\infty (q^{2l};q)_\infty \sqrt{\frac{1-q}{\lambda q^{1/2}}} \frac{w(1 - q^{-1/2}(1-q)\lambda)}{\sqrt{2 - q^{-1/2}(1-q)\lambda}}. \tag{5.13}$$

Consequently, the spectrum of the operator H_1 (that is, a range of λ) coincides with the finite interval $[0, 2q^{1/2}/(1-q)]$. The spectrum is continuous and simple. The continuity of the

8

spectrum means that the eigenfunctions $\xi_\lambda^l(x)$ do not belong to the Hilbert space $\mathcal{H}_l$. They belong to the space of functionals on $\mathcal{L}_l$, which can be considered as a space of generalized functions on $\mathcal{L}_l$. We have thus proved the following theorem.

Theorem 2. *The self-adjoint operator H_1 has the continuous and simple spectrum, which covers the finite interval $[0, 2q^{1/2}/(1-q)]$. The eigenfunctions $\xi_\lambda^l(x)$ are explicitly given by (5.8) and they are related to the basis (2.6) by formula (5.10).*

As we remarked at the beginning of this section, the operator H_1 represents a q-extension of the $su_{1,1}$-operator $J_0^{cl} - J_1^{cl}$. In the limit as $q \to 1$ the finite interval $[0, 2q^{1/2}/(1-q)]$ of the eigenvalues of the operator H_1 extends to the infinite interval $[0, \infty)$. So if one puts $\cos\theta = q^\mu$, then $\lim_{q\to 1} \lambda(q^\mu) = \mu$.

Besides, it is known that the continuous q-Laguerre polynomials $P_n^{(\alpha)}(y|q)$ have the following limit property $\lim_{q\to 1} P_n^{(\alpha)}(q^\lambda|q) = L_n^{(\alpha)}(2\lambda)$ (see [14], formula (5.19.1)). Thus, the coefficients of the series expansion (5.10) in x of the eigenfunctions $\xi_\lambda^l(x)$, $\cos\theta = q^\mu$, coincide with the coefficients of the corresponding expansion of the $su_{1,1}$-eigenfunctions $\eta_\mu^l(x)$ (see (2.4)) in the limit as $q \to 1$.

There exists another, more complicated, one-parameter family of self-adjoint operators, closely related to H_1. They are defined as

$$H_1^{(\varphi)} := \frac{a}{2}\, q^{J_0} - b - q^{J_0/4}\left[\cos\varphi \cdot J_1 - \sin\varphi \cdot J_2\right] q^{J_0/4},$$

where $0 \leq \varphi < 2\pi$, $J_\pm = J_1 \pm \mathrm{i}J_2$ and a, b are the same as in (5.1). These operators are bounded and self-adjoint. Repeating the same reasoning, as for the operator H_1, we arrive at the following theorem.

Theorem 3. *The eigenfunctions of the operator $H_1^{(\varphi)}$ are*

$$\xi_\lambda^l(e^{\mathrm{i}\varphi}x; q) = \frac{(q^{l/2}\, e^{\mathrm{i}\varphi}x; q)_\infty\, (q^{(l+1)/2}\, e^{\mathrm{i}\varphi}x; q)_\infty}{(q^{(1-2l)/4}\, e^{\mathrm{i}(\theta+\varphi)}x; q)_\infty\, (q^{(1-2l)/4}\, e^{-\mathrm{i}(\theta-\varphi)}x; q)_\infty},$$

where $\lambda = (1 - \cos\theta)/(q^{-1/2} - q^{1/2})$. Its spectrum is simple and covers the interval $[0, c]$, where $c = 2q^{1/2}/(1-q)$. The corresponding eigenvalues λ are the same as for H_1.

The operators $H_1^{(\varphi)}$ are q-extensions of $su_{1,1}$-operators $J_0^{cl} - \cos\varphi\, J_1^{cl} + \sin\varphi\, J_2^{cl}$.

5. More Hamiltonians with bounded continuous spectra

This section deals with eigenfunctions $\xi_\lambda^l(x; \varphi)$ and eigenvalues of a one-parameter family of the self-adjoint operators

$$H^{(\varphi)} := \frac{1}{2}(q^{1/4}J_+ + q^{-1/4}J_-)\, q^{J_0/2} + \frac{\cos\varphi}{q^{-1/2} - q^{1/2}}\, q^{J_0} \tag{6.1}$$

of the representation T_l^+ of the algebra $su_q(1,1)$: $H^{(\varphi)}\, \xi_\lambda^l(x; \varphi) = \lambda\, \xi_\lambda^l(x; \varphi)$. Using the relations (2.11)–(2.13) we find that

$$H^{(\varphi)}f(x) = c(x^{-1} - 2q^{(2l+1)/4}\cos\varphi + q^{l+1/2}x)f(qx) - c(x^{-1} + q^{1/2-l}x)f(x),$$

where $c = (q^{(2l-1)/4})/2(q^{1/2} - q^{-1/2})$. By using this expression we find (details are given in [15]), that the eigenfunctions of $H^{(\varphi)}$ are

$$\xi_\lambda^l(x; \varphi) = \frac{(axe^{\mathrm{i}\varphi}; q)_\infty(axe^{-\mathrm{i}\varphi}; q)_\infty}{(bxe^{i(\theta-\varphi)}; q)_\infty(bxe^{i(\varphi-\theta)}; q)_\infty}, \qquad \lambda = \frac{\cos(\theta-\varphi)}{q^{-1/2} - q^{1/2}},$$

where $a = q^{(2l+1)/4}$ and $b = q^{(1-2l)/4}$. A relation between the eigenfunctions $\xi_\lambda^l(x; \varphi)$ and the basis functions $f_n^l(x)$ is now an easy consequence of the generating function

$$\frac{(ae^{i\varphi}t; q)_\infty (ae^{-i\varphi}t; q)_\infty}{(e^{i(\theta-\varphi)}t; q)_\infty (e^{i(\varphi-\theta)}t; q)_\infty} = \sum_0^\infty P_n \left(\cos(\theta - \varphi); a|q\right) t^n$$

for the q-Meixner–Pollaczek polynomials $P_n(y; a|q)$, defined (see [14], section 3.9) as

$$P_n(\cos(\theta + \varphi); a|q) = a^{-n} e^{-in\varphi} \frac{(a^2; q)_n}{(q; q)_n} \, {}_3\phi_2 \left(q^{-n}, ae^{i(\theta+2\varphi)}, ae^{-i\theta} a^2, 0; q, q\right).$$

Thus

$$\xi_\lambda^l(x; \varphi) = \sum_{n=0}^\infty \frac{q^{(1-2l)n/4}}{c_n^\nu} P_n(\cos(\theta - \varphi); q^l|q) f_n^l(x).$$

To find a spectrum of the operator $H^{(\varphi)}$, we note that the q-Meixner–Pollaczek polynomials $P_n(\cos(\theta - \varphi)) \equiv P_n \left(\cos(\theta - \varphi); q^l|q\right)$ are orthogonal and the orthogonality relation has the form

$$\frac{1}{2\pi} \int_{-\pi}^\pi P_m(\cos(\theta - \varphi)) P_n(\cos(\theta - \varphi)) w_\varphi(\cos(\theta - \varphi)) d\theta = \frac{(q^{2l}; q)_n}{(q; q)_n} \delta_{mn},$$

where

$$w_\varphi(\cos(\theta - \varphi)) = (q; q)_\infty (q^{2l}; q)_\infty \left| \frac{(e^{2i(\theta-\varphi)}; q)_\infty}{q^l(e^{i(\theta-\varphi)}; q)_\infty (q^l e^{i\theta}; q)_\infty} \right|^2$$

(see formula (3.9.2) in [14]). This orthogonality relation can be written as

$$\int_a^b \frac{(q; q)_n}{(q^{2l}; q)_n} P_m(\lambda(q^{-1/2} - q^{1/2})) P_n(\lambda(q^{-1/2} - q^{1/2}))) \hat{w}(\lambda) d\lambda = \delta_{mn},$$

where

$$\hat{w}(\lambda) = \frac{w_\varphi(\lambda(q^{-1/2} - q^{1/2}))(q^{-1/2} - q^{1/2})}{\sin(\varphi - \theta)}, \quad a = \frac{-\cos(\pi + \varphi)}{q^{-1/2} - q^{1/2}}, \quad b = \frac{\cos(\pi - \varphi)}{q^{-1/2} - q^{1/2}}. \quad (6.2)$$

Therefore, we may formulate the following theorem:

Theorem 4. *The operator $H^{(\varphi)}$ has continuous and simple spectrum, which completely covers the interval (a, b), where a and b are given by (6.2).*

Continuity of the spectrum means that the eigenfunctions $\xi_\lambda^l(x; \varphi)$ do not belong to the Hilbert space $\mathcal{H}_l$. They belong to the space of functionals on the linear space $\mathcal{L}_l$, which can be considered as a space of generalized functions on $\mathcal{L}_l$.

The classical limit (that is, the limit $q \to 1$) has sense only for the operator

$$H^{(\pi/2)} = \tfrac{1}{2}(q^{1/4} J_+ + q^{-1/4} J_-) q^{J_3/2}.$$

When $q \to 1$ the operator $H^{(\pi/2)}$ tends to the operator $J_1^{(cl)}$: $\lim_{q \to 1} H^{(\pi/2)} = J_1^{(cl)}$. In this limit the basis elements (2.6) turn into the basis elements $g_n^l(x)$ of the representation space for the Lie algebra su(1, 1) and the eigenfunctions $\xi_\lambda^l(x; \pi/2)$ of $H^{(\pi/2)}$ into the eigenfunctions

$$\xi_\lambda^l(x) := (1 + ix)^{-l-i\lambda}(1 - ix)^{-l+i\lambda}$$

10

of the operator $J_1^{(\mathrm{cl})}$. They are related to the eigenfunctions of the operator $J_0^{(\mathrm{cl})}$ as

$$\xi_\lambda^l(x) = \sum_{n=0}^\infty \left(\frac{n!}{(2l)_n}\right)^{1/2} P_n^{(l)}(\lambda; \pi/2)\, f_n^l(x) \equiv \sum_{n=0}^\infty P_n^{(l)}(\lambda; \pi/2)\, x^n\,,$$

where $P_n^{(l)}(\lambda; \pi/2)$ are the classical Meixner–Pollaczek polynomials, defined by the formula

$$P_n^{(l)}(x; \varphi) := \frac{(2l)_n}{n!}\, e^{in\varphi}\, {}_2F_1(-n,\, \nu + ix;\, 2l;\, 1 - e^{-2i\varphi}),\quad l > 0,\ \ 0 < \varphi < \pi.$$

The Meixner–Pollaczek polynomials in the expression for $\xi_\lambda^l(x)$ are a limit case of the corresponding q-Meixner–Pollaczek polynomials (see [14], section 5.9).

6. Hamiltonians with bounded discrete spectra

In this section we consider the operator

$$H_2 = q^{3J_0/4}(J_+ + J_-)q^{3J_0/4} - \left([J_0 - l]_q\, q^{l/2} + [J_0 + l]_q\, q^{-l/2}\right) q^{3J_0/2}$$

(note that this operator depends on the index l of the representation T_l^+). It acts on the basis elements (2.6) by the formula

$$H_2\, f_k^l = a_{k+1} f_{k+1}^l + a_k f_{k-1}^l - q^{3(l+k)/2} d_k f_k^l, \tag{7.1}$$

where

$$a_k = q^{3(l+k)/2 - 3/4}\sqrt{[k]_q\, [2l + k - 1]_q},\quad d_k = [k]_q\, q^{(l-1)/2} + [2l + k]_q\, q^{-(l-1)/2}.$$

By using this action it is easy to check that H_2 is bounded self-adjoint operator. We look for eigenfunctions of the operator H_2 in the form

$$\chi_\lambda^l(x) = \sum_{k=0}^\infty P_k(\lambda) f_k^l(x)\,.$$

The equation

$$H_2\, \chi_\lambda^l(x) = \sum_{k=0}^\infty P_k(\lambda)\, H_2 f_k^l(x) = \lambda \sum_{k=0}^\infty P_k(\lambda)\, f_k^l(x)$$

and the formula (7.1) lead to the following recurrence relation for the polynomials $P_k(\lambda)$, which after simple transformations can be written as

$$-q^{k+l}\, [(1-q^{k+1})(1-q^{2l+k})]^{1/2} P_{k+1}(\lambda) - q^{k+l-1}\, [(1-q^k)(1-q^{2l+k-1})]^{1/2} P_{k-1}(\lambda)$$

$$+ (q^k - q^{2k+2l} + q^{2l+k-1} - q^{2k+2l-1})\, P_k(\lambda) = (1 - q^{-1})\, \lambda\, P_k(\lambda). \tag{7.2}$$

Upon making the substitution

$$P_k(\lambda) = [(q^{2l}; q)_k / (q; q)_k]^{1/2}\, q^{-lk}\, P_k'(\lambda)$$

in this recurrence relation, one derives the equation

$$-q^k\, (1 - q^{2l+k})\, P_{k+1}'(\lambda) - q^{k+l-1}\, (1 - q^k)\, P_{k-1}'(\lambda)$$

11

$$+ (q^k - q^{2k+2l} + q^{2l+k-1} - q^{2k+2l-1}) P'_k(\lambda) = (1 - q^{-1}) \lambda P'_k(\lambda).$$

This is the recurrence relation for the little q-Laguerre (Wall) polynomials

$$p_k(q^y; q^{2l-1}|q) = {}_2\phi_1(q^{-k}, 0; \; q^{2l}; \; q; q^{y+1}) = (q^{1-2l-k}; q)_k^{-1} \, {}_2\phi_0(q^{-k}, q^{-y}; \; -; \; q; q^{y-2l+1})$$

with $q^y = (1 - q^{-1})\lambda$. Thus, we have $P'_k(\lambda) = p_k(q^y; q^{2l-1}|q)$, $q^y = (1 - q^{-1})\lambda$, and, consequently,

$$P_k(\lambda) = [(q^{2l}; q)_k/(q; q)_k]^{1/2} q^{-lk} \, p_k(q^y; q^{2l-1}|q). \tag{7.3}$$

This means that eigenfunctions of the operator H_2 are of the form

$$\chi_\lambda^l(x) = \sum_{k=0}^{\infty} q^{(1-6l)k/4} \frac{(q^{2l}; q)_k}{(q; q)_k} \, p_k(q^y; q^{2l-1}|q) \, x^k, \quad q^y = (1 - q^{-1})\lambda.$$

To sum up the right-hand side of this relation, one needs to know a generating function

$$F(x; t; a|q) := \sum_{n=0}^{\infty} \frac{(aq; q)_n}{(q; q)_n} \, p_n(x; a|q) \, t^n \tag{7.4}$$

for the little q-Laguerre polynomials

$$p_n(x; a|q) := {}_2\phi_1(q^{-n}, 0; \; aq; \; q; qx) = (a^{-1}q^{-n}; q)_n^{-1} \, {}_2\phi_0(q^{-n}, x^{-1}; \; -; \; q; x/a). \tag{7.5}$$

To evaluate (7.4), we start with the second expression in (7.5) in terms of the basic hypergeometric series ${}_2\phi_0$. Substituting it into (7.4) and using the relation

$$(q^{-n}; q)_k/(q; q)_k = (-1)^k q^{-kn+k(k-1)/2} (q; q)_n/(q; q)_k (q; q)_{n-k},$$

one obtains that

$$F(x; t; a|q) = \sum_{n=0}^{\infty} (-aqt)^n q^{n(n-1)/2} \sum_{k=0}^{n} \frac{(x^{-1}; q)_k}{(q; q)_k (q; q)_{n-k}} (q^{-n} x/a)^k. \tag{7.6}$$

Interchanging the order of summations in (7.6) leads to the desired expression

$$F(x; t; a|q) = E_q(-aqt) \, {}_2\phi_0(x^{-1}, 0; \; -; \; q; xt), \tag{7.7}$$

where $E_q(z) = (-z; q)_\infty$ is the q-exponential function of Jackson.

Similarly, if one substitutes into (7.4) the explicit form of the little q-Laguerre polynomials in terms of ${}_2\phi_1$ from (7.5), this yields an expression

$$F(x; t; a|q) = \frac{E_q(-aqt)}{E_q(-t)} \, {}_2\phi_1(0, 0; \; q/t; \; q; qx). \tag{7.8}$$

Using the explicit form of the generating function (7.7) for the little q-Laguerre polynomials, we arrive at

$$\chi_\lambda^l(x) = (q^{(2l+1)/4} x; q)_\infty \, {}_2\phi_0(q^{-y}, 0; \; -; \; q; q^{y-(6l-1)/4} x), \tag{7.9}$$

where, as before, $q^y = (1 - q^{-1})\lambda$. Another expression for $\chi_\lambda^l(x)$ can be written by using formula (7.8).

Due to the orthogonality relation

$$(q^{2l}; q)_\infty \sum_{k=0}^\infty \frac{q^{2lk}}{(q;q)_k} \, p_m(q^k; q^{2l-1}|q) \, p_n(q^k; q^{2l-1}|q) = \frac{q^{2ln}(q;q)_n}{(q^{2l};q)_n} \, \delta_{mn} \qquad (7.10)$$

for little q-Laguerre polynomials (see formula (3.20.2) in [14]), spectrum of the operator H_2 coincides with the set of points $q^n/(1-q^{-1})$, $n = 0, 1, 2, \cdots$. This means that the eigenfunctions

$$\chi^l_{\lambda_n}(x), \quad n = 0, 1, 2, \cdots, \quad \lambda_n = q^n/(1 - q^{-1}), \qquad (7.11)$$

constitute a basis in the representation space. We thus proved the following theorem.

Theorem 5. *The operator H_2 has a simple discrete spectrum, which consists of the points $q^n/(1 - q^{-1})$, $n = 0, 1, 2, \cdots$. The corresponding eigenfunctions $\chi^l_{\lambda_n}$ form an orthogonal basis in the space $\mathcal{H}_l$.*

We conclude this section by calling attention to the circumstance that operators with bounded discrete spectra, representable by a Jacobi matrix, are important for studying families of q-orthogonal polynomials and their dual properties. A detailed discussion of several examples of such type can be found in [16].

References

[1] L. D. Landau and E. Lifshitz, *Quantum Mechanics*, Addison–Wesley, Reading, Mass., 1968.

[2] A. Ballesteros and S. M. Chumakov, *On the spectrum of a Hamiltonian defined on* $\mathrm{su}_q(2)$ *and quantum optical models*, J. Phys. A: Math. Gen. **32** (1999), 6261–6269.

[3] N. M. Atakishiyev and P. Winternitz, *Bases for representations of quantum algebras*, J. Phys. A: Math. Gen. **33** (2000), 5303–5313.

[4] N. M. Atakishiyev and A. U. Klimyk, *Diagonalization of operators and one-parameter families of nonstandard bases for representations of* $\mathrm{su}_q(2)$, J. Phys. A: Math. Gen. **35** (2002), 5267–5278.

[5] N. M. Atakishiyev and A. U. Klimyk, *Hamiltonian type operators in representations of the quantum algebra* $\mathrm{su}_q(1,1)$, Proc. Inst. Math., National Academy of Sciences, Ukraine, to appear.

[6] N. M. Atakishiyev and A. U. Klimyk, *Hamiltonian type operators in representations of the quantum algebra* $U_q(\mathrm{su}_{1,1})$, **e**-arXiv: math.QA/0305368.

[7] N. M. Atakishiyev and A. U. Klimyk, *Hamiltonian operators in noncommutative world*, Contemp. Math., to appear.

[8] M. Li and Y.-S. Wu (eds.), *Physics in Noncommutative World: I. Field Theories*, Rinton Press, Princeton, NJ, 2002.

[9] G. Gasper and M. Rahman, *Basic Hypergeometric Functions*, Cambridge University Press, Cambridge, 1990.

[10] I. M. Burban and A. U. Klimyk, *Representations of the quantum algebra $U_q(\mathrm{su}_{1,1})$*, J. Phys. A: Math. Gen. **26** (1993), 2139–2151.

[11] A. U. Klimyk and I. I. Kachurik, *Spectra, eigenvalues and overlap functions for representation operators of q-deformed algebras*, Commun. Math. Phys. **175** (1996), 89–111.

[12] J. Shohat and J. D. Tamarkin, *The Problem of Moments*, American Mathematical Society, Providence, RI, 1950.

[13] Ju. M. Berezanskii, *Expansions in Eigenfunctions of Selfadjoint Operators*, American Mathematical Society, Providence, RI, 1968.

[14] R. Koekoek and R. F. Swarttouw, *The Askey-scheme of Hypergeometric Orthogonal Polynomials and Its q-Analoque*, Delft University of Technology, Report 98–17; available from `ftp.tudelft.nl`.

[15] N. M. Atakishiyev and A. U. Klimyk, *Diagonalization of representation operators for the quantum algebra $U_q(\mathrm{su}_{1,1})$*, Methods of Functional Analysis and Topology **8**, No.3 (2002), 1–12.

[16] N. M. Atakishiyev and A. U. Klimyk, *On q-orthogonal polynomials, dual to little and big q-Jacobi polynomials*, J. Math. Anal. Appl., to appear; **e**-arXiv: math.CA/0307250.

SEARCH FOR THE MIXED STATES OF STRONG INTERACTION MATTER-- PHASE TRANSITION AT LOW TEMPERATURE.

O.B. Abdinnov,N.S.Angelov,B.Z.Belashev,Ya.G.Guseynaliyev, M.K.Suleymanov,A.S.Vodopianov .

Abstract

The experimental results on some centrality depending characteristics of hadron-nuclear and nuclear-nuclear interactions at high energies demonstrate the regime changes. Appearance of the strong interaction matter's mixed states is considered as a cause of the regime changes. These states are predicted by QCD for temperatures less than critical ones for deconfinement of strong interaction matter . These conditions could be obtained in the energy regions covered by the beams at GSI, Dubna and AGS facilities. The effects of a percolation cluster formation, apparition of the diquark condensate and critical nuclear transparency are considered as the phenomena connected with the mixed states. It is supposed that the results of the analysis of these effects depending on the centrality could give an information on the mixed states.

1. Introduction.

One of the important experimental methods to get the information on the changes of states of nuclear matter with increasing its baryon density is to study the characteristics of hadron-nuclear and nuclear-nuclear interactions depending on centrality of collisions (Q) at high energies. There are some results obtained in these experiments for the interactions of π -mesons, protons and nuclei with nuclei at energies less then SPS' energies which demonstrate the existing of the regime changes in these dependencies . We want to demonstrate some of them and before it is necessary to note that in the different experiments the values of Q are defined by the different ways. Therefore it is very difficult to compare the presented results on Q-dependencies in the different papers .

1.1. Experimental results on the centrality dependencies.

1.2 The interactions of the π^--mesons.

In fig. 1 is shown the Q-dependence of event number for π^- ^{12}C - interactions at the momentum 40 GeV/c. To determine the Q a number of protons with momentum less then 1.0 GeV/c was used. The figure was obtained from papers [1]. The point of regime change is observed in this dependence at the values of Q ~ 3-4 was used to select the events with total disintegration of nuclei(or central collisions).

1.3 The interactions of the protons.

In fig. 2 are shown the average values of pseudorapidity η = -log((tg(θ/2)) for s-particles (the particles with β > 0.7) depending on the number of g-particles (the particles with $\beta \leq 0.7$) for p+Em reactions at the moment P_0 = 4.5; 24.0; 50.0; 67.0 and 200.0 GeV/c. So in this work the Q was defined as the number of g-particles. This figure was obtained from the paper [2]. The dashed line in the figure corresponds to the cascade-evaporation model calculation . There are the points of regime change in these distributions. As we could see the cascade - evaporation model calculations can't numerically describe these distributions.
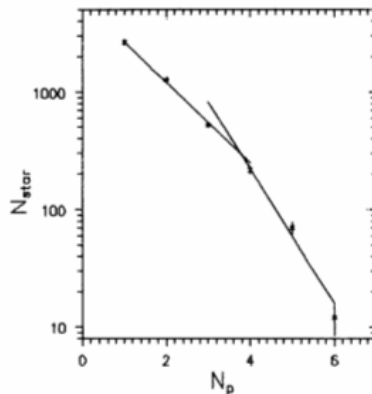
Fig.1.N_p–dependence of the events' number for π^- ^{12}C - interactions at the momentum 40 GeV/c.
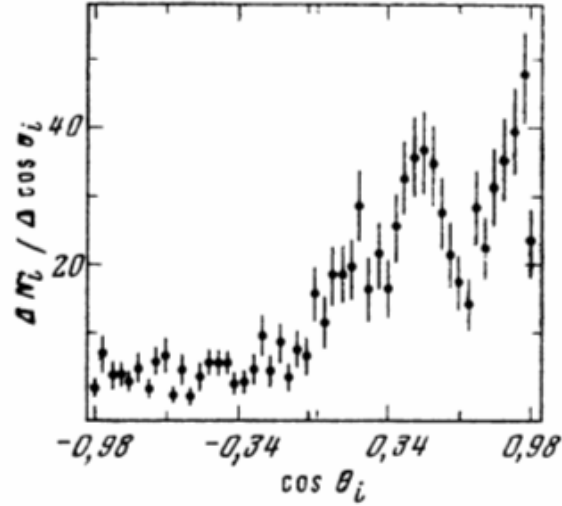
Fig.2 Average values of pseudorapidity $\eta_c=-\log(\tan(\theta/2))$ for s-particles depending on the
g-particles for pEm-reactions . The dashed line correspond to the cascade evaporation
model calculation.

The preliminary integrated K^0_s yield in p+Au reactions at 18 GeV/c versus the number of slow particles emitted in the event is show in next figure (fig.3). The number of slow particles Q was used as the Q. We could also see the points of regime change in this figure. The figure was obtained from paper [3].
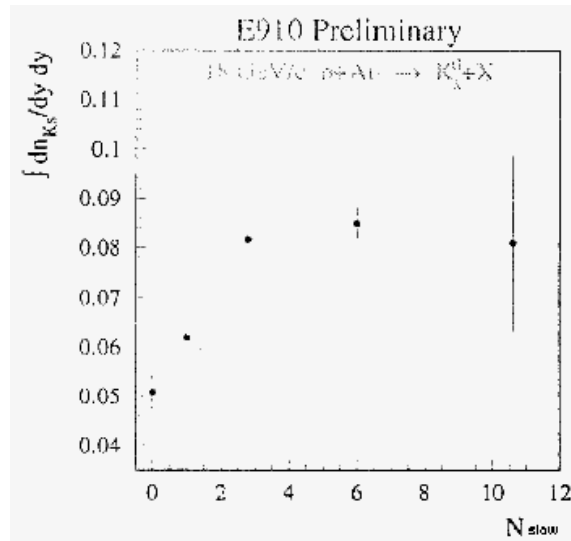
Fig.3. The preliminary integrated K_S^0 yield in p+Au reactions at 18 GeV/c versus
the number of slow particles emitted in the event as measured by E910.

1.4 The interactions of the nuclei.

Fig . 4 shows the Q-dependencies of events' number for dC, ^{4}HeC and ^{12}CC interactions at the momentum 4.2 A GeV/c . The number of all protons in an event was used as the Q. We could see the points of regime changes in this figure. It is also seen that for all considered interactions the forms of distributions are nearly similar.

Fig.4. The Q-dependencies of events' number for dC, ^{4}HeC and ^{12}CC
interactions at the momentum of 4.2 A GeV/c

In fig. 5 the average multiplicity of relativistic charged particles depending on Q are shown for the ^{28}S$_{14}$ + Em -- reactions at the energies of 3.8 and 14.6 GeV per nucleon. To determine the Q a number of charged projectile fragments (Z$_f$) were used. The figures were obtained from the paper [4]. The points of regime change are observed in these dependencies. These points were used by the authors to select the central collisions events.

Fig.5. The average multiplicity of the relativistic charged particles depending
on Q for the ^{28}S$_{14}$ + Em -- reactions at the energies of 3.8(a) and

14.6 GeV(b) per nucleon.

The N_h^B-dedendences (N_h^B is a number of h-particles with emitted angle $\theta > 90^0$) of the average multiplicity $<n_s^F>$ of s-particles (with emitted angle $\theta < 90^0$) for C^{12}Em reactions at the momentum 4.5 GeV/c are shown in fig . 6. The figure was obtained from paper [5]. The number of N_h^B are used as the Q. We could also see the point of regime change in this distribution.

Fig.6. The N_h^B- dependencies of the average multiplicity $<n_s^F>$ of s-particles
for C^{12}Em reactions at the momentum 4.5 GeV/c .

Thus the demonstrated figures show that there are the points of regime change for the behavior of the centrality dependencies for some characteristics of hadron -- nuclear and nuclear -- nuclear interactions . Prof. Zinovyev offered to us to consider the appearance of the mixed states of nuclear matter as a reason of these results. He directed our attention to the some predictions of QCD.

Before then to continue the discussion we want to note that in paper [6] it was found that the experimental results on transverse mass spectra of kaons produced in central Pb+Pb (Au+Au) interactions show an anomalous dependence on the collision energy. The inverse slopes of the spectra increase with energy in the low (AGS) and high (RHIC) energy domains, whereas they are constant in the intermediate (SPS) energy range. They argued that this anomaly is probably caused by a modification of the equation of state in the transition region between confined and deconfined matter and they were writeen that this observation may be considered as a new signal, in addition to the previously reported anomalies in the pion and strangeness production, of the onset of deconfinement located in the low SPS energy domain.

2. Prediction of QCD for mixed states.

QCD predicts that at high energy density, hadronic matter will turn into a plasma of deconfined quarks and gluons [7]. It is expected that the temperature of hadron mutter T will be
$T > T_c \cong$ 150-200 MeV and μ_B will be $\mu_B > \mu_{B\,c}$ (μ_B increases with the barion charge). It is a new phase of nuclear matter. The T_c could be reached at energies of SPS, RICH and LHC.

In fig. 7 are shown the dependence of the values of T on the values of μ_B for the simple QCD model -- the phase diagram (from review [8]). There are three phases in this diagram. The first phase correspond to the values of T $< T_c$ and $\mu_B < \mu_{Bc}$ which are named the phase of hadron matter. The second phase is the phase of diquark condensate at $T < T_c$ and $\mu_B > \mu_{Bc}$. The third phase is the quark gluon plasma one at $T > T_c$ and $\mu_B > \mu_{B\,c}$.

To explain the above mentioned results we consider the possibility of phase transition at $T < T_c$ in the system with high barion density (at high μ_B). In such systems the neighbouring nucleons could form the percolation cluster and neighbouring quarks could form the diquarks (fig.8). So these systems are a mixed system (MS) of pressed nucleons (clusters) and diquarks which could appearance at energies of GSI, Synchrophasotron (Nuclatron) and AGS.

Experimental information on the conditions of appearance of the MS could give the possibilities to fix the onset of the deconfinement which are important for forth separate the effects connected with deconfinement of strong interaction matter from another effects.

3. Experimental possibilities to search signal on mixed states.

The regime changes which were above shown could be better points to appearance of MS in the high energy interactions, but they are not enough to assert it. For full confirm the appearance and existing of the MS it is necessary to get the additional experimental information because to explain the appearance the regime changes could be used many another ideas which don't included the MS and the accompanied effects.

What could experimental information been got to confirm the appearance of MS?

Fig.7 The phase diagram.

Fig.8. Physical picture of MS formation.

Let us discuss the experimental possibilities to get the signal on the MS. First of all we have to answer on one question, what experimental observable effects could the MS be accompanied? It is been clear that the first effect is a cluster formation (in the result of percolation), the second effect could be the appearance of meson condensation (which could form as the result of hadronisation of diquarks). As we have already noted three phase of hadronic matter are consider in review [8] which would correspond to the succession of insulator, superconductor and conductor in atomic matter in the phase diagram. The succession of superconductor will correspond to the MS and therefore the MS appearance could be accompanied with high transparency of nuclear matter. Here it is necessary to note that above mentioned **effects would be had direct relation to the MS only in this case if they appearance as critical phenomena at some values of Q**. It is the more important request.

4. The main points of the proposal

1. The MS could be form at low temperature which could be reached at energies of building GSI's motions.

2. The MS could form and decay at the some critical values of Q, therefore it could be the reason of the appearance of regime changes in the behaviour of the events' characteristics depending on Q.

3. The processes of MS formation could be accompanied by the effects of percolation cluster formation, appearance of meson condensate and the high transparence of the nuclear mutter. These effects could be used as the signals on MS.

There are some experimental results which could be consider as the confirmations of the existing these effects and as a basis to their forth investigations in the new experimental possibility.

5. Percolation cluster production in interaction of high energy nuclei.

5.1 Percolation cluster as the sours of fragments.

There are many papers in which the processes of nuclear fragmentation [9] and the processes of central collisions [10] are considered as a critical phenomena and are offered to use the percolation approach to explain this phenomena. We have used some ideas from these works to experimental search a signal on percolation cluster. We suppose that in hadron-nucleus and nucleus-nucleus collisions the percolation cluster could appear on the some critical values of Q and would decay into fragments and free nucleons. The number of clusters and the number of fragments would increase with Q in the interval less then the critical values of Q (for MS formation) and then their values would decrease with the increasing Q into the central collisions. It could lead to the regime change in the behavior of different characteristics of events depending on Q and the number of fragments. We believed that if the percolation cluster exist and if it is a sours of fragments so the influences of nuclear fragments on the behaviour of the events' characteristics depending on Q could have a critical character.

To test this idea we the behaviors of the events' number depending on Q have been studied by us. The values of Q ware determined in two variants. In the first variant the values of Q were determined as a number of protons emitted in a event and in second variant as a number of protons and fragments emitted in ones. We have used 20407 ^{12}CC events at the momentum of 4.2 A GeV/c [11]. The experimental data were compared with the simulation data coming from the quark-gluon string model (QGSM) without the nuclear fragments [12]. We want to note that the behavior of the events' number depending on Q determined for both variants have to be similar if there are not a percolation cluster and they would be differ if the percolation cluster is exist as a fragments source.

The distributions of events' number depending on Q are shown in fig. 9a,b . The empty starlets corresponds to first variant of Q-determination, the full starlets correspond to second ones(the fragments were included). It is seen that for the cases then the fragments numbers were included to determine Q the form of the distributions sharply changes and has two steps structure (full starlets in figure 9a).

In fig. 9b are shown the Q-dependencies of the events' number coming from the QGSM. The empty starlets correspond to the without the stripping protons cases and the full starlets correspond to the cases with the stripping protons. It is seen that the form of the distribution strongly differ from the experimental one in fig. 9a. There is no two steps structure in this figure. Therefore we could assure that observed difference connects with fragments influence. This result

Fig.9. The distributions of events' number depending on Q for the ^{12}CC events
   at the momentum of 4.2 A GeV/c ; a)the experimental data b) the simulation
   data.

demonstrate that the influence of nuclear fragmentation processes in the behavior of the events' number depending on Q has a critical character.

To explain this result we could suppose that it could be connect with the existence of percolation cluster. It is possible that with increasing Q the probability of cluster formation grows but further increasing the Q (in the region of high Q) leads to the big cluster decay on nuclear fragments and then free nucleons. It could be reason of the observed the two step structure in the distributions. The first step connected with the formation of percolation cluster and second one with its decay(fig.10). The GSI results on multifragment production at high energy nucleus-nucleus interaction could give the additional confirmations for it [13]. So in fig. 11a,b are shown the mean multiplicity of intermediate mass fragments produced in nucleus-nucleus collisions at GSI energies as a function of Z_{bound} (the last fixes the centrality of collisions). It is seen that the mean multiplicity of fragments is maximum in the region of first step.

Fig.10   Physical picture of interaction.

Fig.11a Mean multiplicity of   Fig.11b. Left panel: Mean multiplicity of
intermediate mass fragments   intermediate mass fragments as a function

as a function of Z_{bound} for the reaction Au+Au at E/A=400, 600,800 and 1000 MeV. of Z_{bound} for the reaction ^{238}U on ^{197}Au (circles), ^{197}Au on ^{197}Au (squares) and ^{129}Xe On ^{197}Au(triangles) at E/A=600 MeV. Right panel: the same data after normalizing both quantities with respect to the atomic number Z_p of the projectile.

So the experimental results obtained in the interactions of π-mesons, protons and nuclei with nuclei at high energy demonstrate that the influence of nuclear fragmentation processes in the behavior of the event's number depending on Q has also a critical character. It could be explained with the existence of percolation cluster and with appearance of MS of nuclear matter.

5.2 Anomaly pick in angular distribution of protons.

The existing of percolation cluster could explain the experimental results on the angular distributions of emitted protons in π^{-12}C -interactions at momentum 40 GeV/c[14]. In this experiments the angular distributions of protons (with the momentum less then 1.0 GeV/c) were

Fig.12 Angular distributions of protons emitted in π^{-12}C -interactions at momentum 40 GeV/c.

studied in the events with total disintegration of nuclei (or central collisions). This distribution are shown in fig. 12. It is seen the anomalous peak in this distribution. The result on the angular distributions of protons emitted in π^{-12}C -interactions at momentum 5 GeV/c [15] confirm the existing of anomalous peak (fig.13). Many years we could not explain this result. Now we think that it could connect with formation and decay of the percolation cluster.

6. Meson condensate in nucleus-nucleus collisions at high energies.

The another accompanied effect for the processes of MS formation could be the effect of meson condensate appearance as the result of diquark hadronisation. The idea on meson condensate formation was predicted [16] many years age. But up to now there are no the experimental results direct confirm this idea. It mainly connects by the absent the setup which could high accuracy measure the slow π^0 -mesons' characteristics a long time. Now there are setup TAPS [17] which can measure the slow π^0 -mesons' characteristics with high accuracy. When we analyzed some results from this setup [17] we found the results which could be interesting for the experimental search the meson condensate. In these papers the temperature of the slow π^0 -mesons were defined as a slop of the spectrums which are shown in the fig.14a-c. It were found one temperature for interactions of light nuclei and two temperature for the heavy ions' ones.

It is very interesting the result at low m_t the behavior of the spectrums differ from the exponential law(from these figures). We think that some part of these deviation could connect with the meson condensate . It increase with mass of the interactions nuclei and depend on centrality(fig.14a-c). The last is an main argument confirm that observed deviation could connect with the meson condensate.

We think to study the behaviour of the $f(m_t,y)$ depending on mass of colliding hadrons and nuclei and on the centrality of collisions and the number of fragments could give the information on the meson condensate.

Fig.13 Angular distributions of protons emitted in π^{-12}C -interactions at the momentum 5 GeV/c.

7. Nuclear transparency at high energy hadron-nuclear and nuclear – nuclear interactions

The else one accompanying effect of the MS formation process could be high critical nuclear transparency which could connect with the appearance of the superconductor property of nuclear matter in MS. As we have noted (in section 3) when the MS appearance the conduction of nuclear environment sharply increase and matter is getting the superconductor properties because of that the nucleons mast be bound in the result of nucleon and quark percolation in this system. It could led critical violation of the angular correlations of particle production .

8. Conclusion.

Thus the experimental results obtained in the energies region less then SPS energy on hadron-nuclear and nuclear-nuclear interactions demonstrate the existing of regime changes in the behaviour of events' characteristics depending on centrality. The appearance of the stronginteraction matter mixed states are discussed as a reason of it. The percolation cluster formation , appearance of meson condensate and high critical nuclear transparency are

considered as the accompanied effects of the mixed systems.   Some experimental results obtained in different experimental groups could be considered as the confirmations on the being of percolation cluster and   meson condensate. But for full confirm the formation of mixed systems it is necessary to forth investigation of these effects and their connections with mixed systems.

Fig.14a Transverse-mass spectra of π^0
   and η-mesons in the covered rapidity
   intervals Δy near midrapidity.

Fig.14b Transverse-mass spectra of π^0
   and η-mesons for Au+Au interactions at
   0.8 A MeV.

Fig.14c. Transverse-mass spectra of π^0 and η-mesons for Au+Au interactions at 0.8 A MeV.
    a) in noncentral collisions; b) in central collisions.

1.   O.B. Abdinov et al. JINR Rapid communications No 1[75]-96 p.51].
2.   S.Vokal,M.Sumbera.Yad.Fiz.39:1474(1984)
3.   C.A. Ogilvie.J.Phys.G.Nucl.Part.Phys.,25(1999),p.159.
4.   M.I. Tretyakova. EMU-01 Collaboration. Proceeding of the Xith International Seminar on High Energy Physics Problems. Dubna, JINR, 1994.,p.616-626.
5.   A.Abdelsalam et al. JINR E1-82-509, Dubna,1982.
6.   M.I. Gorensteina,b, M. Ga´zdzickic,d and K.A. Bugaeva. E-print :hep-ph/0303041 v1 5 Mar 2003
7.   H. Satz. Nucl. Phys. A661: 104-118, 1999
8.   H. Satz. E-print: hep-ph/0007069,v1 7 Jul 2000.
9.   J. Desbois, Nucl. Phys. A466, 724 (1987): J. Nemeth et al. Z.Phys.a 325, 347 (1986); S. Leray
    et al. Nucl. Phys. A511 (1990) p. 414- 428; A.J. Santiago and K.C. Chung J. Phys. G:Nucl.
    Part. Phys. 16 (1990) p. 1483 – 1492; G.Musulmanbekov, A.Al-Haidary. Russian
    J.Nuc.Phys.,v.66,N9,pp.1-9,2003.
10. X.Campi, J. Desbois Proc. 23 Int. Winter Meeting on Nucl. Phys. Bormio, 1985; Bauer W. et
    al. Nucl. Phys. 1986.v.452.p.699; A.S. Botvina, L.V. Lanin. Sov. J. Nucl. Phys. 55: 381 -387,
    1992.
11. N.Akhababian et al.- JINR Preprint 1-12114, Dubna, 1979.; N.S.Angelov et al.- JINR Preprint 1-12424, Dubna,
    1989 ; A.I.Bondorenko et al., JINR Communication, P1-98-292, Dubna, (1998); M. K.Suleimanov et al.
    Phys.Rev.C. 1998, v.58, p.351
12. N.S. Amelin, L.V.Bravina, Sov. J. Nucl. Phys. 51,211,1990; N.S. Amelin et al., Sov. J. Nucl. Phys.50,272,1990
13. W.Resisdorf. Dynamics of multufragmentation in Heavy Ion Collisions. E-print: nucl-ex/0004008,   v.1
14. A.I.Anoshin et al.Yad.Fiz.33:164(1981)
15. O.B.Abdinov et al. Preprint JINR,1-80-859,Dubna (1980)
16. A.B.Migdal, Zh ETF (USSR) 61(1971),2210 Jetp (Sov.Phys) 34_ (1972) 1184; Zh ETF (USSR) 63(1972),1933
    JETP (Sov.Phys) 36 _(19730,1052; R.F. Sawyer,Phys.Rev.Lett.29 (1972),382 ;D.J. Scalapino, Phys.Rev.Lett.
    (1972),386; R.F. Sawyer And D.J. Scalapino, Phys.Rev.D7(1972),953.
17. R. Averbeck et al. Z.Phys.A359:65-73,1997 ; A. Marin et al. Phys.Lett.B409:77-82,1997 ; A. R. Wolf et
    al.Phys.Rev.Lett. Vol.80,N 24,P.5281.

AZƏRBAYCANCA-RUSCA-İNGİLİSCƏ FİZİKİ TERMİNLƏR LÜĞƏTİ

AZERBAIJAN-RUSSIAN-ENGLISH DICTIONARY OF THE PHYSICAL TERMS

АЗЕРБАЙДЖАНО-РУССКО-АНГЛИЙСКИЙ ФИЗИЧЕСКИЙ ТЕРМИНОЛОГИЧЕСКИЙ СЛОВАРЬ

Tərtib edənlər: **AME-nın müxbir üzvü**
A.İ. Muxtarov

SSRİ EA-nın müxbir üzvü,

akademik   **H.M. Abdullayev**

Fizika-riyaziyyat elmləri doktoru
T.R. Mehdiyev

Fizika-riyaziyyat elmləri namizədi
E.A. Axundova

N.İ. Acalova

S.İ. Əliyeva

Biz "Fizika" jurnalının birinci nömrəsində başladığımız fizika terminləri lüğətinin nəşrini davam etdiririk. Bu nəşrdə akademik H.M. Abdullayevin nəşr etdirdiyi "Fizika terminləri lüğəti"ndən də istifadə edilmişdir (AREA-nın nəşri, Bakı, 1965-ci il).

Nəşr olunan terminlər haqda öz qeydlərini və terminlərini göndərən şəxslərə redaksiya əvvəlcədən öz təşəkkürünü bildirir.

Müəlliflər və jurnalın redaksiyası

We continue the publication the terminological physical dictionary, which has been began in the journal "Fizika"№1. In the published variant the physical terms, given by academician H.M. Abdullayev are given ("Fizika terminləri lüğəti", AREA, Bakı, 1965).

The edition of the journal is welcome to all, who will send notes and terms for the publishing dictionary.

Authors and edition of journal "Fizika"

Мы продолжаем публикацию терминологического физического словаря, начатую в первом номере журнала "Fizika". В публикуемом варианте мы также используем физические термины, предложенные академиком Г.М. Абдуллаевым ("Fizika terminləri lüğəti", AREA, Bakı, 1965).

Редакция журнала приветствует всех, кто пришлет свои замечания и термины для публикуемого словаря.

Авторы и редакция журнала"Fizika"

Adsorbsiya izotermləri	Adsorbed isotherm	Адсорбционная изотерма
Adsorbsiya ingibitoru	Adsorption inhibitor	Адсорбционный ингибитор
Adsorbsiya indikatoru, təzyiqi ölçən cihaz	Adsorption indicator	Адсорбционный индикатор
Adsorbsiya potensialı	Adsorption potential	Адсорбционный потенциал
Adsorbsiya qatı	Adsorption layer	Адсорбционный слой
Adsorbsiya cərəyanı	Adsorption current	Адсорбционный ток
Adsorbsiya, cisimlərin üz təbəqəsində maye və qazların udulması	Adsorption	Адсорбция
Azeotropiya	Azeotropy	Азеотропия
Azeotrop destillə etmə	Azeotropic distillation	Азеотропная дистилляция
Azeotrop qarışıq	Azeotropic mixture, azeotrope	Азеотропная смесь
Azeotrop nöqtəsi	Azeotropic point	Азеотропная точка
Azimut	Azimuth	Азимут
Azimutal kvant ədədi	Azimuthal quantum number	Азимутальное квантовое число
Azimutal geomaqnit effekti	Azimutal geomagnetic effect	Азимутальный геомагнитный эффект
Azot	Nitrogen	Азот
Nitrat turşusu	Nitrogen acid	Азотная кислота
Azotlu termometr	Nitrogen thermometer	Азотный термометр
Aysberq, polyar dənizlərdə üzən buz dağı	Iceberg	Айсберг
Akvo-ion	Aquo-ion	Акво-ион
Yeni iqlim mühitinə uyğunlaşma	Acclimatization, acclimation	Акклиматизация
Akumulyator	Accumulator	Аккумулятор
Aklin	Acline	Аклина
Aklin əyrisi	Aclinic line	Аклиническая кривая
Adamın aklin oxşarı	Acline twin	Аклиновый двойник
Akselerometr	Accelerometer	Акселерометр
Aksial moda	Axial mode	Аксиальная мода
Aksial simmetriya	Axial symmetry	Аксиальная симметрия
Aksial vektor	Axial vector	Аксиальный вектор
Arximed aksioması	Archimedes's axiom	Аксиома Архимеда
Sonsuzluq aksioması	Axiom of infinity	Аксиома бесконечности
Seçki aksioması	Axiom of choice	Аксиома выбора
Kəsilməzlik aksioması	Axiom of continuity	Аксиома непрерывности
Paralellik haqda aksioma	Axiom of parallels	Аксиома о параллельных
Ayrılıq aksioması	Separation axiom	Аксиома отдельности
Peano aksioması	Peano's axiom	Аксиома Пеано
Say, hesab aksioması	Countability axiom	Аксиома счетности
Aksiomatizasiya	Axiomatization	Аксиоматизация
Çoxluğun aksioamtik nəzəriyyəsi	Axiomatic set theory	Аксиоматическая теория множеств
Üçbucaq aksioması	Triangle axiom	Аксиома треугольника
Aksonometrik proyeksiya	Axonometric projection	Аксонометрическая проекция
Aksoplazma	Axoplasm	Аксоплазма
Aktivləşdirici. fəallaşdırıcı	Activator	Активатор
Həddindən artıq aktivləşdirilmiş gərginlik	Activation overvoltage	Активационное перенапряжение
Aktivatik analiz	Activation analysis	Активационный анализ
Aktivatik potensial	Activation potential	Активационный потенциал
Aktivasiya	Activation	Активация
Aktivasiya	Activation	Активирование

Aktivləşdirilmiş adsorbsiya	Activated adsorption	Активированная адсорбция
Aktivləşdirilmiş hal	Activated state	Активированное состояние
Aktivləşdirilmiş kompleks (toplu)	Activated complex	Активированный комплекс
Aktivləşdirilmiş kömür	Active carbon	Активированный уголь
Aktiv qravitasiya kütləsi	Active gravitational mass	Активная гравитационная масса
Aktiv zona	Core	Активная зона
Aktiv molekul	Active molecule	Активная молекула
Aktiv güc	Active power	Активная мощность
Günəşdə aktiv oblast	Solar active region	Активная область на Солнце
Aktiv keçiricilik	Conductance	Активная проводимость
Aktiv qəfəs	Active lattice	Активная решетка
Aktiv tərkib hissəsi	Active component	Активная составляющая
Aktiv mühit	Active medium	Активная среда
Aktiv sxem	Active circuit	Активная схема
Aktiv turbin	Impulse turbine	Активная турбина
Aktiv maddə	Active substance	Активное вещество
Aktiv müqavimət	Pure resistance	Активное сопротивление
Aktiv hal	Active state	Активное состояние
Aktivlik, fəallıq	Activity	Активность
İonların aktivliyi	Ion activity	Активность ионов
Optik aktivlik	Optical activity	Активность оптическая
Səthi aktivlik	Surface activity	Активность поверхностная
Termodinamik aktivlik	Thermodynamic activity	Активность термодинамическая
Aktiv azot	Active nitrogen	Активный азот
Aktiv hidrogen	Active hydrogen	Активный водород
Aktiv qaz	Active gas	Активный газ
Aktiv ion	Active ion	Активный ион
Aktiv metal	Active metal	Активный металл
Aktiv protuberans, Günəş səthində közərmiş qaz kütlələri	Active prominence	Активный протуберанец
Aktiv təbəqə	Active layer	Активный слой
Aktiv peyk	Active satellite	Активный спутник
Aktiv mərkəz	Active center	Активный центр
Aktiv elektrod	Active electrode	Активный электрод
Aktiv element	Active element	Активный элемент
Aktin	Actin	Актин
Актиниум	Actinium	Актиний
Aktinoid	Actinoid	Актиноид
Aktinoid sıxma	Actinide contraction	Актиноидное сжатие
Aktinometr, Günəş şüalarının intensivliyini ölçən cihaz	Actinometer	Актинометр
Aktinometriya	Actinometry	Актинометрия
Aktinouran	Actinouranium	Актиноуран
Aktomiozin	Actomyosin	Актомиозин
Akustika, səs bəhsi	Acoustics	Акустика
Akustik-maqnit-elektrik effekti	Acoustomagnetoelectric effect	Акустикомагнитоэлектрический эффект
Akustimetr	Acoustimeter	Акустиметр
Akustik qoloqrafiya	Acoustic holography	Акустическая голография
Akustik tutum	Acoustic capacitance	Акустическая емкость
Akustik linza	Acoustic lens	Акустическая линза
Akustik kütlə	Acoustic mass	Акустическая масса
Akustik moda, dəb, adət	Acoustic mode	Акустическая мода
Akustik əks əlaqə	Acoustic feedback	Акустическая обратная связь

Akustik tez təsir altına düşmək	Acoustic compliance	Акустическая податливость
Akustik sistem	Acoustic system	Акустическая система
Akustik tezlik	Acoustic frequency	Акустическая частота
Akustik boru	Acoustic pipe	Акустическая труба
Akustik xarakteristika	Acoustic characteristic	Акустическая характеристика
Akustik dalğalar	Acoustic waves	Акустические волны
Akustik rəqslər	Acoustic oscillation	Акустические колебания
Akustik külək	Acoustic wind	Акустический ветер
Akustik hündürlük ölçən	Acoustic altimeter	Акустический высотомер
Akustik detektor	Acoustic detector	Акустический детектор
Omun akustika qanunu	Acoustic law of Ohm	Акустический закон Ома
Akustik zond	Probe microphone	Акустический зонд
Akustik impedans	Acoustic impedance	Акустический импеданс
Akustik interferometr	Acoustic interferometer	Акустический интерферометр
Akustik səslər qarışığı	Acoustic labyrinth	Акустический лабиринт
Akustik Om	Acoustic ohm	Акустический Ом
Akustik dəyişdirici aparat	Acoustic transformer	Акустический преобразователь
Akustik dərinliyi ölçən	Acoustic depth sounding	Акустический промер глубины
Akustik rezonans	Acoustic resonance	Акустический резонанс
Akustik siqnal	Acoustic signal	Акустический сигнал
Akustik spektr	Acoustic spectrum	Акустический спектр
Akustik filtr	Acoustic filter	Акустический фильтр
Akustik element	Acoustic element	Акустический элемент
Akustik effekt	Acoustic effect	Акустический эффект
Akustik ölçmə	Acoustic measurement	Акустическое измерение
Akustik xəyal	Acoustic image	Акустическое изображение
Akustik müqavimət	Acoustic resistance	Акустическое сопротивление
Akustooptik modulyasiya, səsin bir tonundan digərinə keçmə	Acoustooptic modulation	Акустооптическая модуляция
Akustooptik mühit	Acoustooptical medium	Акустооптическая среда
Akustooptik element	Acoustooptical element	Акустооптический элемент
Akustooptik effekt	Acoustooptical effect	Акустооптический эффект
Akustooptik kənaraçıxma	Acoustooptical deflection	Акустооптическое отклонение
Akustoelektrik cərəyan	Acoustoelectric current	Акустоэлектрический ток
Akustoelektrik effekt	Acoustoelectric effect	Акустоэлектрический эффект
Akseptor,. hidrogen atomunu özünə birləşdirən maddə	Acceptor	Акцептор
Akseptor qarışıq	Acceptor impurity	Акцепторная примесь
Akseptor atom	Acceptor atom	Акцепторный атом
Akseptor səviyyə	Acceptor level	Акцепторный уровень
Protonun akseptoru	Proton acceptor	Акцептор протона
Elektronların akseptoru	Electron acceptor	Акцептор электронов
Cəbr	Algebra	Алгебра
Jordan cəbri	Jordan algebra	Алгебра Жордана
Cəbr həndəsəsi	Algebraic geometry	Алгебраическая геометрия
Cəbr qrupu	Algebraic group	Алгебраическая группа
Cəbri asılılıq	Algebraical dependence	Алгебраическая зависимость
Cəbri əyri	Algebraic curve	Алгебраическая кривая
Cəbri qeyri-asılılıq	Algebraical independence	Алгебраическая независимость
Cəbri məxsusi nöqtə	Algebraic singularity	Алгебраическая особая точка
Cəbri səth	Algebraic surface	Алгебраическая поверхность
Cəbri alt qrup	Algebraic subgroup	Алгебраическая подгруппа
Cəbri sistem	Algebraic system	Алгебраическая система
Cəbri quruluş	Algebraic structure	Алгебраическая структура

Cəbri cəm	Algebraic sum	Алгебраическая сумма
Cəbri topologiya	Algebraic topology	Алгебраическая топология
Cəbri nöqtə	Algebraic point	Алгебраическая точка
Cəbri şaxələnmə nöqtəsi	Algebraic branch-point	Алгебраическая точка разветвления
Cəbri funksiya	Algebraic function	Алгебраическая функция
Cəbri asılı olma	Algebraically dependent	Алгебрачески зависимый
Cəbri qapalı sahə	Algebraically closed field	Алгебрачески замкнутое поле
Cəbri analiz	Algebraic analysis	Алгебраический анализ
Cəbri asılı olmamaq	Algebraically independent	Алгебраический независимый
Cəbri müxtəliflik, cürbəcürlük	Algebraic variety	Алгебраическое многообразие
Cəbri genişlənmə	Algebraic extension	Алгебраическое расширение
Cəbri həll	Algebraic solution	Алгебраическое решение
Cəbri uyğunluq	Algebraic correspondence	Алгебраическое соответствие
Cəbri tənlik	Algebraic equation	Алгебраическое уравнение
Məntiqin cəbri	Algebra of logic	Алгебра логики
Matrisalar cəbri	Matrix algebra	Алгебра матриц
Assosiatik dərəcəli cəbr	Power associative algebra	Алгебра ассоциативными степенями
Cəbrli funksiya	Algebroid function	Алгеброидная функция
Alqoritmik dil	Algorithmic language	Алгоритмический язык
Alidada	Alidade	Алидада
Alifatik birləşmə	Aliphatic compound	Алифатическое соединение
Alisiklik birləşmə	Alicyclic compound	Алициклическое соединение
Alkalimetriya	Alkalimetry	Алкалиметрия
Alkidli qatran	Alkid resin	Алкидная смола
Allometriya	Allometrism	Аллометрия
Allotropluq	Allotropy	Аллотропия
Allosterik ferment	Allosteric enzyme	Аллостерический фермент
Allotropik çevirmə	Allotropyc transformation	Аллотропическое превращение
Almaz quruluşu	Diamond structure	Алмазная структура
Əlifbalı-ədədi	Alphanumeric	Алфавитно-цифровой
Əlifbalı kod	Alphabetic code	Алфавитный код
Albedo	Albedo	Альбедо
Yerin albedosu	Earth albedo	Альбедо Земли
Albedometr	Albedometer	Альбедометр
Aldehid	Aldehyde	Альдегид
Almukantarat	Almucantar	Альмукантарат
Altazimutal montaj etmə	Altazimuth mounting	Альтазимутальная монтировка
Altazimutal qurğu	Altazimuth mounting	Альтазимутальная установка
Alternativ fərziyyə	Alternative hypothesis	Альтернативная гипотеза
Alfa-fəal nüvə	Alpha-radioactive nucleus	Альфа-активное ядро
Alfa-şüalandıran	Alpha emitter	Альфа-излучатель
Alfa-dəmir	Alpha ferrum	Альфа-железа
Alfa-şüalar	Alpha rays	Альфа-лучи
Alfa-çevrilmə	Alpha-decay, alpha disintegration	Альфа-распад
Alfa-spektr	Alpha-ray spectrum	Альфа-спектр
Alfa-spektrometr	Alpha-ray spectrometer	Альфа-спектрометр
Alfatron	Alphatron	Альфатрон
Alfa-zərrəcik	Alpha particle	Альфа-частица
Alüminium kulometri	Aluminium coulometer	Алюминиевой кулометр
Alüminium	Aluminium, aluminum	Алюминий
Amakrin qəfəsi	Amakrine cell	Амакриновая клетка
Amalqama	Amalgam	Амальгама
Amalqam elektrodu	Amalgam electrode	Амальгамный электрод

Adsorbed isotherm	Адсорбционная изотерма	Adsorbsiya izotermləri
Adsorption inhibitor	Адсорбционный ингибитор	Adsorbsiya ingibitoru
Adsorption indicator	Адсорбционный индикатор	Adsorbsiya indikatoru, təzyiqi ölçən cihaz
Adsorption potential	Адсорбционный потенциал	Adsorbsiya potensialı
Adsorption layer	Адсорбционный слой	Adsorbsiya qatı
Adsorption current	Адсорбционный ток	Adsorbsiya cərəyanı
Adsorption	Адсорбция	Adsorbsiya, cisimlərin üz təbəqəsində maye və qazların udulması
Azeotropy	Азеотропия	Azeotropiya
Azeotropic distillation	Азеотропная дистилляция	Azeotrop destillə etmə
Azeotropic mixture, azeotrope	Азеотропная смесь	Azeotrop qarışıq
Azeotropic point	Азеотропная точка	Azeotrop nöqtəsi
Azimuth	Азимут	Azimut
Azimuthal quantum number	Азимутальное квантовое число	Azimutal kvant ədədi
Azimutal geomagnetic effect	Азимутальный геомагнитный эффект	Azimutal geomaqnit effekti
Nitrogen	Азот	Azot
Nitrogen acid	Азотная кислота	Nitrat turşusu
Nitrogen thermometer	Азотный термометр	Azotlu termometr
Iceberg	Айсберг	Aysberq, polyar dənizlərdə üzən buz dağı
Aquo-ion	Акво-ион	Akvo-ion
Acclimatization, acclimation	Акклиматизация	Yeni iqlim mühitinə uyğunlaşma
Accumulator	Аккумулятор	Akumulyator
Acline	Аклина	Aklin
Aclinic line	Аклиническая кривая	Aklin əyrisi
Acline twin	Аклиновый двойник	Adamın aklin oxşarı
Accelerometer	Акселерометр	Akselerometr
Axial mode	Аксиальная мода	Aksial moda
Axial symmetry	Аксиальная симметрия	Aksial simmetriya
Axial vector	Аксиальный вектор	Aksial vektor
Archimedes's axiom	Аксиома Архимеда	Arximed aksioması
Axiom of infinity	Аксиома бесконечности	Sonsuzluq aksioması
Axiom of choice	Аксиома выбора	Seçki aksioması
Axiom of continuity	Аксиома непрерывности	Kəsilməzlik aksioması
Axiom of parallels	Аксиома о параллельных	Paralellik haqda aksioma
Separation axiom	Аксиома отдельности	Ayrılıq aksioması
Peano's axiom	Аксиома Пеано	Peano aksioması
Countability axiom	Аксиома счетности	Say, hesab aksioması
Axiomatization	Аксиоматизация	Aksiomatizasiya
Axiomatic set theory	Аксиоматическая теория множеств	Çoxluğun aksioamtik nəzəriyyəsi
Triangle axiom	Аксиома треугольника	Üçbucaq aksioması
Axonometric projection	Аксонометрическая проекция	Aksonometrik proyeksiya
Axoplasm	Аксоплазма	Aksoplazma
Activator	Активатор	Aktivləşdirici. fəallaşdırıcı
Activation overvoltage	Активационное перенапряжение	Həddindən artıq aktivləşdirilmiş gərginlik
Activation analysis	Активационный анализ	Aktivatik analiz
Activation potential	Активационный потенциал	Aktivatik potensial
Activation	Активация	Aktivasiya
Activation	Активирование	Aktivasiya
Activated adsorption	Активированная адсорбция	Aktivləşdirilmiş adsorbsiya

Activated state	Активированное состояние	Aktivləşdirilmiş hal
Activated complex	Активированный комплекс	Aktivləşdirilmiş kompleks (toplu)
Active carbon	Активированный уголь	Aktivləşdirilmiş kömür
Active gravitational mass	Активная гравитационная масса	Aktiv qravitasiya kütləsi
Core	Активная зона	Aktiv zona
Active molecule	Активная молекула	Aktiv molekul
Active power	Активная мощность	Aktiv güc
Solar active region	Активная область на Солнце	Günəşdə aktiv oblast
Conductance	Активная проводимость	Aktiv keçiricilik
Active lattice	Активная решетка	Aktiv qəfəs
Active component	Активная составляющая	Aktiv tərkib hissəsi
Active medium	Активная среда	Aktiv mühit
Active circuit	Активная схема	Aktiv sxem
Impulse turbine	Активная турбина	Aktiv turbin
Active substance	Активное вещество	Aktiv maddə
Pure resistance	Активное сопротивление	Aktiv müqavimət
Active state	Активное состояние	Aktiv hal
Activity	Активность	Aktivlik, fəallıq
Ion activity	Активность ионов	İonların aktivliyi
Optical activity	Активность оптическая	Optik aktivlik
Surface activity	Активность поверхностная	Səthi aktivlik
Thermodynamic activity	Активность термодинамическая	Termodinamik aktivlik
Active nitrogen	Активный азот	Aktiv azot
Active hydrogen	Активный водород	Aktiv hidrogen
Active gas	Активный газ	Aktiv qaz
Active ion	Активный ион	Aktiv ion
Active metal	Активный металл	Aktiv metal
Active prominence	Активный протуберанец	Aktiv protuberans, Günəş səthində közərmiş qaz kütlələri
Active layer	Активный слой	Aktiv təbəqə
Active satellite	Активный спутник	Aktiv peyk
Active center	Активный центр	Aktiv mərkəz
Active electrode	Активный электрод	Aktiv elektrod
Active element	Активный элемент	Aktiv element
Actin	Актин	Aktin
Actinium	Актиний	Актиниум
Actinoid	Актиноид	Aktinoid
Actinide contraction	Актиноидное сжатие	Aktinoid sıxma
Actinometer	Актинометр	Aktinometr, Günəş şüalarının intensivliyini ölçən cihaz
Actinometry	Актинометрия	Aktinometriya
Actinouranium	Актиноуран	Aktinouran
Actomyosin	Актомиозин	Aktomiozin
Acoustics	Акустика	Akustika, səs bəhsi
Acoustomagnetoelectric effect	Акустикомагнитоэлектрический эффект	Akustik-maqnit-elektrik effekti
Acoustimeter	Акустиметр	Akustimetr
Acoustic holography	Акустическая голография	Akustik qoloqrafiya
Acoustic capacitance	Акустическая емкость	Akustik tutum
Acoustic lens	Акустическая линза	Akustik linza
Acoustic mass	Акустическая масса	Akustik kütlə
Acoustic mode	Акустическая мода	Akustik moda, dəb, adət
Acoustic feedback	Акустическая обратная связь	Akustik əks əlaqə
Acoustic compliance	Акустическая податливость	Akustik tez təsir altına düşmək
Acoustic system	Акустическая система	Akustik sistem
Acoustic frequency	Акустическая частота	Akustik tezlik
Acoustic pipe	Акустическая труба	Akustik boru

Acoustic characteristic	Акустическая характеристика	Akustik xarakteristika
Acoustic waves	Акустические волны	Akustik dalğalar
Acoustic oscillation	Акустические колебания	Akustik rəqslər
Acoustic wind	Акустический ветер	Akustik külək
Acoustic altimeter	Акустический высотомер	Akustik hündürlük ölçən
Acoustic detector	Акустический детектор	Akustik detektor
Acoustic law of Ohm	Акустический закон Ома	Omun akustika qanunu
Probe microphone	Акустический зонд	Akustik zond
Acoustic impedance	Акустический импеданс	Akustik impedans
Acoustic interferometer	Акустический интерферометр	Akustik interferometr
Acoustic labyrinth	Акустический лабиринт	Akustik səslər qarışığı
Acoustic ohm	Акустический Ом	Akustik Om
Acoustic transformer	Акустический преобразователь	Akustik dəyişdirici aparat
Acoustic depth sounding	Акустический промер глубины	Akustik dərinliyi ölçən
Acoustic resonance	Акустический резонанс	Akustik rezonans
Acoustic signal	Акустический сигнал	Akustik siqnal
Acoustic spectrum	Акустический спектр	Akustik spektr
Acoustic filter	Акустический фильтр	Akustik filtr
Acoustic element	Акустический элемент	Akustik element
Acoustic effect	Акустический эффект	Akustik effekt
Acoustic measurement	Акустическое измерение	Akustik ölçmə
Acoustic image	Акустическое изображение	Akustik xəyal
Acoustic resistance	Акустическое сопротивление	Akustik müqavimət
Acoustooptic modulation	Акустооптическая модуляция	Akustooptik modulyasiya, səsin bir tonundan digərinə keçmə
Acoustooptical medium	Акустооптическая среда	Akustooptik mühit
Acoustooptical element	Акустооптический элемент	Akustooptik element
Acoustooptical effect	Акустооптический эффект	Akustooptik effekt
Acoustooptical deflection	Акустооптическое отклонение	Akustooptik kənaraçıxma
Acoustoelectric current	Акустоэлектрический ток	Akustoelektrik cərəyan
Acoustoelectric effect	Акустоэлектрический эффект	Akustoelektrik effekt
Acceptor	Акцептор	Akseptor,. hidrogen atomunu özünə birləşdirən maddə
Acceptor impurity	Акцепторная примесь	Akseptor qarışıq
Acceptor atom	Акцепторный атом	Akseptor atom
Acceptor level	Акцепторный уровень	Akseptor səviyyə
Proton acceptor	Акцептор протона	Protonun akseptoru
Electron acceptor	Акцептор электронов	Elektronların akseptoru
Algebra	Алгебра	Cəbr
Jordan algebra	Алгебра Жордана	Jordan cəbri
Algebraic geometry	Алгебраическая геометрия	Cəbr həndəsəsi
Algebraic group	Алгебраическая группа	Cəbr qrupu
Algebraical dependence	Алгебраическая зависимость	Cəbri asılılıq
Algebraic curve	Алгебраическая кривая	Cəbri əyri
Algebraical independence	Алгебраическая независимость	Cəbri qeyri-asılılıq
Algebraic singularity	Алгебраическая особая точка	Cəbri məxsusi nöqtə
Algebraic surface	Алгебраическая поверхность	Cəbri səth
Algebraic subgroup	Алгебраическая подгруппа	Cəbri alt qrup
Algebraic system	Алгебраическая система	Cəbri sistem
Algebraic structure	Алгебраическая структура	Cəbri quruluş
Algebraic sum	Алгебраическая сумма	Cəbri cəm
Algebraic topology	Алгебраическая топология	Cəbri topologiya
Algebraic point	Алгебраическая точка	Cəbri nöqtə
Algebraic branch-point	Алгебраическая точка разветвления	Cəbri şaxələnmə nöqtəsi
Algebraic function	Алгебраическая функция	Cəbri funksiya
Algebraically dependent	Алгебраически зависимый	Cəbri asılı olma

Algebraically closed field	Алгебраически замкнутое поле	Cəbri qapalı sahə
Algebraic analysis	Алгебраический анализ	Cəbri аnaliz
Algebraically independent	Алгебраический независимый	Cəbri asılı olmamaq
Algebraic variety	Алгебраическое многообразие	Cəbri müxtəliflik, cürbəcürlük
Algebraic extension	Алгебраическое расширение	Cəbri genişlənmə
Algebraic solution	Алгебраическое решение	Cəbri həll
Algebraic correspondence	Алгебраическое соответствие	Cəbri uyğunluq
Algebraic equation	Алгебраическое уравнение	Cəbri tənlik
Algebra of logic	Алгебра логики	Məntiqin cəbri
Matrix algebra	Алгебра матриц	Matrisalar cəbri
Power associative algebra	Алгебра ассоциативными степенями	Assosiatik dərəcəli cəbr
Algebroid function	Алгеброидная функция	Cəbrli funksiya
Algorithmic language	Алгоритмический язык	Alqoritmik dil
Alidade	Алидада	Alidada
Aliphatic compound	Алифатическое соединение	Alifatik birləşmə
Alicyclic compound	Алициклическое соединение	Alisiklik birləşmə
Alkalimetry	Алкалиметрия	Alkalimetriya
Alkid resin	Алкидная смола	Alkidli qatran
Allometrism	Аллометрия	Allometriya
Allotropy	Аллотропия	Allotropluq
Allosteric enzyme	Аллостерический фермент	Allosterik ferment
Allotropyc transformation	Аллотропическое превращение	Allotropik çevirmə
Diamond structure	Алмазная структура	Almaz quruluşu
Alphanumeric	Алфавитно-цифровой	Əlifbalı-ədədi
Alphabetic code	Алфавитный код	Əlifbalı kod
Albedo	Альбедо	Albedo
Earth albedo	Альбедо Земли	Yerin albedosu
Albedometer	Альбедометр	Albedometr
Aldehyde	Альдегид	Aldehid
Almucantar	Альмукантарат	Almukantarat
Altazimuth mounting	Альтазимутальная монтировка	Altazimutal montaj etmə
Altazimuth mounting	Альтазимутальная установка	Altazimutal qurğu
Alternative hypothesis	Альтернативная гипотеза	Alternativ fərziyyə
Alpha-radioactive nucleus	Альфа-активное ядро	Alfa-fəal nüvə
Alpha emitter	Альфа-излучатель	Alfa-şüalandıran
Alpha ferrum	Альфа-железа	Alfa-dəmir
Alpha rays	Альфа-лучи	Alfa-şüalar
Alpha-decay, alpha disintegration	Альфа-распад	Alfa-çevrilmə
Alpha-ray spectrum	Альфа-спектр	Alfa-spektr
Alpha-ray spectrometer	Альфа-спектрометр	Alfa-spektrometr
Alphatron	Альфатрон	Alfatron
Alpha particle	Альфа-частица	Alfa-zərrəcik
Aluminium coulometer	Алюминиевой кулометр	Alüminium kulometri
Aluminium, aluminum	Алюминий	Alüminium
Amakrine cell	Амакриновая клетка	Amakrin qəfəsi
Amalgam	Амальгама	Amalqama
Amalgam electrode	Амальгамный электрод	Amalqam elektrodu
Ambipolar diffusion	Амбиполярная диффузия	Ambipolyar diffuziya
Ameboid movement	Амебоидное движение	Ameboid hərəkət
Americium	Америций	Amerisium
Amino acid	Аминокислота	Aminoturşu
Ammonia maser	Аммиачный мазер	Ammiaç mazer
Shockabsorber	Амортизатор	Amortizator
Amorphous region	Аморфная область	Amorf oblastı
Amorphous phase	Аморфная фаза	Amorf faza

Адсорбционная изотерма	Adsorbsiya izotermləri	Adsorbed isotherm
Адсорбционный ингибитор	Adsorbsiya ingibitoru	Adsorption inhibitor
Адсорбционный индикатор	Adsorbsiya indikatoru, təzyiqi ölçən cihaz	Adsorption indicator
Адсорбционный потенциал	Adsorbsiya potensialı	Adsorption potential
Адсорбционный слой	Adsorbsiya qatı	Adsorption layer
Адсорбционный ток	Adsorbsiya cərəyanı	Adsorption current
Адсорбция	Adsorbsiya, cisimlərin üz təbəqəsində maye və qazların udulması	Adsorption
Азеотропия	Azeotropiya	Azeotropy
Азеотропная дистилляция	Azeotrop destillə etmə	Azeotropic distillation
Азеотропная смесь	Azeotrop qarışıq	Azeotropic mixture, azeotrope
Азеотропная точка	Azeotrop nöqtəsi	Azeotropic point
Азимут	Azimut	Azimuth
Азимутальное квантовое число	Azimutal kvant ədədi	Azimuthal quantum number
Азимутальный геомагнитный эффект	Azimutal geomaqnit effekti	Azimutal geomagnetic effect
Азот	Azot	Nitrogen
Азотная кислота	Nitrat turşusu	Nitrogen acid
Азотный термометр	Azotlu termometr	Nitrogen thermometer
Айсберг	Aysberq, polyar dənizlərdə üzən buz dağı	Iceberg
Акво-ион	Akvo-ion	Aquo-ion
Акклиматизация	Yeni iqlim mühitinə uyğunlaşma	Acclimatization, acclimation
Аккумулятор	Akumulyator	Accumulator
Аклина	Aklin	Acline
Аклиническая кривая	Aklin əyrisi	Aclinic line
Аклиновый двойник	Adamın aklin oxşarı	Acline twin
Акселерометр	Akselerometr	Accelerometer
Аксиальная мода	Aksial moda	Axial mode
Аксиальная симметрия	Aksial simmetriya	Axial symmetry
Аксиальный вектор	Aksial vektor	Axial vector
Аксиома Архимеда	Arximed aksioması	Archimedes's axiom
Аксиома бесконечности	Sonsuzluq aksioması	Axiom of infinity
Аксиома выбора	Seçki aksioması	Axiom of choice
Аксиома непрерывности	Kəsilməzlik aksioması	Axiom of continuity
Аксиома о параллельных	Paralellik haqda aksioma	Axiom of parallels
Аксиома отдельности	Ayrılıq aksioması	Separation axiom
Аксиома Пеано	Peano aksioması	Peano's axiom
Аксиома счетности	Say, hesab aksioması	Countability axiom
Аксиоматизация	Aksiomatizasiya	Axiomatization
Аксиоматическая теория множеств	Çoxluğun aksioamtik nəzəriyyəsi	Axiomatic set theory
Аксиома треугольника	Üçbucaq aksioması	Triangle axiom
Аксонометрическая проекция	Aksonometrik proyeksiya	Axonometric projection
Аксоплазма	Aksoplazma	Axoplasm
Активатор	Aktivləşdirici. fəallaşdırıcı	Activator
Активационное перенапряжение	Həddindən artıq aktivləşdirilmiş gərginlik	Activation overvoltage
Активационный анализ	Aktivatik analiz	Activation analysis
Активационный потенциал	Aktivatik potensial	Activation potential
Активация	Aktivasiya	Activation
Активирование	Aktivasiya	Activation
Активированная адсорбция	Aktivləşdirilmiş adsorbsiya	Activated adsorption
Активированное состояние	Aktivləşdirilmiş hal	Activated state
Активированный комплекс	Aktivləşdirilmiş kompleks (toplu)	Activated complex
Активированный уголь	Aktivləşdirilmiş kömür	Active carbon

Русский	Azərbaycan	English
Активная гравитационная масса	Aktiv qravitasiya kütləsi	Active gravitational mass
Активная зона	Aktiv zona	Core
Активная молекула	Aktiv molekul	Active molecule
Активная мощность	Aktiv güc	Active power
Активная область на Солнце	Günəşdə aktiv oblast	Solar active region
Активная проводимость	Aktiv keçiricilik	Conductance
Активная решетка	Aktiv qəfəs	Active lattice
Активная составляющая	Aktiv tərkib hissəsi	Active component
Активная среда	Aktiv mühit	Active medium
Активная схема	Aktiv sxem	Active circuit
Активная турбина	Aktiv turbin	Impulse turbine
Активное вещество	Aktiv maddə	Active substance
Активное сопротивление	Aktiv müqavimət	Pure resistance
Активное состояние	Aktiv hal	Active state
Активность	Aktivlik, fəallıq	Activity
Активность ионов	İonların aktivliyi	Ion activity
Активность оптическая	Optik aktivlik	Optical activity
Активность поверхностная	Səthi aktivlik	Surface activity
Активность термодинамическая	Termodinamik aktivlik	Thermodynamic activity
Активный азот	Aktiv azot	Active nitrogen
Активный водород	Aktiv hidrogen	Active hydrogen
Активный газ	Aktiv qaz	Active gas
Активный ион	Aktiv ion	Active ion
Активный металл	Aktiv metal	Active metal
Активный протуберанец	Aktiv protuberans, Günəş sət-hində közərmiş qaz kütlələri	Active prominence
Активный слой	Aktiv təbəqə	Active layer
Активный спутник	Aktiv peyk	Active satellite
Активный центр	Aktiv mərkəz	Active center
Активный электрод	Aktiv elektrod	Active electrode
Активный элемент	Aktiv element	Active element
Актин	Aktin	Actin
Актиний	Актиниум	Actinium
Актиноид	Aktinoid	Actinoid
Актиноидное сжатие	Aktinoid sıxma	Actinide contraction
Актинометр	Aktinometr, Günəş şüalarının intensivliyini ölçən cihaz	Actinometer
Актинометрия	Aktinometriya	Actinometry
Актиноуран	Aktinouran	Actinouranium
Актомиозин	Aktomiozin	Actomyosin
Акустика	Akustika, səs bəhsi	Acoustics
Акустикомагнитоэлектрический эффект	Akustik-maqnit-elektrik effekti	Acoustomagnetoelectric effect
Акустиметр	Akustimetr	Acoustimeter
Акустическая голография	Akustik qoloqrafiya	Acoustic holography
Акустическая емкость	Akustik tutum	Acoustic capacitance
Акустическая линза	Akustik linza	Acoustic lens
Акустическая масса	Akustik kütlə	Acoustic mass
Акустическая мода	Akustik moda, dəb, adət	Acoustic mode
Акустическая обратная связь	Akustik əks əlaqə	Acoustic feedback
Акустическая податливость	Akustik tez təsir altına düşmək	Acoustic compliance
Акустическая система	Akustik sistem	Acoustic system
Акустическая частота	Akustik tezlik	Acoustic frequency
Акустическая труба	Akustik boru	Acoustic pipe
Акустическая характеристика	Akustik xarakteristika	Acoustic characteristic
Акустические волны	Akustik dalğalar	Acoustic waves
Акустические колебания	Akustik rəqslər	Acoustic oscillation

Русский	Azərbaycan	English
Акустический ветер	Akustik külək	Acoustic wind
Акустический высотомер	Akustik hündürlük ölçən	Acoustic altimeter
Акустический детектор	Akustik detektor	Acoustic detector
Акустический закон Ома	Omun akustika qanunu	Acoustic law of Ohm
Акустический зонд	Akustik zond	Probe microphone
Акустический импеданс	Akustik impedans	Acoustic impedance
Акустический интерферометр	Akustik interferometr	Acoustic interferometer
Акустический лабиринт	Akustik səslər qarışığı	Acoustic labyrinth
Акустический Ом	Akustik Om	Acoustic ohm
Акустический преобразователь	Akustik dəyişdirici aparat	Acoustic transformer
Акустический промер глубины	Akustik dərinliyi ölçən	Acoustic depth sounding
Акустический резонанс	Akustik rezonans	Acoustic resonance
Акустический сигнал	Akustik siqnal	Acoustic signal
Акустический спектр	Akustik spektr	Acoustic spectrum
Акустический фильтр	Akustik filtr	Acoustic filter
Акустический элемент	Akustik element	Acoustic element
Акустический эффект	Akustik effekt	Acoustic effect
Акустическое измерение	Akustik ölçmə	Acoustic measurement
Акустическое изображение	Akustik xəyal	Acoustic image
Акустическое сопротивление	Akustik müqavimət	Acoustic resistance
Акустооптическая модуляция	Akustooptik modulyasiya, səsin bir tonundan digərinə keçmə	Acoustooptic modulation
Акустооптическая среда	Akustooptik mühit	Acoustooptical medium
Акустооптический элемент	Akustooptik element	Acoustooptical element
Акустооптический эффект	Akustooptik effekt	Acoustooptical effect
Акустооптическое отклонение	Akustooptik kənaraçıxma	Acoustooptical deflection
Акустоэлектрический ток	Akustoelektrik cərəyan	Acoustoelectric current
Акустоэлектрический эффект	Akustoelektrik effekt	Acoustoelectric effect
Акцептор	Akseptor,. hidrogen atomunu özünə birləşdirən maddə	Acceptor
Акцепторная примесь	Akseptor qarışıq	Acceptor impurity
Акцепторный атом	Akseptor atom	Acceptor atom
Акцепторный уровень	Akseptor səviyyə	Acceptor level
Акцептор протона	Protonun akseptoru	Proton acceptor
Акцептор электронов	Elektronların akseptoru	Electron acceptor
Алгебра	Cəbr	Algebra
Алгебра Жордана	Jordan cəbri	Jordan algebra
Алгебраическая геометрия	Cəbr həndəsəsi	Algebraic geometry
Алгебраическая группа	Cəbr qrupu	Algebraic group
Алгебраическая зависимость	Cəbri asılılıq	Algebraical dependence
Алгебраическая кривая	Cəbri əyri	Algebraic curve
Алгебраическая независимость	Cəbri qeyri-asılılıq	Algebraical independence
Алгебраическая особая точка	Cəbri məxsusi nöqtə	Algebraic singularity
Алгебраическая поверхность	Cəbri səth	Algebraic surface
Алгебраическая подгруппа	Cəbri alt qrup	Algebraic subgroup
Алгебраическая система	Cəbri sistem	Algebraic system
Алгебраическая структура	Cəbri quruluş	Algebraic structure
Алгебраическая сумма	Cəbri cəm	Algebraic sum
Алгебраическая топология	Cəbri topologiya	Algebraic topology
Алгебраическая точка	Cəbri nöqtə	Algebraic point
Алгебраическая точка разветвления	Cəbri şaxələnmə nöqtəsi	Algebraic branch-point
Алгебраическая функция	Cəbri funksiya	Algebraic function
Алгебраически зависимый	Cəbri asılı olma	Algebraically dependent
Алгебраически замкнутое поле	Cəbri qapalı sahə	Algebraically closed field
Алгебраический анализ	Cəbri analiz	Algebraic analysis
Алгебраический независимый	Cəbri asılı olmamaq	Algebraically independent
Алгебраическое многообразие	Cəbri müxtəliflik, cürbəcürlük	Algebraic variety

Алгебраическое расширение	Cəbri genişlənmə	Algebraic extension
Алгебраическое решение	Cəbri həll	Algebraic solution
Алгебраическое соответствие	Cəbri uyğunluq	Algebraic correspondence
Алгебраическое уравнение	Cəbri tənlik	Algebraic equation
Алгебра логики	Məntiqin cəbri	Algebra of logic
Алгебра матриц	Matrisalar cəbri	Matrix algebra
Алгебра ассоциативными степенями	Assosiatik dərəcəli cəbr	Power associative algebra
Алгеброидная функция	Cəbrli funksiya	Algebroid function
Алгоритмический язык	Alqoritmik dil	Algorithmic language
Алидада	Alidada	Alidade
Алифатическое соединение	Alifatik birləşmə	Aliphatic compound
Алициклическое соединение	Alisiklik birləşmə	Alicyclic compound
Алкалиметрия	Alkalimetriya	Alkalimetry
Алкидная смола	Alkidli qatran	Alkid resin
Аллометрия	Allometriya	Allometrism
Аллотропия	Allotropluq	Allotropy
Аллостерический фермент	Allosterik ferment	Allosteric enzyme
Аллотропическое превращение	Allotropik çevirmə	Allotropyc transformation
Алмазная структура	Almaz quruluşu	Diamond structure
Алфавитно-цифровой	Əlifbalı-ədədi	Alphanumeric
Алфавитный код	Əlifbalı kod	Alphabetic code
Альбедо	Albedo	Albedo
Альбедо Земли	Yerin albedosu	Earth albedo
Альбедометр	Albedometr	Albedometer
Альдегид	Aldehid	Aldehyde
Альмукант0арат	Almukantarat	Almucantar
Альтазимутальная монтировка	Altazimutal montaj etmə	Altazimuth mounting
Альтазимутальная установка	Altazimutal qurğu	Altazimuth mounting
Альтернативная гипотеза	Alternativ fərziyyə	Alternative hypothesis
Альфа-активное ядро	Alfa-fəal nüvə	Alpha-radioactive nucleus
Альфа-излучатель	Alfa-şüalandıran	Alpha emitter
Альфа-железа	Alfa-dəmir	Alpha ferrum
Альфа-лучи	Alfa-şüalar	Alpha rays
Альфа-распад	Alfa-çevrilmə	Alpha-decay, alpha disintegration
Альфа-спектр	Alfa-spektr	Alpha-ray spectrum
Альфа-спектрометр	Alfa-spektrometr	Alpha-ray spectrometer
Альфатрон	Alfatron	Alphatron
Альфа-частица	Alfa-zərrəcik	Alpha particle
Алюминиевой кулометр	Alüminium kulometri	Aluminium coulometer
Алюминий	Alüminium	Aluminium, aluminum
Амакриновая клетка	Amakrin qəfəsi	Amakrine cell
Амальгама	Amalqama	Amalgam
Амальгамный электрод	Amalqam elektrodu	Amalgam electrode
Амбиполярная диффузия	Ambipolyar diffuziya	Ambipolar diffusion
Амебоидное движение	Ameboid hərəkət	Ameboid movement
Америций	Amerisium	Americium
Аминокислота	Aminoturşu	Amino acid
Аммиачный мазер	Ammiaç mazer	Ammonia maser
Амортизатор	Amortizator	Shockabsorber
Аморфная область	Amorf oblastı	Amorphous region
Аморфная фаза	Amorf faza	Amorphous phase
Аморфное вещество	Amorf maddə	Amorphous substance